TECHNISCHE UNIVERSITÄT MÜNCHEN

Wissenschaftszentrum Weihenstephan
für Ernährung, Landnutzung und Umwelt

On the Theoretical and Numerical Development of lattice Boltzmann Models for Biotechnology and its Applications

Mohamed A. Hussein

Vollständiger Abdruck der von der Fakultät Wissenschaftszentrum Weihenstephan für Ernährung, Landnutzung und Umwelt der Technischen Universität München zur Erlangung des akademischen Grades eines

Doktor-Ingenieurs

genehmigten Dissertation.

Vorsitzender: Univ.-Prof. Dr.-Ing. U. M. Kulozik

Prüfer der Dissertation:

1. Univ.-Prof. Dr.-Ing. Th. Becker
2. Univ.-Prof. Dr.-Ing. D. Weuster-Botz
3. Univ.-Prof. Dr.-Ing. habil. A. Delgado,
   Friedrich-Alexander-Universität Erlangen-Nürnberg

Die Dissertation wurde am 16.08.2010 bei der Technischen Universität München eingereicht und durch die Fakultät Wissenschaftszentrum Weihenstephan für Ernährung, Landnutzung und Umwelt am 17.11.2010 angenommen.

بِسْمِ اللّهِ الرَّحْمنِ الرَّحِيمِ

{وَلاَ يُحِيطُونَ بِشَيْءٍ مِّنْ عِلْمِهِ إِلاَّ بِمَا شَاء}

And they will never compass anything of His Knowledge except that which He wills

Acknowledgements

This thesis was made from 2006 to 2010 and was submitted to the Fakultät Wissenschaftszentrum Weihenstephan für Ernährung, Landnutzung und Umwelt Technische Universität Munchen.

First I would like to express gratitude to my 'Doktorvater' Prof. Dr.-Ing. Thomas Becker for his support, time, and openness to discussions, which were always very useful and constructive. He made this work possible and allowed me wide academic freedom.

I would also like to show my appreciation and gratitude to the Chair and members of my thesis' reviewing committee, Prof. Dr.-Ing. Ulrich Kulozik, Prof. Dr.-Ing. Dirk Weuster- Botz and Prof. Dr.-Ing. Antonia Delgado, for their time and effort in reviewing my thesis.

This work would have been impossible without the help of my colleagues; I would like to thank them for their help and providing me with ideas and comfort in work.

Thanks to my friends for supporting me and coping with me in times of despair and loss.

Thanks to my parents for their patience and support, without which I would have never showed up and done this work.

I can never express my honest gratefulness to my beloved wife, Hala, who always stood by me and smiled in my face, when nobody did.

Thank you all!

Table of Contents

1. Abstract **VI**

2. Publications **VIII**

3. Introduction **1**

3.1. *Short Introduction:* Modelling Philosophy and its Necessity towards Life Science 2

3.2. Modelling Considerations 5

3.2.1. Spatio-Temporal Considerations 5

3.2.2. Basic Similarity and Assumptions 7

3.3. Thesis Organization & Directions 8

4. Lattice Boltzmann Modeling **11**

4.1. Introduction to Lattice Boltzmann Modelling 12

4.1.1. Lattice Boltzmann Vs Continuum Approaches 12

4.1.2. Origins of Lattice Boltzmann Method 14

4.1.3. Lattice Boltzmann Vs Lattice Gas Automata 17

4.2. Applications of the Lattice Boltzmann Method 19

4.2.1. Single Phase Lattice Boltzmann Method 2-D and 3-D 19

4.2.2. Multi-Phase Modelling 24

4.2.3. Diffussion Modelling 26

4.2.4. Modelling of Simultaneous Heat-Moisture Diffusion 28

4.2.5. Advection-Diffusion Modelling 29

4.3. Boundary Conditions 31

2.3.1. Wall Boundary Conditions 31

2.3.1.1. Non Slip Boundary condition: Bounce back 31

2.3.1.2. Slip Boundary condition 32

2.3.1.3. Wall Temperature 33

2.3.1.4. Wall Loci Retrieving in Complex Geometries form Images 34

2.3.2. Flux Conditions: Inflow/Outflow 36

2.3.2.1. Velocity Inlet/Outlet 36

2.3.2.2. Pressure Gradient 36

2.3.2.3. Thermal Flux 37

2.3.2.4. Moisture Flux 38

2.3.3. Active Boundary Conditions 38

2.3.3.1. Absorbing and non-Absorbing Boundary Condition 38

2.3.3.2. Reaction Kinetics of Biologically Active Boundaries 39

4.4. Conclusion 40

3. Summary of Results (Thesis Publications) **42**

5.1. Paper Summary 43

5.2. Paper Copies 46

5.2.1. On the Validation of a 2-D Laminar Flow Solver Using Lattice Boltzmann Method 46
5.2.2. Impulse and mass transport in a cartilage bioreactor using the lattice Boltzmann method 55
5.2.3. On the lattice Boltzmann method simulation of a two-phase flow bioreactor for artificially grown cartilage cells 65
5.2.4. Numerical Modelling of Shear and Normal Stress of Micro-Porous Ceramics for Stimulated in-vitro Cultivation of Bone Cells. 72
5.2.5. An innovative Micro-modelling of Simultaneous Heat and Moisture Transfer during Bread Baking using the Lattice Boltzmann Method 83

4. Conclusion and Outlook 99

4.1. Modelling of biological, chemical and dynamic activity of cells 100
4.2. Micro-Macro Modelling of Heat and Moisture Transfer in Porous Dough 109

5. References 118

Appendix-A 123

A-1. Weight Factors Derivation 124
A-2. Lattice Boltzmann for the Incompressible Navier Stokes Equation 126
A-3. Linear and non-Linear Stability of the Lattice Boltzmann Method 133
A-4. Derivation of Surface Tension Interface Seperation parameter 136

Abstract

This work is contributed for the development of lattice Boltzmann modelling (LBM) for usage in biotechnological aspects. The complexity of living science systems has always hindered researchers in modelling fields. Fortunately, the ability in such methods to model bridged microscale and macroscale phenomena has enlightened the passage to achieve further possibilities in biotechnological modelling. The thesis starts by introducing the philosophy and necessity of modelling and biotechnology. The thesis defines two major quests, where both quests are quite linked in the micro-physical point of view. Both basically express several physical effects occurring in the microscale of the mentioned porous materials. The physical effects spread from reaction kinetics to heat transfer, with all the detailed difficulties and could be summarized as follow:

- The behaviour of cell activity towards substrate by means of transport limitations, reaction kinetics and mechanical stimulation in micro-channelled systems is considered. The task of better cell growth cannot be prevailed without multidisciplinary tasking: implementing the linkage between reaction rates and substrate provision, enhancement or more realistic predictions of the transport by cyclic-pressure driven diffusion coefficient. All those combined effects are discussed and investigated in this task. Several reactor design were investigated for the multidisciplinary effect and produced a 'Bioreactor Transport Map' which presents the reactor performance from the dynamical point of view (Reynolds number & mass flow rate) and its consequence on substrate limitations dominancy, whether Diffusion or advective limited. The substrate limitations were as well investigated in different transport reactor types: single phase bed reactor (dissolved aeration), two phase bed reactor (separate phase aeration) and micro-channelled reactors. As well analogical studies were held to estimate the necessary load combinations for proper stimulated cell growth *(in-vitro)* in the different investigated bioreactors. The analogy was performed between the human cells under realistic conditions and cultivated ones, worth to mention the realistic shear stress from literature is believed to be cyclic and in the

order of *0.1MPa*. The reactor designs were enhanced 4 times until reaching a shear stress value of $5.30473x10^{-4}$ from $1.0x10^{-12}MPa$.

- The understanding of diffusion-driven mass and heat transfer in non regular porous (micro-channelled) mediums such as artificial bones or dough, defines the second quest. Where the non-idealistic micro-channelling effect and its connectivity in the foams were considered. Enhanced diffusion coefficients of both mass flux and thermal flux are developed. The bridging to the macroscale is established by monitoring the bone cell growth or baking process with measurements from literature or proposed experiments in which a discrepancy of 10-15 % is reported and explained in both applications. As well possibilities arise for future work to optimize the transparency of the involved process by means of enhancing porosity and micro channelling effects, which would reflect daily on the economy of the related industrial fields.

To accomplish such objectives or quests the Boltzmann method had to be further developed. An overview of the governing equations of the different physical cases of transport were investigated and further developed, and especially elaborating the stability conditions due to time scale discrepancy between advection and diffusion where the estimated time scale jump of three orders of magnitude, O(3). As well, a detailed look upon necessary boundary conditions, phase separation and stability criterion was established. The inclusion of the sophisticated boundary conditions was elaborated; the transport mechanism through microscaffolds was further worked out. Additionally, the grasping of the complex micro-channels and microscaffolds needed a dip in the image processing to capture the three dimensional edges by analysing stacks of microcomputer tomography 2-D pictures.
The overall investigations in this thesis provided hints for future elaborations and gap points which is necessary to fill to reach more reality in the models and designs.
The research carried out in this PhD-thesis generated a number of papers accepted and published in both peer-reviewed international journals and conference proceedings.

Publications

List of Reviewed Publications

(1) Hussein, M. A., Becker, T.: Do Substrates Diffuse in Bone Tissue with a Pressure Driven Term? Biomechanics and Modeling in Mechanobiology, submitted (2010).

(2) Hussein, M. A., Becker, T.: The modelling of Acoustic Waves using Lattice Boltzmann Method in Water-Sugar solutions. Ultrasonics, submitted (2010).

(3) Hussein, M. A., Becker, T.: An innovative Micro-modelling of Simultaneous Heat and Mois-ture Transfer during Bread Baking using the Lattice Boltzmann Method. Food Biophysics (2010) DOI: 10.1007/s11483-010-9156-1

(4) Moaty Sayed, A., Hussein, M. A., Becker, T.: An innovative lattice Boltzmann model for si-mulating Michaelis–Menten-based diffusion–advection kinetics and its application within a cartilage cell bioreactor. Biomechanics and Modeling in Mechanobiology 9 (2) (2010), 141-51.

(5) Elfawakhry, H., Hussein, M. A., Becker, T.: Characterization of cereal Dough by an Innovative Ultrasonic Measuring Approach. Journal of Food Engineering (2009), (accepted).

(6) Schöck, T.; Hussein, M.; Becker, T.: Sensor array for the combined analysis of water–sugar–ethanol mixtures in yeast fermentations by ultrasound. Food Control 21 (2010), 362–369. DOI: 10.1016/j.foodcont.2009.06.017.

(7) Schöck, T.; Hussein, M.; Becker, T.: Konzentrationsbestimmung in Wasser-Zucker-Ethanol-Gemischen mittels adiabatischer Kompressibilität und Dichte. Tm-Technisches Messen 77 (2010), 30-37.

(8) Hussein, M. A., Becker, T.: Numerical Modelling of Shear and Normal Stress of Micro-Porous Ceramics for Stimulated in-vitro Cultivation of Bone Cells. Microfluidics and Nanofluidics 8 (2009), 665-675.

(9) Hussein, W. B., Hussein, M. A., Becker, T.: Detection of the Red Palm Weevil Using Its Bioacoustics Features. Journal of Bioacoustics 19 (2009).

(10) Hussein, M.A., Esterl, S. , Poertner, R., Wiegandt, K., Becker, T.: On the Lattice Boltzmann Method Simulation of a two Phase Flow Bioreactor for Artificially Grown Cartilage Cells, Journal of Biomechanics, 41 (16) (2008) 3455-3461.

(11) Hussein, M.A., Esterl, S. , Poertner, R., Wiegandt, K., Becker, T: Impulse and Mass Transport in a Cartilage Bioreactor using the Lattice Boltzmann Method, International Journal of Computational Fluid Dynamics, 22(5) (2008) 341-350.

(12) Hussein, M.A., Baumann, G., Sherif, A. O., Esterl, S., T. Becker, On the Validation of a 2-D Laminar Flow Solver Using Lattice Boltzmann Method, Proceedings Of The 8th International Congress on Fluid Dynamics and Propulsion, ASME, Sharm el Sheikh,(2006) ICFDP8-EG 200.

(13) Hussein, M.A. and Sherif, A.O. A Computational Investigation of the Back Step Flow, Proceedings of the 7th International Congress of Fluid Dynamics and Propulsion, ASME. 2001. Cairo, Egypt. ICFDP7-EG-189

List of Conferences

(14) Hecker, F.; Hussein, M.; Becker, T.: Der virtuelle Anlagenführer. 24. Durum- und Teigwaren Tagung, Detmold, 2010-04-28.

(15) Schirmer, M., Jekle, M., Hussein, M. A., Becker, T.: Krusteneigenschaften in Korrelation zur Gasfeuchte im Backraum. 60. Tagung für Bäckerei-Technologie, Detmold, 2009-11-03.

(16) Hecker, F., Hussein, M. A., Becker, T.: Qualitative Klassifizierung von Hartweizen mittels di-gitaler Bildverarbeitung. Sitzung des Durum-und Teigwaren-

Ausschusses Arbeitsgemein-schaft Getreideforschung e. V., Mannheim, Germany, 2009-09-29.

(17) Schirmer, M., Hussein, W. A., Jekle, M., Hussein, M. A., Becker, T.: Betrachtung von Struk-turbildungsreaktionen bei thermischer Behandlung von Getreideprodukten. 27. Jahrestagung der Biotechnologen, Mannheim, 2009-09-13.

(18) Krause, D., Schöck, T., Hussein, M. A., Becker, T.: Measuring Aqueous Liquids with differ-ent Sugar and Ethanol Concentrations using Ultrasound and Multivariate Regression Methods. Processnet/Jahrestagung der Biotechnologen, Mannheim, Deutschland, 2009-09-08.

(19) Moaty, A. A., Hussein, M. A., Becker, T.: An innovative method for the detection of micro-channels in porous medium using solid edge detection schemes and solving the microfluidics kinetics using Lattice Boltzmann method. Processnet/Jahrestagung der Biotechnologen, Mannheim, Germany, 2009-09-08.

(20) Elfawakhry, H., Hussein, M. A., Becker, T.: Characterization of Cereal Dough by an Innova-tive Ultrasonic Measuring Approach. 5th International Technical Symposium on Food Processing, Monitoring Technology in Bioprocesses and Food Quality Management, Potsdam, Germany, 2009-09-01.

(21) Wallhäußer, E., Hussein, M. A., Hinrichs, J., Becker, T.: The acoustic impedance – an indica-tor for concentration in alcoholic fermentation and cleaning progress of fouled tube heat ex-changers. 5th International Technical Symposium on Food Processing, Monitoring Technolo-gy in Bioprocesses and Food Quality Management, Potsdam, Germany, 2009-09-01.

(22) Hussein, W. B., Hussein, M. A., Becker, T.: Application of audio signal processing in the de-tection of the Red Palm Weevil. Eusipco (17th European Signal Processing Confernce) Glas-gow, Scottland, 2009-08-24.

(23) Hussein, W. B., Hussein, M. A., Becker, T.: Application of audio signal processing in the de-tection of the Red Palm Weevil. The 17th European Signal Processing Conference, Glasgow, Scottland, 2009-08-24, 1597-1601.

(24) Krause, D., Schöck, T., Hussein, M. A., Becker, T.: Measuring Aqueous Liquids with differ-ent Sugar and Ethanol Concentrations using Ultrasound and Multivariate Regression Methods. 22. VH-Hefetagung, Berlin, Germany, 2009-04-27.

(25) Elfawakhry, H., Hussein, M. A., Becker, T.: An Innovative Non-Invasive Characterization of Dough Types Using Ultraound. Jahrestreffen des Fachausschusses Lebensmittelverfahrens-technik, Lausanne, Schweiz, 2009-03-23.

(26) Hussein, M. A., Becker, T.: An Innovative Method for the Detection of Microchannels in Porous Medium using Solid Edge Detection Schemes and solving the Microfluidics Using Lattice Boltzmann Method. Jahrestreffen des Fachausschusses Lebensmittelverfahrenstechnik, Lausanne, Schweiz, 2009-03-23.

(27) Krause, D., Schöck, T., Hussein, M. A., Becker, T.: Ultrasonic Characterization of Aqueous Solutions with varying Sugar and Ethanol Content using Multivariate Regression Methods. Jahrestreffen des Fachausschusses Lebensmittelverfahrenstechnik, Lausanne, Schweiz, 2009-03-23.

(28) Moaty, A. A., Hussein, M. A., Becker, T.: On the Usage of Image Processing as an Optimization Tool for Food Applications. Jahrestreffen des Fachausschusses Lebensmittelver-fahrenstechnik, Lausanne, Schweiz, 2009-03-23.

(29) Jekle, M., Moaty, A. A., Hussein, M. A., Becker, T.: Visuelle Teigbewertung. Detmolder Stu-dientage, Detmold, Germany, 2009-02-18.

(30) Hussein, M. A., Moaty, A. A., Becker, T.: On the Flow Investigations inside Cartilage Cell-Breeding Bioreactors using the Lattice Boltzmann Method European BioPerspectives, Han-nover, Germany, 2009-10-07.

(31) Moaty, A. A., Hussein, M. A., Becker, T.: Enhancement of the cyclic load on Cartilage cells grown in a Bioreactor by cyclic wall conditions. European BioPerspectives, Hannover, Ger-many, 2009-10-07.

(32) Hussein, M. A., Schöck, T., Becker, T.: Ultrasonic based sensor array for the simultaneous analysis of sugar and ethanol for the bioethanol production. European BioPerspectives, Han-nover, Germany, 2009-10-7.

(33) Jekle, M., Hussein, M. A., Mitzscherling, M., Becker, T.: Visuelle Teigbewertung. 59. Tagung für Bäckerei-Technologie, Detmold, 2008-11-06.

(34) Hussein, M. A., Becker, T.: On the Simulation and Evaluation of a Two-Phase Bioreactor 66. FEI Jahrestagung, Hohenheim, Germany, 2008-09-02.

(35) Moaty, A. A., Hussein, M. A., Becker, T.: Design Considerations of a Porous Plug Bioreactor using Lattice Boltzmann Method , , . 66. FEI Jahrestagung, Hohenheim, Germany, 2008-09-02.

(36) Elfawakhry, H., Hussein, M. A., Becker, T.: Characterization of cereal doughs by an innova-tive ultrasonic measuring approach. 1st Arab European FoodTech Days, Cairo, Egypt, 2008-08-16.

(37) Hussein, M. A., Baumann, G., Sherif, A. O., Esterl, S., Becker, T.: On the Validation of a 2-D Laminar Flow Solver Using Lattice Boltzmann Method. Proceedings of 8th International Congress of Fluid Dynamics and Propulsion, ASME, Sharm El-Sheikh, Egypt, 2006-12-17.

Publications

List of Reviewed Publications

(1) Hussein, M. A.; Becker, T.: Do Substrates Diffuse in Bone Tissue with a Pressure Driven Term? Biomechanics and Modeling in Mechanobiology, submitted (2010).

(2) Hussein, M. A.; Becker, T.: The modelling of Acoustic Waves using Lattice Boltzmann Method in Water-Sugar solutions. Ultrasonics, submitted (2010).

(3) Hussein, M. A.; Becker, T.: An innovative Micro-modelling of Simultaneous Heat and Moisture Transfer during Bread Baking using the Lattice Boltzmann Method. Food Biophysics (2010), DOI: 10.1007/s11483-010-9156-1

(4) Moaty Sayed, A.; Hussein, M. A.; Becker, T.: An innovative lattice Boltzmann model for simulating Michaelis–Menten-based diffusion–advection kinetics and its application within a cartilage cell bioreactor. Biomechanics and Modeling in Mechanobiology 9 (2) (2010), 141-51.

(5) Elfawakhry, H.; Hussein, M. A.; Becker, T.: Characterization of cereal Dough by an Innovative Ultrasonic Measuring Approach. Journal of Food Engineering (2009), (accepted).

(6) Schöck, T.; Hussein, M.; Becker, T.: Sensor array for the combined analysis of water–sugar–ethanol mixtures in yeast fermentations by ultrasound. Food Control 21 (2010), 362–369.

(7) Schöck, T.; Hussein, M.; Becker, T.: Konzentrationsbestimmung in Wasser-Zucker-Ethanol-Gemischen mittels adiabatischer Kompressibilität und Dichte. Tm-Technisches Messen 77 (2010), 30-37.

(8) Hussein, M. A.; Becker, T.: Numerical Modelling of Shear and Normal Stress of Micro-Porous Ceramics for Stimulated in-vitro Cultivation of Bone Cells. Microfluidics and Nanofluidics 8 (2009), 665-675.

(9) Hussein, W. B.; Hussein, M. A.; Becker, T.: Detection of the Red Palm Weevil Using Its Bioacoustics Features. Journal of Bioacoustics 19 (2009).

(10) Hussein, M.A.; Esterl, S. , Poertner, R.; Wiegandt, K.; Becker, T.: On the Lattice Boltzmann Method Simulation of a two Phase Flow Bioreactor for Artificially Grown Cartilage Cells, Journal of Biomechanics 41 (16) (2008), 3455-3461.

(11) Hussein, M.A.; Esterl, S. , Poertner, R.; Wiegandt, K.; Becker, T: Impulse and Mass Transport in a Cartilage Bioreactor using the Lattice Boltzmann Method, International Journal of Computational Fluid Dynamics 22 (5) (2008), 341-350.

(12) Hussein, M.A.; Baumann, G.; Sherif, A. O.; Esterl, S.; T. Becker.: On the Validation of a 2-D Laminar Flow Solver Using Lattice Boltzmann Method, Proceedings of the 8th International Congress on Fluid Dynamics and Propulsion, ASME (2006), Sharm El-Sheikh, Egypt, ICFDP8-EG 200.

(13) Hussein, M.A.; Sherif, A.O.: A Computational Investigation of the Back Step Flow, Proceedings of the 7th International Congress of Fluid Dynamics and Propulsion, ASME, Cairo, Egypt, ICFDP7-EG-189.

List of Conferences

(14) Hecker, F.; Hussein, M.; Becker, T.: Der virtuelle Anlagenführer. 24. Durum- und Teigwaren Tagung, Detmold, Germany 2010-04-28.

(15) Schirmer, M.; Jekle, M.; Hussein, M. A.; Becker, T.: Krusteneigenschaften in Korrelation zur Gasfeuchte im Backraum. 60. Tagung für Bäckerei-Technologie, Detmold, Germany 2009-11-03.

(16) Hecker, F.; Hussein, M. A.; Becker, T.: Qualitative Klassifizierung von Hartweizen mittels digitaler Bildverarbeitung. Sitzung des Durum- und Teigwaren-Ausschusses Arbeitsgemeinschaft Getreideforschung e. V., Mannheim, Germany, 2009-09-29.

(17) Schirmer, M.; Hussein, W. A.; Jekle, M.; Hussein, M. A.; Becker, T.: Betrachtung von Strukturbildungsreaktionen bei thermischer Behandlung von Getreideprodukten. 27. Jahrestagung der Biotechnologen, Mannheim, Germany, 2009-09-13.

(18) Krause, D.; Schöck, T.; Hussein, M. A.; Becker, T.: Measuring Aqueous Liquids with different Sugar and Ethanol Concentrations using Ultrasound and Multivariate Regression Methods. Processnet/Jahrestagung der Biotechnologen, Mannheim, Germany, 2009-09-08.

(19) Moaty, A. A.; Hussein, M. A.; Becker, T.: An innovative method for the detection of micro-channels in porous medium using solid edge detection schemes and solving the microfluidics kinetics using Lattice Boltzmann method. Processnet/Jahrestagung der Biotechnologen, Mannheim, Germany, 2009-09-08.

(20) Elfawakhry, H.; Hussein, M. A.; Becker, T.: Characterization of Cereal Dough by an Innovative Ultrasonic Measuring Approach. 5th International Technical Symposium on Food Processing, Monitoring Technology in Bioprocesses and Food Quality Management, Potsdam, Germany, 2009-09-01.

(21) Wallhäußer, E.; Hussein, M. A.; Hinrichs, J.; Becker, T.: The acoustic impedance – an indicator for concentration in alcoholic fermentation and cleaning progress of fouled tube heat ex-changers. 5th International Technical Symposium on Food Processing, Monitoring Technology in Bioprocesses and Food Quality Management, Potsdam, Germany, 2009-09-01.

(22) Hussein, W. B.; Hussein, M. A.; Becker, T.: Application of audio signal processing in the detection of the Red Palm Weevil. Eusipco (17th European Signal Processing Confernce) Glasgow, Scottland, 2009-08-24, 1597-1601.

(23) Krause, D.; Schöck, T.; Hussein, M. A.; Becker, T.: Measuring Aqueous Liquids with different Sugar and Ethanol Concentrations using Ultrasound and Multivariate Regression Methods. 22. VH-Hefetagung, Berlin, Germany, 2009-04-27.

(24) Elfawakhry, H.; Hussein, M. A.; Becker, T.: An Innovative Non-Invasive Characterization of Dough Types Using Ultraound. Jahrestreffen des Fachausschusses Lebensmittelverfahrenstechnik, Lausanne, Switzerland, 2009-03-23.

(25) Hussein, M. A.; Becker, T.: An Innovative Method for the Detection of Microchannels in Porous Medium using Solid Edge Detection Schemes and solving the Microfluidics Using Lattice Boltzmann Method. Jahrestreffen des Fachausschusses Lebensmittelverfahrenstechnik, Lausanne, Switzerland, 2009-03-23.

(26) Krause, D.; Schöck, T.; Hussein, M. A.; Becker, T.: Ultrasonic Characterization of Aqueous Solutions with varying Sugar and Ethanol Content using Multivariate Regression Methods. Jahrestreffen des Fachausschusses Lebensmittelverfahrenstechnik, Lausanne, Switzerland, 2009-03-23.

(27) Moaty, A. A.; Hussein, M. A.; Becker, T.: On the Usage of Image Processing as an Optimization Tool for Food Applications. Jahrestreffen des Fachausschusses Lebensmittelverfahrenstechnik, Lausanne, Switzerland, 2009-03-23.

(28) Jekle, M.; Moaty, A. A.; Hussein, M. A.; Becker, T.: Visuelle Teigbewertung. Detmolder Studientage, Detmold, Germany, 2009-02-18.

(29) Hussein, M. A.; Moaty, A. A.; Becker, T.: On the Flow Investigations inside Cartilage Cell-Breeding Bioreactors using the Lattice Boltzmann Method European BioPerspectives, Hannover, Germany, 2009-10-07.

(30) Moaty, A. A.; Hussein, M. A.; Becker, T.: Enhancement of the cyclic load on Cartilage cells grown in a Bioreactor by cyclic wall conditions. European BioPerspectives, Hannover, Germany, 2009-10-07.

(31) Hussein, M. A.; Schöck, T.; Becker, T.: Ultrasonic based sensor array for the simultaneous analysis of sugar and ethanol for the bioethanol production. European BioPerspectives, Hannover, Germany, 2009-10-7.

(32) Jekle, M.; Hussein, M. A.; Mitzscherling, M.; Becker, T.: Visuelle Teigbewertung. 59. Tagung für Bäckerei-Technologie, Detmold, Germany, 2008-11-06.

(33) Hussein, M. A.; Becker, T.: On the Simulation and Evaluation of a Two-Phase Bioreactor 66. FEI Jahrestagung, Hohenheim, Germany, 2008-09-02.

(34) Moaty, A. A.; Hussein, M. A.; Becker, T.: Design Considerations of a Porous Plug Bioreactor using Lattice Boltzmann Method. 66. FEI Jahrestagung, Hohenheim, Germany, 2008-09-02.

(35) Elfawakhry, H.; Hussein, M. A.; Becker, T.: Characterization of cereal doughs by an innovative ultrasonic measuring approach. 1st Arab European FoodTech Days, Cairo, Egypt, 2008-08-16.

(36) Hussein, M.A.; Baumann, G.; Sherif, A. O.; Esterl, S.; T. Becker.: On the Validation of a 2-D Laminar Flow Solver Using Lattice Boltzmann Method, Proceedings of the 8th International Congress on Fluid Dynamics and Propulsion, ASME, Sharm El-Sheikh, Egypt, 2006-12-17.

(37) Hussein, M.A.; Sherif, A.O.: A Computational Investigation of the Back Step Flow, Proceedings of the 7th International Congress of Fluid Dynamics and Propulsion, ASME, Cairo, Egypt, 2001-12-14.

1. Introduction

1 Introduction

1.1 *Short Introduction:*

Modelling Philosophy and its Necessity towards Life Science

The word "modelling" comes from the Latin word *modellus*, which describes the methodology with which humans handle with realism and its consequences. The ability to build abstract models is the most responsible feature for the supremacy of *Homo sapiens* over less developed races such as the *Homo neandertalensis*, as believed by Anthropologists.

Although abstract representations of real *objects* have been in use since the Stone Age, a fact supported by cavemen paintings, the real breakthrough of modelling came with the cultures of the Ancient Near East and with the Ancient Greek.

Several historic findings provide evidence of mathematical modelling of faced problems such as the most ancient mathematical texts:

- Plimpton 322 (Babylonian mathematics c. 1900 BC)
- The Moscow Mathematical Papyrus (Egyptian mathematics c. 1850 BC)
- The Rhind Mathematical Papyrus (Egyptian mathematics c. 1650 BC)
- Greek ancient mechanical calculator (Greek mathematics c. 400 BC)
- The famous models developed by Archimedes (250 BC)

Figure 1.1:
Tablet YBC 7289 (original dated 1800 B.C.), showing a Babylonian approximations to the square root of 2 in the context of Pythagoras' Theorem for an isosceles triangle.
The original tablet is in the in the Yale Babylonian Collection [1].

Figure 1.2:
Egyptian Ahmoss Papyrus (Dated 1650 B.C.) demonstrating awareness of composite and prime numbers; arithmetic, geometric and harmonic means. The papyrus also shows knowledge of solving first order linear equations and summing arithmetic and geometric series.

Figure 1.3:
Greek mathematics and astronomy reached a rather advanced stage during Hellenism, with scholars such as Hipparchus, Posidonius and Ptolemy, capable of the construction of simple mechanical calculator such as the Antikythera (400 BC).

Figure 1.4:
Archimedes of Syracuse (287 BC–212 BC) is generally considered to be the greatest mathematician of antiquity and one of the greatest of all time.

Figure 1.5:
Al-Khwarizmi (c.820) is often called the "father of algebra", for his fundamental contributions to the field. He gave an exhaustive explanation for the algebraic solution of quadratic equations with positive roots, and he was the first to teach algebra in an elementary form and for its own sake. He also introduced the fundamental method of "reduction" and "balancing", referring to the transposition of subtracted terms to the other side of an equation

Knowledge in all its forms, whether orally or scripted, steered the awareness of mankind into easing his basic challenges of feeding, living and adapting. The evolution of modelling and mathematics had emerged and surfaced all darkness ages bringing human race into more consciousness of his surroundings. This enabled humanity to spread and enlighten the passage for improved self-living circumstances.

Until this second, modelling and mathematics play an important role in various applications starting from life threatening needs such as: contamination dispersion, fire, explosion modelling; up to the basic needs occurring on a daily basis such as: health maintain, food production and more generally life science.

> *Food process modelling provides an authoritative review of one of the most exciting and influential developments in the food industry. The modelling of food processes allows analysts not only to understand such processes more clearly but also to control them more closely and make predictions about them. Modelling thus provides the foundation for future improvements in food quality [2]. Simulation tools are often used for supporting decision-making on food supply chain (re)design when logistic uncertainties are in place, building on their inherent modelling flexibility [3].*

Modern modelling supports the basic philosophy that analyses, simulations, and predictions are a good path to efficiency and problem spotting and solving. Mathematical models make it possible to identify uncertainties and pitfalls that could have an effect on vital needs. This insight and control have made mathematical modelling a particularly popular tool.

Modelling methods have continuously provided trends for developing advanced controls for machinery, devices, and processes. Such methods enable the possibility to forecast upcoming trends and difficulties forthcoming in an individual process. Considerately these prediction properties reduce development time sharply as well as the diminishing of time constants. The consequences of changes can be seen already at the model level, such that unnecessary tests can be avoided. Such test can count up to great costs as in biotechnological applications, where the testing costs might be a human life.

> *The cost of failure can be catastrophic for pharmaceutical companies. According to the Tufts Center for the Study of Drug Development, the average cost of bringing a new drug to market is $802 million, and the process can take as long as 12 years.*

Protracted development is costly, especially if the drug ultimately fails to meet the regulatory and clinical tests. But with computer modelling, the assembly of chemical compound libraries can be directed to try the most promising combinations. "You can build models of biological processes at the molecular level—and you can start to do experiments in the computer to see how your models will behave under certain circumstances" [4].

Diverse applications using Modelling for bio-chemistry have reported immense cost savings using modelling and findings prove its vitality. It is also a key underpinning capability for many aspects of the Biotechnology key technology themes, for example

- Design, Engineering and Manufacture - for optimum bio-process design and control
- Sustainable Production & Consumption - for understanding product life cycles
- Bioscience & Healthcare - for fundamental product design
- Advanced Materials - for design and optimisation
- Information & Communication Technology - a high added value application of ICT
- Energy - for design and understanding of alternative technologies

"Mathematical modelling is very powerful," said Ravindra Ahuja, a professor of industrial and systems engineering and the lead researcher on the project. "Companies don't often realize that mathematical models can result in substantial cost savings for them and pay back for the developmental cost in a couple of months, or even sooner" [5].

Life sciences, the past two centuries, have witnessed tremendous progress as human improved their understanding of living things wherein: biology, medicine, food sciences have remain centrepieces, technological advances in molecular biology and biotechnology have led to a burgeoning of specializations and new, often interdisciplinary, fields in life science. Nevertheless insufficient knowledge of the underlying physical principles in such fields is still persisting [6].

The revolutionary growth in the computational knowledge and power has triggered a new era for biotechnologists, who nevertheless need modelling techniques in their work. Such multidisciplinary field requires a well established realization of chemical process and their biological activity in a frame of mass and energy balances combined with the rates of the process in a multi-dimensional manner. Yet, applying micro-modelling theories to the complicate phenomena of biochemical processes have opened further detailed possibilities in perception of kinetics, large scale fermentation, enzymatic processes, tissue engineering, food production control and optimization.

Tissue engineering has recently risen as a life saver for patients of bone damage or disorder due to trauma, tumour, pathological degeneration and congenital deformity.

Recent statistics of expenditure in bone surgery and transplants [7] suggested costs of up to 100 billion US dollars in the states and around 5 billion US dollars in Europe annually. Bone tissue engineering is a multidisciplinary job and has been of great challenge to scientist since it's emerging in the 80's. Due to the works complexity it requires the integration of different scientific fields of biology, chemistry, engineering and medicine under a modelling umbrella in order to save real time trials inside humans [8].

Concluding to the following points:

1. Historical findings prove that ever since humans exist they tried to use preliminary mathematics and in some cases modelling to handle their everyday threats.
2. Up to now, modelling and mathematics provides great help for life essentials: Health maintains food production and more generally life science.
3. Modelling has great perception in test cost and failure cost reduction, which sometimes could be a human life as in Biotechnology and Medicine.
4. Growth in computational power, especially for micro-modelling, has added great value for scientists, as more light resolute complicate underlying phenomena of biochemical processes.

Build upon those thoughts the investigations in this thesis are focussed to life science modelling. Where diverse applications are addressed (Cell kinetics modelling, non-Newtonian modelling, acoustic propagations in mediums, Heat and mess transfer in dough-foam mediums), utilizing computational knowledge to reach s step forth in the investigations of the underlying physics, further details are provided in section 1.3.

1.2 Modelling Considerations

In order to achieve plausible modelling, a thorough look must be realized on the spatial and temporal level of information extract. This can be achieved by considerations of the detailed requirement of the system analysed, In other words, considering only the influential detail on the phenomena investigated. Additionally, the feasibility of the model is determined by means of the proximity of the analogy between the real setup and the numerical one, this could be achieved by means of similarity satisfaction.

1.2.1 Spatio-Temporal Considerations

Modelling in general can be described at different spatial-temporal levels depending on the scale at which the physics or mechanisms of interest exists. Meaning, if the goal is to extract information about microscopic properties at the atomic or molecular scales, then one is forced to model at the molecular scale with convenient molecular mechanisms. On the other hand, if the focus of interest falls within the collective behaviour, then the

microscopic physics can be neglected and a continuum view is adequate. Furthermore if the interest lay in regions where the continuum hypothesis fail and the spatial-temporal resolution is still order of magnitude higher than the molecular ones, mesoscale is sought. In detail, the three main categories can be summarised as follows:

- *Microscopic regime:* Classical mechanics equations are held on the atomic or molecular level by approximations of known physics, giving a view of the motion of the particles (i.e. Molecular Dynamics where Newton's laws apply with a molecular force term for chemical bonds and electro-static forces) This kind of simulation is frequently used in the study of proteins and bio-molecules, as well as in materials science. Although of its rising attractiveness in providing a closer look into systems with high temporal and spatial resolution (fine graining), though it lacks numerical stabilities and computationally quite demanding.
- *Macroscopic regime:* Conservation equations are set to describe the collective motion of continuum mediums which totally fills the space it occupies (i.e. mass, momentum and energy conservations as in Navier-Stokes equations). Such models ignores the fact that matter is made of atoms, on spatial scales much bigger than intermolecular distances such approximations are valid. Such models are quite accurate in large scale applications and are mostly not suitable to handle phenomena occurring in the micro-scale level.
- *Mesoscopic regime:* The models are often an approximation of the microscopic ones, by means of clustering molecules (coarse graining) into sets of particles (i.e. particle mass conservation as in Boltzmann equation) This opens the possibility of accepting statistical rules on the particle sets rather than considering distinction between them, as in the case of molecular dynamics or quantum mechanics. Although of the approximation, such models are quite flexible and have vast fields of applications in modern modelling, especially in life science, as they sustain feasible results in both micro- and macro-scale.

The vast rise of computational power has paved the way to life-scientists to have a closer look at the phenomena occurring. The complex nature of most natural systems in life sciences means that a multidisciplinary approach is required to investigate their functioning: Requiring a deep realization of chemical processes and their biological activity across a broad spectrum of temporal and spatial resolute dynamics. Figure 1.6 illustrates the two different regimes life-scientists have recently used for further understanding underlying phenomena. The Mesoscopic modelling is chosen in this work as a requisite to address broad spectrums of Spatio-temporal realization in the life science applications discussed.

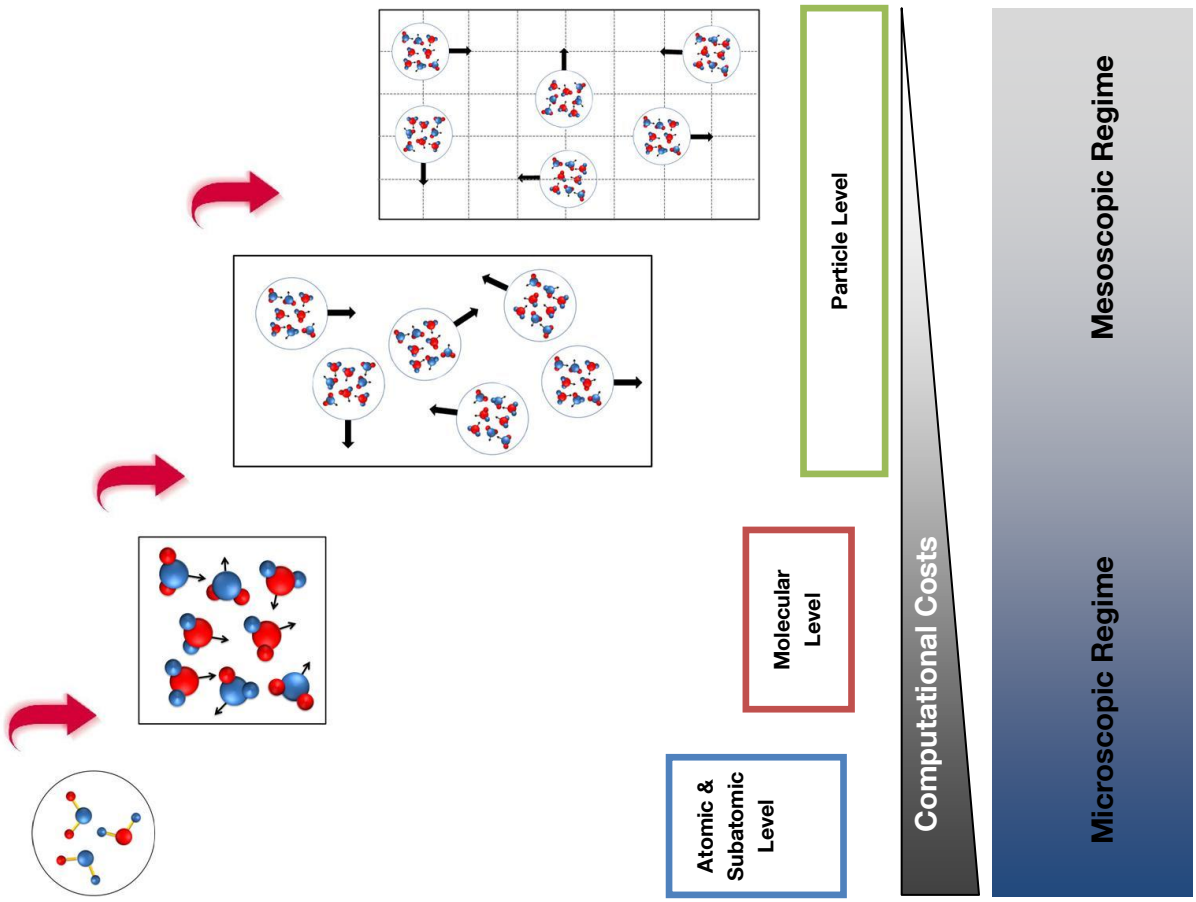

Figure 1.6 This figure illustrates the two different regimes which life-scientists have recently used for further understanding underlying phenomena: Microscopic and Mesoscopic. Showing that an investigation on the atomic scale of a phenomenon would result in immense computational costs which would reduce as the spatial level increases.

The Boltzmann transport equation, is one of the recently emerging particle dynamics techniques, often used for microscale and mesoscale modelling, developed by Ludwig Boltzmann in 1872 . The method describes the statistical distribution of one particle in a fluid. It is one of the most important equations of non-equilibrium statistical meso-mechanics

1.2.2 Basic similarity and assumptions

For successful modelling, the mechanism must be accompanied by similarity analysis to determine the assumed conditions under which the system may be analogous to the real scenario. While the geometry may be simply scaled, other dynamic parameters, such as pressure, temperature, rates and medium properties may need to be altered. Similarity is achieved when testing conditions are created analogous to the real scenario, In other words full geometric, kinematic and dynamic similarity, thus, to achieve absolute similarity in a certain model the following criterion must be fully satisfied:

- *Geometric similarity:* The model must have the same shape and geometry ratios as the real application.

- *Kinematic similarity:* medium transfer rates of the model must be identical to the real application
- *Dynamic similarity:* Mass, Force, momentum and thermal ratios must be indistinguishable from the real case.

It is often quite hard to accomplish straight similarity while modelling a certain application under certain assumptions. Often, this is due to the mathematical stability of the proposed models, which has always been an open field for scientists to enlarge the stable regions for their proposed models. Using microscale modelling has greatly hindered the stability problems occurring in the classical non-microscale models. In chapter 2, detailed investigation of the similarity and stability conditions of each proposed model is reported

1.3 Thesis Organization & Directions

The work in this thesis is divided into 4 coherent chapters, the thesis is written in a query-reply form for an efficient, to the point, handling and understanding. Chapter 1 is an introduction which re-explores the origin and philosophy of modelling. As well, the chapter discusses the necessity of modelling at all, with special focus on life science; sample quotations from key references in the diverse fields of life science are cited. The chapter as well discusses the different spatial-temporal resolutions in modern modelling and showing the differences and reasons for the choice of the Mesoscopic scale. Additionally, guidelines for successful and realistic modelling are pointed.

The second chapter starts by introducing the lattice Boltzmann method, its origin and compares it with its predecessor: lattice gas automata. Then the necessary theoretical workout of the lattice Boltzmann method to cover and investigates life science applications with its living, dynamic rules. Where the following life science applications are addressed: single and multiphase flow, reaction kinetics, cell kinetics modelling, non-Newtonian modelling, acoustic propagations in mediums, simultaneous heat and mass transfer in foams, micro-channel flow, cyclic excited flow and moisture driven flux. Due to the diverse time scales of the mentioned phenomena a confined stability analysis is developed to guarantee reliable physical results.

The research carried out in this PhD-thesis generated a number of papers accepted and published in both peer-reviewed international journals and conference proceedings. The papers are listed below in chronological order, and samples of those papers are included in Chapter 3:

Reviewed papers:

1. Hussein, M. A., Becker, T.: An innovative Micro-modelling of Simultaneous Heat and Moisture Transfer during Bread Baking using the Lattice Boltzmann Method. Food Biophysics (2010) DOI: 10.1007/s11483-010-9156-1
2. Hussein, M. A., Becker, T.: Numerical Modelling of Shear and Normal Stress of Micro-Porous Ceramics for Stimulated in-vitro Cultivation of Bone Cells. Microfluidics and Nanofluidics 8 (2009), 665-675.
3. Hussein, M. A., Esterl, S., Pörtner, R., Wiegandt, K., Becker, T.: On the lattice Boltzmann method simulation of a two-phase flow bioreactor for artificially grown cartilage cells. Journal of Biomechanics 41 (2008), 3455-3461.
4. Hussein, M. A., Esterl, S., Pörtner, R., Wiegandt, K., Becker, T.: Impulse and mass transport in a cartilage bioreactor using the lattice Boltzmann method. International Journal of Computational Fluid Dynamics 22 (2008), 341 - 350.
5. Hussein, M. A., Baumann, G., Sherif, A. O., Esterl, S., Becker, T.: On the Validation of a 2-D Laminar Flow Solver Using Lattice Boltzmann Method. Proceedings of 8th International Congress of Fluid Dynamics and Propulsion, American Society of Mechanical Engineers, Sharm El-Sheikh, Egypt, 2006-12-14, ICFDP8-EG-200.

Conference Proceedings (None reviewed):

6. Hussein, M. A., Becker, T.: An Innovative Method for the Detection of Microchannels in Porous Medium using Solid Edge Detection Schemes and solving the Microfluidics Using Lattice Boltzmann Method. Jahrestreffen des Fachausschusses Lebensmittelverfahrenstechnik, Lausanne, Schweiz, 2009-03-23.
7. Hussein, M. A., Moaty, A. A., Becker, T.: On the Flow Investigations inside Cartilage Cell-Breeding Bioreactors using the Lattice Boltzmann Method European Bio-Perspectives, Hannover, Germany, 2009-10-07.
8. Hussein, M. A., Schöck, T., Becker, T.: Ultrasonic based sensor array for the simultaneous analysis of sugar and ethanol for the bio-ethanol production. European Bio-Perspectives, Hannover, Germany, 2009-10-7.
9. Hussein, M. A., Becker, T.: On the Simulation and Evaluation of a Two-Phase Bio-reactor 66. FEI Jahrestagung, Hohenheim, Germany, 2008-09-02.

The investigation in those papers utilizes the developed methods in chapter 2 for addressing several physical queries in life sciences existing in several applications. I begin the exposition of the papers by the first paper which is a validation paper for the two-Dimensional solver. Using the standard benchmark problems the solver is validated and the computational effort is reported. Once the solver was validated it was used in the second paper to model the transport of substrate to cells in diffused manner and the limitations on such a transport mechanism. The third paper elaborates by introducing another type of reactor where the substrate exists in an independent phase, i.e. two phase system. The challenge here introduces the multi-phase LBM and the solubility effect is included between the two phases. Nevertheless, not only substrate provision could limit the cell growth but as well the loading conditions. In order to develop load carrying-cells (cartilage or skeletal) the stress conditions has to be identical to the realistic ones, this is investigated deeply in the fourth paper. The fifth paper deals with heat and mass transfer inside foams with a special application in food-foams as in dough. The work is investigated with the intention to

understand the the internal moisture transfer for arguments of optimizing the heating process which could reflect on the economy, since dough is a daily requisite for humans. Chapter four discusses the main answers and investigations described in this thesis and accounts for the drawbacks which need further enhancements and overworking. The discussions are divided into two main themes: The modelling of cell activity and the Micro-Macro Bridging in the modelling of simultaneous Heat and mass transfer in porous Dough.

2. Lattice Boltzmann Modelling

2.1 Introduction to Lattice Boltzmann Modelling

Owing to its excellent stability and abilities to model: complicated geometrical boundary conditions, multi-scale flow phenomena, phase transformation in flows, complex solid–liquid interfaces, surface reactions in fluids, liquid–solid flows of colloidal suspensions and turbulence. Lattice Boltzmann Methods (LBM) has risen as a remarkable shift in modelling philosophy when compared to the conventional modelling approaches of continuum dynamics [9-10] and particle dynamics.

2.1.1 Lattice Boltzmann Method Vs Continuum Approaches

Modelling using continuum approaches ignores the fact that matter is made of atoms, and therefore not continuous; however, on length scales much greater than that of inter-atomic distances, such models are highly reliable. Continuum mechanics deals with physical properties of solids and fluids which are independent of any particular coordinate system in which they are observed except the temporal scale, which does not fulfil the Galilean invariance (Physical equations are Spatio-temporal independent).

On the other hand, Lattice Boltzmann methods replace the macroscopic picture underlying the continuum framework by discrete sets of pseudo-particles that are represented by a particle distribution function, both systems are shown in figure 2.1 and 2.2.

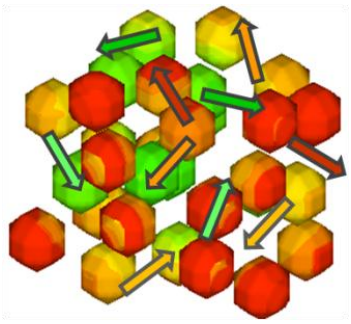

Figure 2.1: Lattice Boltzmann methods use discrete sets of pseudo-particles to model fluid portions and these particles interact following motion and collision rules in the micro- meso-scale.

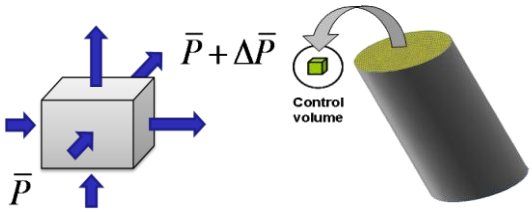

Figure 2.2: The classical continuum approaches, instead, use a control volume approach to model fluid portions and apply the conservation rules on these control volumes.

The particle distribution in the Boltzmann equation are said to follow a Maxwell Boltzmann distribution, which distributes the fluid particle portions in dependence of position, momentum and temperature or the temperature dependent speed of sound. Such distribution benefit from the full coverage of the energy spectrum, this will be explained later in section 2.2.

These fluid particles reside and interact on the nodes of a grid. System dynamics and complexity emerge by the repeated application of local rules for the motion, collision and redistribution of these coarse-grained droplets. The collision term can include different

phenomena influencing the collision by means of diverse energies (Thermal, Kinetic, Magnetic, Acoustic and reactive) allowing the possibility of having different relaxation times for each, which resolves the Galilean variance occurring in the continuum approaches. Nevertheless, it is well known that the original lattice Boltzmann (LB) equation experiences an unphysical velocity-dependent viscosity. This unphysical dependence violates the Galilean invariance and limits the validation domain of the LB method to near incompressible flows; recovery of correct transport phenomena in kinetic equations depends on various transport coefficients. Several publications have upgraded the LB equations to satisfy the Galilean invariance by involving enhanced particle distribution to fulfil high speeds (highly compressible flows) and high energy flows [11]. In this thesis such distribution functions are not used, since the applications addressed do not reach the compressibility limit.

Worth to mention is the straightforward implementation of the grid system in the LBM where, the particle sets can be implemented on a number of different lattices, both cubic and triangular, and with or without rest particles in the discrete distribution function. A popular way of classifying the different methods by lattice is the DnQm scheme. Here "Dn" stands for "n dimensions" while "Qm" stands for "m speeds". For example, D3Q19 is a three-dimensional Lattice Boltzmann model on a cubic grid, with rest particles present. Such lattice experience better transfer and flux equilibrium with neighbour lattices, because of the presence of four connecting vectors per interfacial plane, see figure 2.3.

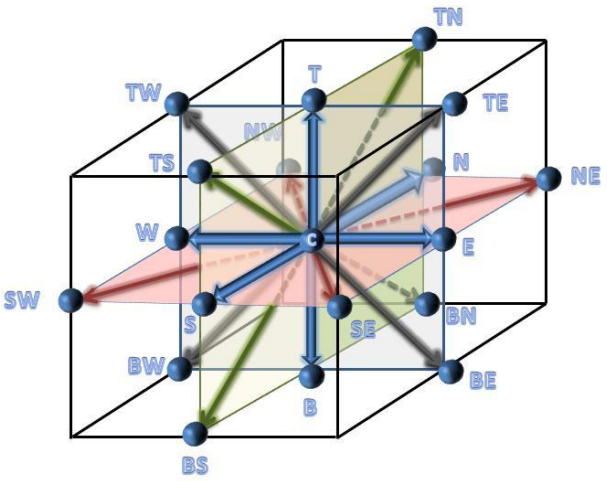

Figure 2.3: D3Q19 is a three-dimensional Lattice Boltzmann model on a cubic grid, with rest particles present. The particle sets reside on 19 nodes, such lattice experience better flux transport and equilibrium with neighbour lattices, because of the presence of four connecting vectors per interfacial plane.

Additionally, the Boltzmann equation describes the statistical distribution of one particle in a fluid with considerations of non-equilibrium statistical mechanics, the area of statistical mechanics that deals with systems far from thermodynamic equilibrium; for instance, when there is an applied temperature gradient or an acoustic field. Most systems found in nature are not in thermodynamic equilibrium because they are not in stationary states, and are continuously and discontinuously subject to flux of matter and energy to and from other systems [12].

Thus, the Boltzmann equation has great potential to study how a fluid transports physical quantities such as heat and waves, and thus to derive transport properties such as conductivity, diffusivity, viscosity, and thermal radiation.

Concluding that lattice Boltzmann method emerged as an enhanced approach for mesoscale and scale-bridging simulations of multi-scales. Additionally, it is capable for tackling particularly those problems which show ubiquitous characteristics of flows in the zones of detailed analysis, such as: material science, bio-engineering and life sciences [13-15].

Namely:

- Flows under complicated geometrical constrains, for example flow in micro-scaffolds.
- Flexibility of modelling micro fluidics with a wide range of Knudsen number ϕ<100μm and Reynolds number.
- Possibility to model non-equilibrium systems existing in none-equilibrium conditions.
- Enhanced reaction kinetics modelling with a higher degree of Spatio-temporal resolution.
- Better Ability to model multiphase and phase separation.
- Complex solid–liquid interfaces, surface reactions in fluids, liquid–solid flows of colloidal suspension.

2.1.2 Origins of Lattice Boltzmann Method

The lattice Boltzmann approach has evolved from the lattice gas models. The basic idea of lattice gas models, generally of cellular automata, is to mimic complex dynamical system behaviour by the repeated application of simple local translation and reaction rules. These rules simulate, in a simplified and coarse-grained mesoscopic fashion, relevant microscopic effects occurring in a real fluid i.e addressing the underlying fluid particles' matrix. This means that lattice-gas automata take a microscopic, though not truly molecular, view of fluid mechanics by conducting fictive micro-dynamics on a lattice.

Lattice gas cellular automata with Boolean particle status residing on fixed nodes were originally suggested by Frisch, Hasslacher and Pomeau in 1986 (FHP lattice gas model) [16] for the reproduction of Navier–Stokes dynamics. A previous formulation for vector automata was already in 1973 suggested by Hardy, Pomeau and de Pazzis (HPP lattice gas model) [17]. However, these earlier versions of lattice gas method were based on a square grid, as seen in figure 2.4, where the particles cannot move diagonally and therefore could not fulfil the requirement of rotational invariance (angular momentum conservation) and were highly anisotropic in an isotropic system. The FHP lattice gas model published later [16] used a

hexagonal two-dimensional lattice which fulfils both, conservation of particle number and rotational invariance.

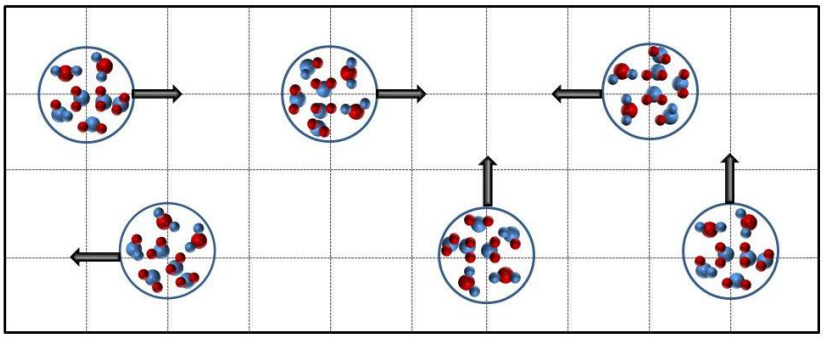

Figure 2.4: Lattice gas automata replace the macroscopic picture underlying the Navier-Stokes framework by discrete sets of fictive particles which carry some properties of real fluid portions. These fictive particles can be regarded as coarse grained groups of fluid (or gas) molecules placed upon square grid (square lattice), the particles in such a model cannot move diagonally, which raise issues of violating Galilean invariance.

All particles in a Boolean lattice gas have the same unit mass and the same magnitude of the velocity vector. The model imposes, as an exclusion principle that no two particles may sit simultaneously on the same node if their direction is identical. For the square lattice originally suggested by the HPP model, implies that there can be at most four particles per node. This occupation principle, originally meant to permit simple computer codes, has the consequence that the equilibrium distribution of the particles follows a Fermi–Dirac distribution. Propagation of the particles consists of moving them from one lattice node to its nearest neighbour in one discrete unit of time according to their given unit momentum vector, figure 2.5. The evolution of system dynamics of the lattice gas takes place in successive steps. The first one is the advection or propagation step. It consists of moving all particles from their nodes to its nearest neighbour nodes in the directions of their respective velocity vectors. The second one is the collision step. It is conducted in such a way that interactions between particles arriving at the same node coming from different directions take place in the form of local instantaneous collisions. The elastic collision rules conserve both mass and momentum. This implies that particles arriving at the same node may exchange momentum if it is compatible with the imposed invariance rules. The third step is (usually) the bounce back step. It imposes no-slip boundary conditions for those particles which hit an obstacle. The fourth step updates all sites. This is done by synchronously mapping the new particle coordinates and velocity vectors obtained from the preceding steps onto their new positions, as explained in figure 2.5. Subsequently the time counter is increased by one unit.

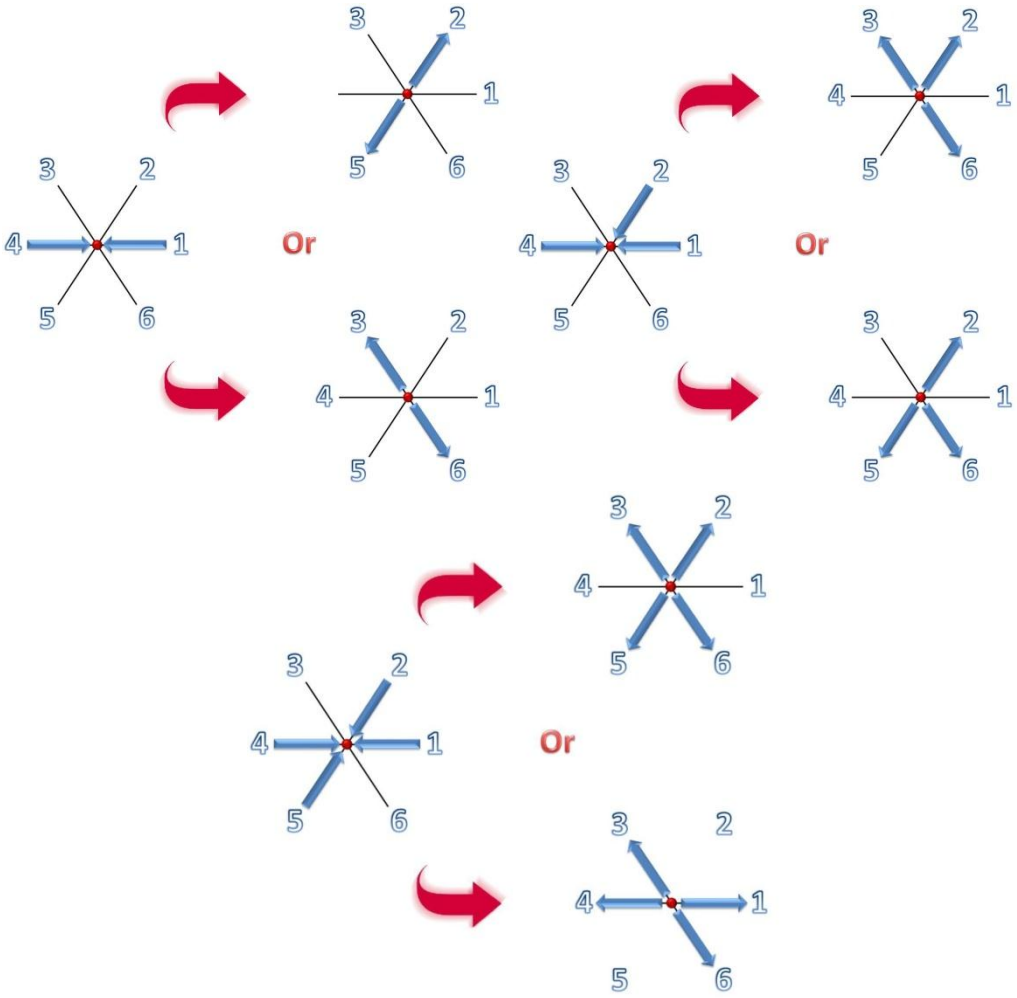

Figure 2.5: Propagation of the particles consists of moving them from one lattice node to their nearest neighbour in one discrete unit of time according to their given unit momentum vector. Collision, on the other hand is conducted in such a way that particles arriving at the same node may exchange momentum.

Nevertheless, the collision rules in the FHP model are not deterministic, in other words not based upon physics of collisions, some input situations produce two possible outcomes, and when this happens, one of them is picked randomly. Since random number generation is computationally time consuming, a pseudorandom process was usually chosen [18].

Other drawbacks of the lattice gas include the lack of Galilean invariance, and statistical noise [18], both are consequence of forcing the particles to propagate and collide into 4 or 6 directions only. Another problem is the difficulty in expanding the model to handle three dimensional problems, requiring the use of more dimensions to maintain a sufficiently symmetric grid to tackle such issues [19]. Three dimensional enhacement was achieved in the 1986 model by D'Humières, Lallemand and Frisch, which employed a face-centered hypercube model [20] by increasing the number of of dimensions.

2.1.3 Lattice Boltzmann Method Vs Lattice Gas Automata

Owing to the discrete treatment of the pseudo-particles and the discreteness of the collision rules Boolean lattice gas automata reveal some intrinsic flaws such as:

- The violation of Galilean invariance is due to the particles inability to propagate diagonally and therefore could not realize the conditions of rotational invariance and perform highly anisotropic in an isotropic system.
- The particle velocities in the lattice Boltzmann scheme are not Boolean variables as in conventional lattice gas automata [16], but real-numbered quantities as in the Boltzmann transport equation. This means that Fermi-Dirac statistics no longer apply, which lack complete energy spectrum coverage [21].

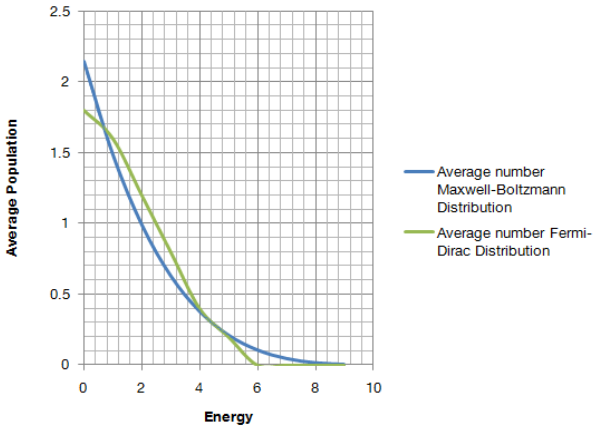

Figure 2.6: The distribution function of the number of particles as a function of energy is plotted for both Maxwell-Boltzmann and Fermi-Dirac statistics. Assuming the presence of nine energy levels taken by the particles, average population of each energy state must be taken. The average for each of the 9 states is shown above compared, low energy states are less probable with Fermi-Dirac statistics than with the Maxwell-Boltzmann statistics while mid-range energies are more probable. This difference is not dramatic in this example for a small number of particles; it becomes very dramatic with large numbers and low temperatures.

Meaning, low energy states are less probable with Fermi-Dirac statistics than with the Maxwell-Boltzmann statistics while mid-range energies are more probable, as seen in figure 2.6. While that difference is not dramatic in this example for a small number of particles, it becomes very dramatic with large numbers and low temperatures.

- It is also important to note that in contrast to the conventional lattice gas method the lattice Boltzmann approach may use pseudo-particles with zero velocity. These are required for simulating compressible hydrodynamics by using a tuneable model sound speed, as well such zero velocity particles are of great importance for the modelling of particles at rest [18-19].
- Another main difference between the original lattice gas and the lattice Boltzmann methods is the fact that the former approach quantifies the particle interactions in

terms of discrete local Boolean redistribution rules (collision rules) while the latter approach conducts (non-Boolean) redistributions of the particle velocity distribution (relaxation rules, collision operator). This condition enhances the statistical noise generated in the former method [22] as seen in figure 2.7, although this advantage can to a certain extent be circumvented by introducing localized averaging procedures [18], but still longer convergence is expected.

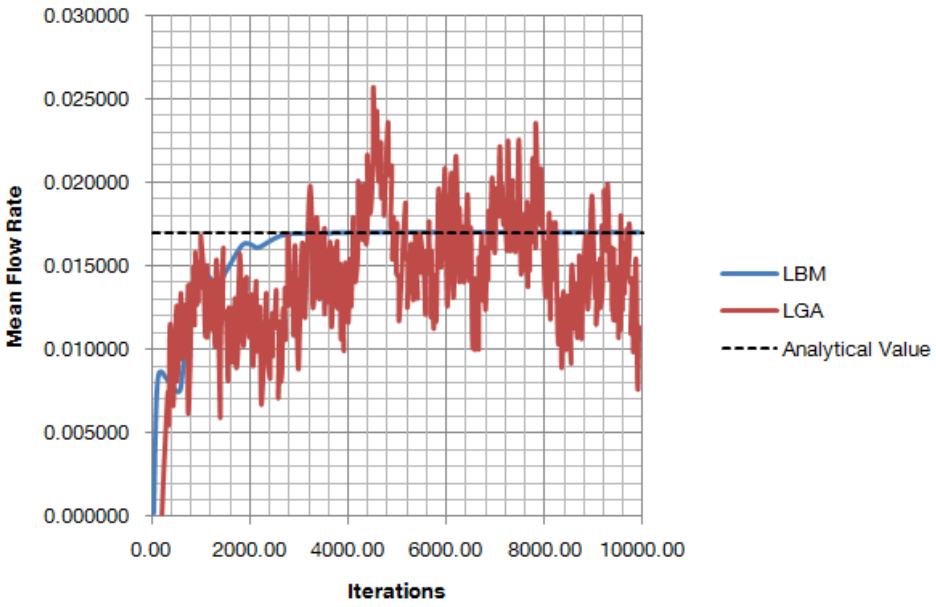

Figure 2.7: Mean flow rate (y-axis) for plane Poiseuille flow Vs. Iteration number (x-axis) for LGA and LB, the dashed line indicates the analytical solution. The plots express how the statistical noise burdens the response of the LGA in comparison to the rapidly converged LB response [22].

- Another consequence of the numerical noise generated is seen in the original lattice gas compared to the lattice Boltzmann method is that small sets of neighbouring nodes in a Boltzmann lattice are capable of creating smooth flow dynamics as opposed to the lattice gas methods which entail rather coarse dynamical behaviour. This means that the Boltzmann method requires less averaging and provides enhanced performance [19].
- An important computational advantage of this method is that any lattice node can be marked as solid, allowing for the integration of arbitrarily complex geometries that would be difficult to physically in some cases using the lattice gas automata, since not all collisions performed are deterministic. This is due to that some input situations produce two possible outcomes, and when this happens, one of them is picked randomly [18].
- Additionally, the complexity in scaling the lattice gas model to handle three dimensional problems, requiring the use of more dimensions to maintain a sufficiently symmetric lattice to handle such issues [19-20].

Accordingly, the lattice Boltzmann method has proven a justified advance for the lattice gas models. Behind the introduction of the lattice Boltzmann automaton is to incorporate the physical nature of fluids from a more statistical standpoint into hydrodynamics solutions than in the classical lattice gas method. According to the underlying picture of the Boltzmann transport equation the idea of the lattice Boltzmann automaton is to use sets of particle velocity distribution functions instead of single pseudo-particles and to implement the dynamics directly on those average values [19-20].

2.2 Applications of the Lattice Boltzmann Method

In the following sub-sections the essential Boltzmann dynamics, for the work in this thesis, of the following phenomena are investigated: single and multiphase flow, substrate diffusion, reaction kinetics, cell kinetics modelling, acoustic propagations in mediums, simultaneous heat and mass transfer in foams, micro-channel flow, cyclic excited flow and moisture driven flux.

2.2.1 Single Phase Lattice Boltzmann Method 2-D and 3-D

The basic idea of Ludwig Boltzmann's equation is to consider fluid composed of interacting particles. This interaction can be modelled by the Boltzmann transport equation where the particle interaction is divided into propagation and collision, both advancing temporally. The Boltzmann equation is an integro-differential equation for the single particle distribution function $f(x,\upsilon,t)$.

$$D_t f = Q(f,f)$$
$$where\, D_t = \frac{\partial}{\partial t} + \upsilon.\nabla \; and \; \nabla f = \frac{\partial f}{\partial x}\hat{\mathbf{x}} + \frac{\partial f}{\partial y}\hat{\mathbf{y}} + \frac{\partial f}{\partial z}\hat{\mathbf{z}} \tag{2.1}$$

The D_t is the total derivative operator, sometimes called convection operator, it includes a temporal derivative and an advective derivative, often used for Spatio-temporal conservation and equilibrium. Boltzmann determined the collision term $Q(f,f)$ resulting solely from two-body collisions between particles that are assumed to be uncorrelated prior to the collision. This assumption was referred to by Boltzmann as the 'Stosszahl Ansatz', and is also known as the 'molecular chaos assumption'. Under this assumption the collision term can be written as a momentum-space integral over the product of one-particle distribution functions:

$$Q(f,f) = Gain - Loss = \int d^3\upsilon_1 \int \left[f(\upsilon_1')f(\upsilon_2') - f(\upsilon_1)f(\upsilon_2) \right] \left| \upsilon_1 - \upsilon_2 \right| \sigma(\Omega) d\Omega \tag{2.2}$$

$Q(f,f)$ is the collision integral $f(x,v,t)\partial^3 x\, \partial^3 \upsilon$ Is the probability to find a particle in the volume $\partial^3 x$ around x and having a particle velocity varying from υ to $\upsilon + \partial\upsilon$ and the accumulation or diminishing of particles at a certain location according to the collision

momentum. Additionally, $\sigma(\Omega)$ is the differential collision cross section for the two-particle collision which transforms the velocities with a relative speed of inward pre-collision of $\upsilon_1 - \upsilon_2$ from $\{\upsilon_1, \upsilon_2\}$ (incoming) into $\{\upsilon_1', \upsilon_2'\}$ (outgoing) around the solid angle Ω.

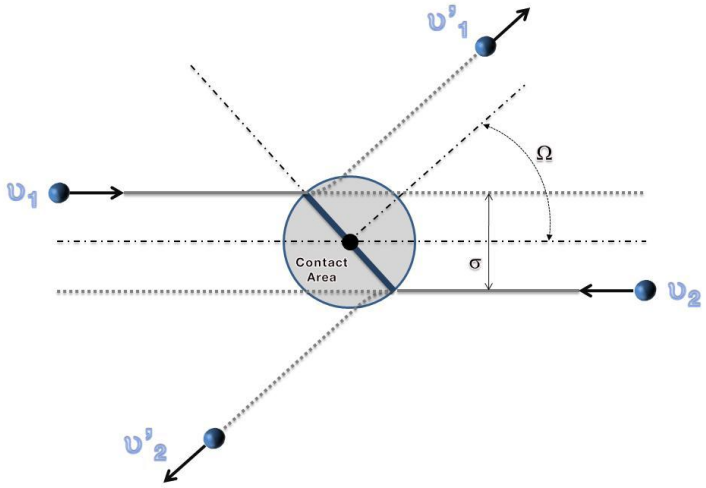

Figure 2.8: Boltzmann expressed the collision term resulting solely from two-body collisions between particles that are assumed to be uncorrelated precede to the collision. σ is the differential collision cross section for the two-particle collision which transforms the velocities from $\{\upsilon_1, \upsilon_2\}$ (incoming) into $\{\upsilon_1', \upsilon_2'\}$ (outgoing) around the solid angle Ω.

Within this collision the particle distribution is evolved into a difference between gain and loss. The body forces are neglected in this assumption and will be included further in the following sections.

Due to the complexity of the collision integral term (equation 2.2) a replacement collision operator $J(f)$ is often used which replaces the collision integral $Q(f,f)$. The collision operator should follow a Maxwellian-Boltzmann distribution. This operator has been approximated by Koelmann (1991) [23] using the Bhatnagar-Gross-Krook (BGK) model, also known as single-relaxation-time (SRT) model. The operator $J(f)$ contributes for the collision of molecules basically predicting the influence of the collision on the distribution functions, and accounts for positive or negative influence in a much simpler manner.

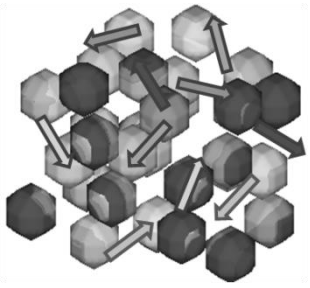

Figure 2.9: The collision of particles basically accounts for positive or negative momentum influence.

$$J(f) = -\frac{1}{\tau}(f - f^{equ}) \tag{2.3}$$

The equation expresses that the collision of particles is considered as relaxation (see Figure 2.10) towards a local equilibrium of distribution f_{equ} and taking relaxation time τ, leading to the B-BGK equation.

$$\frac{\partial f}{\partial t}+\upsilon.\nabla f=-\frac{1}{\tau}(f-f^{equ}),\omega=1/\tau \qquad (2.4)$$

Where the reciprocal of the relaxation time $1/\tau$ can be replaced by the relaxation frequency (ω), which is sometimes referred to as the relaxation parameter.

The equilibrium distribution function follows a Maxwell-Boltzmann distribution:

$$f^{equ}=\frac{\rho}{(2\pi\theta)^{D/2}}e^{\left[\frac{-(\upsilon-u)^2}{2\theta}\right]} \qquad (2.5)$$

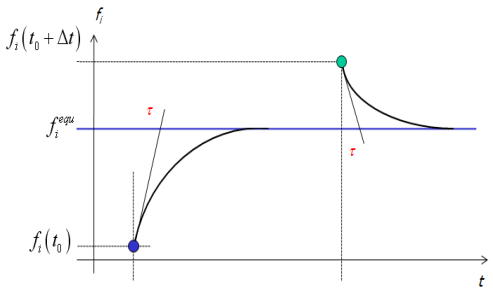

Figure 2.10: The collision of particles is considered as relaxation towards a local equilibrium of distribution and taking relaxation time τ

Where D is the spatial dimension, and ρ,u and $\theta=K_BT/m$ are the macroscopic density, mean flow velocity and specific thermal energy (normalized temperature), respectively, where K_B is the Boltzmann constant and ***T*** is the temperature.

The distribution can be expanded in a Taylor series for incompressible fluid as a second order expansion in u meaning: $A+Bu+Cu^2$ [18]. Another reason for this second order is the contribution of the dynamic collision invariants $I\equiv\left[1,mu,mu^2/2\right]$ (number, momentum, kinetic energy) [19]. Revealing the following second order approximation of Maxwellian Boltzmann distribution:

$$f^{equ}=\rho w(\upsilon)\left[1+\frac{3(\upsilon.u)}{c^2}+\frac{9(\upsilon.u)^2}{2c^4}-\frac{3u^2}{2c^2}\right],w(\upsilon)=(2\pi\theta)^{-D/2}e^{\left[\frac{-\upsilon^2}{2\theta}\right]} \qquad (2.6)$$

Where $c=\Delta x/\Delta t$ is the lattice speed, meaning the lattice distance a particle propagates per unit time, and usually taken as one lattice distance per one unit time. For ideal cases, since the state equation is $p=\rho\theta$, the specific thermal energy defines the speed of sound as $\theta=c_s^{\,2}$ and for this case $c=\sqrt{3}c_s$. This model works well in cases of incompressible flow $u/c_s<0.3$.

In this thesis two kinds of lattices are investigated: D2Q9 and D3Q19 for the 2-D and 3-D modelling respectively. The choice of these lattices sizes are made as compromise between accuracy and computational effort, both models have been extensively used in literature and have proven significantly accurate [24-25]. The conservation is made on the particle scale and each set of particles, for example in the D3Q19 model have19 possible direction to follow rather than the classical X, Y and Z.

Hence the equation could be written for each direction vector denoted by i choosing the D3Q19, meaning nineteen velocity directions representing the 3-D lattice as in Figure 2.8.

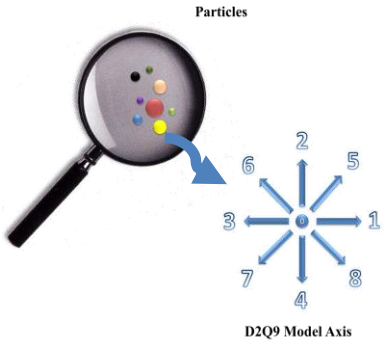

Figure 2.11: Particles can be represented by distribution functions along nine directions

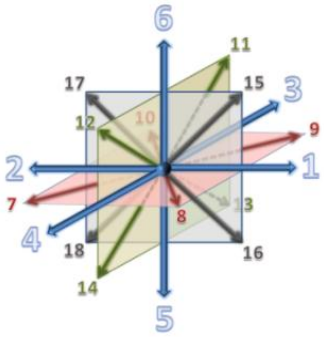

Figure 2.12: D3Q19 model for higher precision, which resembles nineteen velocity directions representing the 3-D lattice.

After applying basic discretization rules, by means of Taylor series expansions, to equation (2.4), the difference Lattice Boltzmann equation could be retrieved as follows:

$$\frac{f_i(x,t+\Delta t)-f_i(x,t)}{\Delta t}+\upsilon\frac{f_i(x+\Delta x,t+\Delta t)-f_i(x,t+\Delta t)}{\Delta x}=-\frac{1}{\tau}\left(f_i-f_i^{equ}\right)$$

$$\frac{f_i(x,t+\Delta t)-f_i(x,t)}{\Delta t}+\frac{f_i(x+\Delta x,t+\Delta t)-f_i(x,t+\Delta t)}{\Delta t}=-\frac{1}{\tau}\left(f_i-f_i^{equ}\right)$$

$$\frac{f_i(x+\Delta x,t+\Delta t)-f_i(x,t)}{\Delta t}=-\frac{1}{\tau}\left(f_i-f_i^{equ}\right)$$

$$f_i(x+\Delta x,t+\Delta t)=f_i(x,t)-\frac{1}{\tau}\left(f_i-f_i^{equ}\right)=f_i(x,t)-\omega\left(f_i-f_i^{equ}\right) \quad (2.7)$$

Equation 2.7 carries the core procedure, which could be divided into two main parts advection and relaxation step (including the local equilibrium calculation).The procedure is summarized as follows in equation (2.8-2.10)

Propagation
$$f_i(t+1,r+1)=f^a{}_i(t,r) \quad (2.8)$$

Relaxation
$$f_i^a(t,r)=f_i(t,r)-\omega(f_i(t,r)-f_i^{equ}(t,r)) \quad (2.9)$$

Local Equilibrium
$$f_i^{equ}=w_i\rho\left[1+3\frac{\hat{e}_i.\upsilon}{c^2}+\frac{9}{2}\frac{(\hat{e}_i.\upsilon)^2}{c^4}-\frac{3}{2}\frac{\upsilon^2}{c^2}\right] \quad (2.10)$$

In equation (2.10), $\hat{e}_i\equiv\hat{\upsilon}_i, w_i$ are the discrete unit vectors (the i[th] direction) of the particles velocities (defined in equation (2.2)), the discretized weighting factor defined in equation (2.6), respectively. For the chosen lattices it could be easily proven that the following weighting factors for the defined direction vectors are as listed in table 2.1 and 2.2 [19], for detailed prove see Appendix A-1.

Table 2.1 Values of weighting factors according to the unit directions for a D2Q9 lattice.

Direction $\hat{e}_i$	wi
0	4/9
1,2,3,4	1/9
5,6,7,8	1/36

Table 2.2 Values of weighting factors according to the unit directions for a D3Q19 lattice.

Direction $\hat{e}_i$	wi
0	1/3
1,2,3,4,5,6	1/18
7,8,…..,18	1/36

Application of the Chapman-Enskog expansion on the Boltzmann equation yields the Navier-Stokes equation under the assumptions of low compressibility, as chosen in equation (2.6), the pressure could be evaluated as $\rho\theta = \rho K_B T/m = \rho c_s^{\,2}$, Analogous comparison between the Navier-Stokes equations and the expanded Boltzmann equation (see Appendix A-2) reveals that the kinematic viscosity could be evaluated as:

$$\nu = \frac{K_B T}{m}\left(\frac{1}{\omega}-\frac{1}{2}\right) = c_s^{\,2}\left(\frac{1}{\omega}-\frac{1}{2}\right) = \frac{1}{6}\left(\frac{2}{\omega}-1\right) = \frac{1}{6}(2\tau-1) \tag{2.11}$$

The relaxation time is chosen to satisfy the Von Neumann stability condition [18] for τ, prove is derived in appendix A-3.

$$|1-\omega|<1 \rightarrow \quad 0<\omega<2 \quad or \quad \frac{1}{\omega}=\tau>\frac{1}{2} \tag{2.12}$$

Conversion between Physical Domain and Lattice Domain For the model to deliver results in the realistic domain, a similarity analysis must be achieved as mentioned in section 1.2.2; The dynamic parameters may be related through the non-dimensional parameter, Reynolds number, which is solely considered here and further on more dynamic similarity parameters are presented in the thesis when appropriate.

$$Re = \frac{v \cdot l}{\nu} \tag{2.13}$$

V, l, ν is the velocity, characteristic length and kinematic viscosity, respectively. The Reynolds number is defined as the ratio of inertia forces to the viscous forces, and as a similarity parameter it stays the same independent of axis or transformation, such that, if two fluids have the same Reynolds number they are considered dynamically equivalent. Leading to:

$$\left.\frac{v \cdot l}{\nu}\right|_{Real} \equiv \left.\frac{v \cdot l}{\nu}\right|_{LU} \rightarrow v_{LU} = \frac{\nu_{LU} \cdot v_{Real} l_{Real}}{\nu_{Real} \cdot l_{LU}} \tag{2.14}$$

Therefore, it is possible to solve the Lattice Boltzmann equation in lattice units and relate the results with a physical flow that possesses the same Reynolds number and the same flow geometry. From the modelling side, the characteristic length l_{LU} is chosen and therefore

known in Lattice Units. Considering the velocity in lattice units v_{LU} is calculated from equation (2.14) once a stable relaxation time τ is chosen for the simulation.

After calculating v_{LU}, the main conversion factors are calculated to relate any physical quantity to its value in lattice units.

$$Variable = Conversion_{fact} \times Variable_{LU} \tag{2.15}$$

For example, the conversion factors for some basic quantities such as length *l* in m, velocity *v* in m/s, time in s and mass in Kg which is fixed for convenience to 1gram per 1 lattice mass are listed below.

$$\begin{aligned} l_{fact} &= \frac{l}{l_{LU}} \\ v_{fact} &= \frac{v}{v_{LU}} \\ \frac{1}{t_{fact}} &= \frac{t_{LU}}{t} = \frac{v_{fact}}{l_{fact}} \\ 1\,Lattice\,mass &= 0.001Kg, M_{fact} = 0.001 \end{aligned} \tag{2.16}$$

With the same method any other variable can be transferred from the lattice domain to the real physical domain or vice versa through a conversion factor calculated from a combination of the basic conversion factors for the basic quantities.

2.2.2 Multi-Phase Modeling

Lately, the LBM has received great considerations as an alternative for modelling complex phenomena of particle dynamics and has proven successful and capable for simulating multi-component fluid flows. The first multi-phase models were developed 1991, and was based on surface tension separation schemes, using a repulsive interaction force (Gunstensen and Rothman 1991) [26]. Shortly, a further method which exploited the interaction force potential function to model gas-liquid phase evolution was proposed (Shan and Chen 1993) [13]. The free energy approach was also used to build up an algorithm using the theory of free energy (Swift et al. 1995) [14]. Two-phase immiscible fluids with large density differences were as well reported possible; the method was functional for two-phase fluids with high density ratios up to 1000 and was used for simulating bubble flows and capillary waves (Inamuro et al. 2004) [15].

The multi-phase model of Gunstensen [26] is used in this work, due to the reduced computational effort and the unnecessary evaluation of high density ratio energy functions, as in the Shan model [13].

The Gunstensen model is achieved by resolving each phase separately with individual distribution function, as the phases only interact at interfaces. Applying this perception to equation (2.17) the multiphase lattice Boltzmann equation can be rewritten as:

$$f_i^k(t+\Delta t, r+\upsilon\Delta t) = f_i^k(t,r) + Q_i^k \tag{2.17}$$

The superscript *k* denotes the first phase *(k=1)* and *(k=2)* denotes the second phase and additional phases can be implemented in a similar fashion. In the multiphase model the collision operator includes the regular collision effect and the extra attraction and repulsion force controlled by surface tension, the collision operator Q is divided into two parts:

$$Q_i^k = \left|Q_i^k\right|_1 + \left|Q_i^k\right|_2 \tag{2.18}$$

The first term which contributes for the collision of molecules, predicts the influence of the collision on the distribution functions, and accounts for positive or negative influence. This operator has been approximated by Koelman [23].

$$\left|Q_i^k\right|_1 = -\frac{1}{\tau_k}(f_i^k - f_i^{k(equ)}) \tag{2.19}$$

The local equilibrium distribution takes the Maxwellian form as in equation (2.6 & 2.10), which is applied for each phase separately:

$$f_i^{equ} = w_i\rho\left[1 + 3\frac{\hat{e}_i.u}{c^2} + \frac{9}{2}\frac{(\hat{e}_i.u)^2}{c^4} - \frac{3}{2}\frac{u^2}{c^2}\right] \tag{2.20}$$

The second term in the collision operator contributes at the two phase interface.

$$\left|Q_i^k\right|_2 = -\frac{A_k}{2}|F|\left[\frac{(\hat{e}_i.F)^2}{|F|^2} - \frac{1}{2}\right] \tag{2.21}$$

Where A_K , is a free surface parameter that corresponds to the surface tension, while *F* is the local frequency gradient between the two phases, and can be written for a two phase field as:

$$F(x) = \sum_i \hat{e}_i\left[\sum_i f_i^{k=1}(x+1) - \sum_i f_i^{k=2}(x+1)\right] \tag{2.22}$$

It is worth mentioning that in a single phase region *F=0* and thus diminishing the second collision term, which only has a contribution at the phase interfaces.

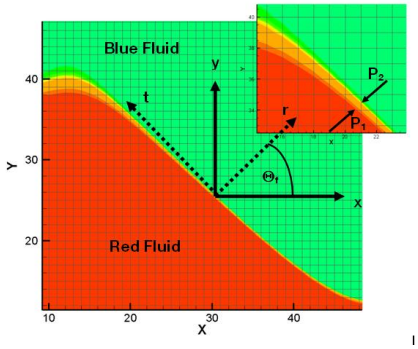

Figure 2.13: Red-Blue fluid interface, where r is the interface normal unit vector and t is the tangential. The interface is determined based upon the two fluid stress tensor differences

Equation (2.22) could be easily derived from the definition of the surface tension, details in Appendix A-4

$$\sigma = \int\left(P_1.\hat{r} - P_2.\hat{r}\right)dr \tag{2.23}$$

Where P_1, P_2, $\hat{r}$ and σ are the stress tensor in red fluid, blue fluid, unit vector normal to the interface and the surface tensor coefficient, respectively as seen in figure 2.13. Finally the local density of each phase can be expressed as:

$$\rho^k = \sum_i f_i^k \tag{2.24}$$

The total density ρ, momentum fluxes ρu, viscosity ν, Pressure P and Shear Stress τ can be written as follows for each phase:

$$\rho = \rho^{k=1} + \rho^{k=2},\ \rho u = \sum_{i=1}^{8} \hat{e}_i f_i = \sum_{i=1}^{8} \hat{e}_i f_i^{eq},$$
$$\nu = \frac{1}{6}\left(\frac{2}{\omega} - 1\right), P = C_s{}^2 \rho \tag{2.25}$$

$$\tau = -\left(1 - \frac{1}{2\tau}\right)\sum_{i=1}^{8}\left[f_i - f_i^{eq}\right] \times \left(e_{ix} e_{iy} - \frac{1}{2} e_i . e_i \delta_{xy}\right) \tag{2.26}$$

Where C_s is the speed of sound; δ_{xy}, kronecker delta; ie *x, y,* component unit vectors in x- and y-directions of the unit vector e_i.

2.2.3 Diffusion Modeling

Diffusion is a time-dependent process, constituted by random motion of given entities and causing the statistical distribution of these entities to spread in space. The concept of diffusion is tied to notion of mass transfer, driven by a concentration gradient, but diffusion can still occur when there is no concentration gradient. Two classical applications of flux driven diffusion are heat diffusion and molecular diffusion. Their mathematical description was elaborated by Joseph Fourier in 1822 and Adolf Fick in 1855. Referring to Fick's second law, the mass and heat diffusion equation in presence of no advection (diminished mean velocity flow) would be:

$$\frac{\partial C}{\partial t} = D\nabla(\nabla . C) = D\nabla^2 C,\ \frac{\partial T}{\partial t} = \alpha \nabla^2 T \tag{2.27}$$

$$\nabla^2 = \frac{\partial^2}{\partial x^2} + \frac{\partial^2}{\partial y^2} + \frac{\partial^2}{\partial z^2} \tag{2.28}$$

Where C, D, T,α are the mass concentration of the diffused fluid, the diffusion coefficient which is chosen to be spatially independent in this case, Temperature and Thermal diffusivity, respectively. The Laplacian operator, ∇^2, expresses the spatial flux gradient. Wolf-Gladrow [18] proposed an analogous lattice Boltzmann model for diffusion to Fick's model and derived a relation for the diffusion relaxation time in terms of the diffusion coefficient. The model was further enhanced presenting a lattice Boltzmann scheme for simulating the diffusion-advection system with chemical reaction [30]. Additionally, a developed a lattice Boltzmann model for simulating one dimensional diffusion-reaction equation for ideal binary gaseous mixture with solute concentrations at parts per million levels [31]. The model was validated with experimental measurements for adsorption/desorption data of organic vapour (toluene) on silica gel under varying conditions of temperature, concentration and flow rates. More recently, a model was proposed for modelling complex solute transport problems using lattice Boltzmann method [32].Hussein et al. [33] modelled the diffusion of oxygen enriched water in cartilage cell breeding reactor.

The flow field was simulated using the lattice Boltzmann method while the oxygen diffusion was decoupled from the flow field then modelled using a finite difference diffusion-advection-kinetic model.

The modelling of the diffusion for mass and heat diffusion using the Boltzmann equation-BGK could be summarized by:

$$\frac{\partial C}{\partial t} + \upsilon.\nabla C = -\frac{1}{\tau_C}\left(C - C^{equ}\right) \tag{2.29}$$

$$\frac{\partial T}{\partial t} + \upsilon.\nabla T = -\frac{1}{\tau_T}\left(T - T^{equ}\right) \tag{2.30}$$

Where τ_c, is the water content relaxation time and τ_T, is the relaxation time. Additionally, Equations (2.29 & 2.30) could be discretized in a similar fashion to equation (2.17). The relation between the molecular diffusion coefficient *D*, thermal diffusivity α and the concentration relaxation time and thermal relaxation, respectively, is given by [18] as:

$$D = \frac{1}{6}\left(2\tau_c - 1\right); \alpha = \frac{1}{6}\left(2\tau_T - 1\right) \tag{2.31}$$

Therefore, the concentration relaxation time in the main Lattice Boltzmann equation for concentration is determined by the effective molecular diffusion coefficient for the corresponding system as:

$$\tau_C = 3D + \frac{1}{2} \tag{2.32}$$

Similarly the temperature relaxation time can be related to the thermal diffusivity such that:

$$\tau_T = 3\alpha + \frac{1}{2} \tag{2.33}$$

The absences of the viscous terms have made it convenient to use the SRT model which produces independent Eigen value for each equation on its own without any energy unbalances in the equations. Thus, for a stable solution both relaxation times should be greater than 0.5.

$$\lambda_C = 1 - {}^{1}\!/_{\tau_C}; \lambda_T = 1 - {}^{1}\!/_{\tau_T} \rightarrow \left|\lambda_{C,T} < 1\right| \rightarrow \tau_{C,T} \geq 0.5 \tag{2.34}$$

Since the equation (2.29-2.30) are assuming that mass and heat transfer only occurring by means of mass and thermal diffusion, respectively. This is an acceptable assumption in non-convective heating chambers, where the macroscopic velocity is zero (u = 0). In the contrary, the particle velocity in the different directions can still be non-zero (υ = 0). Therefore, the discrete Maxwellian equilibrium distribution, equation (2.6), of the temperature and water content takes the form:

$$T_i^{equ} = w_i T,\ C_i^{equ} = w_i C \tag{2.35}$$

The macroscopic Temperature and water content can be evaluated as:

$$T = \sum_i T_i \; ; C = \sum_i C_i \tag{2.36}$$

For the model to deliver results in the realistic domain a similarity analysis must be achieved, this takes two major parts: Geometric and Dynamic. While the geometry may be simply scaled, the dynamic parameters may be related through the non-dimensional parameter, Fourier number (*Fo*), which is the ratio of heat conduction to the rate of thermal energy storage. The Fourier number can also be defined for transient mass transfer by diffusion, respectively in equation (2.37).

$$Fo_T = \frac{\alpha \cdot t}{l^2} \; or \; Fo_C = \frac{D \cdot t}{l^2} \tag{2.37}$$

Such that, any two different diffusion problems, if they have the same Fourier number they are equivalent. Therefore, it is possible to solve the Lattice Boltzmann equation in lattice units and relate the results with a physical flow that possesses the same Fourier number and the same flow geometry. From the modelling side, the characteristic length l_{LU} is chosen to satisfy geometrical scaling and therefore known in Lattice Units. Considering the mass Diffusion coefficient in lattice units D_{LU} is calculated from equation (2.31) once a relaxation time is chosen for the simulation.

$$t_{LU} = \frac{Fo_C \cdot {l_{LU}}^2}{D_{LU}} \tag{2.38}$$

After calculating t_{LU}, the main conversion factors are calculated to relate any physical quantity to its value in lattice units in a similar fashion to equations (2.25-2.16).

2.2.4 Modeling of Simultaneous Heat-Moisture Diffusion

Investigation of the coupled heat and mass transfer in porous materials is of interest to many engineering and environmental fields. Examples of such applications range from thermal insulation in buildings to moisture migration during drying in food manufacturing process, with products ranging from sugar, coffee, corn-starch, flour mixes, dried fruits, breakfast food, pasta products, baked goods, and many others [34-39]. During the last few years, important experimental and analytical studies as well as computational modelling were conducted in an effort to understand the mechanism of the coupled diffusive phenomena [36-39].

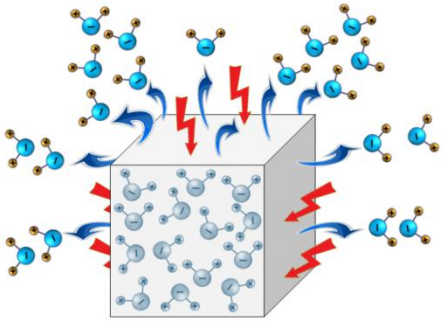

Figure 2.14: Coupled heat and moisture transfer in porous material is a typical problem in food industry [39].

Simultaneous heat and moisture transfer in a porous material involves complex physical phenomena. The strength of this complexity depends on how the mutual effect of heat on mass transfer and vice-versa is dealt with. In reality the relative humidity of the surroundings affects greatly the thermal characteristics of the porous medium where at high relative humidity some of the pores may contain water at liquid phase.

For a simultaneous diffusive heat and mass transfer system lacking evaporation-condensation modelling the Boltzmann equation using single relaxation term (SRT) can be rewritten as:

$$\frac{\partial f_i}{\partial t} + \upsilon.\nabla f_i = \Omega_i$$
$$f_i = \begin{bmatrix} T_i \\ C_i \end{bmatrix}; \Omega_i = \begin{bmatrix} -\frac{1}{\tau_T}\left(T_i - T_i^{(equ)}\right) \\ -\frac{1}{\tau_C}\left(C_i - C_i^{(equ)}\right) \end{bmatrix} \quad (2.39)$$

Where *T*, the particle temperature; *C*, is the water content (whether Vapour or liquid), due to the assumption of no evaporation-condensation; τ_c, is the water content relaxation time and τ_t, is the temperature relaxation time.

Assuming that mass and heat transfer only occur by means of mass and thermal diffusion, respectively. This is an acceptable assumption in non-convective heating chambers ($\upsilon = 0$). Therefore, the Maxwellian equilibrium distribution of the temperature and water content takes the form:

$$\left\{f_i^{equ}\right\} = \begin{bmatrix} T_i^{equ} \\ C_i^{equ} \end{bmatrix} = w_i \begin{bmatrix} T(r) \\ C(r) \end{bmatrix} \quad (2.40)$$

The local Temperature and water content can be expressed as:

$$T = \sum_i T_i \; ; C = \sum_i C_i \quad (2.41)$$

The equation set (2.39) is a combination of the previous sections and attributes for the simultaneous mass and thermal diffusion without an advective term. The set of equations are quite realistic in cases where both temporal and thermal diffusion relaxations exist in close vicinity. The combination is very important where both parameters influence each other as in the modelling of moisture transport in stagnant domains or foams.

2.2.5 Advection-Diffusion Modeling

The advection-diffusion equation has great significance in chemical applications, where quantities such as mass, heat, energy and vorticity transport are transported by means of advection and diffusion [40, 41]. Additionally, the Transport of soluble chemicals in porous media follows the same equations and due to the large variability of flow and transport

properties research is still active in this field [41]. Furthermore, modelling of moisture transfer has gathered a lot of attention in literature, where the difficulties of phase transformation occurs, namely evaporation-condensation phenomenon, in such cases diffusion-advection models' upgrade are investigated [42].

The typical advection-diffusion equation could be written as:

$$\begin{aligned} &\frac{\partial C}{\partial t} + u.\nabla C = D\nabla^2 C,\ \frac{\partial T}{\partial t} + u.\nabla T = \alpha\nabla^2 T \\ &or\ D_t C = D\nabla^2 C,\ D_t T = \alpha\nabla^2 T, \\ &where\, D_t = \frac{\partial}{\partial t} + u.\nabla, \nabla C = \frac{\partial C}{\partial x}\hat{\mathbf{x}} + \frac{\partial C}{\partial y}\hat{\mathbf{y}} + \frac{\partial C}{\partial z}\hat{\mathbf{z}} \end{aligned} \tag{2.42}$$

Where u is the macroscopic local velocity, D_t is the total derivative operator, it is defined as a temporal derivative and an advective derivative, often used for Spatio-temporal conservation and equilibrium. The Laplacian operator, ∇^2, expresses the spatial flux gradient as in equation (2.27).

The Boltzmann model of this equation is identical to the set of equation (2.29-2.33) the main difference occurs in the equilibrium term where the macroscopic flow field velocity is restored.

$$C_i^{equ} = w_i C\left[1 + 3\frac{\hat{e}_i.u}{c^2} + \frac{9}{2}\frac{(\hat{e}_i.u)^2}{c^4} - \frac{3}{2}\frac{u^2}{c^2}\right] \tag{2.43}$$

$$T_i^{equ} = w_i T\left[1 + 3\frac{\hat{e}_i.u}{c^2} + \frac{9}{2}\frac{(\hat{e}_i.u)^2}{c^4} - \frac{3}{2}\frac{u^2}{c^2}\right] \tag{2.44}$$

The macroscopic Temperature and water content can be evaluated as:

$$T = \sum_i T_i\ ; C = \sum_i C_i \tag{2.45}$$

The same relation between the molecular diffusion coefficient D, thermal diffusivity α and the concentration relaxation time, thermal relaxation time, respectively, could be used as in equation (2.31-2.33), since the derivation included no velocity field term, variations in the equations are not expected:

$$D = \frac{1}{6}(2\tau_c - 1); \alpha = \frac{1}{6}(2\tau_T - 1) \tag{2.46}$$

Keeping into consideration the compressibility limit has to be satisfied, since the Chapman-Enskog expansion was performed neglecting compressible terms of $(u/c_s)^3$, therefore:

$$\begin{aligned} &u/c_s < 0.3\ or\ (u/c_s)^2 < 0.3^2 \\ &mu^2/K_B T < 0.09 \end{aligned} \tag{2.47}$$

In the case of diffusion-advection modelling its more practical to use an advective dynamic similarity parameter, Bodenstein number (Bo_c), which is defined as the ratio of momentum

diffusivity to mass diffusivity. The thermal Bodenstein number (Bo_T), is also defined as the ratio of momentum diffusivity to thermal diffusivity.

$$Bo_C = \frac{u_\infty \cdot l}{D}, Bo_T = \frac{u_\infty \cdot l}{\alpha} \tag{2.48}$$

Where l is the Characteristic length, u_∞ is the upstream macroscopic inflow velocity and the D is the diffusion coefficient.

The Bodenstein number will hold the similarity condition, such that after choosing a stable relaxation parameter as in equation (2.34) a reciprocal of the conversion factor of the velocity is reached:

$$\frac{u_{LU}}{u_\infty} = \frac{l_{LU} D}{\frac{l}{6}(2\tau - 1)} \tag{2.49}$$

Revealing a temporal conversion factor:

$$\frac{t_\infty}{t_{LU}} = \frac{D}{\frac{1}{6}(2\tau - 1)} \tag{2.50}$$

It is noteworthy to discuss the time scale jump between the two phenomena (advective transport and diffusive transport) which will simultaneously take part. With careful considerations to the kinematics viscosity ($\nu = 1.6074 \cdot 10^{-6}\, m^2/s$) and the diffusion coefficient ($D = 2.339 \cdot 10^{-9}\, m^2/s$) in the case of water with aeration, one can estimate the time scale jump of three orders of magnitude, *O(3)*. This elaborates the reason for the choice of the time relaxation dependent on the diffusion coefficient and not the viscosity. In other words, the parameter which occurs in the slower rate is often taken as the deterministic value for the time scale, as it will include the parameter with the faster rate anyway. Although this may sound computationally tedious, but at least more realistic microscopic effect is resulted.

2.3 Boundary Conditions

Several boundary conditions are detailed in this work, which are the necessary conditions for simulating the applications in this work: The wall (slip and non-slip), the Drichlet inlet/outlet and Neumann inlet/outlet Flux boundary condition.

2.3.1 Wall Boundary Conditions

2.3.1.1 Non Slip Boundary condition: Bounce back

The non-slip conditions often referred to as the Bounce-back conditions in LBM, is derived from the elastic collision condition:

$$f_i^{in} \cdot \hat{n}^{in} = f_i^{out} \cdot \hat{n}^{out} > 0 \tag{2.51}$$

Bounce-back conditions are quite efficient to implement and to calculate as seen in Figures 2.15 and 2.16 for the D2Q9 model for easier illustration. The particle at time *t* has distributions of different magnitudes in directions 1, 8 and 4. After an incremental time *t+⊿t* the distributions are reversed in direction after bouncing from the wall conserving there magnitude but directly opposing there direction. If the wall location exactly fits on the lattice a 1st order accuracy is obtained.

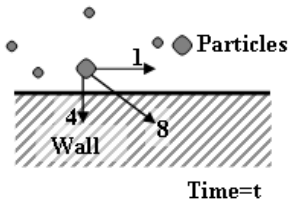

Figure 2.15: A set of particles about to hit a wall at time t.

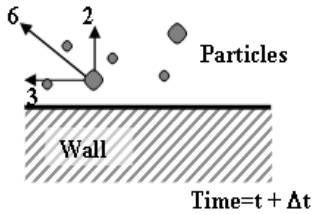

Figure 2.16: The set of particles bouncing back at time t+Δt.

On the other hand if the wall is in mid lattice i.e. the distance between the lattice and the wall is *⊿x/2* then 2nd order accurate Boundary condition is claimed [19].

For inclined walls a staircase of vertical and horizontal walls may be applied but queries have arisen concerning the artificial increase in rugousity, but it still merits for its simplicity. Chen and Martinez [43] have produced a decent method for dealing with inclined planes using extrapolation schemes.

In some applications problems exhibit when inelastic collision occurs, in such complex regimes a restitution coefficient may be included such that:

$$f_i^{in} \cdot \hat{n}^{in} = C_r \left(f_i^{out} \cdot \hat{n}^{out} \right) \tag{2.52}$$

Where C_r is the restitution coefficient or bounciness of an object is a fractional value representing the ratio of velocities after (u^{out}) and before (u^{in}) an impact, which could be defined as:

$$C_r = \frac{u^{out}}{u^{in}} \tag{2.53}$$

An object with a C_r of 1 collides elastically, while an object with a $C_r < 1$ collides inelastically. For a $C_r = 0$, the object effectively "stops" at the surface with which it collides, not bouncing further at all. The reason for the velocity retardation could be due to kinetic energy dissipation as in the case of highly deformed walls due to overheating. This case is out of scope of this thesis, but could be interesting for further applications.

2.3.1.2 Slip Boundary condition

This boundary condition treats the presence of a wall sliding with a certain velocity *Uw*. The wall exhibits tangential velocities on the particles nearby. In LBM this is translated to a Wall

velocity affected density distributions. By simple x-momentum and y-momentum equilibrium we reach the bounce back distributions as a function in wall velocity *Uw*.

$$\begin{aligned} &X-Momentum: \\ &J_x = f_5 - f_6 + f_8 - f_7 + f_1 - f_3 \\ &J_x = \rho U_w \\ &Y-Momentum: \\ &J_y = f_5 - f_8 + f_6 - f_7 + f_2 - f_4 \\ &J_x = 0 \end{aligned} \tag{2.54}$$

To finalize the formulation it is needed to introduce adjustable reflection coefficients p, q and using them to adjust the particles speed next to the wall to become the wall velocity.

$$\begin{bmatrix} f_7 \\ f_4 \\ f_8 \end{bmatrix} = \begin{bmatrix} p & 0 & q \\ 0 & 1 & 0 \\ q & 0 & p \end{bmatrix} \begin{bmatrix} f_5 \\ f_2 \\ f_6 \end{bmatrix} \tag{2.55}$$

Solving equation (2.54) an expression for p, q as a function of the Uw and the known distributions 2, 5 and 6. Which are the distributions prior to the bouncing back from the moving wall; this is seen clear in Figures 2.17 and 2.18.

$$p = 1 - \frac{\rho U_w}{2(f_5 - f_6)}, q = \frac{\rho U_w}{2(f_5 - f_6)} \tag{2.56}$$

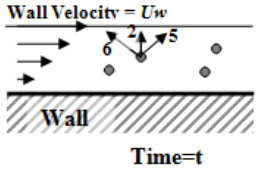

Figure 2.17: A particle about to hit a sliding wall at a time *t*

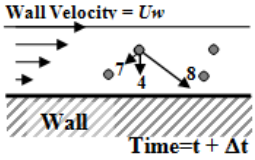

Figure 2.18:A particle bouncing back from a sliding wall at time *t*+Δt

2.3.1.3 Wall Temperature

The wall temperature can be distributed upon the near wall particles by assigning the wall particles with their corresponding equilibrium values [45, 46] as in equation (2.44),

$$T_i^{equ} = w_i T_{Wall} \left[1 + 3\frac{\hat{e}_i.u}{c^2} + \frac{9}{2}\frac{(\hat{e}_i.u)^2}{c^4} - \frac{3}{2}\frac{u^2}{c^2} \right]. \tag{2.57}$$

Where $\hat{e}_i$ is the unit vector in the ith direction, u is the local (macroscopic) velocity, T_{Wall} is the wall temperature. Isothermal boundary means $\sum_i \Delta T_i = 0$. Meanwhile, constant temperatures on the boundaries also imply no temperature gradient and therefore no heat conduction along the boundaries. This implementation would cause the discontinuity of the thermal properties and temperature jump at boundaries as soon as propagation occurs or at the corners. A solution for this would be to constantly implement the condition that no

temperature variations along thermal boundaries $\partial T/\hat{t}\big|_{boundary} = 0$, where $\hat{t}$ is the tangential unit vector of the thermal boundaries [44].

2.3.1.4 Wall Loci Retrieving in Complex Geometries from Images

In some applications the recognition of the walls is quite challenges, such as in the case of fine structured ceramics for the generation of micro scaffolds for cell growth.

The difficulty of modelling such complex micro-structures always lies in retrieving the geometry into the solver as edges. The edge detection techniques have been used as a base of the image segmentation in order to find the boundaries of each enclosed region (pour or solid structure) in the digital image. Combining the edge detection with the region growing method produced much better results for image segmentation than what would have been obtained by either technique alone [45]. In general, the region growing is a procedure that works to group pixels or sub regions into larger regions based on predefined criteria [46]. Starting with a set of seed points, regions are grown from these by appending to each seed those neighbouring pixels that have properties similar to the seed as in figure 2.19. These properties could be grey level or color amplitude. The region growing uses the following formulation for determining the different regions:

$$region(R) = \bigcup_{i=1}^{n} R_i \qquad for\ all \bigcap_{i=1}^{n} R_i = \phi \tag{2.58}$$

Where: R_i are the connected regions, i=1, 2, ..., n

$$R_i \bigcap R_j = \phi \qquad for\ all\ i \neq j \tag{2.59}$$

Where: R_i and R_j are the separate not connected regions, i, j=1, 2, ..., n

$$H(R_i) = true \qquad for\ all\ i \tag{2.60}$$

Where: H is homogeneity criterion that control the selection of the enclosed regions. For example select a homogeneity condition depending on the marginal difference in colour intensity (ΔI) between the starting seed and the neighbourhood pixels. Therefore, the algorithm will examine the colour intensity of the neighbourhood pixels and decide whether to stop the region growth or continue.

$$H(R_i \bigcup R_j) = false \qquad for\ all\ i \neq j \tag{2.61}$$

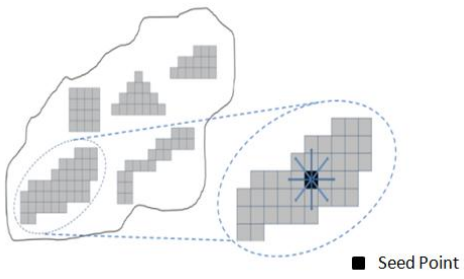

Figure 2.19: Regions growing from the seed point to those neighbouring pixels that have properties similar to the starting seed by propagating in a 2-D lattice in 8 directions.

The conventional approach for edge detection was used based upon either thresholding the first derivative (gradient) of the image or locating zero crossings of its second derivative (Laplacian) [47].

$$\nabla(\text{IMAGE}) \;||\; \nabla 2(\text{IMAGE}) = 0 \qquad (2.62)$$

The edge detector algorithm detects the edges and uses it to automatically generate the seed points for the region growing algorithm. Regions are grown from the current pixel relative to the region pixel and edge pixel. Image edges act as hard barriers during region growing [48]. Figure 2.20 shows an example of processing one Micro-CT image for a small portion of a micro-scaffold ceramic disk. Starting with original image, the edges were detected by capturing the zero crossing of the Laplacian derivative of the image (see figure 2.20-b). The edges were used to enhance the region growing algorithm until fined the areas enclosed by solid ceramic particles.

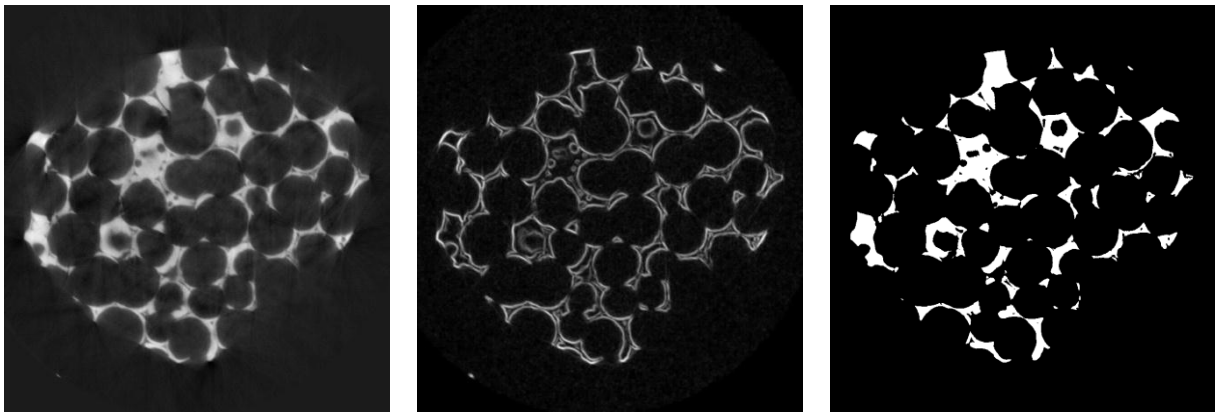

(a) original Micro-CT Image (b) edge detection (c) solid region detection

Figure 2.20: The steps of processing a sample cross sectional Micro-CT image until finding the area enclosed by the ceramic solid particles.

For using this methodology to generate such a 3-D geometrical model, an assembly process has to take place. In this process, a set of processed binary 2-d images (regions and edges were detected) were assembled together forming a 3-D geometrical model of the scaffolds (see Figure 2.21).

Figure 2.21: From the Micro-CT images 430 hundred 2-d binary edge images are assembled forming a 3-D binary file of the scaffolds.

The generated geometrical model will define the parts enclosed by the solid material of the scaffold allocated in a three dimensional matrix as solid obstacles. Fortunately, the LBM solver uses the concept of bounce-back for satisfying the boundary conditions, this makes

it much easier for the propagation of the particles in the flow field. Meaning, if a solid obstacle approaching the particles reflects back and if the path is obstacle free particles propagate.

2.3.2 Flux Conditions: Inflow/Outflow

2.3.2.1 Velocity Inlet/Outlet

A prescribed inflow velocity u_{in} and density ρ are easily implemented by filling the distribution with their corresponding equilibrium value, such that:

$$f_i(x=0,y) = f^{equ}{}_i(\rho, u_{in}) \tag{2.63}$$

It is common to apply zero-gradient outlet condition, which is also implemented by setting the distributions with their equilibrium values after calculating the exit velocities. But this may produce backward propagation of disturbances influencing the flow field if the exit is too close, due to its non physical condition. This issue can be resolved by applying the so called 'porous plug', [19].

This is achieved by correcting the exit velocity with the reflection probability defined by:

$$r = 1 + 4\left(\frac{u - u_{in}}{1 - 2u}\right) \tag{2.64}$$

Thus if $r = 1$ no correction is needed and if $r > 1$ then to keep the flow in global balance, the outgoing distribution must be over reflected, in order to reabsorb the excess speed $u - u_{in}$.

A better boundary condition to conserve the momentum is the pressure gradient condition.

2.3.2.2 Pressure Gradient

A typical pressure gradient [49] along the x-axis is applied for both phases, which is reasonable to model the pumped in feeds; this is seen in equation 65.

$$\tilde{f}_i(x,t) = f_i(x,t) - w_i \frac{3}{c^2}\left|\frac{dp}{dx}\right| \hat{e}_i . \hat{x}. \tag{2.65}$$

Denoting the dp/dx as the applied pressure gradient over the bioreactor satisfying the pump differential Pressure and the overall Reynolds number; $\hat{x}$ represents the unit vector of the pressure gradient direction which is in this case in the x-direction. The equation resembles the update of the particle distribution at time t with the pressure gradient effect to reach the new distribution $\tilde{f}_i^k(x,t)$

Additionally an oscillating boundary condition was developed for modelling oscillating flow fields or oscillating pressure fields as in the application of acoustic wave propagation. This was implemented by providing an oscillating pressure gradient term:

$$\tilde{f}_i(x,t) = f_i(x,t) - w_i \frac{3}{c^2}\left|\frac{dp}{dx}\sin(\varpi t)\right|\hat{e}_i.\hat{x}. \tag{2.66}$$

The equation is stable provided low pressure amplitude fluctuations $\delta P/P$. Accordingly the Reynolds number for the dynamic similarity condition as in equation (2.13) should be upgraded to include the oscillating pressure field variations such that:

$$\mathrm{Re}_{Pressure} = \frac{c_s \lambda}{\nu} \tag{2.67}$$

Where c_s is the speed of soundor speed of pressure wave propagation in the field, λ is the pressure wavelength and ν is the kinematic viscosity. The relation between the speed of sound at which the pressure wave travels, the wavelength and the frequency of oscillations could be expressed as:

$$\lambda = \frac{2\pi \cdot c_s}{\varpi} \tag{2.68}$$

2.3.2.3 Thermal Flux:

In natural heating process the heat energy is transferred first from the surrounding environment to the heated surface then the heat is conducted through the interfacial boundary to the inner core of the heated unit.

The heating process passes two steps: Heat loss, heat conduction and then heat diffusion in the inner core Figure 2.22.

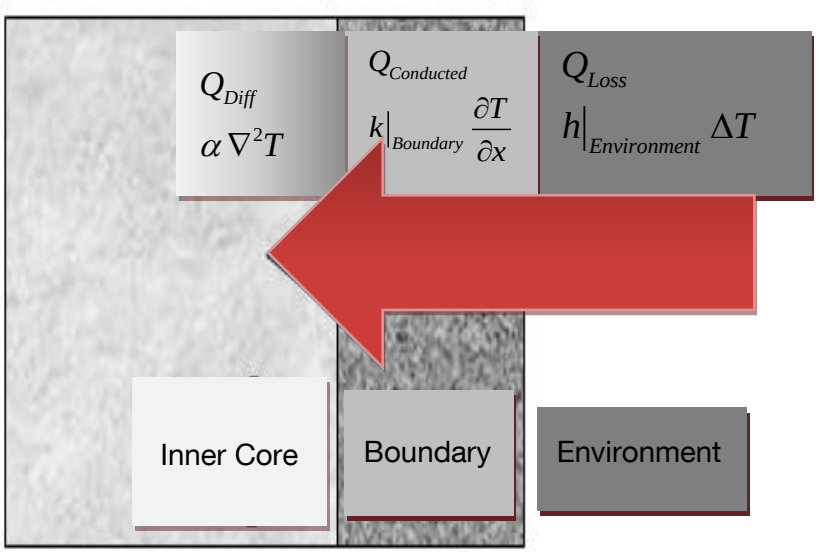

Figure 2.22: Heat energy is transferred first from the surrounding environment to the heated surface then the heat is conducted through the interfacial boundary to the inner core

Fourier's law for heat conduction, equation (2.69), is applied for conduction from the hot surrounding to the heated body. This, states that the rate of heat transfer through a material is proportional to the negative gradient in the temperatures [50].

$$Q_{Loss} = Q_{Conducted}$$
$$h|_{Heating\ Environment} \Delta T = k|_{Boundary} \frac{\partial T}{\partial x} \tag{2.69}$$

The heat transfer coefficient, *h*, is the proportionality factor responsible for transferring the heat to the first layer. Additionally, the thermal conductivity, *K,* will act to transfer this heat from the very first dough layer to the second layer inwards.

2.3.2.4 Moisture flux:

The mechanisms by which heat and moisture are transferred in a material basically depend on the physical micro-structure and chemical composition of the material. This can be classified accordingly in respect to its water binding properties (hygroscopic). In the case of hygroscopic material; the trend at which the moisture content inside matter dries out is commonly dependent upon the partial pressure as a function of temperature. The moisture content flux *J* can be expressed using Fick's first law of diffusion.

$$J = \nabla C = K\left(P_{Matter}(T_{Matter}) - P_{\infty}(T_{\infty})\right) \tag{2.70}$$

In equation (2.70) *C* moisture content, *K* material constant, $P_{Matter}(T_{Matter})$ water partial pressure in matter, $P_{\infty}(T_{\infty})$ water partial pressure in the surrounding environment [39]. The moisture content is the driving flux of the moisture content. Furthermore, if $P_{Matter}(T_{Matter}) > P_{\infty}(T_{\infty})$ a positive flux exhibits which means a moisture drive from the matter to the surrounding as demonstrated in Figure 2.23.

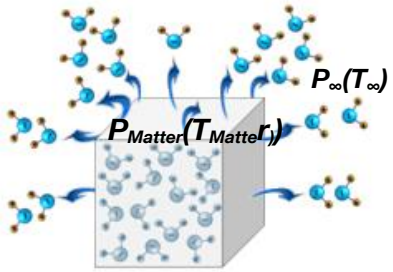

Figure 2.23: As long as the partial pressure provides a positive flux $P_{Matter}(T_{Matter}) > P_{\infty}(T_{\infty})$ a moisture flux exhibits which means moisture driven from the matter to the surrounding.

2.3.3 Active Boundary Conditions

2.3.3.1 Absorbing and non-Absorbing Boundary Condition

For non-absorbing boundary conditions through an interface or wall, the particle distribution flux through the interface would be similar to the bounce back condition, equation (2.71):

$$flux_{in} = flux_{out},\ f_i^{in} \cdot \hat{n}^{in} = f_i^{out} \cdot \hat{n}^{out} \tag{2.71}$$

For non-reactive absorbing interfaces, some solute particles are reflected and some are absorbed such that:

$$\begin{gathered} Flux_{absorb} = C_{absorb}\left(f_i^{in} \cdot \hat{n}^{in}\right) Flux_{reflect},\ Flux_{reflect} = \left(1 - C_{absorb}\right)\left(f_i^{in} \cdot \hat{n}^{in}\right), \\ f_i^{in} \cdot \hat{n}^{in} = Flux_{absorb} + Flux_{reflect} \end{gathered} \tag{2.72}$$

Where C_{absorb} is the absorbed fraction of the solute and for a flux balance both absorbed and reflected flux must resemble the inflowing flux. In this thesis we will focus only upon gas into liquid absorption.

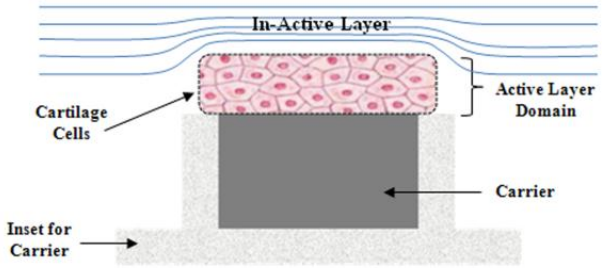

Figure 2.24: The active layer domain could be physically packed cells inside a flow reactor at which the substrate transport is only achieved using diffusion and not advection.

In the case of gases absorbed in liquids, Henry's Law of solubility could be used to determine the maximum absorbed solute concentration [52-53].

$$C_{\max} = K_{solute} X_{solute} \tag{2.73}$$

Where K_{solute} is the Henry's constant for the solute, and X_{solute} is the partial pressure of the gas in equilibrium with the liquid.

2.3.3.2 Reaction Kinetics of Biologically Active Boundaries

The active layer can be defined as the domain at which nodes have activity towards the substrate concentration. Usually the active layer is either a sink or a source for this substrate.

A typical application of active layers is the substrate consumption by the cells, at which the cells' activity can be regarded as an active layer. The cells' activity and enzyme kinetics could be modelled by means of monod-Michaelis-Menten kinetics [53-56], developed by Michaelis-Menten (1913) . This methodology was used widely in the literature [53] to model the drug absorption kinetics, also used the same approach in the simulation of Immobilized Enzyme reactor [54], moreover, the approach was further used to model tissue reaction kinetics for nasal extraction of inhaled hydrogen sulphide in rats [56].

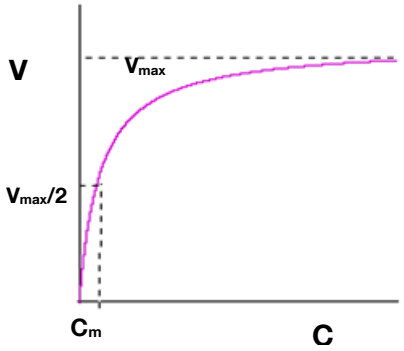

Figure 2.25: The Michaelis-Menten model describes the reaction rate as function of substrate supply, nevertheless a limitation exhibits upon the reaction rate limiting it to V_{max} independently of substrate supply.

In this thesis the process of the biological activity of cells is considered towards substrate or nutrition as these cells respire or feed. The transport inside the active layer can be modelled by adding a sink term to the transport equation, at the location of such active boundaries, using the Michaelis-Menten model for reaction rate. Inside this active layer the diffusion in the transport equation dominates as the velocity vector diminishes thus, it's more physical

to neglect the advection term. The rate of substrate uptake or the reaction rate, V, could be written as:

$$Sink\,Term = V(C) = -V_{\max}\frac{C}{C_m + C} \tag{2.74}$$

V_{max} is the maximum substrate rate of reaction; C_m is the substrate concentration at which the reaction rate is half its value. Noteworthy, This monod-Michaelis-Menten kinetic model is relevant to situations where simple kinetics can be assumed, it lacks substrate inhibition or limitations, product inhibition or growth model. The growth model could be included as a differential equation [57]:

$$\frac{dX}{dt} = V(C)\cdot X \tag{2.75}$$

Where X is the biomass contcentration, often excessive limitations on the substrate supply exhibits. Such as diffusion limitations, transport limitations and biomass growth limitations.

2.4 Conclusion

A comparison between different modelling techniques has been provided, which concluded to the supremacy of LBM in the following points above the continuum approaches:

- The provision of the possibility to predict process at different time scales such as the diffusion transport and the advection transport process.
- LBM enhances non-equilibrium considerations of a system by including in the particle distribution, since most of the systems existing in nature are not in energetic equilibrium. Thus, a step forward for life science modelling.
- Ability to model micro fluidics, such as flow in micro scaffolds, and a Wide range of Knudsen number ϕ<*100μm*, without violating equilibrium rules. This is quite practical in bioreactor flow fields. This helps to increase the zoom of monitoring (higher degree of Spatio-temporal resolution) in complicated phenomena such as: reaction kinetics, Better Ability to model multiphase and phase separation, Complex solid–liquid interfaces, surface reactions in fluids, liquid–solid flows of colloidal suspension.
- Better processing power and memory reduction

As well, in the comparison to the lattice gas automata, the lattice Boltzmann method has proven a necessary successor to the lattice gas models, by means of:

- Galilean invariance by provision of more isotropic propagation and collision of the particles.
- The exchange of the Fermi-Dirac statistics to Maxwell-.Boltzmann distributions, this provides enhanced energy spectrum coverage.

- Less statistical noise, enhanced convergence and more smoother dynamics is achieved by the usage of non-Boolean particle distributions.
- Collision rules are much more deterministic and follow physical conditions, rather than the random choice of possible outcomes in some cases.

The lattice Boltzmann method, therefore, is a powerful approach for mesoscale and scale-bridging simulations. It is capable for tackling particularly those problems which have a detailed Spatio-temporal resolution which reflects to the macroscopic picture, namely, flows under complicated geometrical boundary conditions, multi-scale flow phenomena, multi-phase flows, complex solid–liquid interfaces, surface reactions in fluids, liquid–solid flows of colloidal suspensions and reactions.

The necessary theoretical background has been detailed in this chapter for the investigations performed in this thesis. Where the introduction to LBM modelling presented will be the base stone for the published papers in the next chapter. As already mentioned, the work covers several challenges from life science engineering: single and multiphase flow, substrate diffusion, substrate solubility, reaction kinetics, cell kinetics modelling, biologically active conditions, acoustic propagations in mediums, simultaneous heat and mass transfer in foams, moisture flux, micro-channel flow, cyclic excited flow and moisture driven flux.

3. Summary of Results (Thesis Publications)

3.1 Paper Summary

In this chapter the points of interest in each paper investigation are described and followed by copies of these papers.

Hussein, M. A., Baumann, G., Sherif, A. O., Esterl, S., Becker, T.: On the Validation of a 2-D Laminar Flow Solver Using Lattice Boltzmann Method. Proceedings of 8th International Congress of Fluid Dynamics and Propulsion, American Society of Mechanical Engineers, Sharm El-Sheikh, Egypt, 2006-12-14, ICFDP8-EG-200.

We present benchmarking of the 2-D lattice Boltzmann code developed. Where two classical test cases are used: Lid driven cavity and the Backstep flow. Both cases are tested up to the end of the laminar zone as no turbulence modelling is yet included. The voirtical structure sizes and the pressure fields were used for quantitative comparison, the vertical edges were determined using the zero vorticity condition. Both test cases has shown quite good agreement to literature results. As well the computational effort is reported in comparison to an existing optimized Navier-Stokes solver developed by the author, showing speeding of up to 9 times and memory usage reduction of 4.88 times.

Hussein, M. A., Esterl, S., Pörtner, R., Wiegandt, K., Becker, T.: Impulse and mass transport in a cartilage bioreactor using the lattice Boltzmann method. International Journal of Computational Fluid Dynamics 22 (2008), 341 - 350.

Modelling the bio-chemical substrate transfer efficiently with the ability of substrate consumption by cells is one of those great challenges in tissue modelling. This would contribute strongly in the cell growth rates, due to malnutrition or waste contamination.

This paper basically, addresses the single-phase diffusive transport mechanism around such cell in the micro-scale dynamics seeing that the process prevails in such scale. This investigation produces 'bioreactor performance map' for each specific bioreactor which relates the different substrate concentration to the dynamics of the reactor and differentiating between each design conditions falling whether into a diffusion limited zone or transport limited. The investigation concludes that appropriate transport needs more resident time but for very high residence times the diffusion overrides the process and blocks it. As well increasing the inlet dissolved substrate concentration is limited with the maximum solubility condition for each substrate type in the carrier fluid (solvent). For further bioreactor designs, the stress conditions and distributions should be in similarity with realistic cases.

Hussein, M. A., Esterl, S., Pörtner, R., Wiegandt, K., Becker, T.: On the lattice Boltzmann method simulation of a two-phase flow bioreactor for artificially grown cartilage cells. Journal of Biomechanics 41 (2008), 3455-3461.

A similar investigation to the second paper is carried out but in the case of multiphase bioreactor, where the substrate has an independent phase and dissolves across the two phase interface into the carrier fluid to the cells. The paper includes the modelling of the

substrate transfer with the ability of substrate consumption by cells using monod-Michaelis-Menten kinetics, modelling of both together would contribute strongly in the understanding of cell growth rates. The numerical substrate content of the carrier fluid at the bioreactor exit are compared with experimental results producing a similar trends up to *16* minutes, but discrepancies occur later on which is reported to be of experimental setup deficiencies or for using a linear solubility model for a non linear solubility phenomena. Nevertheless, the overall substrate levels proved consistent with the measurements after *1h* showing a difference of *7%*. The stress conditions are as well reported to mismatch the realistic case, concluding to further design considerations to raise the stress level in the bioreactor.

Hussein, M. A., Becker, T.: Numerical Modelling of Shear and Normal Stress of Micro-Porous Ceramics for Stimulated in-vitro Cultivation of Bone Cells. Microfluidics and Nanofluidics 8 (2009), 665-675.

As mentioned in the two previous investigations: the stress levels in the bioreactor mismatches the real case, where the cells originally grow. This is a top priority influence in load carrying cells such as: Cartilage cells and Skeletal cells both are usually growing inside humans under moderate cyclic mechanical loadings. Stress is transferred between the cells by two means: loading and perfusion. In this paper an analogical study is carried out between the realistic stresses expected in humans and the simulated ones inside microscaffolds, reporting different discussion aspects to bring the designed structures to a more realistic stage. A novel edge detection algorithm which spots the colour change by means of gradient calculations was successful to scan the Micro-CT (computer tomography) images and gather a binary file for the 3-D scaffolds of *430* sections for a *3mm*. Different porosity sizes and pore orientations were investigated to achieve this, reporting that the geometry configuration (expressed by the porosity and channelling angles) and the flow dynamics (expressed by Darcy's Reynolds number) can limit the stress at three cases: high channel angle *(>45°)*, at low porosity *(0.47)* and at higher porosity *(0.91)*. Thus it is not always a win–win situation. Using micro-porous scaffolds have proven much more realistic in imitating the human bone shear load conditions *(0.1 MPa)* with at least two orders of magnitude closer *(5.3x10-4 MPa)* than previously published results *(1.09x10-6 Pa)*. Further work should be done to realise closer shear loads to measured data in humans.

Hussein, M. A., Becker, T.: An innovative Micro-modelling of Simultaneous Heat and Mois-ture Transfer during Bread Baking using the Lattice Boltzmann Method. Food Biophysics (2010) DOI: 10.1007/s11483-010-9156-1

Dehydration is a vital aspect in the food industry, with food foams espicially baked goods, due to its daily basis necessity. A substantial fraction of the energy consumed in process industries is required for drying operations. From a transport phenomena point of view,

bread baking has been considered as a simultaneous heat and mass transfer (SHMT) problem in a porous medium. Several previous works has addressed the same problem with trials of modelling different aspects of bread baking process but often proceeded with the assumptions that the thermo-physics occur in the macro-scale, which is in fact not true. In this paper simultaneous heat and moisture transfer models using LBM were developed to accomplish the mechanisms included, in the microscale and reflecting back to the macroscale, to predict moisture transfer, heat transfer, measurement of effective moisture diffusivity, thermal conductivity and diffusivity. The models were quantified and validated with measurements in order to assess the predictive models.

A step forward to descriptive analysis and investigation of micro-macro dough baking is presented in this part in a detailed modelling approach using the lattice Boltzmann methods. The micro structure of the dough samples investigated were obtained using Micro-computer tomography Images from the samples prior to baking. The simulated crust development has shown a crust thickness of *0.8 cm,* which is slightly higher than similar experimental results in which a dehydrated thickness of *0.5–0.6 cm* was reported. Additionally, investigations were made on the influence of different porosities *(11–16%)* of the bread; the boundary layer temperature at porosity of *11%* was reached after *25 min* and after *17.5 min* at porosity of *16%*. Therewith, the results showed that, with increasing porosity, the heat transfer rate towards the centre was higher, which could be a step forward for optimizing the baking procedure which would reflect heavily on the economics.

Proceedings of ICFDP 8:
8th International Congress of Fluid Dynamics and Propulsion
Dec. 14-17, 2006, Sharm El-Sheihk, Sinai, Egypt
ICFDP8-EG-200

On the Validation of a 2-D Laminar Flow Solver Using Lattice Boltzmann Method

Mohamed A. Hussein[1], Gerd Baumann[2], Atef O.Sherif[3], Stefan Esterl[4], Thomas Becker[5]

[1] Fachgebiet Prozessanalytik, Universität Hohenheim, Stuttgart
[2] Mathematics Department, German University in Cairo, New Cairo City
[3] Aerospace Department, Cairo University, Giza
[4] Fachgebiet Prozessanalytik, Universität Hohenheim, Stuttgart
[5] Fachgebiet Prozessanalytik, Universität Hohenheim, Stuttgart

Abstract

In this paper 2-D laminar flow is modeled using the Lattice Boltzmann method LBM .The solver, which operates at moderate Reynolds numbers, is being validated using benchmarks such as Backstep flow and Driven Cavity. This is achieved by comparing the qualitative and quantitative results obtained by LBM with the traditional solution approach for such problems. The D2Q9 lattice model is used to carry out the calculations for the flow field, with a first order bounce back boundary condition. The processing time speed up and memory usage are reported.

Keywords: Lattice Boltzmann equation; 2-D Flow; Laminar; Backstep; Driven Cavity

Introduction

In the last 18 years extensive work has been developed in the newly evolving Lattice Boltzmann method LBM.

The basic idea of Ludwig Boltzmann's equation is to consider gas as composed of interacting particles, and that this interaction can be modeled by classical mechanics. Of course, there are so many particles such that statistical approach is essential. The Lattice Boltzmann's equations relate the particle distribution per unit time in a certain control volume to the convective motion and collision.

After solving this equation it is essential to calculate the fluid properties from the distribution functions. This was first proposed by McNamara and Zanetti[1] along with others who developed it further, notably, Higuera and Jiménez[2], Koelmann[3], Qian et al. [4] and d´Humières[5].

Governing Equations

The particle mechanics is basically governed by *Boltzmann's equation*:

$$\frac{\partial f}{\partial t} + \upsilon \bullet \nabla f = Q \qquad (1.1)$$

Where:

f : *particle distribution function*

υ : *particle velocity*

Q : *collision operator*

The collision operator Q which contributes for the collision of molecules basically predicts the influence of the collision on the distribution functions, and accounts for positive or negative influence.

This operator has been approximated by Koelmann[3] in 1991 using the *Bhatnagar-Gross-Krook (BGK[6])* model, also known as *single-relaxation-time (SRT)* model.

$$Q = -\frac{1}{\tau}(f - f^{equ}) \qquad (1.2)$$

Where:

f^{equ} : *equilibrum distribution function*

τ : *relaxation time*

Meaning that the collision of particles is considered as relaxation towards a local equilibrium of distribution f^{equ} and taking relaxation time τ .

Leading to the *B-BGK equation*

$$\frac{\partial f}{\partial t} + \upsilon.\nabla f = -\frac{1}{\tau}(f - f^{equ}) \qquad (1.3)$$

Where the reciprocal of the relaxation time $1/\tau$ maybe replaced by the relaxation frequency `ω´, sometimes referred to as the relaxation parameter.

$$\omega = 1/\tau \qquad (1.4)$$

Now representing the space directions with a set of finite velocities υ_i and associated distribution functions f_i, the *Discrete Boltzmann equation* is retrieved.

$$\frac{\partial f_i}{\partial t} + \upsilon_i \bullet \nabla f_i = -\omega(f_i - f_i^{equ}) \qquad (1.5)$$

This is the basic equation to determine a distribution function representing the number of particles along the directions of υ_i .

Choosing the D2Q9, meaning nine velocity directions representing the 2-D lattice as in Fig.1.

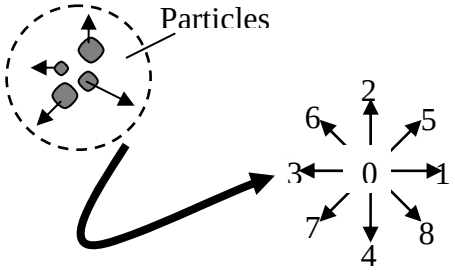

Fig.1 Particles can be represented by distribution functions along nine directions

Discretizing equation (1.5) by basic finite difference rules, we get the *Lattice Boltzmann equation.*

$$f_i(t+1, r+1) = f_i(t,r) - \omega(f_i(t,r) - f_i^{equ}(t,r)) \qquad (1.6)$$

Which is divided into two parts advection and relaxation steps.

$$Advection - Step:\quad f_i(t+1, r+1) = f^a{}_i(t,r)$$

$$\text{Re}laxation - Step:\quad f_i^a(t,r) = f_i(t,r) - \omega(f_i(t,r) - f_i^{equ}(t,r)) \qquad (1.7)$$

Defining:

$$f_i^{equ} = w_i \rho(r)\left[1 + 3\frac{\hat{e}_i \bullet \upsilon}{c^2} + \frac{9}{2}\frac{(\hat{e}_i \bullet \upsilon)^2}{c^4} - \frac{3}{2}\frac{\upsilon^2}{c^2}\right] \qquad (1.8)$$

Where

$\hat{e}_i : unit\ vector\ in\ i^{th} - direction$

$\upsilon : macroscopic\ velocity$

$c = \Delta r/\Delta t : basic\ speed\ of\ lattice$

$w_i : direction\ weighting\ factor$

$\rho(r) : density$

The weighting factor can be obtained from the following table

Direction $\hat{e}_i$	w_i
0	4/9
1,2,3,4	1/9
5,6,7,8	1/36

Table.1 Values of weighting factors according to the unit directions.

The density, momentum fluxes and viscosity can be obtained as follows:

$$\rho = \sum_{i=0}^{8} f_i = \sum_{i=0}^{8} f_i^{equ}$$

$$\rho\upsilon = \sum_{i=1}^{8} \hat{e}_i f_i = \sum_{i=1}^{8} \hat{e}_i f_i^{equ} \qquad (1.9)$$

$$\nu = \frac{1}{6}\left(\frac{2}{\omega} - 1\right)$$

Boundary Conditions

In this work only three major boundary conditions are discussed: The wall (non-slip), the Von Neumann inlet/outlet Flux boundary condition and the sliding wall boundary condition

The Wall Boundary Condition:

In LBM often referred to as the *Bounce-back* boundaries. These boundaries are very easy to implement and don't need special programming and they are one of the most powerful characters of LBM.

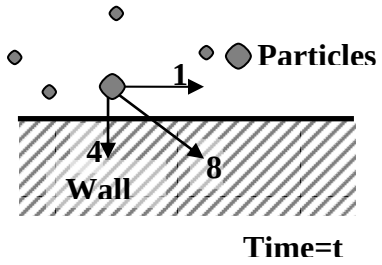

Fig.2 A particle about to hit a wall at time *t*

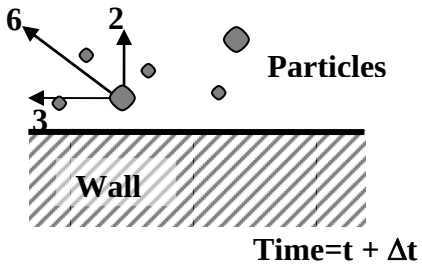

Fig.3 A particle bouncing back at time $t+\Delta t$

As seen in figures 2 and 3 the particle at time t had distributions of different magnitudes in directions 1,8 and 4.After an incremental time $t+\Delta t$ the distributions are reversed in direction after bouncing form the wall conserving there magnitude but directly opposing there direction.

If the wall location exactly fits on the lattice a 1st order accuracy is obtained. On the other hand if the wall is in mid lattice i.e. the distance between the lattice and the wall is $\Delta x/2$ then 2nd order accurate Boundary condition is claimed, Succi[7].

For inclined walls a staircase of vertical and horizontal walls may be applied but queries have arisen concerning the artificial increase in rugosity, but it still merits for its simplicity. Chen and Martinez[8] have produced a decent method for dealing with inclined planes using extrapolation schemes, which is out of the focus of this work.

The Inlet / Outlet Boundary Condition:

A prescribed inflow velocity U_∞ and density ρ_∞ are easily implemented by filling the distribution with their corresponding equilibrium value, such that:

$$f_i(x=0,y) = f^{equ}{}_i(\rho_\infty, U_\infty) \quad (1.10)$$

It is common to apply zero-gradient outlet condition, which is also implemented by setting the distributions with their equilibrium values after calculating the exit velocities. But this way may produce backward propagation of disturbances influencing the flow field if the exit is too close, This issue can be resolve by applying the so called 'porous plug', Succi[7].

This is achieved by correcting the exit velocity with the reflection probability defined by:

$$r = 1 + 4\left(\frac{\upsilon - U_\infty}{1-2u}\right) \quad (1.11)$$

Thus if $r = 1$ no correction is needed and if $r \succ 1$ then, outgoing distribution must be over reflected.

This topic is out of the scope of this work and not considered. The exit boundary condition is placed in the far field to overcome this issue and a regular zero gradient is implemented.

The Sliding Wall Boundary Condition:

This boundary conditions treats the presence of a wall sliding with a certain velocity Uw.This wall exhibits tangential velocities on the particles near by. In LBM this is translated to a Wall velocity affected density distributions.

By simple x-momentum and y-momentum equilibrium we reach the bounce back distributions as a function in wall velocity Uw.

$$\begin{aligned} &X-Momentum: \\ &J_x = f_5 - f_6 + f_8 - f_7 + f_1 - f_3 \\ &J_x = \rho U_w \\ &Y-Momentum: \\ &J_y = f_5 - f_8 + f_6 - f_7 + f_2 - f_4 \\ &J_x = 0 \end{aligned} \quad (1.12)$$

To finalize the formulation it is needed to introduce adjustable reflection coefficients p, q and using them to adjust the particles speed next to the wall to become the wall velocity.

$$\begin{bmatrix} f_7 \\ f_4 \\ f_8 \end{bmatrix} = \begin{bmatrix} p & 0 & q \\ 0 & 1 & 0 \\ q & 0 & p \end{bmatrix} \begin{bmatrix} f_5 \\ f_2 \\ f_6 \end{bmatrix} \quad (1.13)$$

Solving together with equation (1.11) an expression for p, q as a function of the Uw and the known distributions 2, 5 and 6. Which are the distributions prior to the bouncing back form the moving wall; this is seen clear in figure 4 and 5.

$$p = 1 - \frac{\rho U_w}{2(f_5 - f_6)}, q = \frac{\rho U_w}{2(f_5 - f_6)} \quad (1.14)$$

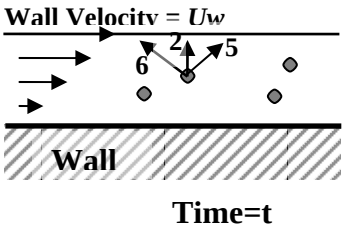

Fig.4 A particle about to hit a sliding wall at a time *t*

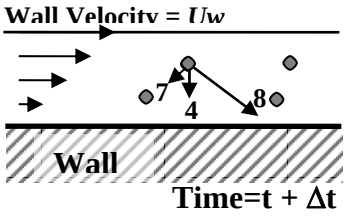

Fig.5 A particle bouncing back from a sliding wall at time $t+\Delta t$

Algorithm

The algorithm is quite simple starting with the relaxation-advection step equation (1.7), followed by the boundary condition application namely 'bounce back'.

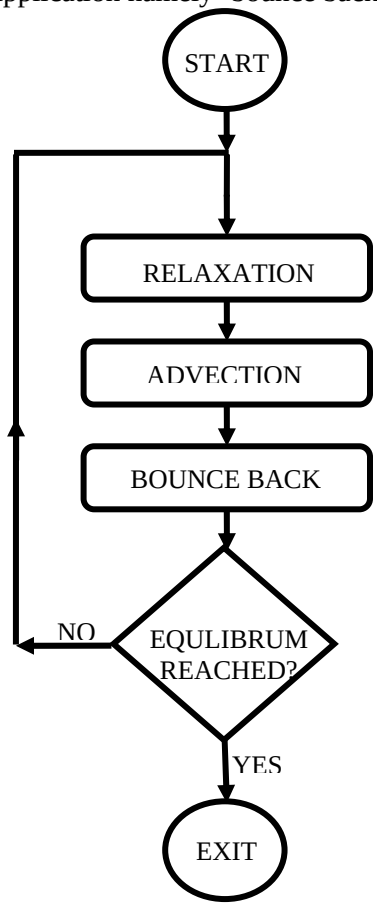

Fig.6 Main solver algorithm

The loop is iterated until equilibrium state is reached. The main solver blocks are seen below in figure 6.

Test Case1: Lid Driven Cavity

This problem has been extensively used in research to test the accuracy of solvers. The geometry consists of a square cavity covered with a constant velocity moving lid, which represents a sliding wall.

A Lattice size of 100×100 was used to simulate the flow .The solution was obtained for four Re´s: 100, 400, 1000 and 3200.

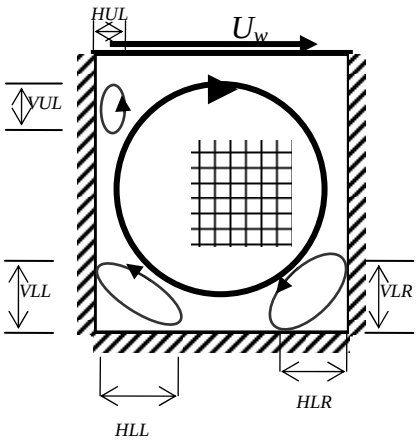

Fig.7 Cavity problem Geometry showing the main three vortices dimensioning

The stream lines and Pressure contours are compared with other LBM published data such as d´Humières and Krafczyk et al[9] and traditional Navier-Stokes solvers of Ghia[10]et al.

To acquire a quantitative comparison, the size of the three secondary and tertiary vortices, which evolves at the Upper left `UL´, Lower left `LL´ and lower right `LR´ as defined by Ghia[10] et al in 1982.

Figures 8a and 8b show the streamline results from Krafczyk[9] and this work at Re = 100.The trends are almost the same. Figure 9 shows the pressure iso-lines which also proof to be almost the same. The same accounts for figure 11a and 11b at Reynolds number 1000.

The only obvious difference is the lattice size used in both calculations which is 100×100 for this work and 50×50 for Krafczyk[9].

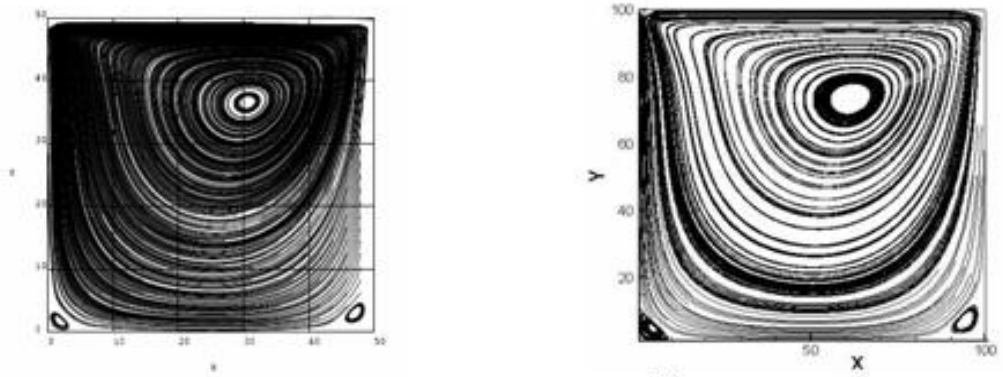

Fig.8a,8b Stream lines at Re=100 from Krafczyk[9*] (left) and form this work (right).

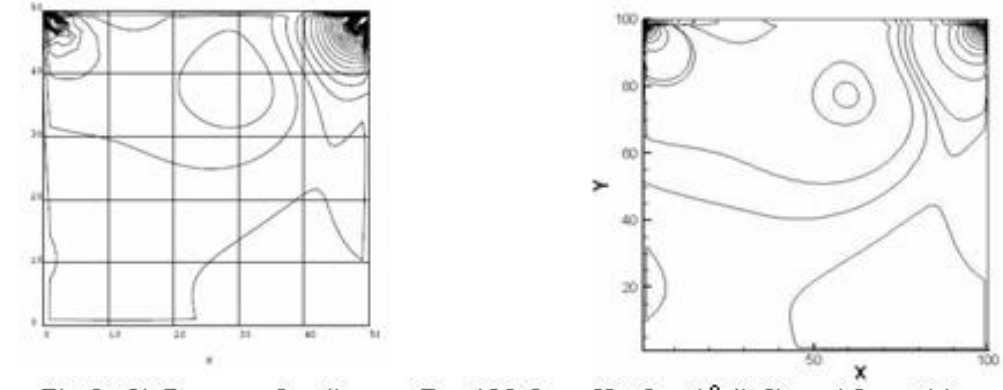

Fig.9a,9b Pressure Iso-lines at Re=100 from Krafczyk[9] (left) and form this work (right).

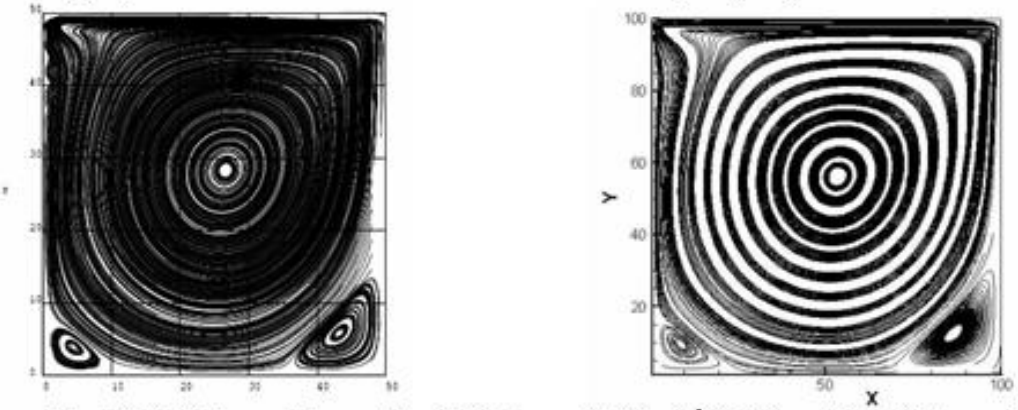

Fig.10a,10b Stream lines at Re=1000 from Krafczyk[9] (left) and form this work (right).

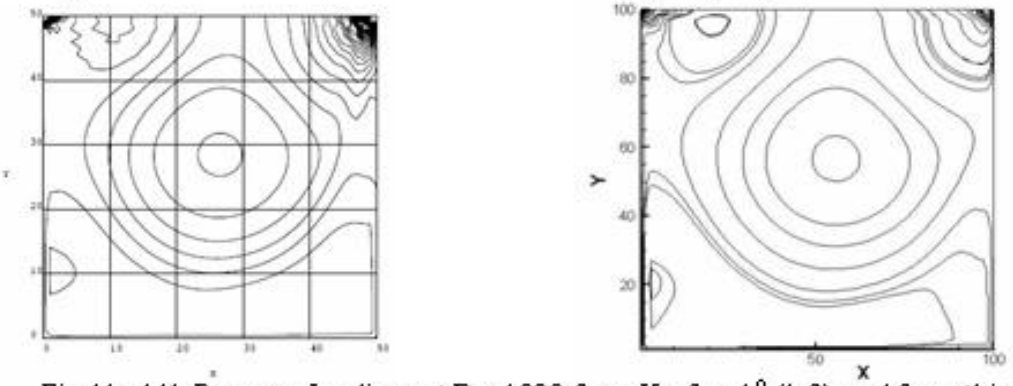

Fig.11a,11b Pressure Iso-lines at Re=1000 from Krafczyk[9] (left) and form this work (right).

He reported the use of multi relaxation scheme and multi grid blocking instead of the single relaxation scheme used in this work, this accounts for the ability to obtain accurate results using smaller grids.
Since qualitative results are never enough, the quantitative results are essential. Defined by the size of the vortices as in figure 7 .The comparison is made between the vortical sizes of this work and of Ghia[10].

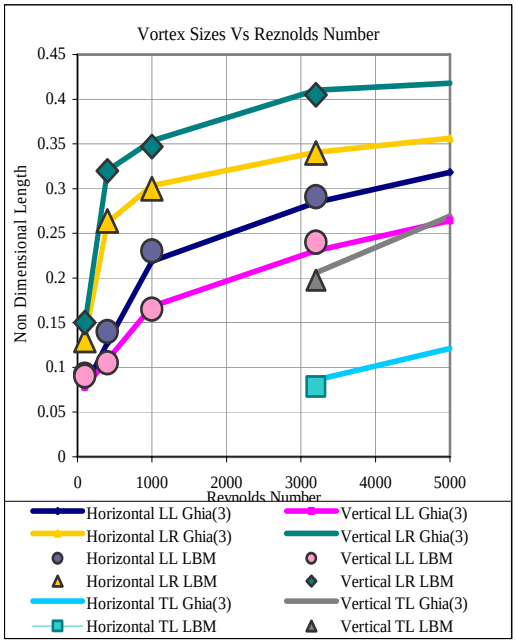

Fig.12 Quantitative comparison between Ghia[3] and this work.

Figure 12 shows how the vortex sizes defined in figure 7 change with Reynolds number. This work results are plotted as markers, whilst Ghia[10] results are solid lines. It is seen that this works results follow the same trend with slight deviations, but still keeping the same trend. This further proves that the solver is of standing capability.

Test Case2: The Backstep Flow

The Backstep problem continuously served as a tough benchmark problems for decades. This was due to the high gradients occurring at the sudden expansion zone and to the fact that it is also an inflow outflow problem.
Scientists have continuously tried to trend the Armaly[11] measurements made by laser Doppler anemometry. One of the successful numerical Navier stokes solvers which proved consistency with Armaly[11] was the work of the first and third author: Hussein and Sherif[12, 13]
The main task in this case is: the investigation of the primary vortex size dependency on the Reynolds number.

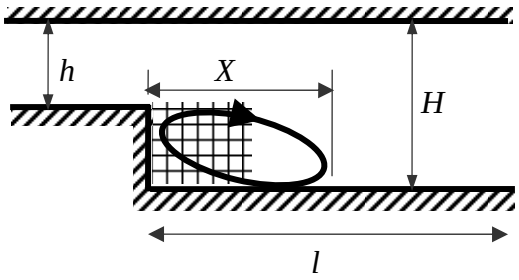

Fig.13 Backstep Geometry

The geometry is seen above in Figure 13 where the expansion ratio '*ER*' is defined as $ER = h/H = 0.5$ .The length of the channel '*l*' after the expansion should satisfy the inequality $l/h \gg 20$ in order that the outflow boundary condition doesn't affect the vortex size.
Also keeping into account that the primary vortex from laminar Reynolds number can reach a size of $X/h = 20$. A grid of 1500×50 was used.
In Figure 14 a shot from the solution was taken at Re=140, the primary vortex can be spotted easily, it is the big vortex on the lower wall of the Backstep problem.
Also a secondary vortex can be spotted on the upper wall, as well as a small tertiary vortex structure just at the corner after the expansion. The main quantity of concern here is the x-dimension stretching length of the primary vortex, which is $X/h = 4$ at this Reynolds number.
Several zooms were taken showing the velocity profiles at each vortex type, several backflow regions can be spotted.
The same is done for several Reynolds numbers: Re=265, 340 and 600. It is shown that as the Reynolds number raises the more complex the flow field becomes

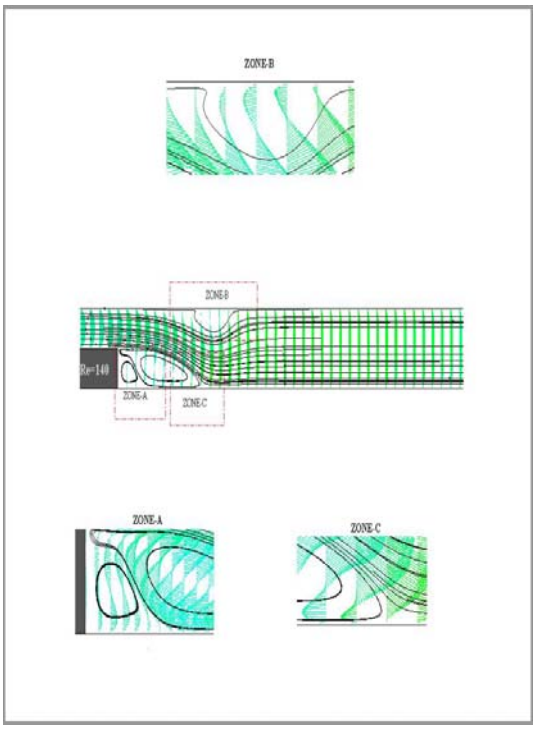

Fig.14 Streamlines and velocity vectors at Re=140

The sudden expansion of the flow field causes presence of high gradients which increase dramatically with Reynolds number.

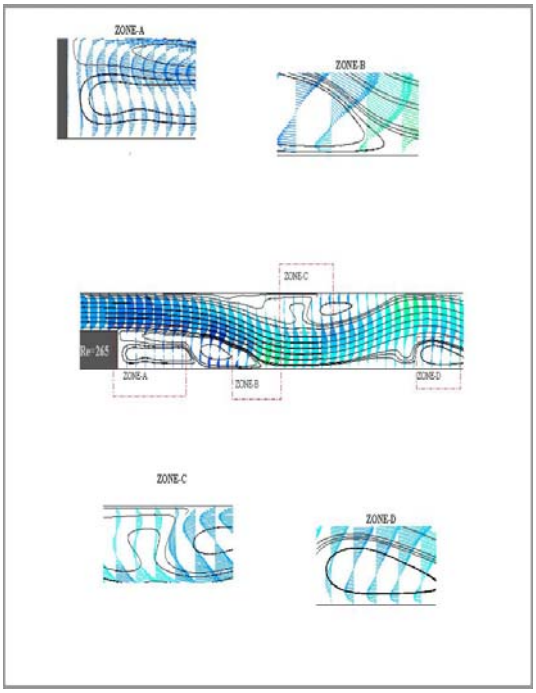

Fig.15 Streamlines and velocity vectors at Re=265

The primary vortex seems to engulf several other secondary and tertiary vortices but still it's major x-length can be determined. It is seen to extend from 4 at Reynolds number 140 passing by 9.2 at Re=430 and reaching almost 12 ratios of *h* at Re=605.

An automated methodology of predicting the vortex start and end may be done by using the fact that at the vortex start or end the Pressure gradient and Vorticity 'ζ' is almost zero.

$$\frac{dP}{dx} \approx 0 \qquad (1.15)$$
$$\zeta = \nabla \times \upsilon \approx 0$$

In figure 16, several shots of the stream lines are put in a combined figure so that the differences can be spotted easily. The flow pattern is seen as it changes further downstream as the Reynolds number increases. More and more secondary or tertiary vortices are created additionally vortex stretching is obvious

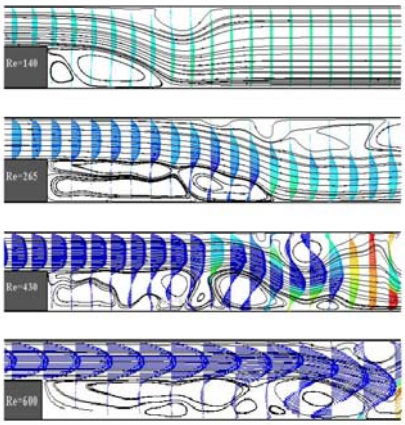

Fig.16 Streamlines and velocity vectors at Re=340

The results were obtained for different Reynolds number up to the borders of the transition region which is 1200 for this problem; this is seen in figure 17. The reattachment length is plotted on the Y-axis and the Re on the Y-axis. The results of

Armaly[11] results are in red diamonds and the results of the traditional numerical work made by Hussein[12, 13] are yellow squares.

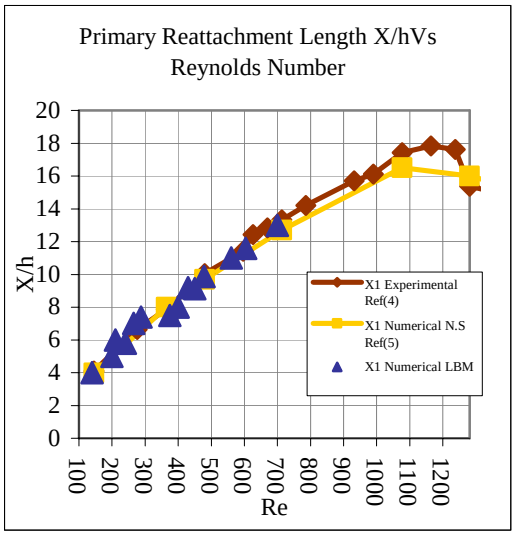

Fig.17 Primary vortex reattachment length Vs Re

The LBM solver results of this case seem to be of good trend and quality in context of this problem. This proves the ability of the solver to capture accurate results in complex flow phenomena.

Processing Time and Memory Usage

The method proves low memory usage, to simulate cavity of a 100*100 lattice a usage of 0.72 MB was achieved, whereas using traditional Navier stokes in Hussein needs 3.52 MB for the same lattice. Thus a quite noticeable memory reduction ratio of 4.88 achieved.

To compare the processing power of the method the number of nodes per second to reach steady state is calculated by LBM and using results from Hussein and Sherif[12, 13] whilst using same CPU for calculations. This gives an estimate of the processing power of the 2 methods. This is shown in figure 18. The nodes per second used by LBM starts with a two order of magnitude higher than the traditional solver, and then it falls two one order only at a bigger grid size. Also the speed up factor is calculated showing the relation between both solvers and is also plotted in figure 18. This shows a linear speedup of LBM up to a value of 10, which then depreciates with a very low rate, maintaining an average speed up factor of 9 in this scope of number of nodes.

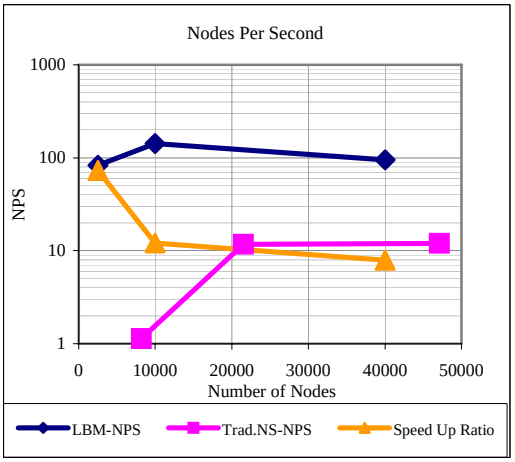

Fig.18 Comparison of Processing Performance between traditional solver and LBM

Conclusion

The lattice Boltzmann method further proves its ability in predicting complex flow patterns with high qualitative and quantitative consistency with the traditional CFD and Experimental work.

Along with a powerful processing speeding up ability up to 8 times and memory usage reduction of up to 4.88 times .The work needs to be enhanced in the direction of multi-relaxation time schemes and in means of curved boundary conditions.

References

1. McNamara G, Zanetti G. Use of the Boltzmann equation to simulate lattice-gas automata. Phys Rev Lett 1988; 61:2332–5.
2. Higuera FJ, Jiménez J. Boltzmann approach to lattice gas simulations. Europhys Lett 1989;9:663–8.
3. Koelman JMVA. A simple lattice Boltzmann scheme for Navier–Stokes fluid flow. Europhys Lett 1991; 15:603–7.
4. Qian YH, d´Humières D, Lallemand P. Lattice BGK models for Navier Stokes equation. Europhys Lett 1992; 17:479–84.
5. D´Humières D. Generalized lattice Boltzmann equations. In: Shizgal D, Weaver DP, editors. Rarefied Gas Dynamics: theory and simulations. Prog Astronaut Aeronaut 1992; 159:450–8.

6. Bhatnagar PL, Gross EP, Krook M. A model for collision processes in gases, I. small amplitude processes in charged and neutralone-component system. Phys Rev 1954; 94:511–25.
7. Succi S. The lattice Boltzmann equation for fluid dynamics and beyond. New York: Oxford University Press, 2001.
8. Chen S, Martınez D, Mei R. On boundary conditions in lattice Boltzmann method. Phys Fluids 1996; 8:2527–36.
9. D´Humières D, Ginzburg I, Krafczyk M, Lallemand P, Luo L-S. Multiple-relaxation-time lattice Boltzmann models in three dimensions. Philos Trans R Soc London 2002; 360:437–51.
10. Ghia U., Ghia K., Shin C., High-Re Solutions for Incompressible Flow Using the Navier Stokes Equations and Multi-Grid Method. J. Comput. Phys., vol.48, pp.387-401, 1982.
11. Armaly, B. F., Durst, F., Pereira, J. C. F., Schönung, B.: Experimental and theoretical investigation of backward-facing step flow. J. Fluid Mech.127, 473–496 (1983).
12. Sherif A.O, Hussein M.A.,A Computational investigation of the Back Step Flow, The Seventh International Congress on Fluid Dynamics and Propulsion,ASME,Cairo,2001
13. Hussein M. A., On the Two dimensional Viscous flow Modeling Using Vorticity-Stream Formulation, M.Sc Thesis, Cairo University, Cairo, 2003.

International Journal of Computational Fluid Dynamics
Vol. 22, No. 5, June 2008, 341–350

Impulse and mass transport in a cartilage bioreactor using the lattice Boltzmann method

M.A. Hussein[a,*], S. Esterl[a], R. Pörtner[b], K. Wiegandt[b] and T. Becker[a]

[a]*Department of Process-Analysis, Faculty of Natural Sciences, University of Hohenheim, Stuttgart, Germany;* [b]*Institute of Bioprocess and Biosystems Engineering, Hamburg University of Technology, Hamburg, Germany*

(Received 14 September 2007; final version received 5 February 2008)

Mass and Impulse transport of oxygen enriched water in cartilage cell breeding reactor are simulated using the lattice Boltzmann method (LBM). The solver is attached with a shear stress and pressure calculator to quantify the load distribution on the cells. The solver was validated using the backward-facing step flow, which is a classical benchmark of similar discrete geometry for the bioreactor. This is achieved by comparing the qualitative and quantitative results obtained by LBM with the traditional solution and experimental approach for such a problem. The D2Q9 lattice model is used to carry out the calculations for the flow field, with a first order bounce-back boundary condition. Oxygen consumption efficiency levels in the bioreactor were reported.

Keywords: lattice Boltzmann equation; backward-facing step; oxygen concentration; cartilage bioreactor; BGK model

1. Introduction

Cartilage damage in humans is very common and costly: according to Forbes Inc. cartilage transplant uptakes 75 million US dollars annually, and in Europe, according to Fraunhofer Institute System and Innovation Research (Karlsruhe, Germany), costs up to 50 million US dollars per annum with Germany taking almost half the share of it (Figure 1).

On the other hand, in Asia and Australia Commonwealth Scientific and Industrial Research Organisation (CSIRO) biotechnology reported costs of 25 million US dollars annually. Hence, there exists a high research demand to artificially grow cartilage cells.

The environmental conditions have crucial influence on the cells' morphology, a better understanding of it is appropriate and the suspected influences on the cartilage growth are:

- nutrition
- mechanical stresses.

Several bioreactors were built to reach optimised cell growing. One of the reactors built is the flow bed reactor; it is simulated in order to evaluate the effect of fluid mechanics on those conditions.

Major benefits could be achieved by numerical modelling of the bioreactor, such as human, material and time costs could be saved by simulation. Simulations vastly reduce the experimental trials as the optimum configurations of geometry and flow conditions could be estimated from the numerical runs. For example, the processes of preparing the first layer of cells which are installable in the bioreactor pass several steps: domestic pig cells are expanded for two weeks, then they are encapsulated in alginate for two weeks, afterwards the cartilage-carrier-constructs are prepared and cultivated for three weeks in the reactor, after which the bioreactor is ready to operate. This suggests that the process is mainly time dominant in addition to the fact that tissue engineering is expensive, further costs for the media, the carrier, chemicals and growths factors are unavoidable. Thus, each experiment cannot be repeated before at least seven weeks. Experimentation is unavoidable but with modelling costs is greatly reduced, since modelling gives estimates and predictions of flow conditions.

The LBM is used to model the flow properties inside the flow bed bioreactor. The method has established worldwide respect in modelling complex flow phenomena. Although the method advances are not fully utilised here, this work may be considered as an intermediate step towards the full modelling of the bioreactor, including species transport, kinetics and multiphase flow regimes which gives a future prospect for the choice of LBM.

In the last two decades extensive work has been developed in the LBM, the method has received significant attention as an alternative for simulating complex flow phenomena (McNamara and Zanetti 1988, Higuera and Jimenez 1989, Koelman 1991).

The basic idea of Ludwig Boltzmann's equation is to consider fluid composed of interacting particles. This interaction can be modelled by the Boltzmann transport equation. The lattice Boltzmann's equations (LBE) relate the particle distribution per unit time f in a certain

*Corresponding author. Email: mohamedh@uni-hohenheim.de

ISSN 1061-8562 print/ISSN 1029-0257 online

DOI: 10.1080/10618560802077806
http://www.informaworld.com

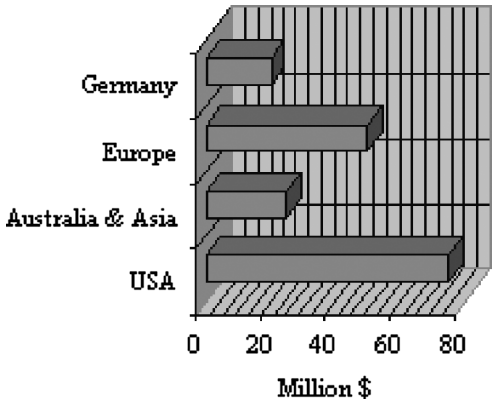

Figure 1. Amount spent on cartilage treatment around the world in million $ US dollars.

control volume to the convective motion and collision. There are so many particles such that a statistical approach is essential. The particle collision can be approximated using the Bhatnagar–Gross–Krook (BGK) model (Bhatnagar *et al.* 1954 and Koelman 1991) where the distribution function relaxes to equilibrium after collision during a constant relaxation time (Qian *et al.* 1992, D'Humieres 1992).

After solving the LBE equation, it is necessary to calculate the fluid properties, such as: density (ρ), momentum flux (ρU) and shear stress (τ), from the distribution functions, in order to get the flow properties within comprehensible quantities.

The modelling of substrate transport by means of diffusion and advection is plausible using the mass balance equation independently from the LBE as long as the substrate mass proportion is negligible in comparison to the fluid mass proportion. Furthermore, the substrate consumption by the cells can be simulated by the Michaelis–Menten kinetics. This approach has been extensively used in literature: by Wood and Thakker (1982) in the drug absorption kinetics, in the simulation of immobilised enzyme reactor (Esterl *et al.* 2003) and also in nasal tissue reaction kinetics (Schroeter *et al.* 2006). In most biological reactors, the flow speeds are kept minimal to insure complete substrate diffusion and to avoid the risk of damaging biological cells and tearing them into the fluid from their carriers (Esterl *et al.* 2003).

In this work, an LBM solver published by Hussein *et al.* (2006) is used to model the flow field associated with a substrate transport (O_2) inside the cartilage cell breeding reactor. Also for details concerning production of cartilage – implants and details, refer to Portner and Koop (1997), Fassnacht and Portner (1999), Nagel-Heyer *et al.* (2005) and Portner *et al.* (2005).

The oxygen transfer and consumption efficiencies factors are represented along with the flow field properties. Two main case studies were investigated, which are crucial in this funded research: the efficiency factors of concentration variation with Reynolds number, inlet concentration and the load distributions inside the reactor. This concludes with three main questions:

- does a higher flow speed mean a better substrate transport or not?;
- does a higher inlet concentration mean a better substrate supply to all cells?; and
- how does the load vary with Reynolds number?

2. Governing equations

The particle mechanics are basically governed by Boltzmann's equation:

$$\frac{\partial f}{\partial t} + v \cdot \nabla f = Q, \tag{1}$$

where f is particle distribution function; v, particle velocity; and Q, collision operator.

The collision operator Q, which contributes for the collision of molecules, basically predicts the influence of the collision on the distribution functions and accounts for positive or negative influence. This operator has been approximated by Koelmann (1991) using the BGK model, also known as single-relaxation-time model:

$$Q = -\frac{1}{\tau}(f - f^{\mathrm{equ}}), \tag{2}$$

where f^{equ} is equilibrium distribution function; and τ, relaxation time.

This means that the collision of particles is considered as relaxation towards a local equilibrium of distribution f^{equ} and taking relaxation time (τ), leading to the B-BGK equation

$$\frac{\partial f}{\partial t} + v \cdot \nabla f = -\frac{1}{\tau}(f - f^{\mathrm{equ}}), \quad \omega = 1/\tau, \tag{3}$$

where the reciprocal of the relaxation time $1/\tau$ can be replaced by the relaxation frequency (ω), which is sometimes referred to as the relaxation parameter. Choosing the D2Q9, means that nine velocity directions represent the 2D lattice as in Figure 2.

After applying basic discretisation rules to Equation (3), the *difference LBM equation* is retrieved:

$$f_i(t+1, r+1) = f_i(t, r) - \omega\big(f_i(t, r) - f_i^{\mathrm{equ}}(t, r)\big), \tag{4}$$

which is divided into two parts: advection and relaxation steps.

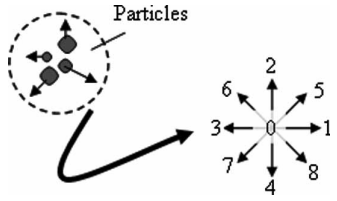

Figure 2. Particles can be represented by distribution functions along nine directions.

Advection-step:

$$f_i(t+1, r+1) = f_i^{\mathrm{a}}(t, r). \tag{5}$$

Relaxation-step:

$$f_i^{\mathrm{a}}(t,r) = f_i(t,r) - \omega\left(f_i(t,r) - f_i^{\mathrm{equ}}(t,r)\right)$$
$$f_i^{\mathrm{equ}} = w_i\rho(r)\left[1 + 3\frac{\hat{e}_i\cdot\upsilon}{c^2} + \frac{9}{2}\frac{(\hat{e}_i\cdot\upsilon)^2}{c^4} - \frac{3}{2}\frac{\upsilon^2}{c^2}\right], \tag{6}$$

where $\hat{e}_i$ is unit vector in ith-direction; υ, macroscopic particle velocity; $c = \Delta r/\Delta t$, basic speed of lattice; w_i, direction weighting factor; and $\rho(r)$, density.

The weighting factor can be obtained from the following Table 1.

The density, momentum fluxes, viscosity, pressure and shear stress can be obtained as follows:

$$\rho = \sum_{i=0}^{8} f_i = \sum_{i=0}^{8} f_i^{\mathrm{equ}}, \quad \rho\upsilon = \sum_{i=1}^{8} \hat{e}_i f_i = \sum_{i=1}^{8} \hat{e}_i f_i^{\mathrm{equ}},$$
$$v = \frac{1}{6}\left(\frac{2}{\omega} - 1\right), \quad P = C_{\mathrm{s}}\rho, \tag{7}$$

$$\tau = -\left(1 - \frac{1}{2\tau}\right)\sum_{i=1}^{8}\left[f_i - f_i^{\mathrm{equ}}\right] \times \left(e_{ix}e_{iy} - \frac{1}{2}e_i\cdot e_i\delta_{xy}\right), \tag{8}$$

where C_{s} is speed of sound; δ_{xy}, kronecker delta; and $e_{ix,y}$, discrete unit vector components in x- and y-directions.

2.1 Substrate mass balance in a biologically inactive domain

The oxygen transport is considered to follow Fick's law and is of negligible mass in comparison to the fluid. Thus, the substrates mass transport could be decoupled from the fluid mass balance safely. The diffusion advection equation in dimensionless form could be written as:

$$\frac{\partial C}{\partial t} + \upsilon\cdot(\nabla C) = \frac{1}{Bo}\nabla\cdot(\nabla C), \tag{9}$$

where C is substrate dimensionless oxygen concentration (O_2); υ, local particle velocity; and Bo, Bodenstein number.

The Bodenstein number is defined as the ratio of momentum diffusivity to mass diffusivity.

$$Bo = \frac{U_\infty l}{D}, \tag{10}$$

where l is characteristic length (inlet diameter); U_∞, inflow velocity; and D, inactive layer substrate diffusion coefficient.

Table 1. Values of weighting factors according to the unit directions.

Direction $\hat{e}_i$	w_i
0	4/9
1, 2, 3, 4	1/9
5, 6, 7, 8	1/36

2.2 Substrate mass balance in a biologically active layer domain

The active layer can be defined as the domain at which the nodes have activity towards the substrate concentration. Usually, the active layer is either a sink or a source for this substrate. Typically, an example of this process is the activity of biological cells towards oxygen as these cells perform respiration. The oxygen transport inside the active layer can be modelled by adding a sink term using the Michaelis–Menten (1913) approach:

$$\text{Sink term} : -\mathrm{RR}\frac{C}{1+C}, \tag{11}$$

where RR is dimensionless reaction rate.

The dimensionless reaction rate can be defined as:

$$\mathrm{RR} = \frac{V_{\max} l}{K_{\mathrm{m}} U_\infty}, \tag{12}$$

$V_{\max}$ is maximum rate of substrate reaction (sink); and K_{m}, substrate concentration at which the reaction rate is half its value (Michaelis–Menten constant).

Inside this active layer the diffusion in the transport equation dominates as the velocity vector diminishes, thus it is more physical to neglect the advection term:

$$\frac{\partial C}{\partial t} - \frac{1}{Bo_{\mathrm{Active}}}\nabla\cdot(\nabla C) = -\mathrm{RR}\frac{C}{1+C}, \tag{13}$$

where Bo_{Active}, Bodenstein number in the active layer.

3. Boundary conditions

Two major boundary conditions are detailed in this work, which are the necessary conditions for the bioreactor geometry: the wall (non-slip), the Von Neumann inlet–outlet flux boundary condition. The rest of the conditions which are used in the test case are adequately described in Hussein *et al.* (2006).

The non-slip conditions often referred to as the bounce-back conditions in LBM, which are quite efficient to implement and to calculate are seen in Figures 3 and 4. The particle at time t has distributions of different magnitudes in directions 1, 8 and 4. After an incremental time $t + \Delta t$ the distributions are reversed in direction after bouncing from the wall conserving their magnitude but directly opposing their direction. If the wall location exactly fits on the lattice a first-order accuracy is obtained.

For a no mass transfer (mass–flux) through the wall the correct boundary condition for the concentration equation would be:

$$\frac{\partial C}{\partial \hat{n}} = 0 \tag{14}$$

A prescribed inflow velocity U_∞ and density ρ_∞ are easily implemented by filling the distribution with their corresponding equilibrium value, such that:

$$f_i(x = 0, y) = f_i^{\text{equ}}(\rho_\infty, U_\infty) \tag{15}$$

It is common to apply a zero-gradient outlet condition, which is also implemented by setting the distributions with their equilibrium values after calculating the exit velocities. But this way may produce backward propagation of disturbances influencing the flow field if the exit is too close; this is avoided by implementing the inlet and exit further away from the main flow field:

$$C(x = 0, y) = C_{\text{inlet}} \tag{16}$$

For the substrate inlet value there exists a maximum concentration of substrate that will dissolve in water $C_{\max}$. Since the speeds would be relatively very slow in the reactor, Henry's law of solubility could be used to determine $C_{\max}$:

$$C_{\max} = K_{O_2} X_{O_2}, \tag{17}$$

where K_{O_2} is Henry's constant; and X_{O_2}, oxygen partial pressure.

This gives a maximum of 0.2175 mMol/l of dissolved O_2 per litre of water. Whilst at the exit a regular convection is made.

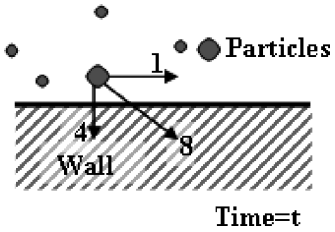

Figure 3. A particle about to hit a wall at time t.

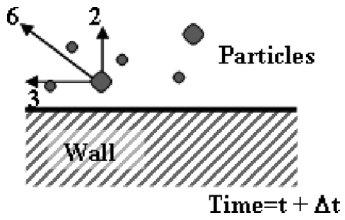

Figure 4. A particle bouncing back at time $t + \Delta t$.

4. Algorithm and computational considerations

Before speaking about the algorithm it is noteworthy to discuss the time scale jump between the two decoupled phenomena (viscous flow and substrate transport) which are about to be simulated.

With careful considerations to the kinematics viscosity ($\nu = 1.6074 \times 10^{-6}\,\text{m}^2/\text{s}$) and the diffusion coefficient ($D = 2.339 \times 10^{-9}\,\text{m}^2/\text{s}$), one can estimate the time scale jump of three orders of magnitude $\sim$ O(3). Thus, it is convenient not to solve both phenomena simultaneously, first the flow field solution is achieved to an equilibrium with a rather small time step (Δt), then the concentrations is solved utilising the reached flow field with a higher time step to quicken the reach of this three order of magnitude time jump without violating the stability of the transport equation Courant-Friedrichs-Lewy condition (CFL) ≤ 1.

The algorithm is quite simple as seen in Figure 5, starting with the relaxation–advection step Equation (5), followed by the boundary condition application, namely 'bounce-back'.

Once the equilibrium is reached in the LBM flow solver, the macroscopic values (momentum flux ρu, shear stress τ and pressure P) are calculated using

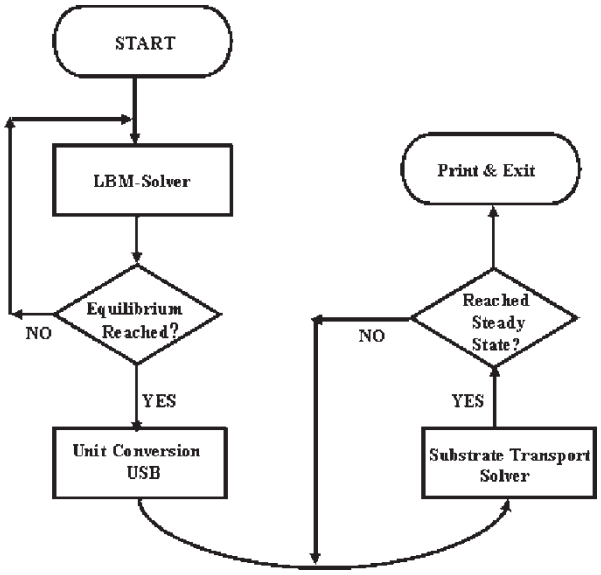

Figure 5. Solver algorithm.

Equations (7) and (8). For further details, please refer to Hussein *et al.* (2006):

$$\Delta x = \frac{L_{\mathrm{SI}}}{L_{\mathrm{LU}}}, \quad \Delta t = \frac{\Delta x}{C_{\mathrm{SSI}}}, \qquad 1\ \text{lattice mass} = 0.001\ \text{kg} \tag{18}$$

Before entering into the substrate solver at least all the flow properties used by the second solver should be converted from lattice units (LU) to SI units. In Equation (18), the conversion factors are described. To get the length conversion factor, the length in SI units is divided by the length in LU units. Similarly, the time factor is obtained by dividing the length factor with the speed of sound in SI units. Usually, it is common to state the mass of one lattice particle and in this work it is chosen as 0.001 kg. With the knowledge of mass, time and length factors it is possible to retrieve all flow properties in SI units to get a better sensitivity towards numbers. Afterwards, the substrate solver starts using the flow properties in SI units and iterates until steady-state is reached. Steady state solution is defined using the second norm as:

$$L_2 = \sqrt{\frac{\sum_{\mathrm{Domain}} \|C(t+1) - C(t)\|^2}{\sum_{\mathrm{Domain}} \|C(t+1)\|^2}} \leq \varepsilon, \quad \varepsilon = 10^{-12} \tag{19}$$

A single test case is presented to show the reliability of the proposed LBM-solver, which could be read in detail in Hussein *et al.* (2006). Last but not least, the bioreactor application is reported in detail.

5. Test case

The solver has been validated broadly in Hussein *et al.* (2006), and a single test case is presented. The test case validates the solver in perspective of momentum and continuity and further validation should be made in terms of species transport.

The back-step problem continuously served as a tough benchmark problem for decades. This is due to the high gradients occurring at the sudden expansion zone and to the fact that it is also an inflow outflow problem.

The main task in this test case is: the investigation of the primary vortex size dependency on the Reynolds number. The geometry is seen in Figure 6 where the expansion ratio 'ER' is defined as ER $= h/H = 0.5$. A grid of 1500 × 50 lattices was used.

The comparison could be seen in Figure 7. The reattachment length is plotted on the *y*-axis and the *Re* on the *x*-axis.

The results of Armaly *et al.* (1983) are in diamonds, the results of the traditional numerical work made by Hussein (2003) are squares and finally the results of the LBM solver published by Hussein *et al.* (2006) which is also used to for this work are marked with circles.

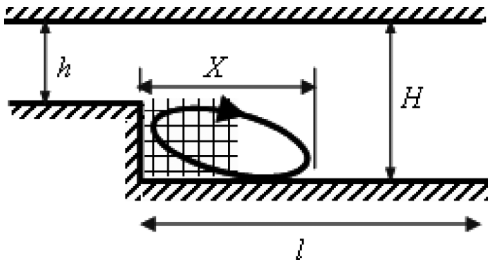

Figure 6. Back-step geometry.

The sudden expansion of the flow field causes the presence of high gradients which increases the primary vortex dramatically with Reynolds number. It is seen to extend from four at $Re = 140$, passing by 9.2 at $Re = 430$ and reaching almost 12 ratios of h at $Re = 605$. The LBM solver results of this case seem to be of good trend and quality in the context of this problem.

6. Application: simulation of the bioreactor

For simplicity, the bioreactor may be assumed of a single phase-flow with a dissolved oxygen source at the inlet. The cartilage cells consumption of oxygen for respiration may be considered as a sink term for the oxygen and can be simulated by means of Michaelis–Menten kinetics. The cell activity/growth rate may be implemented by choosing the appropriate parameters for the kinetics.

The geometry of the reactor is basically composed of a channel flow with six carriers on the lower channel wall, which the cells grow on.

A sketch of the geometry can be seen in Figure 8(a). A sectional cut shows the inside of the reactor where three of the six carriers can be seen. Each carrier is

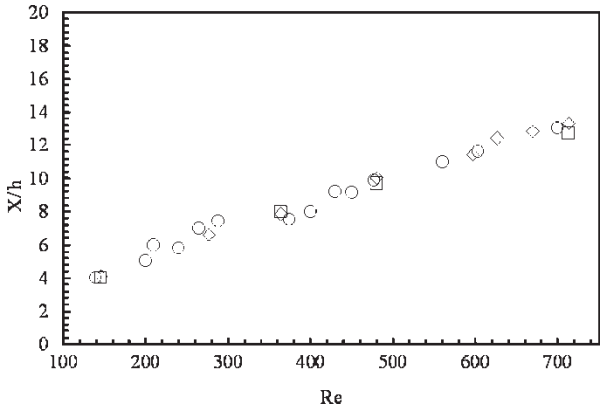

Figure 7. Primary vortex reattachment length vs. *Re* for the back-step flow. Where (◇) corresponds to experimental work by Armaly *et al.* (1983), (□) corresponds to the results of the traditional Navier–Stokes solver by Hussein (2003) and (○) corresponds to the current LBM solver used in this work by Hussein *et al.* (2006).

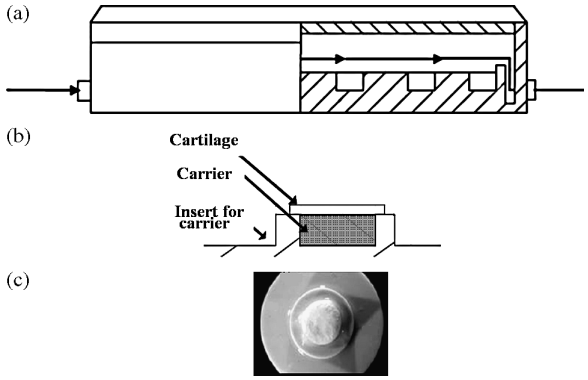

Figure 8. (a) A sketch of the bioreactor showing a section demonstrating three of the six carriers. (b) A section inside a carrier. (c) A top view photo of a carrier showing the cartilage cells on top.

composed of an insert for the carrier, the carrier itself and on top of the carrier grows the cartilage cells; this is seen in detail in Figure 8(b). A top view photo is also shown in Figure 8(c), the cartilage cells are seen growing on the top of the carrier.

From the point of view of computations, a channel flow is to be simulated with an inlet substrate concentration and with the presence of rectangular obstacles in the flow field (active layer).Where only diffusion occurs, the presence of sinks (cells) occurs, i.e. no convection. The computational domain is shown in Figure 9.

6.1 Numerical setup

A non-dimensional concentration value will be used in all calculations, such that:

$$C_{\mathrm{N-D}} = \frac{C}{K_{\mathrm{m}}} \tag{20}$$

The appropriate physical values of the constants used in the non-dimensional substrate-transport Equations (9)–(13) are listed in Table 2. The values of constants involved in the substrate transport are obtained from experimental work made with the cartilage cells by the co-authors of this work.

Using the value for K_{m} from Table 2, simply it is found that the maximum value of oxygen concentration that dissolves in water would be equivalent to $C = 21\,K_{\mathrm{m}} \rightarrow C_{\mathrm{N\text{-}D}} = 21$.

Several values for the non-dimensional inlet concentration $C_{\mathrm{N\text{-}D}}$ are used to investigate the response of the cells to those values. On the other hand, several Reynolds numbers were used for this investigation to monitor the transport of the substrate dependency on *Re*.

Steady state solutions were obtained for a reliable comparison between different test cases.

6.2 The reactor efficiency factors

To evaluate the performance of the substrate transport, diffusion and overall cell activity, several efficiency factors were introduced; (see Esterl *et al.* 2003).

The transport performance could be estimated by calculating the transfer from the fluid to the active layer through the interface surface. This is achieved by calculating the integral of the kinetics term on the interface area using the concentration values on the surface, then once more with the inlet concentration value and then dividing them together as in Equation (21). Thus, this gives a solid measure for the transport limitation of the bioreactor:

$$\begin{aligned}
\text{Rate real}_{\text{External}} &= \oint_{\text{Perimeter}} \frac{C_{\text{Surface}}}{1 + C_{\text{Surface}}}\,\mathrm{d}s, \\
\text{Rate optim}_{\text{External}} &= \oint_{\text{Perimeter}} \frac{C_{\mathrm{o}}}{1 + C_{\mathrm{o}}}\,\mathrm{d}s, \\
\eta_{\text{External}} &= \frac{\text{Rate real}_{\text{External}}}{\text{Rate optim}_{\text{External}}}
\end{aligned} \tag{21}$$

To evaluate the performance of the diffusion in the active layer alone without external effects, the area integral of the kinetic term is evaluated inside the active layer, using the concentration values in the active layer and then dividing it by the same term but using the values on the surface of the active layer, as seen in Equation (22). Therefore, evaluating the diffusion limitations inside the active layer:

$$\begin{aligned}
\text{Rate real}_{\text{Internal}} &= \oint_{\text{Area}} \frac{C}{1 + C}\,\mathrm{d}A, \\
\text{Rate optim}_{\text{Internal}} &= \oint_{\text{Area}} \frac{C_{\text{Surface}}}{1 + C_{\text{Surface}}}\,\mathrm{d}A, \\
\eta_{\text{Internal}} &= \frac{\text{Rate real}_{\text{Internal}}}{\text{Rate optim}_{\text{Internal}}}
\end{aligned} \tag{22}$$

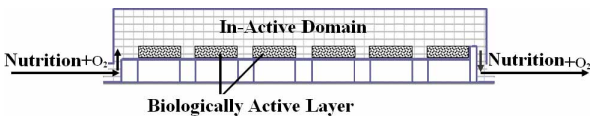

Figure 9. Computational domain of the bioreactor.

Table 2. Appropriate physical values of the constants used *n* the substrate-transport equation.

Constant	Value	Units
V_{max} (max reaction rate)	2.778×10^{-8}	(mol/s)
K_m (Michaelis–Menten-constant)	1.075×10^{-5}	(mol)
D (diffusion-coefficient)	2.3376×10^{-9}	(m^2/s)

The global performance of the bioreactor could be estimated similarly by using the values in the active layer and the inflow concentration. Therefore, this gives an overall measure of transport and diffusion efficiency in the bioreactor:

$$\text{Rate real}_{\text{Internal}} = \oint_{\text{Area}} \frac{C}{1+C}\,\mathrm{d}A,$$
$$\text{Rate optim}_{\text{Global}} = \oint_{\text{Area}} \frac{C_{\text{Inflow}}}{1+C_{\text{Inflow}}}\,\mathrm{d}A, \qquad (23)$$
$$\eta_{\text{Global}} = \frac{\text{Rate real}_{\text{Internal}}}{\text{Rate optim}_{\text{Global}}},$$

Those equations allow the complete evaluation of a bioreactor performance due to geometry and dynamic effects.

6.3 *Results and discussion*

To achieve an overall analysis of the problem, not only the real experimental Reynolds number is used but a limited range around it was also tested: $Re = 0.604$, 8.1 and 27.1.

The same approach was made with the concentration $C_{\text{N-D}} = 0.1$, 5, 20 and 300.

6.3.1 *Load results*

The load distribution takes an important role in the cell morphology. The shear stress and pressure distribution are calculated for different Reynolds numbers, it is expected to see variations in the load as the flow regime changes from very slow flow at $Re = 0.6$ to a viscous laminar flow field at $Re = 27.1$. The pressure and shear stress variation with Reynolds numbers are plotted in Figures 10 and 11, respectively. The pressure seems to fall steadily up to 10% from an inlet value of one bar, which could lead to different cell morphology between the carriers, as the percentage change cannot be neglected.

On the other hand, the shear stress distribution is much more uniform, with only some irregularity at the thin vertical inlet and exit. This is due to the high speeds existing in this zone of contraction. The response to the shear stress is quite acceptable: as the Reynolds number, rise so does the velocity leading to higher near wall gradients which exactly contribute to a higher shear stress.

An additional point worth mentioning is that as the Reynolds numbers rise a vortex is created just before the first carrier, when the flow just turns around the corner Figure 12(b). This leads to higher velocity gradients and therefore contributing to an up and down bump in the shear distribution, which is not seen in the creeping flow regime as in Figure 12(a).

On the whole, the order of magnitude of the shear stress is in the 10^{-4} N/m^2 range at a $Re = 27.1$ and of order 10^{-6} for both $Re = 8.1$ and 0.6 which is very low and could be of worse effects on the cartilage cell growth. Since in real life the knee is subjected to cyclic heavy loading according to the human weight, thus higher shear stress and pressure loading are desirable conditions for the cartilage cells growth. This should be further

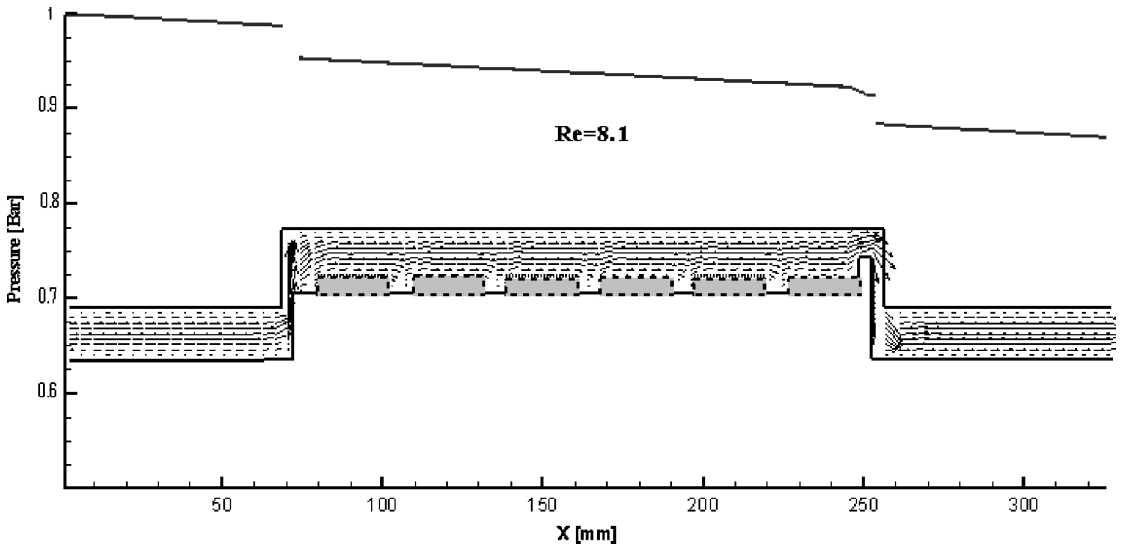

Figure 10. Pressure distribution in the mid planes of each section of the bioreactor along with the velocity field.

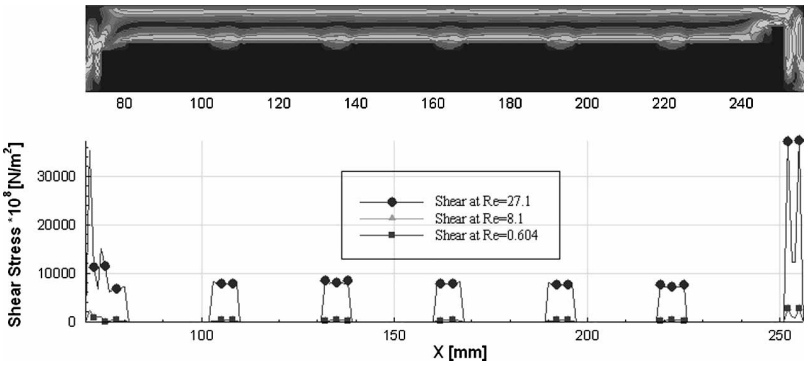

Figure 11. Particles can be represented by distribution functions along nine directions.

considered in detail with comparisons to available knee load models to get a more appropriate reactor design.

6.3.2 *Substrate results*

In Figure 13, the global efficiency is plotted vs. the inlet concentration for different Reynolds numbers. From the first look it is obvious that the efficiency rises as the inlet concentration rises, which is somehow logical since the cells are supplied with more and more oxygen.

But the question is why does it need a concentration one order of magnitude higher than what the water can carry for it to asymptote 100% efficiency?

This question can be answered in two phrases: cell activity and diffusion. As oxygen is transferred through the interface area the first layer respires a certain amount leaving less and less to the lower layers, i.e. there exists a gradient in the concentration level through the layers.

What makes this gradient lower is the slow diffusion between the layers which acts as a resistance to the oxygen spreading through the layers. Thus, the cells need a much higher oxygen level to reach 100% efficiency everywhere.

On the other hand, with a second look at the graph it could be seen that different Reynolds numbers have different performance curves. The lower the Reynolds the better the efficiency curve, which sounds strange but makes sense if careful considerations are made to the flow field figures given in Figure 12, which could be thought of by means of residence time considerations. Meaning if the oxygen particles have more time to spend in the reactor, the more probable it is that the oxygen would diffuse everywhere to reach almost all of the cells. Thus, it gives a better supply of oxygen for the cells in a unit time.

Also, the formation of vertical structures adds to the effect of short residence time in higher speed flow as it usually reduces the mass transfer around it. This can be recognised in Figure 12(b) at $Re = 27.1$, when vortices are formed in each corner the flow turns around and the concentration distribution near them is lower than the rest of the flow field. But once a concentration of 30 K_m is reached, all cases perform similarly.

Figure 14 gives an estimate of the internal efficiency variations with the Reynolds number, giving an estimate for the Diffusion limitations of the bioreactor.

It is seen that the Reynolds numbers cause a decrease in the diffusion efficiency. But as the inlet concentration is raised, the efficiency recovers for all Reynolds numbers in such a way that at an inlet concentration of

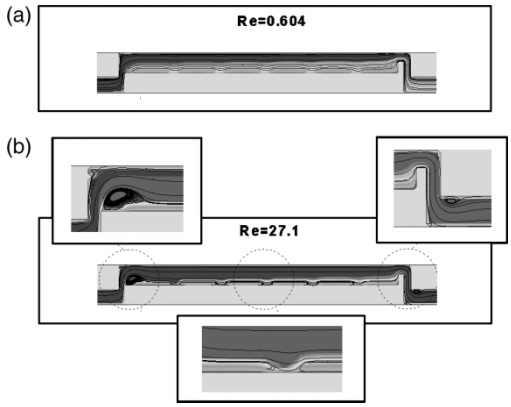

Figure 12. Streamlines inside the bioreactor at $Re = 0.604$ and 27.1.

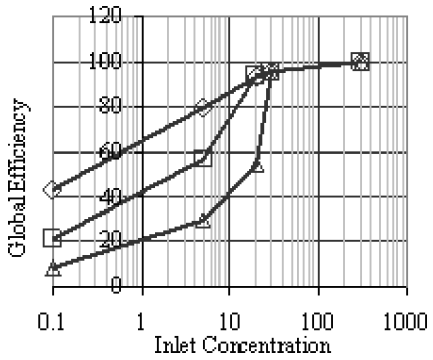

Figure 13. Global efficiency for different inlet concentration and different Reynolds numbers. The square (□) represents $Re = 0.604$, the triangle (△) represents $Re = 8.1$ and the diamond (◇) corresponds to $Re = 27.1$.

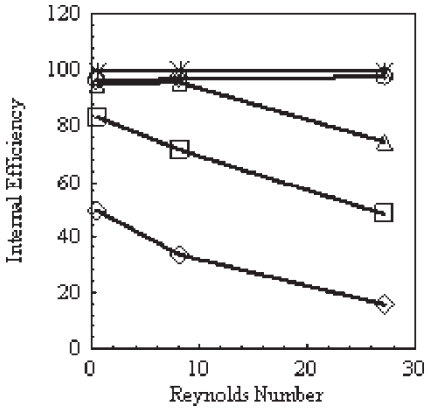

Figure 14. Internal efficiency for different Reynolds numbers at different inlet concentrations. The diamond (◇) represents an inlet concentration = 0.1. The square (□) corresponds to an inlet concentration = 5, the triangle (△) represents an inlet concentration = 20, (○) corresponds to an inlet concentration of 30 and finally the (∗) represents an inlet concentration of 300.

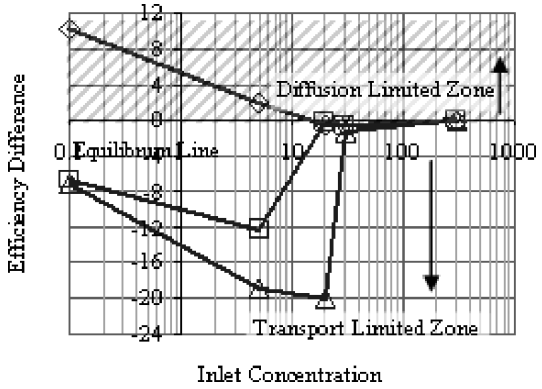

Figure 15. Efficiency difference for different inlet concentration at different Reynolds numbers, Where, the square (□) represents $Re = 8.1$, the triangle (△) represents $Re = 27.1$ and the diamond (◇) corresponds to $Re = 0.604$.

30 K_m all cases perform the same.

In order to get a feeling whether the diffusion or the transport is acting as a limitation to the substrate, both efficiencies are subtracted such that:

$$\eta_{\text{Difference}} = \eta_{\text{External}} - \eta_{\text{Internal}}, \tag{24}$$

$$\eta_{\text{Difference}} \begin{cases} > 0 & \text{diffusion limited} \\ = 0 & \text{equilibrium} \\ < 0 & \text{transport limited} \end{cases} \tag{25}$$

Thus, if $\eta_{\text{Difference}}$ is greater than zero then the internal efficiency is less, which means it is more limiting to the process and vice versa. Figure 15 shows a plot of $\eta_{\text{Difference}}$ vs. Reynolds number for all cases of inlet concentration. All the data points above the equilibrium line are diffusion limited; obviously most of the points are transport limited except for the points on the $Re = 0.604$ which are positioned before the inlet concentration of 20.

It could be said that the lower the Reynolds number the more the process becomes diffusion limited. Furthermore, the higher the inlet concentration, the more equilibrium the process has.

7. Conclusion

The solver used provided reliable results in the context of Cartesian problems (with no curved boundaries) and enabled the possibility of simulating substrate transfer efficiently with the modelling of substrate consumption by cartilage cells. This would contribute strongly in the bioreactor geometry enhancement, i.e. saving manufacturing time by just simulating different designs and choosing most appropriate ones for manufacture. The different results and simulations made in this work helped to provide a better understanding of the response of the cells to different conditions. Some explanation can be made to the questions proposed in the introduction.

7.1 Does a higher flow speed mean better substrate transport or not?

Now it is quite obvious that it is almost the opposite way around, better transport needs more resident time for the substrate to transport, but not forgetting that even at very high residence time the diffusion will limit the process as seen in Figure 15.

Damköhler numbers can be used to estimate clearly the effect of the transport on the substrate reaction:

$$Da = \frac{T_{\text{transport}}}{T_{\text{reaction}}}, \tag{26}$$

where Da is Damköhler number; $T_{\text{transport}}$, transport time scale; and T_{reaction}, reaction time scale.

A low Da suggests a reaction limited phenomena, meaning that the transport is much quicker. On the other hand, a high Da suggests a transport control meaning that the reaction could be quicker. For this specific reactor the Damköhler number is estimated to be approximately 1000, which suggests a transport limited zone as predicted by Figure 15 for $Re = 8.1$.

7.2 Does a higher inlet concentration mean a better substrate supply to all cells?

Both limitations could be conceded if the inlet concentrations are raised higher but this approach has a limitation itself! The maximum substrate dissolved is calculated by Henry's law (see Equation 17) and in this case it is 21 K_m, and exceeding it is not physical anymore.

7.3 How does the load vary with Reynolds number?

There is almost no difference in the pressure distribution with Reynolds number, but due to the geometry of the reactor the carriers are not subject to symmetric loading along the reactors axis; this should be reconsidered in further designs.

The shear stress distribution is quite low in comparison and further work should be done to scale it in favour of better conditions for cartilage cells. New designs should take into consideration available knee load models to subject the cells to a load environment, which imitates the real knee. For this specific reactor with the physical inflow properties, a maximum internal, external and global efficiency of $\sim 95\%$ is achieved. This could be enhanced by geometry changes since the Henry concentration limit is reached. Further work should be done to improve the solver by means of enabling 3D modelling which could alter the flow field results and concentrations near the walls. Progress should be made towards the modelling of species transport, kinetics and multiphase flow regimes using LBM.

Extensive work should be made in the modelling of real load environment for the knee; this should be used as a blueprint for a successful bioreactor design.

Acknowledgements

This work was sponsored by the Deutsche Forschungsgesellschaft DFG Grant Number: BE 2245/2-1.

References

Armaly, B.F., Durst, F., Pereira, J.C.F., and Schonung, B., 1983. Experimental and theoretical investigation of backward-facing step flow. *Journal of Fluid Mechanics*, 127, 473–496.

Bhatnagar, P.L., Gross, E.P., and Krook, M., 1954. A model for collision processes in gases. I. Small amplitude processes in charged and neutral one-component system. *Physical Review*, 94, 511–525.

D'Humieres, D., 1992. Generalized lattice Boltzmann equations. *Rarefied gas dynamics: theory and simulations*. Vol. 159 Washington, DC: Progress in Astronaut Aeronaut, 450–458.

Esterl, S., Ozmutlu, O., Hartmann, C., and Delgado, A. 2003. Three-dimensional numerical approach to investigate the substrate transport and conversion in an immobilized enzyme reactor. *Biotechnology and Bioengineering*, 83, 780–789.

Fassnacht, D. and Portner, R., 1999. Experimental and theoretical considerations on oxygen supply for animal cell growth in fixed bed reactors. *Journal of Biotechnology*, 72, 169–184.

Higuera, F.J. and Jimenez, J., 1989. Boltzmann approach to lattice gas simulations. *Europhysics Letters*, 9, 663–668.

Hussein, M.A., 2003. *On the two dimensional viscous flow modeling using vorticity-stream formulation*, Thesis (MSc). Cairo University, Cairo.

Hussein, M.A., 2006. On the validation of a 2-D laminar flow solver using lattice Boltzmann method. *The eighth international congress on fluid dynamics and propulsion*, ASME, Sharm el Sheikh, ICFDP8-EG-200

Koelman, J.M.V.A., 1991. A simple lattice Boltzmann scheme for Navier–Stokes fluid flow. *Europhysics Letters*, 15, 603–607.

Mcnamara, G. and Zanetti, G., 1988. Use of the Boltzmann equation to simulate lattice-gas automata. *Physical Review Letters*, 61, 2332–2335.

Nagel-Heyer, S., Goepfert, C., Feyerabend, F., Petersen, J.P., Adamietz, P., Meenen, N.M., and Pörtner, R., 2005. Flow-chamber bioreactor culture for generation of three-dimensional cartilage-carrier-constructs. *Bioprocess and Biosystems Engineering*, 27, 273–280.

Pörtner, R. and Koop, M., 1997. A model for oxygen supply in fixed bed reactors with immobilized hybridoma cells. *Bioprocess and Biosystems Engineering*, 17, 269–275.

Pörtner, R., Nagel-Heyer, S., Goepfert, C., Adamietz, P., and Meenen, N.M., 2005. Bioreactor design for tissue engineering. *Journal of Bioscience and Bioengineering*, 100 (3), 235–245.

Qian, Y.H., D'Humieres, D., and Lallemand, P., 1992. Lattice BGK models for Navier–Stokes equation. *Europhysics Letters*, 17, 479–484.

Schroeter, J.D., Kimbell, J.S., Bonner, A.M., Roberts, K.C., Andersen, M.E., and Dorman, D.C., 2006. Incorporation of tissue reaction kinetics in a computational fluid dynamics model for nasal extraction of inhaled hydrogen sulfide in rats. *Toxicological Sciences*, 90, 198–207.

Succi, S., 2001. *The lattice Boltzmann equation for fluid dynamics and beyond*. New York, NY: Oxford University Press.

Wood, J.H. and Thakker, K.M., 1982. Michaelis–Menten absorption kinetics in drugs: examples and implications. *European journal of clinical pharmacology*, Springer-Verlag 23, 183–188.

Journal of Biomechanics 41 (2008) 3455–3461

Contents lists available at ScienceDirect

Journal of Biomechanics

journal homepage: www.elsevier.com/locate/jbiomech
www.JBiomech.com

On the lattice Boltzmann method simulation of a two-phase flow bioreactor for artificially grown cartilage cells

M.A. Hussein [a,*], S. Esterl [a], R. Pörtner [b], K. Wiegandt [b], T. Becker [a]

[a] Process-Analysis Department, Faculty of Natural Sciences and Biotechnology, University of Hohenheim, Garbenstraße 21, D-70599 Stuttgart, Germany
[b] Institute of Bioprocess and Bio-System-Technology, Technical University of Hamburg-Harburg, Denickestraße 15, D-21071 Hamburg, Germany

ARTICLE INFO

Article history:
Accepted 8 September 2008

Keywords:
Multi-phase lattice Boltzmann method
Oxygen concentration
Cartilage bioreactor
Chemical kinetics

ABSTRACT

Owing to the growing demand of cartilage tissue repair and transplants, engineered cartilage cells have emerged as a prospective solution. Several bioreactors were built for artificially grown cartilage cells. In this work, a recently designed flow bed bioreactor is numerically investigated and compared with experimental results.

The flow field inside the bioreactor was modelled using the lattice Boltzmann method. The flow consists of two phases which are the liquid component (nutrition supply) and gas component (oxygen supply). The flow field is simulated using the multi-phase lattice Boltzmann method, whilst the cell activity is modelled using Michaelis–Menten kinetics.

The oxygen diffusion level at the exit of the nutrition phase is used as an evaluation process between the numerical and experimental results reporting the possibility of using the proposed model to fully simulate such bioreactors, though greatly saving time and money. Shear stress and pressure distributions are as well compared with published human cartilage load measurements to estimate the dynamic similarity between the bioreactor and the human knee. The predicted oxygen levels proved consistent trends with the experimental work with a 7% difference after 1 h measuring time. The shear stress levels recorded 10–11 orders of magnitude lower than in humans and also one order of magnitude lower in the pressure distribution.

1. Introduction

According to Forbes Inc., Fraunhofer Institute and Common wealth Scientific and Industrial Research Organisation (CSIRO) cartilage transplant takes up 150 million US dollars worldwide annually. There exists a high research request to artificially developed cartilage cells. Artificially grown cells are subject to environmental conditions which have crucial influence on the cells' morphology. Basically for such junction tissues the nutrition level and loading stresses are fundamental circumstances, better considerations of these factors are essential. Several bioreactors were built to investigate such effects on the cartilage-cell morphology. A two-phase Flow Bed reactor was proposed which showed some substantial advantages over the others. The reactor is simulated in order to evaluate the effect of fluid mechanics on those conditions both numerically and experimentally. The simulations were made using the multi-phase lattice Boltzmann method (MLBM).

Recently, the MLBM has received great considerations as a substitute for modelling complex phenomena of particle dynamics and has proven successful and promising for simulating multi-component fluid flows. The first model dates back to 1991, and was based on surface tension separation schemes, using a repulsive interaction force (Gunstensen and Rothman, 1991). Shortly, another method which utilizes the interaction force potential function to model gas–liquid phase transition was proposed (Shan and Chen, 1993). The free energy approach was also used to construct an algorithm using the theory of free energy (Swift et al., 1995). Two-phase immiscible fluids with large density differences were as well simulated; the method was applied for two-phase fluids with high density ratios up to 1000 and was used for simulating bubble flows and capillary waves (Inamuro et al., 2004).

Cell oxygen consumption has been widely reported in literature using the Michaelis–Menten kinetics. The approach was used in the simulation of immobilized enzyme reactor (Esterl et al., 2003). Furthermore, the method was used to model reaction kinetics in nasal tissue and proved comparable results (Schroeter et al., 2005). The same model was used to investigate the oxygen consumption by cartilage cells in a single-phase bioreactor and transport efficiencies were reported (Hussein et al., 2008). In this work, oxygen saturation levels in the nutrition exit are reported and compared with experimental results, shear and pressure distributions are compared with published measurements.

* Corresponding author. Tel.: +49 711 459 24389; fax: +49 711 459 23259.
E-mail address: mohamedh@uni-hohenheim.de (M.A. Hussein).

0021-9290/$ - see front matter © 2008 Elsevier Ltd. All rights reserved.
doi:10.1016/j.jbiomech.2008.09.034

2. Bioreactor chamber description

The bioreactor is of simple geometry with two inlets and two exits. One inlet/exit set for the nutrition phase and the other for the gas phase. The inside geometry of the reactor is basically comprised of two opposing phases in a channel flow with six carriers on the lower channel wall, on which the cells grow upon.

A sketch of the geometry could be seen in Fig. 1a. A sectional cut shows the inside of the reactor where three of the six carriers could be seen. Each carrier pit has an insert to install the carrier into, the carriers are ready for the cells to grow on top of, and this is seen in detail in Fig. 1b. A top-view photo is also shown in Fig. 1c, where the cells are seen growing on the top of the carrier.

3. Numerical description

A numerical model of the bioreactor is seen in Fig. 2, where the inlets and exits are seen. It is expected that the exit of the nutrition phase carries some dissolved oxygen. The flow field in the bioreactor is modelled using a decoupled system (Hussein et al., 2008), since the modeling of substrate transport independently is possible as long as the mass proportion between the substrate and the solvent is negligible which can be estimated as

$$\frac{\rho_{O_2}}{\rho_{H_2O}} = \frac{1.429\,(g/L)}{998\,(g/L)} = 1.4318 \times 10^{-3}. \quad (1)$$

The modeling system is divided into two parts:

1. Two-phase LBM.
2. Oxygen transport.

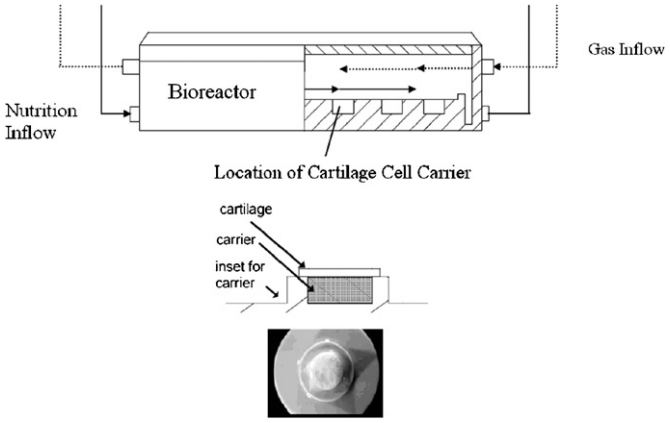

Fig. 1. (a) A sketch of the bioreactor showing a section demonstrating 3 of the 6 carriers. (b) A section inside a carrier. (c) A top view photo of a carrier showing the cartilage cells on top.

The first part solves the flow field including the two-phase interaction using the two-phase LBM; the second part simulates the transport of the oxygen from the gas phase to and through the liquid (nutrition) phase using the diffusion–advection transport equation.

3.1. Two-phase flow LBM

The MLBM is used to model the flow properties inside the Flow Bed bioreactor. The approach describes fluid composed of interacting particles which can be modelled by Boltzmann transport equation. Although the method's full potential are not fully utilized here, such as species transport, chemical kinetics and three dimensionality. But this work may be considered as a transitional step towards the full modeling of the bioreactor.

The lattice Boltzmann's Eq. (2) relates the particle distribution per unit time f in a certain lattice to the propagation motion and collision. The presence of numerous particles makes a statistical treatment an obligation.

$$\frac{\partial f}{\partial t} + \upsilon \cdot \nabla f = Q. \quad (2)$$

The equation expresses the evolution of the particles with time, where υ is the particle velocity and Q is the collision operator. When a 2-D lattice of several unit vectors is chosen, the particle dynamics equation can be satisfied on each direction independently. Hence the equation could be written for each direction vector denoted by i choosing the D2Q9, meaning nine velocity directions representing the 2-D lattice as in Fig. 3.

The multi-phase model of Gunstensen and Rothman (1991) is used in Eq. (3), this is achieved by resolving each phase separately with individual distribution function, and they only interact at interfaces. After applying some basic discretization rules and denoting each direction vector by i, the equation can be rewritten as

$$f_i^k(t + \Delta t,\ r + \upsilon\,\Delta t) = f_i^k(t,\ r) + Q_i^k. \quad (3)$$

The superscript k denotes either nutrition ($k = 1$) or gas phase ($k = 2$) and the differential time step is designated as Δt. In the multi-phase model the collision operator includes the regular collision effect and the extra attraction and repulsion force controlled by surface tension, the collision operator Q is divided into two parts

$$Q_i^k = |Q_i^k|_1 + |Q_i^k|_2. \quad (4)$$

The first term which contributes for the collision of molecules, predicts the influence of the collision on the distribution functions, and accounts for positive or negative influence. This operator has been approximated by Koelman (1991).

$$|Q_i^k|_1 = -\frac{1}{\tau_k}(f_i^k - f_i^{k(equ)}). \quad (5)$$

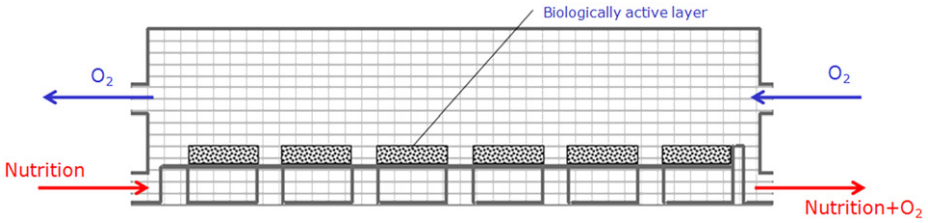

Fig. 2. Numerical model of the bioreactor, showing one inlet/exit set for the gas phase and the other for the nutrition phase. The exit of the nutrition phase carries some dissolved oxygen as well.

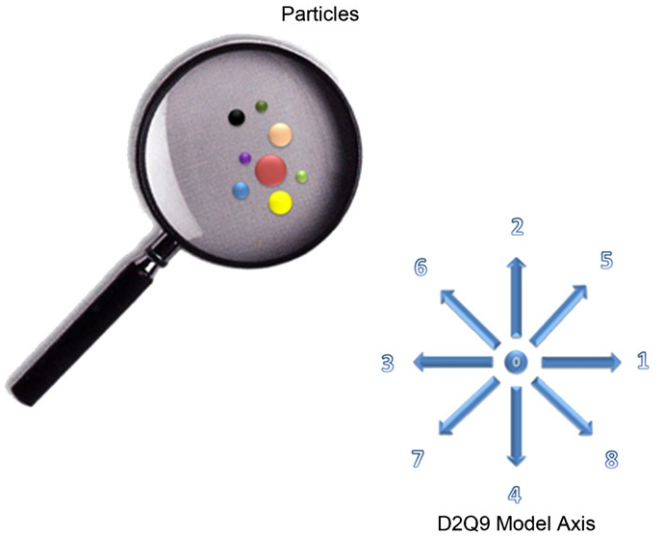

Fig. 3. A set of particles can be represented by distribution functions along 9 directions.

Table 1
Values of weighting factors according to the unit directions.

Direction $\hat{e}_i$	w_i
0	4/9
1,2,3,4	1/9
5,6,7,8	1/36

The collision of particles is considered as a relaxation towards a local equilibrium distribution f^{equ} and taking relaxation time τ. The local equilibrium distribution takes the Maxwellian form

$$f_i^{equ} = w_i \rho(r)\left[1 + 3\frac{\hat{e}_i \cdot u}{c^2} + \frac{9}{2}\frac{(\hat{e}_i \cdot u)^2}{c^4} - \frac{3}{2}\frac{u^2}{c^2}\right]. \quad (6)$$

In Eq. (6) $\hat{e}_i$ is the unit vector in the ith direction, u is the local (macroscopic) velocity, $\rho(r)$ is the local density, c is the basic lattice speed, whereas, the weighting factor w_i is specified in Table 1.

The second term in the collision operator contributes at the two-phase interface.

$$|Q_i^k|_2 = -\frac{A_k}{2}|F|\left[\frac{(\hat{e}_i \cdot F)^2}{|F|^2} - \frac{1}{2}\right], \quad (7)$$

where A_K is a free surface parameter that corresponds to the surface tension, while F is the local frequency gradient between the two phases, and can be written for a two-phase field as

$$F(x) = \sum_i \hat{e}_i\left[\sum_i f_i^{k=1}(x+1) - \sum_i f_i^{k=2}(x+1)\right]. \quad (8)$$

It is worth mentioning that in a single-phase region $F = 0$ and thus diminishing the second collision term, which only has a contribution at the phase interfaces. Finally, the local density of each phase can be expressed as

$$\rho^k = \sum_i f_i^k. \quad (9)$$

The total density ρ, momentum fluxes ρu, viscosity v, pressure P and shear stress τ can be written as follows for each phase:

$$\rho = \rho^{k=1} + \rho^{k=2}, \quad \rho u = \sum_{i=1}^{8} \hat{e}_i f_i = \sum_{i=1}^{8} \hat{e}_i f_i^{eq},$$
$$v = \frac{1}{6}\left(\frac{2}{\omega} - 1\right), \quad P = C_s^2 \rho, \quad (10)$$

$$\tau = -\left(1 - \frac{1}{2\tau}\right)\sum_{i=1}^{8}[f_i - f_i^{eq}]\left(e_{ix}e_{iy} - \frac{1}{2}e_i e_i \delta_{xy}\right), \quad (11)$$

where C_s is the speed of sound, δ_{xy} the Kronecker delta, $e_{i,x,y}$ is component unit vectors in x- and y- directions of the unit vector e_i. A typical pressure gradient (Mei et al., 2002) along the x-axis is applied for both phases, which is reasonable to model the pumped in feeds; this is seen in following equation:

$$\tilde{f}_i^k(x,t) = f_i^k(x,t) - w_i \frac{3}{c^2}\left|\frac{dp}{dx}\right|^k \hat{e}_i \cdot \hat{x}. \quad (12)$$

Denoting the dp/dx as the applied pressure gradient over the bioreactor satisfying the pump Δpressure and the overall Reynolds number,and $\hat{x}$ represents the unit vector of the pressure gradient direction which is in this case the x-direction. The equation resembles the update of the particle distribution at time t with the pressure gradient effect to reach the new distribution $\tilde{f}_i^k(x,t)$.

3.2. Oxygen transport

The diffusion–advection equation in dimensionless form could be written as

$$\frac{\partial C}{\partial t} + u \cdot (\nabla C) = \frac{1}{Bo}\nabla \cdot (\nabla C), \quad (13)$$

where C is defined as the substrate concentration (oxygen), u is the local velocity and Bo is the Bodenstein number which is defined as the ratio of momentum diffusivity to mass diffusivity.

$$Bo = \frac{U_\infty l}{D}, \quad (14)$$

where l is the characteristic length, U_∞ is the upstream inflow velocity and the D is the diffusion coefficient which takes two values depending on whether inside active layer or inside inactive layer. The active layer can be defined as the domain at which the nodes (cells) are packed and have activity towards oxygen. Typically an example of this process is the activity of biological cells towards oxygen as these cells perform respiration. Whilst assuming that the products released from the respiration process is neglected in this model. The oxygen transport inside the active layer can be modelled by adding a sink term using the Michaelis and Menten (1913) approach.

$$\text{sink term} : -RR\frac{C}{1+C}. \quad (15)$$

The dimensionless reaction rate RR can be defined as

$$RR = \frac{V_{max} l}{K_m U_\infty}, \quad (16)$$

where V_{max} is the maximum rate of substrate reaction (sink), K_m is the substrate concentration at which the reaction rate is half its value (Michaelis–Menten constant).

The active layer domain (Fig. 4) consists of physically packed cartilage cells at which the substrate transport is only dominated using diffusion and not advection, as the velocity diminishes between the cells.

It is sensible to consider the diffusion inside this active layer to dominate the transport equation as the velocity vector diminishes

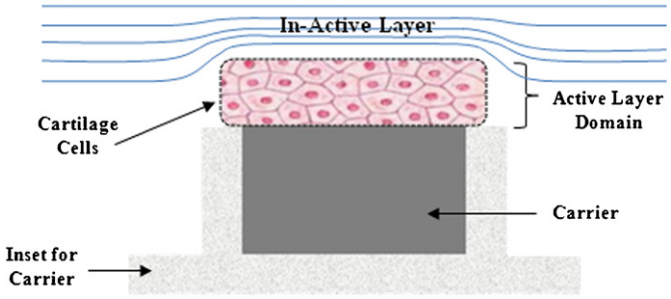

Fig. 4. The active layer domain is physically packed cartilage cells at which the substrate transport is only achieved using diffusion and not advection.

Table 2
Appropriate physical values of the constants used in the substrate-transport equation.

Constant	Value	Units
V_{max} (max reaction rate)	2.778×10^{-8}	mol/s1
K_m (Michaelis–Menten constant)	1.075×10^{-5}	mol/l
D (diffusion coefficient)	2.3376×10^{-9}	m^2/s

between the cells, thus

$$\frac{\partial C}{\partial t} - \frac{1}{Bo_{Active}} \nabla \cdot (\nabla C) = -RR \frac{C}{1+C}. \quad (17)$$

The Bo_{Active} represents the Bodenstein number inside the active layer.

3.3. Numerical setup

The Reynolds number in the nutrition phase is $Re = 8.15$ and in the gas phase the Reynolds number is $Re = 0.087$, the Reynolds number is calculated based upon the inlet diameter of each phase using

$$Re = \frac{ul}{v}, \quad (18)$$

where u is the inlet velocity and v is the kinematic viscosity of the considered phase. The Reynolds numbers involved are quite low thus the flow is almost creeping, this stabilizes the interface between the two phases. The maximum oxygen concentration that will dissolve in water will be designated as: C_{max}. For very low Reynolds number, which is the case in this reactor, Henry's

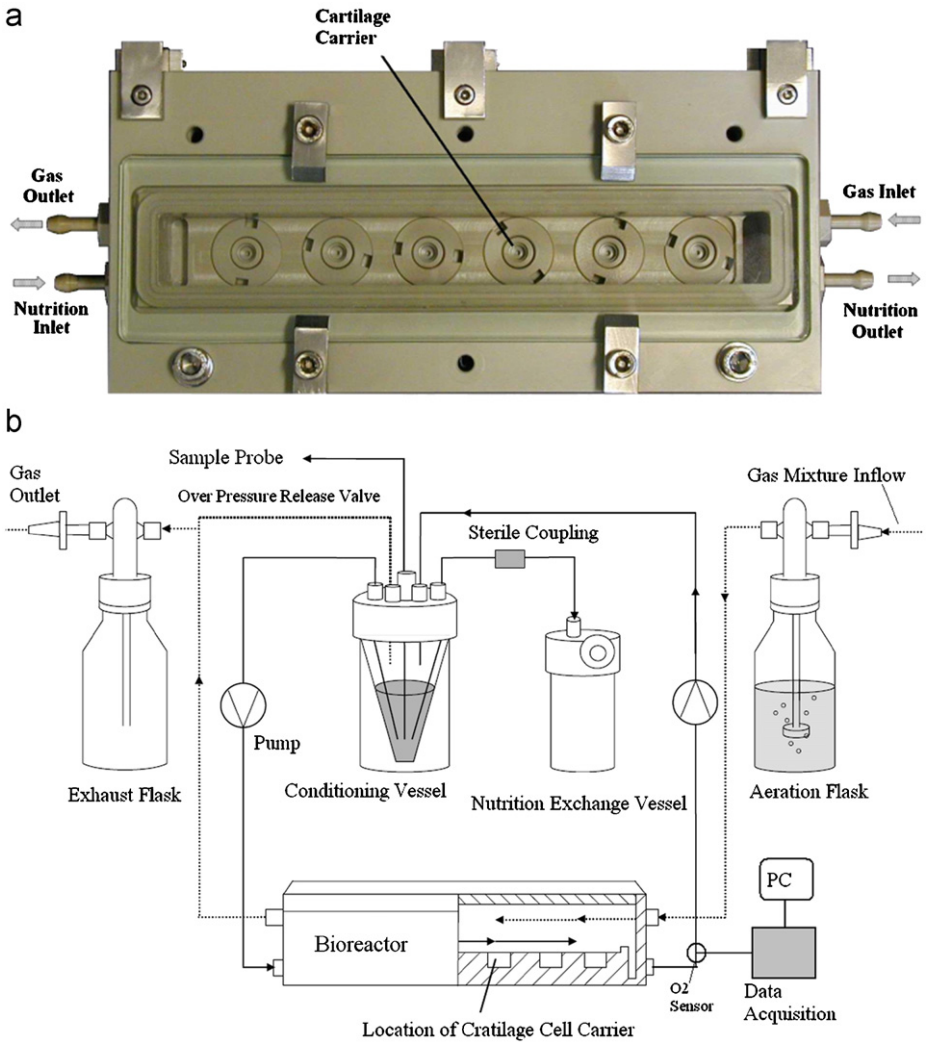

Fig. 5. (a) An image of the bioreactor showing the gas phase inlet/exit, the nutrition phase inlet/exit and the cartilage carrier. (b) The experimental setup consists of a gas source and a nutrition source. The gas source is aerated before entering the chamber and the nutrition feed is conditioned also before entering the chamber.

Law of solubility could be applied to determine C_{max}.

$$C_{max} = K_{O_2} X_{O_2}, \quad (19)$$

where K_{O_2} is the Henry's Const. and X_{O_2} is the oxygen partial pressure.

The equation gives an approximate simple model for the determination of the resistance of oxygen transport across the two-phase interface. The cell activity/growth rate may be implemented by choosing the appropriate parameters for the kinetics transport equation (13); values were experimentally obtained and listed in Table 2.

The oxygen saturation level is reported at the exit of the nutrition section and compared with the measured values.

4. Experimental description

An image of the reactor could be seen in Fig. 5. The nutrition and gas phase inlets/exits are opposed in order to reduce the possibility of accumulation of gas particles. This would lead to the formation of bubbles, which will disturb the flow field and could lead to cell distortion and tear. The complete experimental setup consists of a gas source and a nutrition source. The gas feed is moisturized before entering the bioreactor in an aeration flask in order to supply the cells with O_2. The nutrition feed is conditioned before being pumped into the bioreactor. A peristaltic pump is used to do the pumping of the nutrition, keeping the nutrition feed as sterile as possible.

A 2 mm optical fibre oxygen sensor (*PreSens*©) is fitted inside a duct at the nutrition exit. The sensor is connected to a data acquisition system which is connected to a PC. The accuracy of the sensor is 0.15% error at low oxygen saturations and reaches 1% error at 100% oxygen saturations which is reasonably enough. The nutrition in feed is always with 1% oxygen saturation. The experiments were made without cartilage cells in the carriers as a preliminary evaluation of the bioreactor since the cell cultivation takes at least 4 weeks. The conditions in the setup are seen in Table 3.

Table 3
Flow conditions in the experimental setup.

Parameter	Value	Units
Gas flow rate	4	l/h
Nutrition(1% O_2 saturation)	0.5	ml/min
Temperature	26	°C
Nutrition	Distilled water	
Gas	Air	
Cells	N/A	

5. Results and discussion

Both measured and predicted oxygen saturation levels are compared. Shear and pressure distributions are also compared with cartilage load measurements.

5.1. Substrate results

The oxygen saturation level is monitored at the exit of the nutrition phase. The experimental results are measured without the presence of the cartilage cells and are plotted as a sold line with average error bars of 0.5% in Fig. 6. The experimental plot is seen starting at 2% saturation, this could be due to the fact that the nutrition in feed is always with 1% saturation and the duct impermeability is not 100%.

The numerical results for the same experiment (without cell activity) is plotted in squares (□) but the inlet level is fixed to start from 0% saturation as the numerical work does not face the technical difficulties as in the experimental work and the proper experiment should be made starting with 0% saturation for a more precise monitoring of cell growth and activity towards oxygen levels. Both the numerical and experimental are in good agreement up to 16 min, after which the deviation becomes larger. The reason for the deviation in the middle part

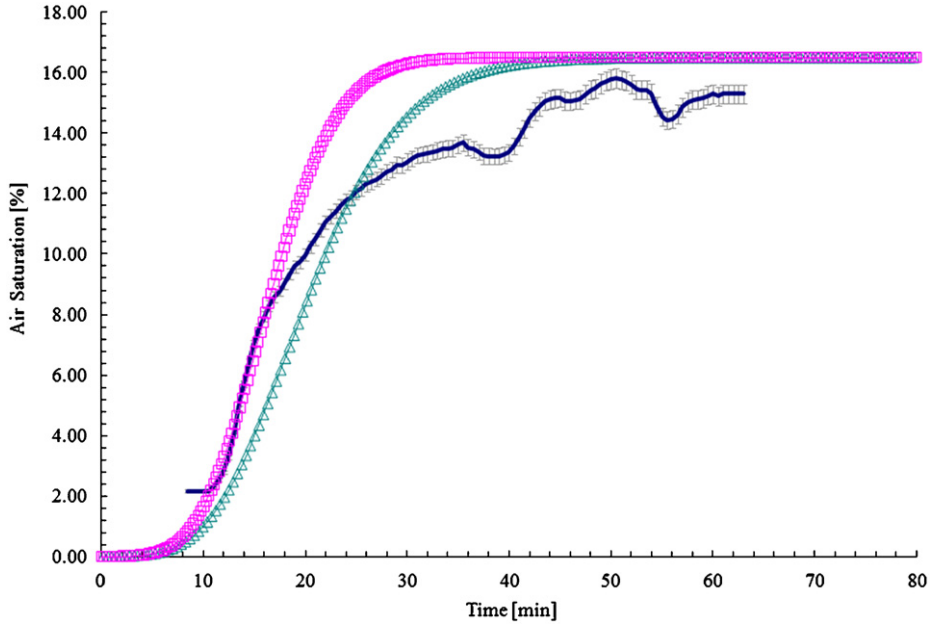

Fig. 6. Air saturation, where the square (□) represents the oxygen saturation with no cell activity, the triangle (△) represents the oxygen saturation with cell activity and the solid line with error bars represents the experimental results without cell activity.

of the curves could be hard to explain but several points could be stated:

- The peristaltic pump oscillatory consequence in the pipes may have not been fully diminished in the bioreactor, which could lead to unsteadiness in the chamber.
- The usage of a homogenous linear solubility rule (Henry's Law) for the oxygen diffusion modelling at the phase interface may have been very coarse for such complex phenomena.
- The fact that the ducts used were not 100% impermeable may have lead to some of the discrepancies between the curves.
- Nevertheless both values seem to report close end readings, as in Table 4.

Table 4
Results for numerical and experimental after 1 h.

Experiment (no cell activity)	15.24% saturation
Numerical (no cell activity)	16.5% saturation

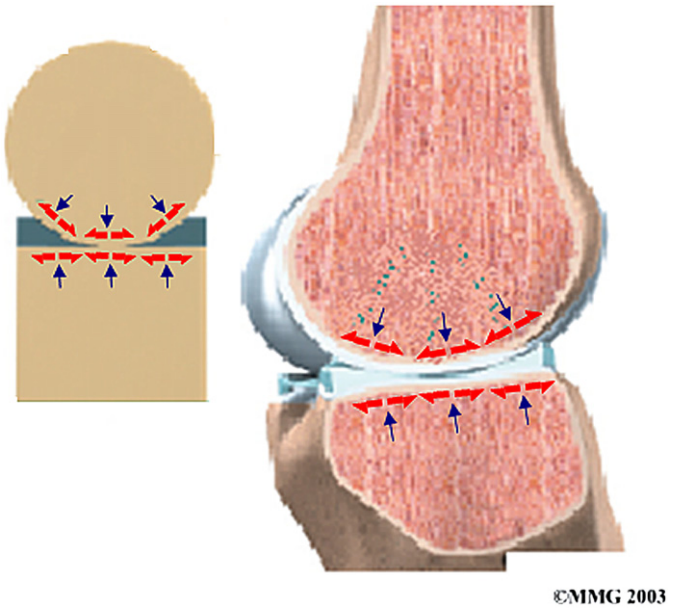

Fig. 7. Pressure and shear stress shown inside a section of human knee (image courtesy of Medical Multimedia Group LLC, 2003).

The second curve represents a numerical prediction in case of cell activity presence. The curve seems logic, as it shows that the cell activity only contributes in the measurements as a time delay. Because sooner or later the gas phase will further saturate the nutrition phase with oxygen as the supply is much higher than the cell demand. The short residence time for the flow particles in both phases may be the reason that both numerical curves report identical steady-state results for oxygen saturation i.e., this is the maximum saturation that could be achieved with such velocities in this exchanger.

5.2. Load results

The load distribution takes an important role in the cell morphology. Inside a human knee, the cartilage cells are continuously under load, both shear stress and pressure as seen in Fig. 7. The shear stress and pressure distribution are calculated and seen in Fig. 8. The pressure reported unsymmetrical loading with values between (0.988 and 0.984 bar), due to the overall pressure gradient in the nutrition phase.

Therefore, there exists always a lower-pressure downstream, which is not a perfect condition for growing similar cells upstream and downstream. This can lead to the growth of non-similar cartilage units in a single bioreactor.

On the other hand, the shear stress reported almost symmetrical patterns and reported an average of 400×10^{-8} N/m^2, except for the first and last pit due to geometry considerations at inlet and exit. The loads inside cartilages of humans are much different than those values reported in this bioreactor. Published

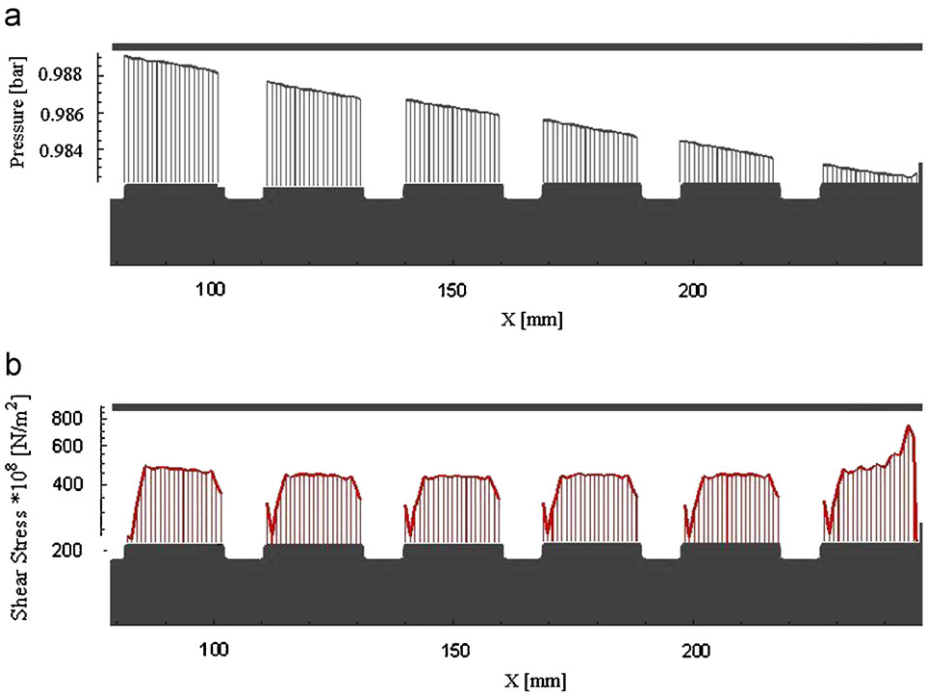

Fig. 8. Pressure distribution and shear stress on the top of the active layer.

Table 5
Shear and pressure comparison to other published data.

MPa	Measurement, walking (D'Lima et al., 2006)	Measurement, jogging (D'Lima et al., 2006)	Multi-phase
Pressure	0.668	1.33	0.0988
Shear stress	0.094	0.282	0.48×10^{-11}

experimental results of human knee load measurements were used for comparison (D'Lima et al., 2006), the work reported usage of wireless strain gauges, which were implanted inside a 70 kg human knee for load estimations, the average results are reported in Table 5.

The pressure is one order of magnitude lower than the values recorded inside human knees. Also, the shear stress in the bioreactor is 10^{-11} orders of magnitude lower than the measured values, which is expected due to the very low Reynolds number in the flow field. From experimental observations the cartilage cells are very sensitive towards loading conditions which greatly affect the compactness of the cells. It is expected that cells which would grow in this reactor will not be able to carry proper loads.

6. Conclusion

The numerical model used proved consistent trends in comparison to experimental work and enabled the possibility of simulating substrate transfer efficiently with the ability of substrate consumption by cartilage cells. This would contribute strongly in the bioreactor geometry enhancement i.e., saving manufacturing time by just simulating different designs and making the choices accordingly. The different results and simulations made in this work, helped to develop a better understanding of the integral phenomena in the bioreactor.

The shear stress distribution is quite low in comparison to measured values in human knees and further considerations in the designs should be done to enlarge the loads in favour of more realistic environment for the cells. The loading may be adjusted by means of over pressurization or introducing cyclic load generation units in the reactor by means of MEMS technology.

Acknowledgement

This work was supported by the Deutsche Forschungsgesellschaft DFG Grant no. BE 2245/2-1.

References

D'Lima, D.D., Patil, S., Steklov, N., Slamin, J.E., Colwell, C.W., 2006. Tibial forces measured in vivo after total knee arthroplasty. Journal of Arthroplasty 21 (2), 255–262.

Esterl, S., Ozmutlu, O., Hartmann, C., Delgado, A., 2003. Three-dimensional numerical approach to investigate the substrate transport and conversion in an immobilized enzyme reactor. Biotechnology and Bioengineering 83 (7), 780–789.

Gunstensen, A.K., Rothman, D.H., 1991. Lattice Boltzmann model of immiscible fluids. Physics Review A 43 (8), 4320–4327.

Hussein, M.A., Esterl, S., Poertner, R., Wiegandt, K., Becker, T., 2008. Impulse and mass transport in a cartilage bioreactor using the lattice Boltzmann method. International Journal of Computational Fluid Dynamics 22 (5), 341–350.

Inamuro, T., Ogata, T., Tajima, S., Konishi, N., 2004. A lattice Boltzmann method for incompressible two-phase flows with large density differences. Journal of Computational Physics 198 (2), 628–644.

Koelman, J.M.V.A., 1991. A simple lattice Boltzmann scheme for Navier–Stokes fluid flow. Europhysics Letters 15 (6), 603–607.

Medical Multimedia Group LLC, 2003. 〈www.eOrthopod.com〉.

Mei, R.W., Yu, D.Z., Shyy, W., Luo, L.S., 2002. Force evaluation in the lattice Boltzmann method involving curved geometry. Physical Review E 65 (4).

Michaelis, L., Menten, M., 1913. Die kinetik der invertinwirkung. Biochemische Zeitschrift 49, 333–369.

Schroeter, J.D., Kimbell, J.S., Bonner, A.M., Roberts, K.C., Andersen, M.E., Dorman, D.C., 2005. Incorporation of tissue reaction kinetics in a computational fluid dynamics model for nasal extraction of inhaled hydrogen sulfide in rats. Toxicological Sciences.

Shan, X.W., Chen, H.D., 1993. Lattice Boltzmann model for simulating flows with multiple phases and components. Physical Review E 47 (3), 1815–1819.

Swift, M.R., Osborn, W.R., Yeomans, J.M., 1995. Lattice Boltzmann simulation of nonideal fluids. Physical Review Letters 75 (5), 830.

Microfluid Nanofluid
DOI 10.1007/s10404-009-0499-1

RESEARCH PAPER

Numerical modelling of shear and normal stress of micro-porous ceramics for stimulated in-vitro cultivation of bone cells

M. A. Hussein · T. Becker

Received: 25 April 2009 / Accepted: 25 August 2009

Abstract Tissue engineering is a multidisciplinary job and has been of great challenge to scientist since its emerge in the 1980s. Special problems arise in this science, since bone cells are usually growing inside humans under moderate cyclic mechanical loadings (0.66–1.5 MPa); it is expected to grow them in a similar background. An innovative contribution is made where the shear stress is modelled inside in micro-channels reporting the various important design considerations of scaffolds, providing a more appropriate understanding of geometry change versus shear stress and Darcy's Reynolds number in micro-channels. The geometry of the scaffolds was captured by analysing and processing batches of images with edge detection techniques which mainly works on the colour contrasts. A novel edge detection algorithm which spots the colour change by means of gradient calculations was successful to scan the Micro-CT (computer tomography) images and gather a binary file for the 3-D scaffolds of 430 sections for a 3 mm. The 3-D Lattice Boltzmann was successful in modelling the transport phenomena and reporting the shear stress distribution in straight micro-channels and in the complicated micro-scaffolds. An analogical study is as well made between the realistic stresses expected in humans and the simulated ones, reporting different discussion aspects to bring the designed structures to a more realistic stage. Using micro-porous scaffolds have proven much more realistic in imitating the human bone shear load conditions (0.1 MPa) with at least two orders of magnitude closer (5.3×10^{-4} MPa) than previously published results (1.09×10 Pa). Further study should be done to realise closer shear loads to measured data in humans.

Keywords Micro-fluidics · Lattice Boltzmann method · Tissue engineering

1 Introduction

Tissue engineering has recently risen as a life saver for patients of bone damage or disorder due to trauma, tumour, pathological degeneration and congenital deformity. Recent statistics of expenditure in bone surgery and transplants published by Medical News Today (MediLexicon International Ltd 2009) suggested costs of up to 100 billion US dollars in the states and around 5 billion US dollars in Europe annually.

Bone tissue engineering is a very promising technique as it can eliminate problems of graft shortage, immune rejection, infection and chronic pain (Hill et al. 1999; Seiler and Johnson 2000). As well as in synthetic bone substitutes, such as hydroxyapatite or bone cement, in both subsists the difficulty of being resorbed on the long run along with the low mechanical properties of such materials (Yuasa et al. 2001; Yuan et al. 1999).

Bone tissue engineering is a multidisciplinary job and has been of great challenge to scientist since its emerge in the 1980s. Due to the works complexity it requires the integration of different scientific fields of biology, chemistry, engineering and medicine. To properly develop skeletal tissue in ex-vivo the conditions must be identical to such cells in-vivo. Starting from the appropriate nutrition for a sustained growth rate, along with the convenient chemical adhesion components and providing the suitable

M. A. Hussein (✉) · T. Becker
Group of (Bio)-ProcessTechnology and Process Analysis, Life Science Engineering Department, Technischen Universität München, Weihenstephaner Steig 20, 85354 Freising, Germany
e-mail: hussein@wzw.tum.de

Published online: 07 October 2009

perfusion environment which transfers the great mechanical stress ($\sim$1 MPa) which the cells carry (Fig. 1). All the mentioned surrounding conditions for the cells should combine together, providing the skeletal cells with the same multidisciplinary circumstances which are present in the native cells.

It is quite unaffordable to expect an instantaneous imitation of such a complex integrated job and providing such surroundings to tissue engineered cells in a simple bioreactor. In this study a preliminary step was made to investigate micro-fluidic stresses and manipulating it to bone tissue needs.

Further investigations proved that the application of a cyclic compression force are essential for the assembly of an elastic tissue engineered cartilage which resist wear and carry the friction and pad between bones as well as correctly transferring the load to the next bone at the joint (Ishaug et al. 1997). Some studies reported such loads reaching 6–18 MPa (Mega Pascal) (D'Lima et al. 2006), others (Knothe et al. 1998) reported an experimented range between 0.66 and 1.5 MPa in a single knee for walking and jogging, respectively.

Investigation in micro-fluidics has proven of great challenge to fluid dynamists, as the basic Navier–Stokes equations are limited in the micro-scale and the nano-scale, i.e. at $\Phi < 100$ μm. Another limitation is the complications in modelling the nutrients transport through the complex scaffolds. As well, the scaffold generation and boundary conditions provide great challenges against the conventional codes based upon stokes equations. Additionally, codes based upon such equations cannot handle non-Newtonian effects easily and have always proved computationally expensive. On the other hand in the last two decades

Fig. 1 Appropriate nutrition for a sustained growth rate, along with the convenient chemical adhesion components and providing the suitable perfusion environment which transfers the great mechanical stress the cells carry, are the four basic corners of successful skeletal tissue engineering

extensive study has been developed in the Lattice Boltzmann Method (LBM); the method has received significant attention as an alternative for simulating complex flow phenomena (Higuera and Jimenz 1989; Keóelman 1991). The basic idea of Ludwig Boltzmann's equation is to consider fluid composed of interacting particles. This interaction can be modelled by the Boltzmann transport equation. The model treats with the particle dynamics directly, thus enabling almost all kinds of regimes of high Knudsen number and low Knudsen. Along with the enhanced ability of complex geometry solutions, the method deals with the walls as a bounce back effect. Besides, the ability to fully model different chemical reactions and kinetics especially cell activity was as well achieved (Hussein 2006; Hussein et al. 2008a, b; Moaty et al. 2009). In consequence, LBM has proven relieving all sophistications in modelling such complicated biotechnological aspects. A previously developed code for the multi-phase LBM is utilised in this study (Hussein 2006; Hussein et al. 2008a, b) which has proven fit for modelling the nutrition transport and kinetics of cartilage cells in such micro-scale environment. The code was benchmarked in several test cases involving both meso- and micro-scale phenomenon.

The main intention of this study is to report the important design considerations of scaffolds for tissue engineering applications. The study tries to elaborate the effect of geometry and flow-dynamics on the shear stress.

With the aid of image processing and edge detection techniques the complicated geometry of the scaffolds was captured. An enhancement on the edge detection techniques was as well established, which is based upon the lattice propagation technique to achieve the scanning of the micro-CT (computer tomography) images in order to create and gather a binary file from 430 micro-CT sections forming the 3-D geometry file.

A comparative study is as well made between the realistic loads measured in humans and the modelled data, results were discussed in order to achieve better conditions for the cells.

In this study basically four points are addressed:

- Investigations of bone tissue from a mechanical point of view.
- The possibilities of using image processing in capturing micro-scaffolds and Lattice Boltzmann method for modelling transports in the scaffolds.
- The dynamic and geometric influences of the shear stress in micro-channels
- Reporting of shear stress levels in micro-scaffolds bioreactors and comparing them to conventional bioreactors and realistic bone loads in humans.
- Further modifications to enhance bioreactor design of such load baring cells.

2 Theoretical aspects

2.1 Bone tissue from a mechanical point of view

From the mechanical point of view the provision of mechanical stimulation is believed to be essential for the functional assembly of skeletal tissues. The stressing is presumed to be transferred to the cells by two means, contact loading and perfusion. The nature of the loading part is conveniently cyclic, which raises the stiffness of the cells as well acting as a dynamic stimulus. Previous study reports loads realising 6–18 MPa (Ishaug et al. 1997), others (D'Lima et al. 2006) reported by experimentation a range between 0.66 and 1.5 MPa in a single knee for walking and jogging, respectively. On the other hand, the perfusion functions dynamically but in a non variable shear load condition, which is useful as a static stimulus and as a transport for nutrition and removing of cell waste (Fig. 2). The two type of loading potential distribution may predict towards which cell type a stem cell will differentiate (Bancroft et al. 2002; Sarah et al. 2003; Sikavitsas et al. 2003; Braccini et al. 2005; Holtorf and al 2005; Grayson and Et al 2007; Petrović et al. 2009; Ishaug and Crane 1997). By a mechanical sense the cells which are subjected to high compression stress evolves into flexible pressure resistant tissues such as, cartilage cells. Whereas, the cells which are constantly subjected to shear will tend to densify and establish a higher stiffness, therefore stimulating into dense stiff material such as, bone tissue.

Studies have suggested that tissue engineered bone cells' growth rates were considerably improved by provision of higher shears rates in the reactors (Bancroft et al. 2002; Sarah et al. 2003; Sikavitsas et al. 2003; Braccini et al. 2005; Holtorf and al 2005; Grayson and Et al 2007; Petrović et al. 2009; Ishaug and Crane 1997). As well as reducing the shear rates is in fact limiting the diffusion, which was proven as a great constrain towards tissue growth. This defect has proved to limit the tissue growth in PLAGA foam to a depth of 200–800 μm (Xiaojun et al. 2004; Ateshian et al. 2003).

Although that diffusion was always thought of as a major contributing mechanism for the transport of molecules and ions across the endothelial layer of bone capillaries, diffusive mechanisms may not be sufficient to ensure adequate transport to and from osteocytes that are not in close vicinity of Haversian canals (Cowin 2001). Theoretical investigations of bone tissue diffusion coefficients shows values of order O (10 μm/h), revealing great discrepancies in transport times towards individual osteocytes depending on their proximity towards Haversian capillary (Gatzka et al. 1999). As well, the transport of large molecules through the tissue is highly dependent on tissue permeability, membranes and obstacles. Proving that the concept of free diffusion, as the major mechanism of nutrition exchange between the blood vessels and the bone tissue, is surely doubtful (Fig. 3).

A rightful answer of the capable transport mechanism, which is able to defeat all earlier mentioned constrains, is the cyclic pressure gradient developed by physiological activity. Mechanical loading of bone tissue during physiological activity results in a tissue stress state comprising cyclic dilatational and deviatoric components. The effect of

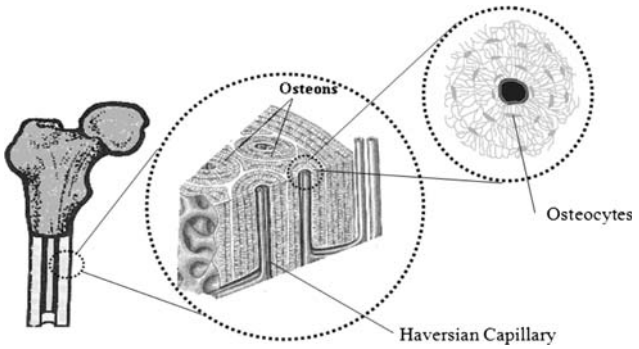

Fig. 3 Dissection of a femur bone, showing the Haversian channels containing the blood vessels and nerves

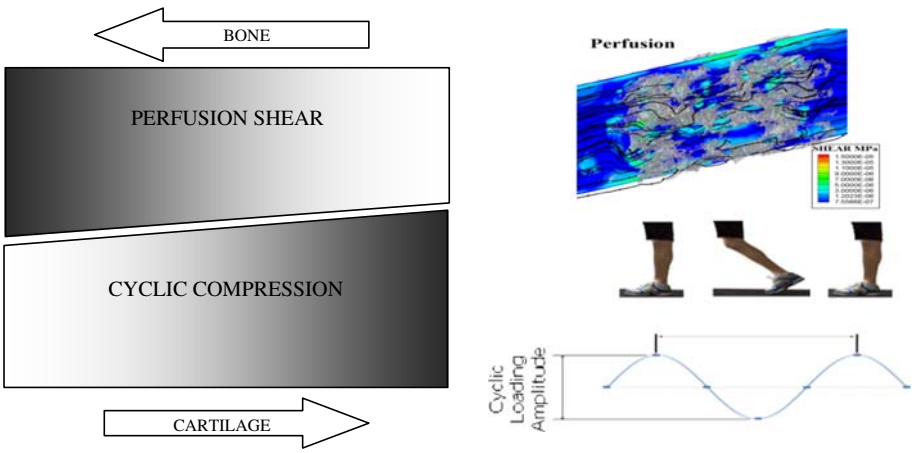

Fig. 2 In tissue engineering the stressing is presumed to be transferred to the cells by two means contact loading and perfusion. The nature of the loading part is conveniently cyclic, which raises the stiffness of the cells as well acting as a dynamic stimulus. On the other hand, the perfusion functions dynamically but in a non variable shear load condition, which is useful as a static stimulus and as a transport for nutrition and removing of cell waste

dilatation or pressure imposed by cyclically loading of bone tissue is the motor for fluid movement within tissues (Cowin 2001). As well the oscillating high shear flow induced by the oscillating pumping mechanism provides the bone tissue with a stiffness education schedule, with which the bone tissue achieve its stiff-solid features.

It is rationally expected that the bone tissue experience nearly the same stresses as shown in Fig. 4, ranging from 0.1 to 0.7 MPa for ~1 s walking cycle (Munting and Verhelpen 1993; Iarovici et al. 2004) and those stresses are the appropriate mechanical environment for a sustained growth.

2.2 Micro-porous scaffolds and edge detection

A micro-porous ZrO_2 Sponceram® ceramic of fine porosity and pore size of 600 μm is modelled. This ceramic structure has proven worthy for cultivating bone tissues (Kasper et al. 2007). The fine structure provides a highly perfusive micro-channelling domain for the supply of nutrition to the tissues as well as a shearing load agent; both aspects enhance the growth factors.

The difficulty of modelling such complex micro-structures always lies in retrieving the geometry into the solver as edges. Edge detection algorithms are based upon highlighting discontinuities in images and were first developed for satellite images. The technique has become well-known and was further developed and widely used for other image processing applications. The conventional approach for edge detection is based upon either thresholding the first derivative (gradient) of the image or locating zero crossings of its second derivative (Laplacian) (Turgut et al. 1996). During the detection procedures, usually all the image size is processed, which leads to redundant calculations of areas containing no edge information (Tadrous 1995). In this study a redundant avoiding algorithm is developed which searches for the threshold value in the image and then propagates around it in a 2-D lattice in eight directions (Fig. 5), until an edge is hit. The method has proven time saving and as well enables the possibility of parallel processing of the image, as each threshold value can be scanned and dealt with independently.

After the predictions of the edges, the 2-d binary edge images are assembled forming a 3-D binary file of the scaffolds (Fig. 6). Fortunately the LBM code uses the concept of bounce-back for satisfying the boundary conditions, this makes it much easier for the propagation of the particles in the flow field. Meaning, if a solid obstacle approaching the particles reflects back and if the path is obstacle free particles propagate.

2.3 Lattice Boltzmann method

The Ludwig Boltzmann's Eq. 1 relates the particle distribution, *f*, per unit time in a certain lattice to the propagation motion and collision. The presence of numerous particles makes a statistical treatment an obligation.

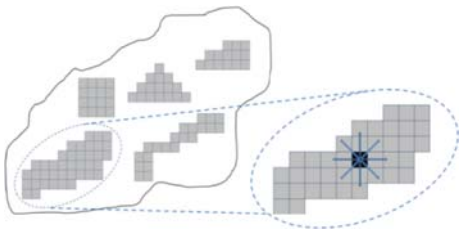

Fig. 5 The scanning procedure for gradient changes propagates in an eight directional lattice until an edge is hit

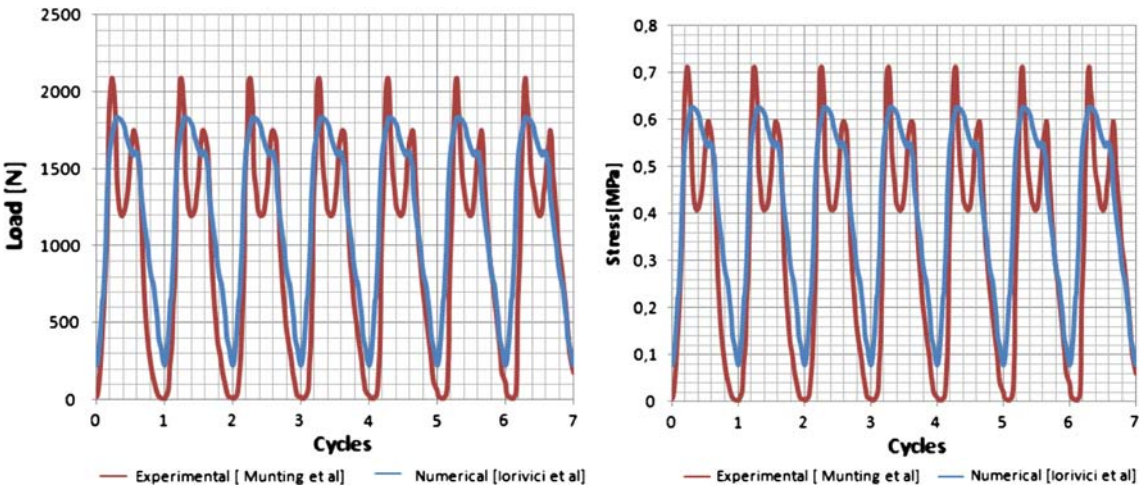

Fig. 4 Cross sectional load and stress inside a 70 kg femur bone showing a cyclic load on the femur while in a seven normal walking cycle of 0.9–1 s each (Munting and Verhelpen 1993; Iarovici et al. 2004)

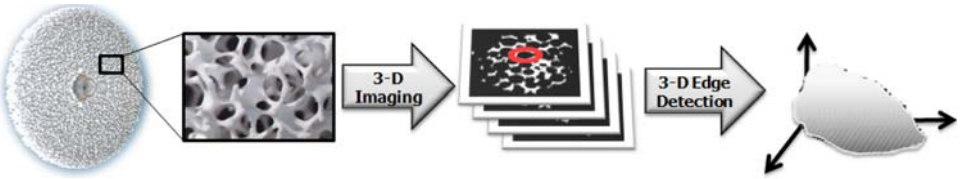

Fig. 6 From the micro-CT images 430 hundred 2-D binary edge images are assembled forming a 3-D binary file of the scaffolds

$$\frac{\partial f}{\partial t} + \upsilon \nabla f = Q \tag{1}$$

The equation expresses the evolution of the particles with time, where, υ is the particle velocity and Q is the collision operator.

When a 3-D lattice of several unit vectors is chosen, the particle dynamics equation can be satisfied on each direction independently. Hence the equation could be written for each direction vector denoted by, i, choosing the D3Q19, meaning 19 velocity directions representing the 3-D lattice as in Fig. 7.

The collision term of molecules, basically predicts the influence of the collision on the distribution functions, and accounts for positive or negative influence. This operator has been approximated (Mcnamara and Zanetti 1988) using the Bhatnagar–Gross–Krook (BGK) model, also known as single-relaxation-time (SRT) model.

$$Q_i = -\frac{1}{\tau}[f_i - f_i^{(\mathrm{equ})}] \tag{2}$$

Equation 2 can be explained as: the collision of particles is considered as a relaxation towards a local equilibrium distribution, f^{equ}, and taking relaxation time (τ).The reciprocal of the relaxation time, $1/\tau$, may be replaced by the relaxation frequency 'ω', sometimes referred to as the relaxation parameter.

The local equilibrium distribution takes the Maxwellian form:

$$f_i^{\mathrm{equ}} = w_i \rho(r)\left(1 + 3\frac{\hat{e}_i u}{c^2} + \frac{9(\hat{e}_i u)^2}{2\ c^4} - \frac{3u^2}{2c^2}\right) \tag{3}$$

In Eq. 3, $\hat{e}_i$, is the unit vector in the ith direction, u is the local (macroscopic) velocity, $\rho(r)$is the local density, $c = \frac{1}{\sqrt{3}}$ is the basic lattice speed, whereas, the weighting factor w_i, are specified in Table 1.

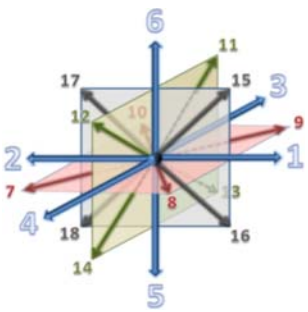

Fig. 7 D3Q19 model for higher precision, which resembles 19 velocity directions representing the 3-D lattice

Table 1 Values of weighting factors according to the unit directions

Direction $\hat{e}_i$	w_i
0	1/3
1,2,3,4,5,6	1/18
7,8,…..,18	1/36

The local density of each phase can be expressed as:

$$\rho = \sum_i f_i \tag{4}$$

The momentum fluxes, ρu, viscosity, v, pressure, P and shear stress, τ, can be written as follows for each phase:

$$\begin{aligned} \rho u &= \sum_{i=1}^{18} \hat{e}_i f_i = \sum_{i=1}^{18} \hat{e}_i f_i^{\mathrm{eq}}, \\ v &= \tfrac{1}{6}\left(\tfrac{2}{\omega} - 1\right), \quad P = C_s \rho \end{aligned} \tag{5}$$

$$\tau = -\left(1 - \frac{1}{2\tau}\right)\sum_{i=1}^{18}[f_i - f_i^{eq}] \times \left(e_{ix}e_{iy} - \frac{1}{2}e_i.e_i\delta_{xy}\right) \tag{6}$$

where ω is the relaxation frequency sometimes referred to as the relaxation parameter; C_s is the speed of sound; δ_{xy}, kronecker delta; $e_{ix,y}$, component unit vectors in x- and y- directions.

A typical pressure gradient (Mei et al. 2002) is applied along the x-axis; this is seen in Eq. 7. The pressure gradients are chosen to meet the appropriate flow conditions in the bioreactor.

$$\tilde{f}_i(x,t) = f_i(x,t) - w_i\frac{3}{c^2}\left|\frac{\mathrm{d}p}{\mathrm{d}x}\right|\hat{e}_i\hat{x} \tag{7}$$

Denoting the $\mathrm{d}p/\mathrm{d}x$ as the applied pressure gradient over the bioreactor satisfying the pump pressure and the overall Reynolds number; $\hat{x}$ represents the unit vector of the pressure gradient direction which is in this case the x-direction. The equation resembles the update of the particle distribution at time, t, with the pressure gradient effect to reach the new distribution, $\tilde{f}_i(x,t)$.

3 Results and discussion

3.1 Straight micro-channels investigations

In an introductory investigation, aligned micro-channels are studied for considerations of stress as a stimulus for

stem cells to form bone tissue. Several studies were made for different geometry aspects, such as inclination angle and porosity where the porosity, Φ, is defined as:

$$\Phi = \frac{A_{\text{pores}}}{A_{\text{total}}} \tag{8}$$

where A_{pores} is the area of pores and A_{total} is the total area including the solid and pore components and both areas are calculated perpendicular to the flow direction in general (Y-axis)

The straight channel investigations are a simple clearing of how shear stress changes with different basic geometry variation. The analysis made for straight micro-channels cover:

1. Inclinations linearly varying from 0° to 45° were studied at a fixed porosity of 91% as in Fig. 8a.
2. Straight micro-channels at 0° but varying porosity from 0 to 95% as in Fig. 8b, and as well varying Darcy's Reynolds Number.

$$Re_{\text{Darcy}} = \frac{V\phi}{\upsilon} \tag{9}$$

where the V is the micro-porous velocity, υ is the kinematic viscosity and ϕ porous average diameter.

In a complicated micro-porous structure such as the system existing in bone tissues it is necessary to understand basic effects individually. In this analysis the effect of the misalignment of the porous channels to the momentum direction is investigated. The angles investigated were: 0°, 22°, 58°, and 71°. The effect of those micro-channels angular variations on the shear stress was calculated, as several previously established bioreactors have nearly achieved the appropriate pressure field. The shear stress was evaluated by finding an integral average on the whole micro-channel area.

The results are plotted in Fig. 9, and the stress is seen to rise up to a critical angle value. The reason for this shear stress increase can be easily explained by analysing the axial incoming momentum and then as well analysing the angular deviated momentum. Comparing both exactly resembles a nozzle effect which by continuity conservation rules, raises the velocity and accordingly the velocity gradient which is basically the shear stress. Up to a threshold at which the momentum energy cannot overtake the high angle anymore, this is the critical symmetric angle: 45°, reasonably after which the stress deteriorates in the same manner. This threshold is expected to vary from geometry to geometry and as well would vary with the flow properties as it indicates the limit when the momentum rate change is zero, and the rest of the energy is exhausted in the vertical component to climb the angled direction.

The porosity investigations were made independent of the angle investigations in order to isolate and to understand the consequences, i.e. at a fixed angle of 0°.

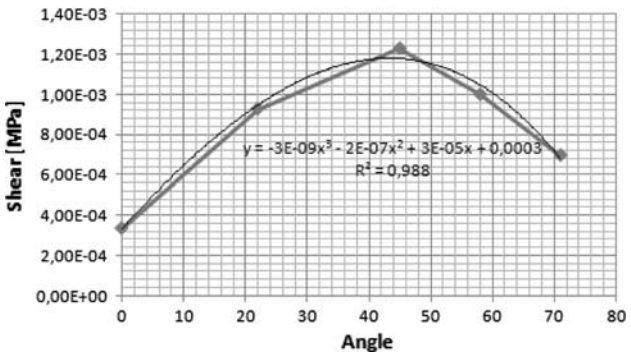

Fig. 9 Micro-porous channels with a porosity of 91% and at different channelling angles of: 0°, 22°, 58° and 71° were simulated and the average shear stress plotted. Reporting a critical angle of 45° at which the kinetic energy is over balanced by the higher angular resistance

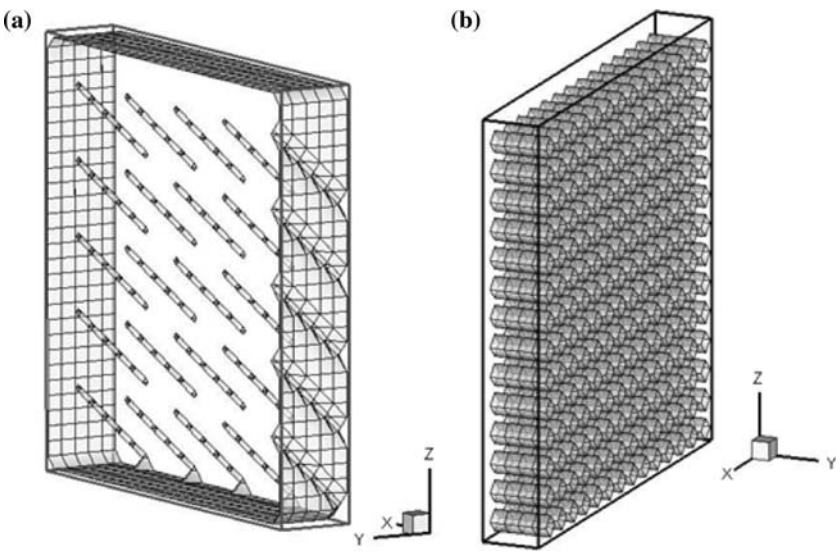

Fig. 8 **a** Micro-porous channels at 45° and 91% porosity; and **b** channels at 0° and 55% porosity

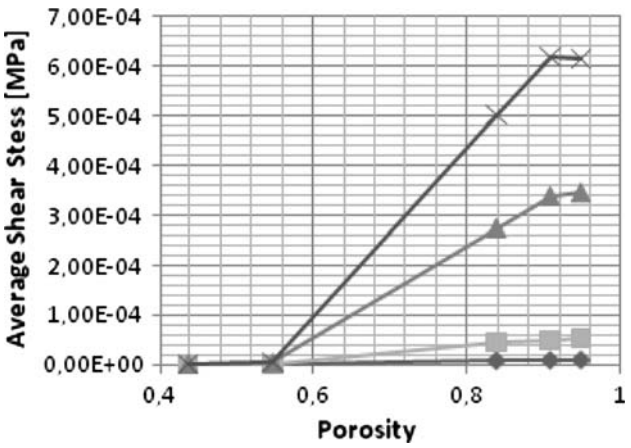

Fig. 10 Investigations on combined effect of porosity and Darcy's Reynolds number on shear stress, revealing two critical points: when porosity is over blocking the flow and when pores are oversized and therefore dissipating the momentum flux, where, the *diamond* represents the stress at $Re = 0.189$, the *square* represents stress at $Re = 0.94$, the *triangle* represents the stress at $Re = 5.68$ and the *cross* represents the stress at $Re = 9.466$

Nevertheless, Darcy's Reynolds number was changed from 0.18 to 9.4 for further knowledge of the combined effect of both the porosity and the Reynolds number on the shear stress.

Regardless of the sounding simplicity of the numerical experiment, a further deeper look on Fig. 10 shows some complications. As the pore size falls, a quick guess would be rising of the velocity which is not true up to a certain point, since the flow could be rather blocked than speeding up. This point is seen explicitly at 0.47 porosity, whatever value the Reynolds number takes, the flow momentum sustains blocked. In consequence very low shear stress exhibits which ranges from 5.43E-8 to 6.49E-3 Pa at Reynolds number 0.1–9.4, respectively. After this point the trend becomes typical; as the porosity rises more flow mass is allowed which resembles higher shear stress and of course higher levels for higher Reynolds number. Excluding when the pores are oversized and therefore dissipating the momentum flux. Afterwards a bottleneck occurs again; the continuity applies again revealing higher pore size slightly lowers the velocity and therefore slightly lowers the stress. This can be clearly seen once Fig. 10 is examined carefully for $Re = 5.68$ and 9.4 starting from porosity 0.9 to 0.95. It is not senseful to raise the Reynolds number further, since from past experimental experience tissue cells are torn out and destroyed at Reynolds number higher than 10 (Hussein et al. 2008a, b).

Concluding, that the geometry configuration (expressed by the porosity and channelling angles) and the flow dynamics (expressed by Darcy's Reynolds number) can limit the stress at three cases: high channel angle ($\sim 45°$), at low porosity (0.47) and at higher porosity (0.91). Thus it is not always a win–win situation and of course special investigations should be made on each problem specifically as more alterations than the standard problem may cause more complications, as in the second case studied. But as a general rule those limits exist but the exact values vary accordingly.

3.2 Micro-porous investigations

Additional investigations were performed on modelling 3-D porous ceramic (Sponceram©), which was successfully used to stimulate Osteoblast cells by a co-working group. The porous ceramic was simulated and investigated for the developed shear stress. Implications of deviating flow angles and slightly varying pore sizes exhibits. The problem presents a combination of both cases but at fixed Reynolds number. The sample used, Fig. 11, for this simulation was of size 3 mm, 350 μm and 350 μm in *z*-direction, *x*-direction and *y*-direction, respectively. The geometry was uploaded on the solver as explained earlier by collective segmenting and edge detection techniques. The stress levels are calculated using two approaches: the first method is an estimation made by convoluting the preliminary results obtained for straight micro-channels; secondly, the full geometry of the scaffolds is numerically solved and a precise stress calculation is reported. Both results are compared for reasons of providing a cheaper and quicker stress level estimator inside the reactor during the blue print stage by means of the first approach.

3.2.1 Initial calculation

Initial calculations are performed to roughly estimate the stress levels occurring inside the bioreactor, the preliminary calculations could be used as blue prints for experimentation design.

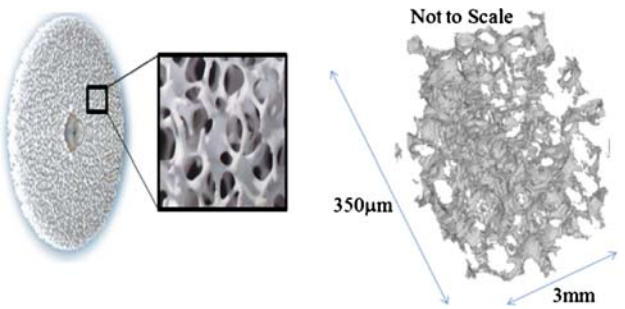

Fig. 11 The sample used for this simulation was of size 3 mm, 350 μm and 350 μm in *z*-direction, *x*-direction, *y*-direction, respectively, and a porosity of 90.06%. The geometry was uploaded on the solver by a combined segmenting and edge detection technique. The porous ceramic (Sponceram©), which was successfully used to stimulate Osteoblast cells by a co-working group of *Dr. Cornelia Kasper Institut für Technische Chemie, Leibniz Universität Hannover*

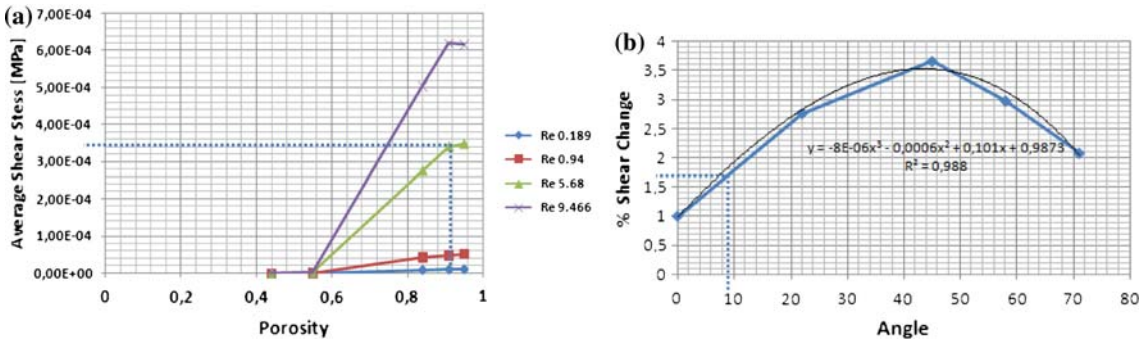

Fig. 12 Straight micro-channel results (angle and porosity Fig. 7, 8) can be combined to estimate what shear stress is expected the micro-porous structure. From a 91% porosity at $Re = 6$ resembles a stress of 3.402e-4 MPa and correcting it with the angular stress deviation by a correction factor of 1.75 present an estimated stress of 5.9535e-4 MPa

The material has an average porosity of 90.06% and an estimated integral inclination angle shift of 10°. Using the straight micro-channels results, both cases can be combined to estimate what shear stress is expected in such a simulation. From Fig. 12a 91% porosity at $Re = 6$ resembles a stress of 3.402e-4 MPa and correcting it with the angular stress deviation from Fig. 12b, a correction of 1.75 is necessary, thus readjusting the estimated stress to a value of 5.9535 e-4 MPa.

3.2.2 Full calculation

The full geometry of the scaffolds is numerically solved and a precise stress calculation is reported. The solver reported an average integral magnitude shear stress of 5.30473e-4 MPa for the simulation of the full porous medium, this was obtained by finding the resultant magnitude stress of the three shear stress components (τ_{xy}, τ_{xz} and τ_{yz}); the magnitude stress distribution and stress components can be seen in Fig. 13. Comparing with the preliminary results obtained from the straight micro-channel investigations a difference of 12% is found, which is quite high for such an accuracy-sensitive engineering problem.

The sources of error could be due to the slightly varying porosity from plane to plane in the full porous model or due to the simple convoluted combination of both preliminary results to obtain the stress. Nevertheless, the preliminary calculations could be used as blue prints for experimentation design, since the full modelling needed 40 h processing time.

On the whole using micro-porous scaffolds have proven much more realistic in imitating the human bone shear load conditions (0.1 MPa) with at least two orders of magnitude closer (5.3×10^{-4} MPa) than previously published results (1.09×10^{-6} MPa; Table 2). Further work should be done to realise closer shear loads to measured data in humans.

4 Conclusion

In this study several aspects of bone tissue engineering are investigated from a mechanical point of view, providing further awareness of stresses' level and nature induced inside bones. The study as well, explores the possibilities of modelling the complex geometries, by means of image processing. Besides, the study shows the possibility to model the transport phenomena, using LBM, inside the micro-network of scaffolds. This work mainly addresses the mentioned aspects via four major points, which were mentioned in the introduction, further remarks and explanations can be made to the points proposed in the introduction:

Investigations of Bone Tissue from a Mechanical Point of View

- Loading and perfusion are the means of stress transfer between the cells. The loading part is cyclic and it acts as a dynamic stimulus which raises the stiffness of the cells. These loads were reported reaching 6–18 MPa (Mega Pascal) (Ishaug et al. 1997), meanwhile their experimental range was reported between 0.66 and 1.5 MPa (D'Lima et al. 2006) in a single knee for walking and jogging, respectively.
- For the theoretical investigation of the bone tissue diffusion coefficient, values of order O (10 μm/h), are reported which shows great discrepancies in transport times which leads to the questioning of the concept of free diffusion as the major mechanism of nutrition exchange between the blood vessels and the bone tissue.
- During physiological activity, the mechanical loading of bone tissue leads to a tissue stress state composing of cyclic dilatational and deviatoric components. The cyclic pressure gradient is the main transport pump such that the fluid movement in tissue is due to the

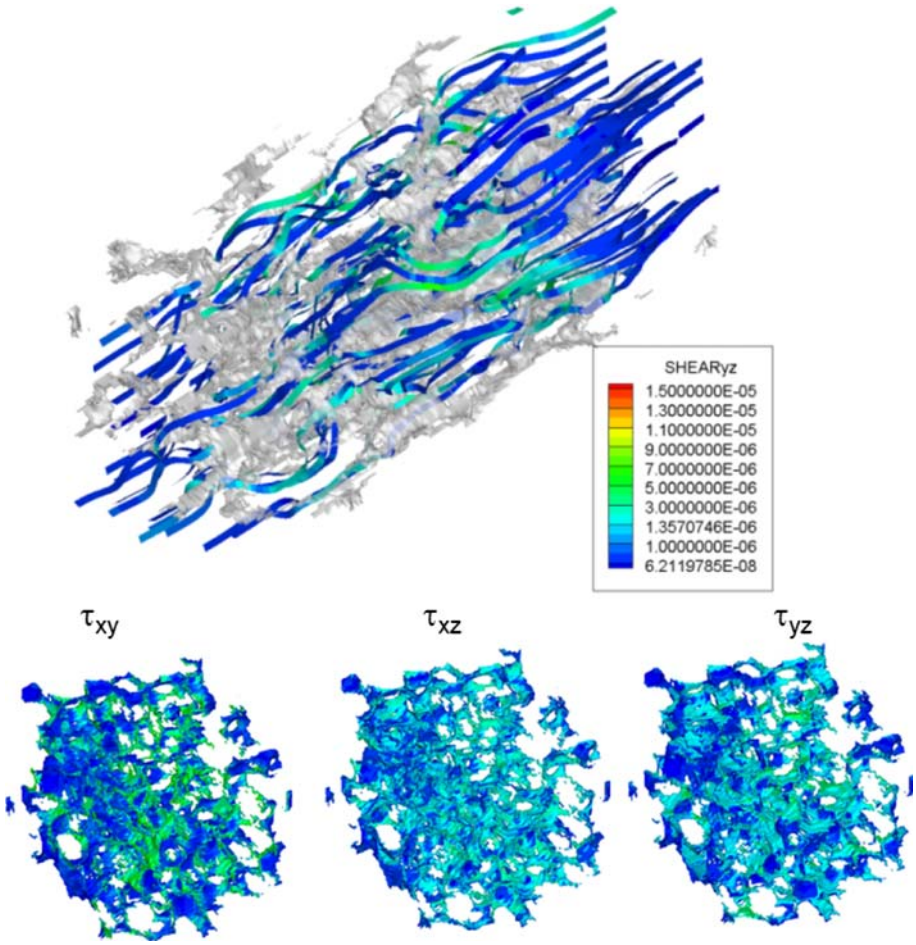

Fig. 13 An integral magnitude shear stress of 5.30473e-4 MPa was calculated from the three shear stress components for the micro-porous scaffolds at $Re = 6$

Table 2 The average shear stress load applied on the cartilage cells

Method	~Shear [MPa]
Measured (D'Lima) Walking (D'Lima et al. 2006)	$0.94 \times 10^{-1} \rightarrow 0.1$
Measured (D'Lima) Jogging (D'Lima et al. 2006)	$0.28 \rightarrow 0.7$
Modelled (Hussein et al. 2008)	0.48×10^{-11}
Moaty et al. (2009)	1.09×10^{-6}
Micro-porous Scaffolds (This work)	5.30473×10^{-4}

effect of dilatation or pressure imposed by cyclically loading of bone tissue meanwhile the oscillating high shear flow induced by the oscillating pumping mechanism provides the bone tissue with a stiffness education schedule.

- For a sustained growth, the mechanical environment of for the tissue should allow for a cyclic load ranging from 0.1 to 0.7 MPa for ~1 s which is the real load bone tissue experience during a walking cycle (Munting and Verhelpen 1993; Iarovici et al. 2004).

The possibilities of using image processing in capturing micro-scaffolds and Lattice Boltzmann method for modelling transports in the scaffolds.

- *An algorithm which* searches for the threshold value in the image and then propagates around it in a 2-D lattice in eight directions, until an edge is hit is developed. This algorithm is a redundant avoiding algorithm which has proven much more reliable in predicting complicated edges. It is also time saving and as well enables the possibility of parallel processing of the image, as each threshold value can be scanned and dealt with independently. This method has predicted the scaffolds inside the ceramic sample successfully and the algorithm was able to build up the 3-D micro-structures from the 2-D sections.
- the transport phenomena and the shear stress distribution in straight micro-channels and in the complicated micro-scaffolds were modelled successfully using the code developed previously for the multi-phase Lattice Boltzmann.

The dynamic and geometric influences of the shear stress in micro-channels

- Different dynamic and geometric properties affect the shear stresses induced in micro-porous scaffolds. These scaffolds are investigated in this work in order to understand more about such effect. Both property types have proven stress limiting at high channel angle $\sim 45°$ and at low porosity 0.47 and at high porosity 0.91.
- Tissue cells are torn out and destroyed once the Reynolds number is raised above 10 hence limiting cell growth. So, each problem should be investigated on its own, since altered parameters can result in different complications, as in the second case studied.
- The stress levels occurring inside the reactor can be roughly estimated by combining both the dynamic and geometric results and could be used as blue prints for experimentation design.

Reporting of Shear stress levels in micro-scaffolds bioreactors and comparing them to conventional bioreactors and realistic bone loads in humans.

- The full scaffold geometry is modelled and numerically solved reporting an accurate stress calculation. An average integral magnitude shear stress of 5.30473e-4 MPa was obtained by finding the resultant magnitude stress of the three shear stress components (τ_{xy}, τ_{xz} and τ_{yz}) for the full porous medium.
- Stresses with a round off difference up to 12% in the micro-porous scaffolds can be estimated from the Superposition of both dynamic and geometric variations in the straight channels work. This difference could be resulting from the slightly varying porosity from plane to plane in the full porous model or from the simple convoluted combination of both preliminary results to obtain the stress.
- Full modelling needs about 2 days of processing time, as a consequence, the preliminary calculation can be used as a proposal for experimentation design.
- For the imitation of human bone shear load conditions, the use of micro-porous scaffolds proved to be more realistic with 0.1 MPa which is at least two orders of magnitude closer 5.3×10^{-4} MPa than previous published results 1.09×10^{-6} MPa. In order to have a closer shear load to that measured in humans, more investigation and further studies are required. Pulsating pressure fields by means of low frequency piezo elements embedded in the bioreactor could be a promising modification.

Further modifications to enhance bioreactor design of such load baring cells.

- Further studies should be done to realise higher shear loads:
  - Investigations should be done on changing scaffolds geometric properties (porosity, micro-channel diameter, integral inclination angle) these parameters would certainly have great influence on the produced shear stress.
  - If the reactor flow field exhibits a pulsating pressure fields, this can lead to more realistic conditions for the cyclic load baring cells. This cyclic flow field can be achieved by means of low frequency piezo elements embedded in the bioreactor, which can be a promising modification, but investigation on the presence of an electric field on the grown cells may be necessary.
  - Other ideas of pressurised moving flow field have shown promising result (Moaty et al. 2009), this could be further investigated and applied on the scaffolds.
- On the other hand special care should be made in new designs to provide the cells with uniform growing conditions of adequate symmetric nutrition supply which would have great influence on the grown cells, and as well the provision of a waste removal system by means fluid motion (Hussein et al. 2008a, b).

References

Ateshian GA, Hung CT, et al (2003) Functional properties of native articular cartilage in Guilak. Functional Tissue Engineering. NY, Springer: 46–68

Bancroft GN, Sikavitsas VN et al (2002) Fluid flow increases mineralized matrix deposition in 3D perfusion culture of marrow stromal osteoblasts in a dose-dependent manner. Proceed Natl Acad Sci USA 99:12600–12605

Braccini A, Wendt D et al (2005) Three-dimensional perfusion culture of human bone marrow cells and generation of osteoinductive grafts. J Stem Cells 23:1066–1072

Cowin SS (2001) Handbook of bone mechanics. CRC Press

D'Lima DD, Patil S et al (2006) Tibial forces measured in vivo after total knee arthroplasty. J Arthroplast 21(2):255–262

Gatzka C, Knothe U, Niederer P, Schneider E, Knothe Tate ML (1999) A novel ex vivo model for investigation of fluid displacements in bone after endoprosthesis implantation. J Mater Sci Mater Med 10:801–806

Grayson WL, Bhumiratana S, et al (2007) Increased perfusion rate and cell seeding density enhance tissue engineering of human bone. 53rd Annual Meeting of the Orthopaedic Research Society, San Diego, CA, 11–14

Higuera FJ, Jimenz J (1989) Boltzmann approach to lattice gas simulations. Europhys Lett 9:663–668

Hill NM, Horne JG, Devane PA (1999) Donor site morbidity in the iliac crest bone graft. Aust N Z J surg 69(10):726–728

Holtorf HL, Sheffield TL, et al (2005) Flow perfusion culture of marrow stromal cells seeded on porous biphasic calcium phosphate ceramics. Ann Biomed Eng (33):1238–1248

Hussein, MA, et al (2006) On the Validation of a 2-D Laminar Flow Solver Using Lattice Boltzmann Method, Proceedings of the 8th International Congress on Fluid Dynamics and Propulsion, ASME, Sharm el Sheikh, ICFDP8-EG,200

Hussein MA, Esterl S et al (2008a) Impulse and mass transport in a cartilage bioreactor using the Lattice Boltzmann method. Int J Comput Fluid Dyn 22(5):341–350

Hussein MA, Esterl S et al (2008b) On the Lattice Boltzmann method simulation of a two phase flow bioreactor for artificially grown cartilage cells. J Biomech 41(16):3455–3461

Iarovici A, Capitanu L, et al (2004) The total hip arthroplasty effects on the mechanical behaviour of the femur. Annual Symposium of Solid Mechanics

Ishaug SL, Crane GM et al (1997a) Bone formation by three-dimensional stromal osteoblast culture in biodegradable polymer scaffolds. J Biomed Mater Res 36:17–28

Ishaug SL, Crane GM, et al (1997) Bone formation by three-dimensional stromal osteoblast culture in biodegradable polymer scaffolds. J Biomed Mater Res (36):17–28

Kasper C, Suck K, et al (2007) A Newly Developed Rotating Bed Bioreactor for Bone Tissue Engineering. Top Tissue Eng, 3

Keóelman JMVA (1991) A simple lattice Boltzmann scheme for Navier–Stokes fluid flow. Europhys Lett 15:603–607

Knothe T, Niederer P, Knothe U (1998) In vivo tracer transport through the lacunocanalicular system of rat bone in an environment devoid of mechanical loading. Bone 22(2):107–117

Mcnamara G, Zanetti G (1988) Use of the Boltzmann equation to simulate lattice-gas automata. Phys Rev Lett 61:2332–2335

MediLexicon International Ltd., 2009 <www.medicalnewstoday.com>. Accessed 2 Jan 2009

Mei RW, Yu DZ, Shyy W, Luo LS (2002) Force evaluation in the lattice Boltzmann method involving curved geometry. Phys Rev E 65 (4)

Moaty AA, Hussein MA, Becker T (2009) An innovative Lattice Boltzmann model for simulating Michaelis Menten based diffusion-advection-kinetics and its application within a cartilage cell bioreactor. J Biomech Model Mechanobiol. doi: 10.1007/s10237-009-0164-3

Munting E, Verhelpen M (1993) Mechanical simulator for the upper femur. Acta Orthropedicae Belgica 59(2):123–129

Petrović M, Mitraković D et al (2009) A novel bioreactor with mechanical stimulation for skeletal tissue engineering. J Chem Ind Chem Eng Q 15(1):41–44

Sarah H, Cartmell et al (2003) Effects of media perfusion rate on cell seeded 3D bone constructs in vitro. Tissue Eng 9(6):1197–1203

Seiler JG, Johnson J (2000) Iliac crest autogenous bone grafting: donor site complications. J South Orthop Assoc 9:91–97

Sikavitsas VI, Bancroft GN, et al (2003) Mineralized matrix deposition by marrow stromal osteoblasts in 3D perfusion culture increases with increasing fluid shear forces. Proc Natl Acad Sci USA (100) 14683–14688

Tadrous PJ (1995) A simple and sensitive method for directional edge detection in noisy images. J Pattern Recognit 28(10):1575–1586

Turgut A, Yemez Y, et al (1996) Differential block coding of bilevel images. IEE Trans Image Proces, 5(9):1368–1370

Xiaojun Yu, Edward A, et al (2004) Bioreactor-based bone tissue engineering: The influence of dynamic flow on osteoblast phenotypic expression and matrix mineralization. PNAS (101), 31:11203–11208

Yuan H, Kurashina K et al (1999) A preliminary study on osteoinduction of two kinds of calcium phosphate ceramics. Biomaterials 20:1799–1806

Yuasa T, Miyamoto Y et al (2001) In vitro resorption of three apatite cements with osteoclasts. J Biomed Mater Res 54:344–350

Food Biophysics
DOI 10.1007/s11483-010-9156-1

ORIGINAL ARTICLE

An Innovative Micro-Modelling of Simultaneous Heat and Moisture Transfer during Bread Baking Using the Lattice Boltzmann Method

Mohamed Ahmed Hussein · Thomas Becker

Abstract A considerable fraction of the energy consumed in bread manufacturing is used for the baking process. A thorough understanding of internal moisture transfer mechanisms are important to optimise both the quality of the product and the economics of the process. From a transport phenomena point of view, bread baking has been considered as a simultaneous heat and mass transfer problem in a porous medium. Nevertheless, most efforts previously made have avoided modelling the phenomenon occurring in the microscale, although the mechanism occurs primarily in the microscale. In this work heat and moisture transfer models were developed to accomplish the mechanisms included, both in the microscale and the macroscale by means of Boltzmann's equation. Modelling and predictions of moisture transfer, heat transfer, modelling of effective moisture diffusivity, thermal conductivity and diffusivity have been investigated in this work. The microstructure in the dough samples was obtained using micro-computer tomography images from the samples prior to baking. The models were quantified and validated with measurements from the literature in order to assess the predictive models. The simulated crust development has shown a crust thickness of 0.8 cm, which is slightly higher than similar experimental results in which a dehydrated thickness of 0.5–0.6 cm was reported. The crust over-estimation in this work fits to the overheating occurring in the model. Additionally, investigations were made on the influence of different porosities (11–16%) of the bread; the boundary layer temperature at a porosity of 11% was reached after 25 min and after 17.5 min at a porosity of 16%. Therewith, the results showed that, with increasing porosity, the heat transfer rate towards the centre was higher, which matches the knowledge of experienced bakers.

Keywords Heat transfer · Moisture transfer · Bread baking · Dough microstructure · Modelling · LBM

Nomenclature

a_w	Water activity
C	Moisture content, kilogrammes per kilogramme
c_p	Heat capacity at constant pressure (mass-based), Joules per·kilogramme Kelvin
D	Diffusion coefficient, square metres per second
D_{eff}	Effective diffusion coefficient, square metres per second
$\hat{e}_i$	Unit vector in the ith lattice direction
f	Particle distribution function
h	Heat transfer coefficient, watts per square metre kelvin
J	Moisture flux, kilogrammes metre per kilogramme second
K	Thermal conductivity, watts per metre kelvin
K_{C}	Mass transfer coefficient, per Pascal metre second
L	Characteristic length, metre
L_2	The 2nd norm error
P_{Dough}	Water partial pressure in dough, Pascal
P_∞	Water partial pressure in the surrounding environment, Pascal
P	Vapour pressure of the food, Pascal
P_{o}	Vapour pressure of water, Pascal
P_{sat}	Saturation pressure, Pascal
Q	Heat flux, watts per square metre
RH	Relative humidity, percent

M. A. Hussein (✉) · T. Becker
Group of (Bio-) Process Technology and Process Analysis,
Faculty of Life Science Engineering,
Technische Universität München,
Weihenstephaner Steig 20,
85354 Freising, Germany
e-mail: hussein@wzw.tum.de

Published online: 17 April 2010

T_{Dough}	Water temperature in dough, kelvin
T_{∞}	Temperature in oven environment, kelvin
u	Particle velocity in Lattice units
W	Water content, kilogrammes per kilogramme
w_i	Weighting factor

Greek symbols

α	Thermal diffusivity, square metres per second
δ	Constrictivity
$\varnothing$	Average pore diameter, metres
Φ	Porosity
ρ	Density, kilogrammes per cubic metre
τ	Tortuosity
τ_r	Relaxation time
τ_c	Concentration relaxation time
τ_T	Temperature relaxation time
$\Psi(r)$	Local physical property at current position, r
ω	Relaxation frequency
$\forall$	Volume, cubic metre
Ω	Collision term
ζ	Curve length, metres
ξ	Chord length, metres

Subscripts

eff	Effective
fact	Conversion factor
LU	Lattice units
i	Counter number in Lattice directions
∞	Free stream, oven environment
w	Water

Introduction

Since prehistoric age man has prepared and baked bread as an essential constitute for his daily meal. Early archaeological evidences reflect back to the ancient Egyptian era. Bread was constantly baked by recipe from experience, which guided the constitution and preparation environment. Due to renewed interests for product quality, stability, weights and costs, engineers in the last two decades have persistently modelled bread baking process. A considerable fraction of the energy consumed in bread manufacturing is used for the baking process. Therefore, understanding internal moisture transfer mechanisms are important to optimise both the quality of the product and the economics of the process.

The thermo-physics involved in dough baking is quite complicated. Two phenomena work simultaneously:

- Heat transfer
- Moisture transfer, both together often called the simultaneous heat and mass transfer (SHMT)

Difficulties arise in such systems due to the presence of two coupled phenomena: heat and moisture transfer. Both phenomena occur simultaneously, and each contributes to the other, which boosts the difficulties of understanding such a complicated system.

Modelling techniques have proven of great help in combined engineering problems, due to its cheap price in comparison to experimentation. It enables the isolation of each phenomena independently for intensive investigations as well. On the other hand, it is sometimes quite complicated to propose a mathematical model for certain physics occurring.

Several previous works have addressed the same problem with trials of modelling different aspects of bread baking process. For instance, the evaporation–condensation theory proposed by Sluimer[1] was incorporated in a model of SHMT in dough and crumb, not involving the crust zone.[2] Good results were obtained when comparing experimental and simulated core temperature values, Thorvaldsson[3] took into account evaporation and condensation of water for modelling the drying of bread crumb and developed a model for heat, liquid water and water vapour transfer including an empirical parameter named as evaporation rate (i.e. times per second the vapour content is set at the saturated partial water vapour pressure). Another approach was taken by Lostie[4] to incorporate evaporation–condensation in a model for the ‘‘heating up’’ period of cake baking; this mechanism was included in the heat balance through an effective thermal conductivity.

Investigation in micro-dynamics has proven of great challenge to system dynamists, as most of the mathematical governing equations are restricted in the microscale and the nano-scale, and in contrast, most sophisticated dynamic phenomenon persist in the microscale. Another limitation is the complications in modelling the transport through the complex micro-scaffolds. The scaffold generation and boundary conditions play an overwhelming role against the conventional algorithms as well.

In the last 20 years, extensive work has been developed in the Lattice Boltzmann method (LBM). The method has received significant respect as an alternative for simulating complex flow phenomena in different scales.[5, 6] This method is based on the Ludwig Boltzmann’s equation 1872 that considers gases are composed of interacting particles, which makes it quite fit for microscale modelling.

In consequence, LBM has proven relieving all sophistications in modelling such complicated biotechnological aspects. A previously developed code by Hussein[7–9] for the Lattice Boltzmann method is utilised in this work which has proven fit for modelling the substrate transport and kinetics in such microscale environment. The code was benchmarked in several test cases involving both meso- and microscale phenomenon.

In this work, an innovative contribution is made by modelling and simulating bread baking process in the microscale using LBM, considering both heat transfer and mass transfer. The heat and moisture transfer models were developed to accomplish the mechanisms included, both in the microscale and the macroscale, to predict moisture transfer, heat transfer, modelling of effective moisture diffusivity, thermal conductivity and diffusivity. The microstructure in the dough samples was obtained using micro-computer tomography images from the samples prior to baking. The models were quantified and validated with measurements in order to assess the predictive models.

Dough Thermo-physics

This section describes in detail the physics associated in the process of heat and mass transfer in dough while baking. All the included parameters and physical properties are discussed and detailed providing all the used models and its limitations. The mass transfer physics is described first and followed by the heat transfer; all considered models are then summarised in Table 1.

Hygroscopic Property

The mechanisms by which heat and moisture are transferred in a material basically depend on the physical microstructure and chemical composition of the material. This can be classified accordingly in respect to its water binding properties (hygroscopic). Dough in general is considered hygroscopic; the trend at which the moisture content inside dough dries out is commonly dependent upon the partial pressure difference between the heating environment and the dough surface as a function in temperature.

The moisture content flux (J) from the dough surface can be expressed by Fick's first law of diffusion.

$$J = -D\nabla C = K_C\left(P_{\text{Dough}}\left(T_{\text{Dough}}\right) - P_\infty(T_\infty)\right) \tag{1}$$

The moisture flux, which is the driving force of the moisture content across the dough surface boundary, is indirectly dependent upon the temperature difference. Furthermore, when $P_{\text{Dough}}\left(T_{\text{Dough}}\right) > P_\infty(T_\infty)$ a positive flux exhibits which means a moisture drive from the dough surface to the surrounding as demonstrated in Figure 1.

Water Activity

Water activity (a_w) is the driving force for water content transfer between food and its surrounding. In general, water migrates from areas of high a_w to areas of low a_w, and it is defined as the ratio of vapour pressure in the food to that of saturated water at the same temperature.

$$a_w(T) = p/p_o \tag{2}$$

Where p is the vapour pressure of the food and p_o is the vapour pressure of pure water at the same temperature. In this work, the Oswin model[10] is used with coefficients obtained by Zhang,[11] such that the water activity is expressed function in the local moisture content (C) and local temperature (T) as follows:

$$a_W(T,C) = \left[\left(\frac{100C}{e^{-0.0056T+5.5}}\right)^{\frac{-1}{0.38}} + 1\right]^{-1} \tag{3}$$

This model can be used to update and eases the calculation for the moisture content flux such that:

$$\begin{aligned} P_{\text{Dough}}\left(T_{\text{Dough}}\right) &= a_W P_{\text{Sat}}\left(T_{\text{Dough}}\right) \\ P_\infty(T_\infty) &= RH.P_{\text{Sat}}(T_\infty) \end{aligned} \tag{4}$$

The oven will technically not have a fully saturated humid environment and would rather have a relative humidity (RH) of known percentage from the fully saturated condition.

Overall, the moisture content difference between the oven internal environment and the moisture in the bread is the moisture flux driving force. This can be tuned by changing the oven humidity by steam spraying. Apparently, humidity tuning resembles better thermal conductivity and softer, cooked end product.

Porosity, Constrictivity, Tortuosity and Mass Diffusion Coefficient

The micro-porous structure of dough has an important effect on transport mechanism of moisture and heat. Porosity is defined as the ratio of void space to the total volume of the material:

$$\Phi = \frac{\forall_{\text{pores}}}{\forall_{\text{total}}} \sim \frac{\sum \phi^3_{\text{pores}}}{\forall_{\text{total}}} \tag{5}$$

Constrictivity is a dimensionless parameter used to describe transport processes (often molecular diffusion) in porous media. Constrictivity (δ) is viewed to depend on the ratio of the diameter of the diffusing particle to the pore diameter. The value of constrictivity is always less than 1. The constrictivity is defined not for a single pore, but as the parameter of the entire pore space considered. The resistance to transport in porous media increases because the viscosity of the fluid (which fills the pores) increases in the vicinity of the pore walls. This effect is important in very narrow pores

Table 1 Heat and mass transfer processes involved in the process of baking, stating the property and the positions of influence along with the necessary constants

	Property	Location	Equation	Constants and necessary definitions
Mass transport	Moisture diffusion	Inside medium	$D_{\text{eff}}\|_{\text{Moisture}} = \begin{cases} 5e^{-10}T - 1e^{-8} & \text{, in Crumb} \\ 0.0013 \times (5e^{-10}T - 1e^{-8}) & \text{, in Crust} \\ 2e^{-7}T + 2e^{-5} & \text{, in Air} \end{cases}$	T, temperature at spot, °K
	Moisture flux across boundaries	Oven–dough interface	$-D_{\text{eff}}\|_{\text{Moisture-Crust}} \frac{\partial C}{\partial \hat{n}} = K_C\left(P_{\text{Dough}}\left(T_{\text{Dough}}\right) - P_\infty(T_\infty)\right)$	Moisture diffusion coefficient in the crust, $D_{\text{eff}}\|_{\text{Moisture-Crust}} = 0.0013 \times (5e^{-10}T - 1e^{-8}), m^2 s^{-1}$ Mass transfer coefficient between oven and crust and considers crust formation, $K_C = 1.4e^{-11}, Pa^{-1} ms^{-1}$ Water partial pressure in dough, $P_{\text{Dough}}\left(T_{\text{Dough}}\right) = a_W P_{\text{Sat}}\left(T_{\text{Dough}}\right)$where the water activity is defined in reference to saturated conditions for temperature, T and moisture content, C as: $a_W(T, C) = \frac{P_{\text{Dough}}}{P_{\text{Sat}}} = \left[\left(\frac{100C}{e^{-0.0056T+5.5}}\right)^{\frac{-1}{0.38}} + 1\right]^{-1}$ Water partial pressure in oven, $P_\infty(T_\infty) = RH\ P_{\text{Sat}}(T_\infty)$where RH is the relative humidity in the oven in all experiments kept at 35%
Heat transport	Thermal diffusion	Inside medium	$\alpha = \begin{cases} \alpha_{\text{air}} & if(x,y,z) = (x,y,z)_{\text{air}} \\ C\alpha_{\text{water}} + (1-C)\alpha_{\text{Zanoni}} & if(x,y,z) = (x,y,z)_{\text{water}} \end{cases}$	Where the Zanoni diffusivity model is defined in terms of the porosity and crumb–crust differentiation: $\alpha_{\text{Zanoni}} = \begin{cases} e^{0.01\phi - 15.25} & \text{in crumb} \\ e^{0.0062\phi - 15.30} & \text{in crust} \end{cases}$
	Thermal conduction	Oven–dough interface	$h\|_{\text{Heating environment}} \Delta T = -k\|_{\text{Boundary}} \frac{\partial T}{\partial x}$	Heat transfer coefficient between oven and crust, $h = 7.68,\ Wm^{-2}K^{-1}$ Thermal conductivity, $K(T)$, in watts per metre kelvin, acts in the oven–dough interface and considers the drying function of the crust $K(T) = \begin{cases} -2e^{-9}T^5 + 4e^{-7}T^4 - 3e^{-5}T^3 - 0.018T + 0.314 & T < T_\infty \\ 0.2 & T \geq T_\infty \end{cases}$

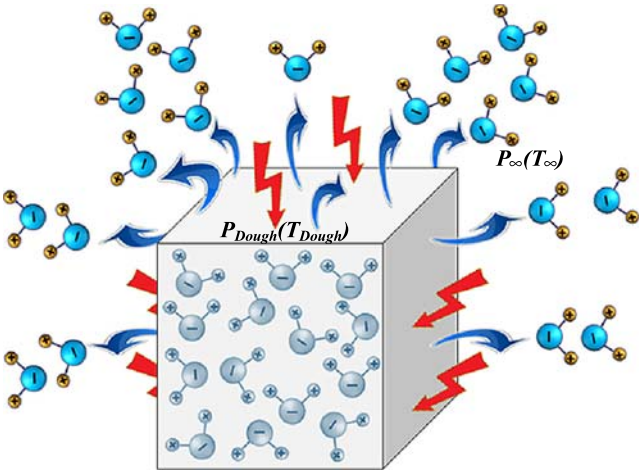

Fig. 1 The $P_{\text{Dough}}(T_{\text{Dough}}) > P_{\infty}(T_{\infty})$ a positive flux exhibits which means a moisture drive from the dough to the surrounding

and in pores narrowing their diameter to the same size as the diameter of the diffusing particles.

The simplest mathematic method to estimate tortuosity (τ) is arc–chord ratio: ratio of the length of the curve (ξ) to the distance between its ends (ζ):

$$\tau = \frac{\xi}{\zeta} \tag{6}$$

The main difficulty in heating hygroscopic material is that, usually, shrinkage occurs with dehydration which may alter the mechanism by which moisture or vapour migrates through the material. Reversely, in dough, as the water moisture migrates to the outer environment, heating of the crumb develops slowly inwards and the temperature of the dough will rise quickly from 25 °C to 50 °C, during this period the fermenting agents will degrade sugar into CO_2 very rapidly and will increase the bread volume. As the temperature rises further, the CO_2 bubbles thermally expand, thus enhancing the development of the bread and thus allowing the formation of cavities inside, which eventually changed the porosity, constrictivity and tortuosity. Nevertheless, dough can be assumed of isotropic properties and that the major expansion happening in the crumb is due to the higher thermal expansivity of the CO_2.

Diffusion is the mechanism by which mass is transported from one part to another derived by a concentration gradient and defined usually for a substrate–solvent system together. In micro-porous systems, the diffusion coefficient is corrected by the constrictivity and tortuosity such that:

$$D_{\text{eff}} = \frac{D\Phi\delta}{\tau} \tag{7}$$

While crust is formed, porosity, constrictivity and tortuosity are changed; the microstructure of the crust pores tend to be smaller than in the crumb region as shown in Figure 2, resulting in a dense porous matrix and thus increasing the resistance to mass transport due to increasing constrictivity. Zhang[11] estimated the overall correction factor (which includes the porosity, constrictivity and tortuosity) for the diffusion coefficient in the crust to be 0.0013.

Another aspect is the dependency of the diffusion coefficient on the temperature. The diffusion coefficient is strictly temperature-dependent and takes different forms in liquid phase and in solid phase. The problem arises due to the phase changing in the dough as the gluten coagulates; an approximation proposed for the diffusion coefficient by Thorvaldsson[3] is considered.

Three completely different diffusion coefficients are used in the modelling. Firstly, a moisture diffusion coefficient through the dough crumb which is temperature-dependent (Figure 3). Secondly, for the crust region, a diffusion coefficient including the crust correction factor is defined. Finally, a third factor is defined for the moisture diffusion in the air region, as seen in Figure 4, surrounding the baked goods, which is temperature-dependent as well.

$$D_{\text{eff}}|_{\text{Moisture}} = \begin{cases} 5e^{-10}T - 1e^{-8} & ,\textit{in crumb} \\ 0.0013 \times (5e^{-10}T - 1e^{-8}) & ,\textit{in crust} \\ 2e^{-7}T + 2e^{-5} & ,\textit{in air} \end{cases} \tag{8}$$

The moisture diffusivity in the dough crumb is seen to be 2~3 orders of magnitude lower than that in air; this gives the dough enough time to cook and stay soft; otherwise, it dries out and develops a much bigger crust.

Thermal Properties

In the natural heating process, the heat energy is transferred first from the surrounding environment to the heated surface; then, the heat is conducted through the interfacial boundary to the inner core of the heated unit. The heating process passes three steps: heat loss, heat conduction and then, heat diffusion in the inner core (Figure 5).

Thermal Conductivity

An effective thermal conductivity is utilised which implicitly imitates the evaporation–condensation mechanism. Equation 9 is valid for dough, crumb and crust,

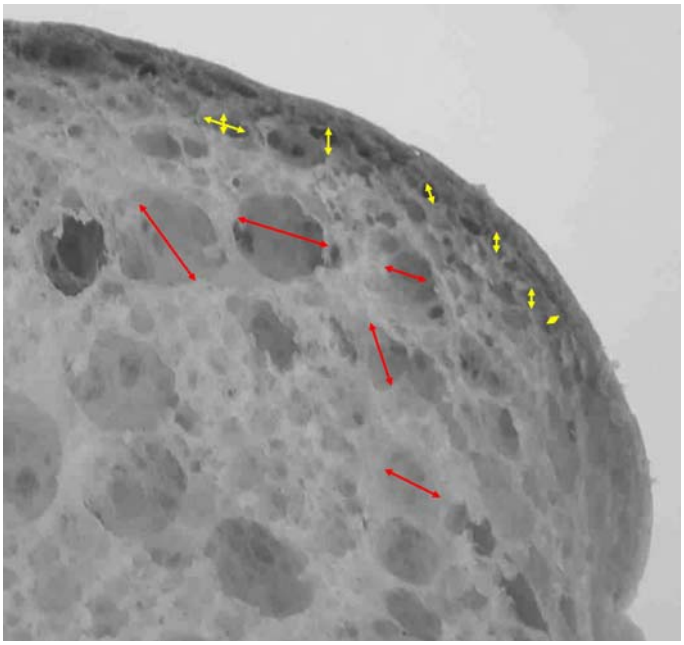

Fig. 2 While crust is formed, porosity, constrictivity and tortuosity are changed; the microstructure and diameter of the crust pores tend to be smaller than in the crumb region

which provides a piecewise function for the diverse working conditions, Purlis.[12, 13]

$$K(T) = \begin{cases} -2e^{-9}T^5 + 4e^{-7}T^4 - 3e^{-5}T^3 - 0.018T + 0.314 & T < T_\infty \\ 0.2 & T \geq T_\infty \end{cases} \quad (9)$$

The thermal conductivity (K) change with temperature is plotted in Figure 6; the first part is obtained from experimentation made by Jury[15] and shows an increase in conductivity with temperature. The second part of the curve represents the conductivity in the crust; this drop is due to the fall of the water content in the crust which resembles a drop in the conductivity. The conductivity falls to 0.2 which is similar to other predictions in the literature by Rask.[16]

Fourier's law for heat conduction, Eq. 10, is applied for the conduction from the hot surrounding to the heated body. This states that the rate of heat transfer through a material is proportional to the negative gradient in the temperatures. The equation will serve in the heating boundary interface between the oven environment and the dough surface.

$$Q_{\text{Loss}} = Q_{\text{Conducted}}$$
$$h|_{\text{Heating environment}} \Delta T = -k|_{\text{Boundary}} \frac{\partial T}{\partial x} \quad (10)$$

The heat transfer coefficient, h, which is the proportionality factor for responsible for transferring the oven heat to the first layer of dough can be taken as a constant value of 7.68 $\text{W}\cdot\text{m}^{-2}\text{K}^{-1}$. Whereas, the thermal conductivity defined

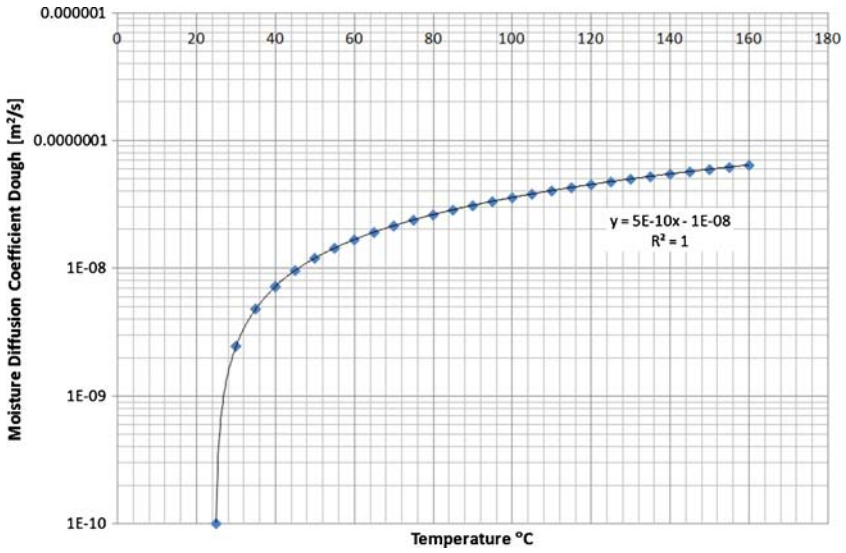

Fig. 3 Moisture diffusion coefficient through the dough crumb is temperature-dependent

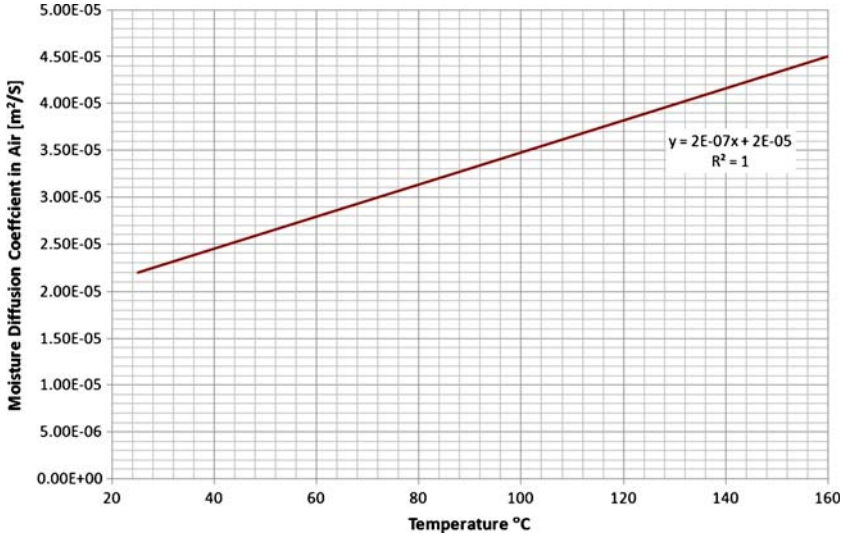

Fig. 4 The moisture diffusion in the air region, surrounding the baked goods, which is temperature-dependent as well

before will act to transfer this heat from the very first dough layer to the second layer inwards.

Thermal Diffusion

Thermal diffusivity, (α), is the ratio of thermal conductivity to the volumetric heat capacity. It basically describes the spatial rate spread of thermal heat.

$$\alpha = K/\rho c_p \tag{11}$$

Considering the micro-porous structure of dough one can consider dough consisting of water–air bubble mixture. Revealing a position dependent thermal diffusivity such that:

$$\alpha = \begin{cases} \alpha_{\text{air}} & if\ (x,y,z) = (x,y,z)_{air} \\ C\alpha_{\text{water}} + (1-C)\,\alpha_{\text{Zanoni}} & if\ (x,y,z) = (x,y,z)_{water} \end{cases} \tag{12}$$

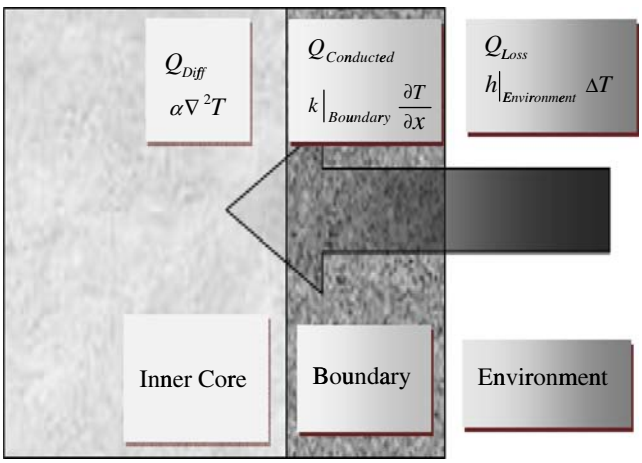

Fig. 5 Heat energy is transferred first from the surrounding environment to the heated surface, then the heat is conducted through the interfacial boundary to the inner core

Where C is the moisture content and α_{Zanoni} is defined in Eq. 13.

The reason for the differentiation is due to the fact that water and air have diverse thermal diffusion coefficients which vary with temperature as shown in Figure 7.

Purlis[12, 13] suggested a different methodology of varying c_p including an enthalpy for phase change, but due to the un-explicit phase change in this work, it will be contradicting to follow a similar approach. While the experimental model of Zanoni[14] for crust and crumb diffusivity provides a better handling of the diverse micro-presence of the porosity, Φ and crumb–crust differentiation. Therefore, in this work, an enhanced model for the Zanoni diffusivity model is suggested dealing more precisely with microstructure of dough as well including the temperature contribution, which was not incorporated in the Zanoni model.

$$\alpha_{\text{Zanoni}} = \begin{cases} e^{0.01\phi - 15.25} & \text{in crumb} \\ e^{0.0062\phi - 15.30} & \text{in crust} \end{cases} \tag{13}$$

Simultaneous Heat and Mass Transfer Using LBM

Considerations of coupled heat and mass transfer phenomena must be achieved simultaneously, since decoupling would result in lagged, incoherent time-response modelling. Coherently, Luikov[17] showed that the moisture transport inside a material may result from a significant thermo-gradient, concluding the contribution of both mass and heat in the transport of each other concurrently.

In this work, the lattice Boltzmann method is used to model such a simultaneous heat and mass transfer case. In the last two decades, extensive work has been developed in the (LBM), the method has received significant attention as an alternative for simulating complex flow phenomena.[18] Based on a previously developed code published by Hussein,[7–9] the model was further enhanced to include

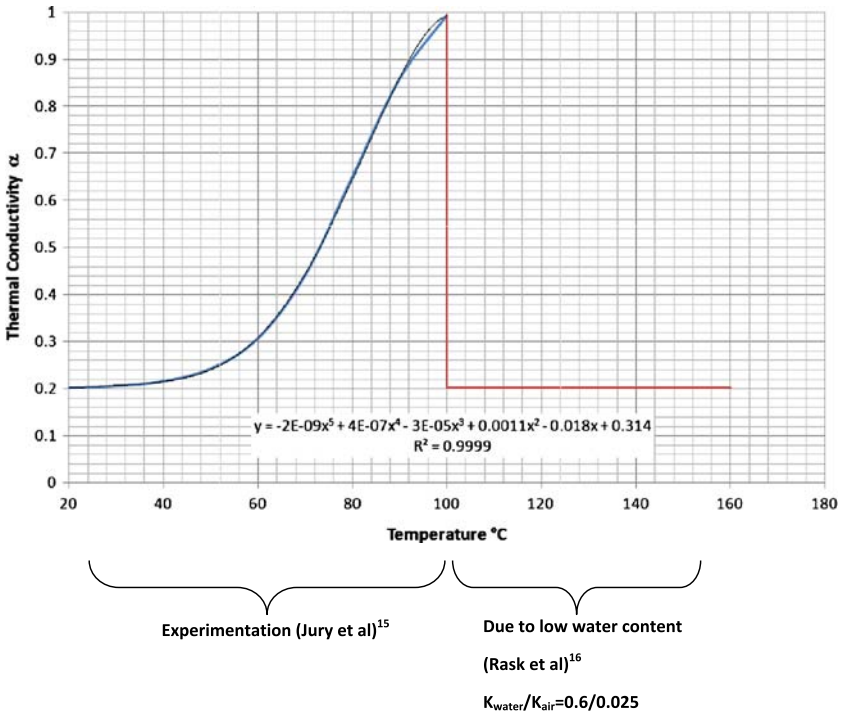

Fig. 6 The first part of the thermal conductivity curve is obtained from experimentation made by Jury[15] and shows an increase in conductivity with temperature. The *second part* of the *curve* represents the conductivity in the crust; this drop is due to the fall of the water content in the crust which resembles a dive in the conductivity. The conductivity falls to 0.2 [W/m2°K] which was predicted in literature (Rask)[16]

thermal effects. This work is considered as an innovative approach for the micro-modelling of simultaneous heat and mass transfer in such a complex hygroscopic system as dough.

The conventional Boltzmann's Eq. 14 relates the particle distribution f per unit time in a certain lattice to the propagation motion and collision. The presence of numerous particles makes a statistical treatment an obligation.

$$\frac{\partial f}{\partial t} + u.\nabla f = \Omega \tag{14}$$

The equation expresses the evolution of the particles with time. In a three-dimensional (3-D) lattice of several unit vectors, the particle dynamics equation can be satisfied on each direction independently. Hence, the equation could be written for each direction vector denoted by i choosing the D3Q19, means 19 velocity directions representing the 3-D lattice as in Figure 8.

The collision term of molecules basically predicts the influence of the collision on the particle distribution functions in each of the 19 directions and accounts for positive or negative influence in each direction. This operator has been approximated by Koelman,[6] using the

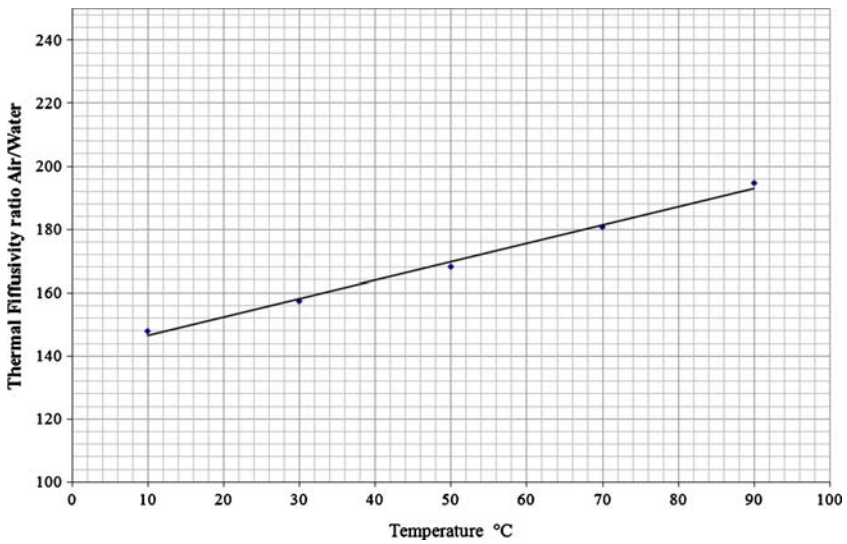

Fig. 7 Water and air have diverse thermal diffusion coefficients which vary with temperature. Air diffuses two orders of magnitude higher than water

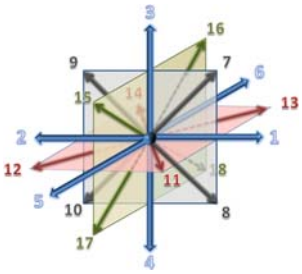

Fig. 8 D3Q19 model for higher precision, which resembles 19 velocity directions representing the 3-D lattice

Bhatnagar–Gross–Krook model, also known as single relaxation time (SRT) model.

$$\Omega_i = -\frac{1}{\tau_r}\left(f_i - f_i^{(\mathrm{equ})}\right) \tag{15}$$

Equation 15 can be explained using Figure 9: The collision of particles is considered as a relaxation towards a local equilibrium distribution, f^{equ}, and taking relaxation time, τ_r. The reciprocal of the relaxation time, $1/\tau_r$, may be replaced by the relaxation frequency, ω, sometimes referred to as the relaxation parameter. The collision of particles is considered as a relaxation towards a local equilibrium distribution and taking relaxation time, τ_r. Normally, the local equilibrium distribution takes the Maxwellian distribution form:

$$f_i^{\mathrm{equ}} = w_i \Psi(r)\left[1 + 3\frac{\hat{e}_i.u}{c^2} + \frac{9}{2}\frac{\left(\hat{e}_i.u\right)^2}{c^4} - \frac{3}{2}\frac{u^2}{c^2}\right]. \tag{16}$$

In Eq. 16, $\hat{e}_i$ is the unit vector in the ith direction; u is the local (macroscopic) velocity; $\Psi(r)$ is the local physical property; c is the basic lattice speed which determines the rate at which the physical property propagates to the next lattice, and usually taken as 1. Whereas, the weighting factor w_i is specified in Table 2.

Assuming that mass and heat transfer inside the domains only occur by means of mass and thermal diffusion,

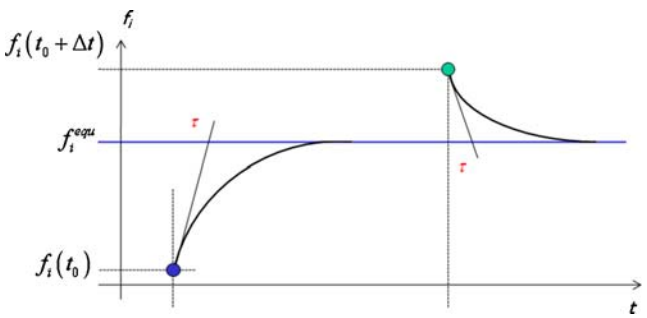

Fig. 9 The collision of particles is considered as a relaxation towards a local equilibrium distribution *f*equ and taking relaxation time (τ)

Table 2 Values of weighting factors according to the unit directions

Direction $\hat{e}_i$	w_i
0	1/3
1,2,3,4,5,6	1/18
7,8,.....,18	1/36

respectively. This is an acceptable assumption in non-advective ($u=0$) heat and mass transfer systems. Therefore, the equilibrium distribution of the temperature and moisture content takes a simpler form:

$$f_i^{\mathrm{equ}} = \begin{bmatrix} T_i^{\mathrm{equ}} \\ C_i^{\mathrm{equ}} \end{bmatrix} = w_i \begin{bmatrix} T \\ C \end{bmatrix} \tag{17}$$

The local Temperature and water content can be expressed as follows, respectively:

$$T = \sum_i T_i \; ; \; C = \sum_i C_i \tag{18}$$

It was convenient to assume the absence of evaporation–condensation in this preliminary model due to the highly heated surrounding in oven interior, measurement recordings suggest temperatures of an average 200±10°C. The consequence of this will reflect on the temperature and the moisture phase change. Since heat is gained and lost by condensation and evaporation, respectively. In order to increase the accuracy of the model further work should be done to incorporate this mechanism. Therefore, in a simultaneous heat and mass transfer system lacking the evaporation–condensation model, lattice Boltzmann equation using SRT can be rewritten in vector form as:

$$\begin{aligned} &\tfrac{\partial f_i}{\partial t} + \upsilon.\nabla f_i = \Omega_i \\ &f_i = \begin{bmatrix} T_i \\ C_i \end{bmatrix}; \Omega_i = \begin{bmatrix} -\frac{1}{\tau_T}\left(T_i - T_i^{\mathrm{equ}}\right) \\ -\frac{1}{\tau_C}\left(C_i - C_i^{(\mathrm{equ})}\right) \end{bmatrix} \end{aligned} \tag{19}$$

Where T is the particle temperature; C is the local water content (whether vapour or liquid); τ_c is the (water content) mass relaxation time, and τ_t is the (temperature) thermal relaxation time.

The relation between the molecular diffusion coefficient and the mass relaxation time was given by Wolf–Gladrow.[19] Similarly, the thermal diffusivity relation to the thermal relaxation time could realised in a similar fashion, as seen in Eq. 20.

$$D = \frac{1}{6}(2\tau_c - 1); \alpha = \frac{1}{6}(2\tau_T - 1) \tag{20}$$

To be more precise, the mass relaxation time in the concentration Lattice equation is determined by the

effective molecular diffusion coefficient for the corresponding system as:

$$\tau_C = 3D_{\text{eff}} + \frac{1}{2} \tag{21}$$

Similarly, the thermal relaxation time can be related to the thermal diffusivity such that:

$$\tau_T = 3\alpha + \frac{1}{2} \tag{22}$$

For stability considerations, the absences of the advective terms have made it convenient to use the SRT model which produces independent Eigen value for each equation on its own without any energy unbalances in the equations. Thus, for a stable solution, both relaxation times should be greater than 0.5.

$$\lambda_C = 1 - 1/\tau_C;\ \lambda_T = 1 - 1/\tau_T \rightarrow \left|\lambda_{C,T} < 1\right| \rightarrow \tau_{C,T} \geq 0.5 \tag{23}$$

Conversion between Physical Domain and Lattice Domain

For the model to deliver results in the realistic domain, a similarity analysis must be achieved; this takes two major parts: geometric and dynamic. While the geometry may be simply scaled, the dynamic parameters may be related through the non-dimensional parameter, Fourier number (*Fo*), which is the ratio of heat conduction to the rate of thermal energy storage. The Fourier number can also be defined for transient mass transfer by diffusion, respectively, in Eq. 24.

$$Fo_T = \frac{\alpha \cdot t}{L^2} or Fo_C = \frac{D \cdot t}{L^2} \tag{24}$$

Such that, any two different diffusion problems having the same Fourier number are equivalent. Therefore, it is possible to solve the Lattice Boltzmann equation in lattice units and relate the results with a physical flow that possesses the same Fourier number and the same flow geometry. From the modelling side, the characteristic length L_{LU} is chosen and therefore known in Lattice Units. Considering that the mass diffusion coefficient in lattice units D_{LU} is calculated from Eq. 20 once a relaxation time is chosen for the simulation.

$$t_{LU} = \frac{Fo_C \cdot L_{LU}^2}{D_{LU}} \tag{25}$$

Table 3 The second norm of several published results of the Gaussian pulse problem compared with LBM (this work)

Method	L^2 norm error
Noya[20]	1.24E-04
Kalita[21]	1.02E-04
Karaa[22]	5.62E-05
LBM (this work)	1.78E-09

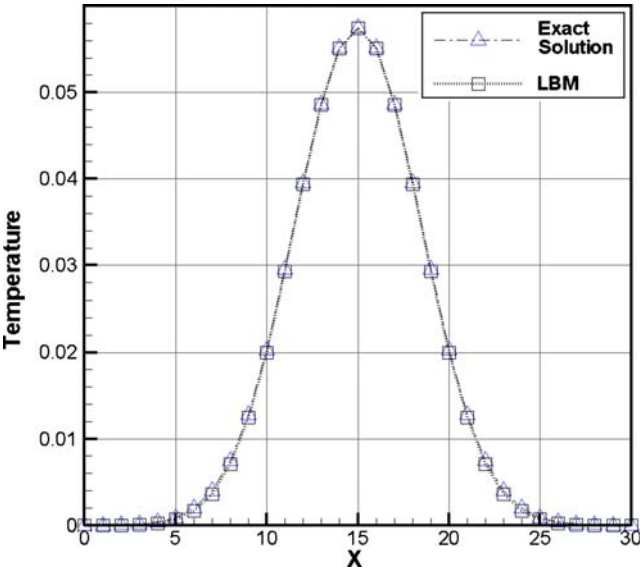

Fig. 10 The decayed-pulse thermal distribution for the exact solution provided by the Gaussian Eq. 18 as *open square* points, and the LBM results as the *dotted line* with *open triangle* markers. An almost identical curve is seen

After calculating t_{LU}, the main conversion factors are calculated to relate any physical quantity to its value in lattice units.

$$\text{Variable} = \text{Conversion}_{\text{fact}} \times \text{Variable}_{\text{LU}} \tag{26}$$

For example, the conversion factors for some basic quantities such as length in metres, time in seconds and mass in kilogrammes which is fixed for convenience to 1 g per 1 lattice mass are listed below.

$$L_{\text{fact}} = \frac{L}{L_{\text{LU}}}$$
$$t_{\text{fact}} = \frac{t}{t_{\text{LU}}} \tag{27}$$
$$1\ \text{Lattice mass} = 0.001\ Kg, M_{\text{fact}} = 0.001$$

With the same method, any other variable can be transferred from the lattice domain to the real physical domain or vice versa through a conversion factor calculated from a combination of the basic conversion factors for the basic quantities.

Finally, in order to preserve the time ratio between the thermal heat transfer and the thermal conduction the dimensionless Biot number is conserved between the lattice domain and the physical domain as well like the Fourier number, as mentioned earlier.

$$Bi = \frac{h \cdot L}{K} = \frac{h_{\text{LU}} . L_{\text{LU}}}{K_{\text{LU}}} \tag{28}$$

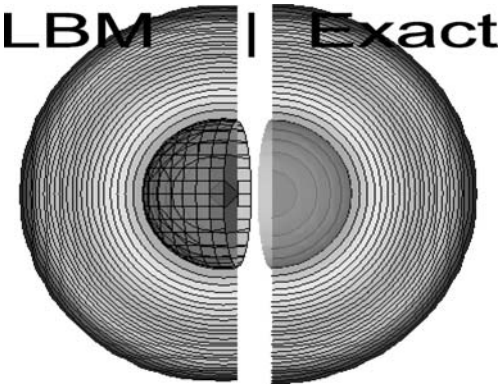

Fig. 11 Isothermal surfaces of the exact solution and the LBM solution, where the LBM isotherms are on the *left* and the exact are on the *right*

Results and Discussion

The results are divided into three parts: To start with, the thermal solver is validated with a dynamic benchmark; In the second part, thermal investigations of the dough were performed, taking into considerations the microstructure of the dough while using the complex physical properties of dough mentioned in the previous section; Finally, a full baking model of dough is investigated while considering the simultaneous heat and mass transfer with all the dynamically varying properties, except the void thermal expansion, which will be considered in future work.

Thermal Solver Validation

The thermal diffusion LBM was validated with the well-reported benchmark proposed by Noye.[20] The problem describes the diffusion of an initial Gaussian pulse initiated inside a rectangular domain with $x \in [0,2], y \in [0,2]$ and $z \in [0,2]$. The pulse is advected and damped along a straight line with constant velocity. The initial pulse is described as:

$$C(x,y,z,0) = \exp\left(\frac{-1}{D}\left((x-x_0)^2 + (y-y_0)^2 + (z-z_0)^2\right)\right) \quad (29)$$

The three-dimensional analytical solution takes the exponential decaying form:

$$C(x,y,t) = \frac{1}{4t+1}\exp\left(-\frac{1}{D(4t+1)}\left((x-Ut-x_0)^2 + (y-Vt-y_0)^2 + (z-Wt-z_0)^2\right)\right) \quad (30)$$

Where D is the diffusion coefficient; t is the time; U, V and W are the 3-D velocity components and x_o, y_o *and* z_o are the starting centre of the initial pulse. The initial pulse was centred at $(x_0, y_0, z_0) = (0.5, 0.5, 0)$ with a pulse height of 1. The diffusion coefficient in both x and y direction was chosen to be $D = D_{x,y,z} = 0.01$ The pulse moves with velocity $U = V = W = 0.8$. The problem was solved with the LB diffusion solver, and the results compared with the exact solution, Eq. 30. The results are compared at t=1.25 using the second norm, Eq. 31, an average error of 1.78 E-09 is achieved, the results of the LBM code has reached more accurate results when compared to published results: Noye,[20] Kalita[21] and Karaa.[22] Table 3 shows the different published results, this

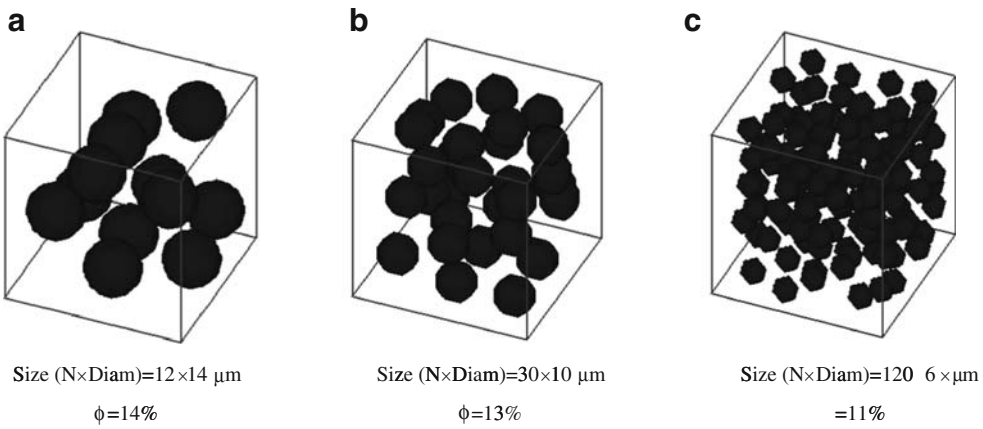

Fig. 12 **a-c** Dough samples of slightly different porosity have been investigated, while subjected to constant temperature boundaries of 200 °C. Cubic samples of similar size, 55 μm, but different porosity

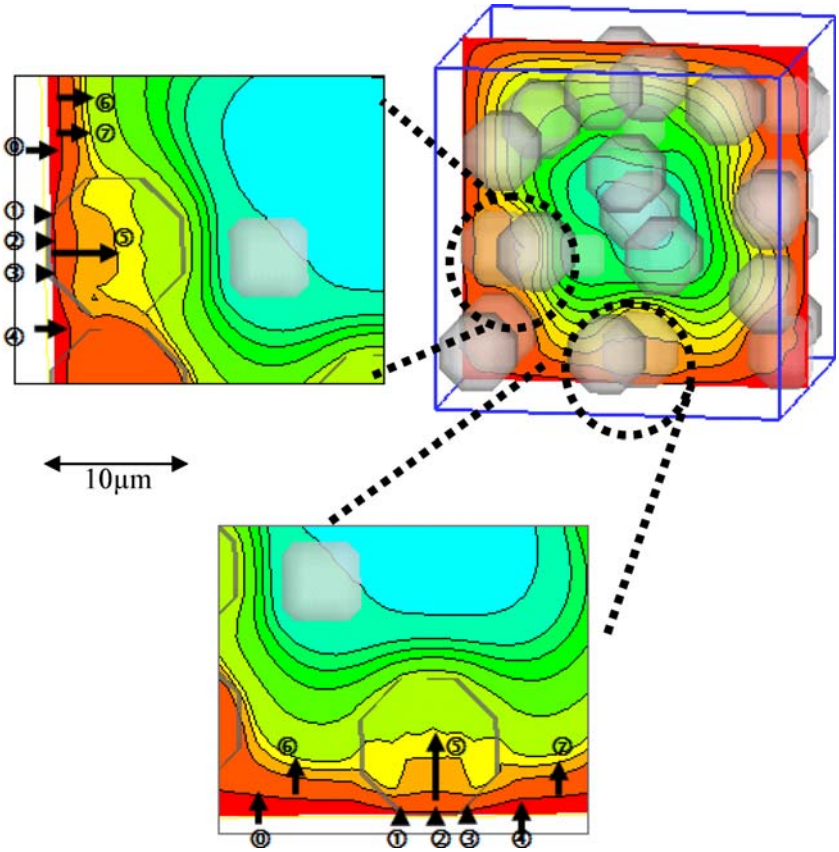

Fig. 13 *Arrows* (①②③) correspond to the thermal heat transfer when an air bubble is touching the hot surface; whereas *arrows* (⓪④) correspond to the transfer when water is the conducting medium; *arrows* (⑤) correspond to the heat diffusion inside the air bubbles; *arrows* (⑥⑦) correspond to the diffusion inside water

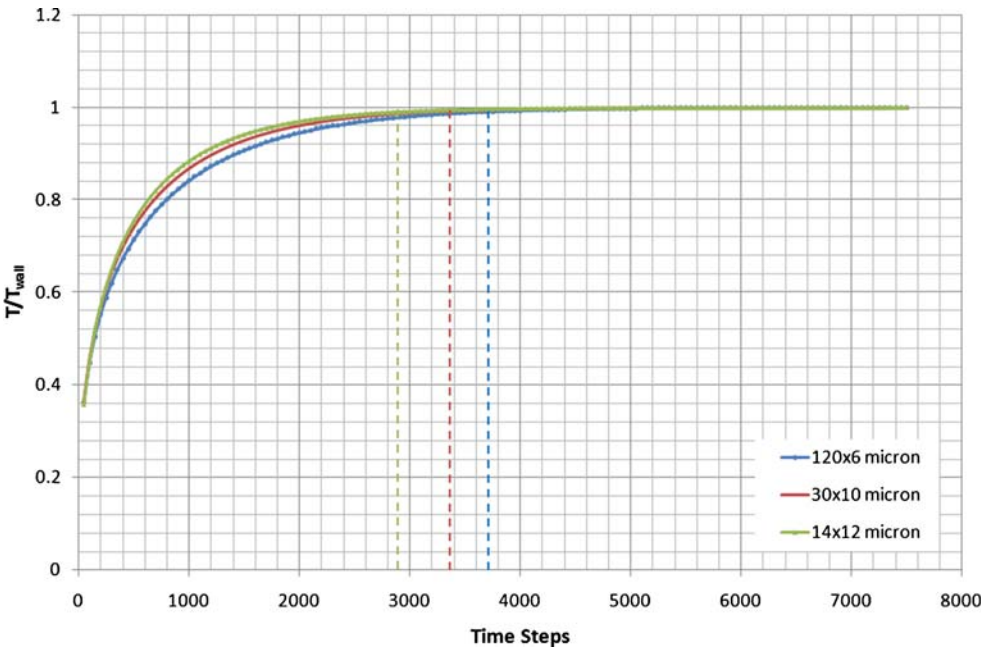

Fig. 14 Different porosity was investigated; the samples were simulated until the entire domain had at least 99% of the boundary temperature [boundary layer temperature, (BLT)]

Table 4 Different porosity was investigated and when the timings to reach the BLT were recorded for the different porosities

Porosity (%)	Time LU	Time real (s)	Time ×(Vreal/Vsample)
11	3,650	7.3E-03	25
13	3,150	6.3E-03	21.57
14	2,850	5.7E-03	19.52
16	2,555	5.1099E-03	17.5

work has produced four to five orders of magnitude lower error.

$$L_2 = \|\varepsilon\|_2 = \sqrt{\sum \left| C_i^{\mathrm{LBM}} - C_{\mathrm{Exact}}^{i} \right|^2} \tag{31}$$

Figure 10 shows the decayed-pulse thermal distribution for the exact solution provided by the Gaussian Eq. 30 as square (□) points and the LBM results as the dotted line with triangle (△) markers. Obviously, both are almost identical. Additionally, the isothermal surfaces of both are surfaced in Figure 11, where the LBM isotherms are on the left and the exact are on the right.

The mass transport validation has been extensively published in previous work of the authors Hussein,[7–9] where both diffusive and convective transports models have been deeply investigated.

Investigation of Thermal diffusion in the Dough Microstructure

Dough samples of slightly different porosity have been investigated while subjected to constant temperature boundaries of 200°C. Cubic samples of similar size 55 μm but different porosity: 14%, 13% and 11%, which was achieved by changing virtually the number of bubbles and their sizes in the simulation; all three types are listed in Figure 12a–c.

The porosity values were carefully chosen to understand what minor changes have on the overall temperature response.

Different thermal diffusivity for the crumb, crust and air bubbles was used in Eqs. 11–13. Air has a better thermal diffusivity than water; air spreads around two orders of magnitude quicker than water. On the microscale, this resembles quicker or slower heat spreading depending whether more or less air bubbles exist, respectively, next to the hot boundaries. On the other hand, water has very good heat-conductive properties, but weak heat spreading properties, which makes it more complicated to understand the overall heat transfer. Figure 13 provides a detailed explanation of the combined phenomenon occurring: Arrows (①②③) correspond to the thermal heat transfer when an air bubble is touching the hot surface, whereas arrows (⓪④) correspond to the transfer when water is the conducting medium; arrows (⑤) correspond to the heat diffusion inside the air bubbles; arrows (⑥⑦) correspond to the diffusion inside water.

This means that, if water is the surface conducting material, a higher temperature profile occurs on the boundary unlike the air, and once an air bubble is crossed, it transfers the heat quicker. In conclusion, water is a better conductor (five times better as seen in Figure 6) and air is a better diffusion medium (100 times better, estimated from Figure 5). Therefore, heat energy can be reduced by increasing the porosity, coherently on the account of the water content which will act as a limitation to this reduction, further work has to be done in this aspect.

On the whole, the contribution of the different porosity was investigated; the samples were simulated until the entire domain had at least 99% of the boundary temperature [boundary layer temperature (BLT)] (Figure 14).

In general, this testing shows on a macroscale the different combination for the previous part. The test shows that 14% porosity reaches BLT after 3150 times step (21.6 min); the results were scaled up with the help of a simulation made for a dough sample of 20×20×20 cm and an average porosity of 16%. The contribution of the different porosity (11–16%) on the heating time is seen in Table 4.

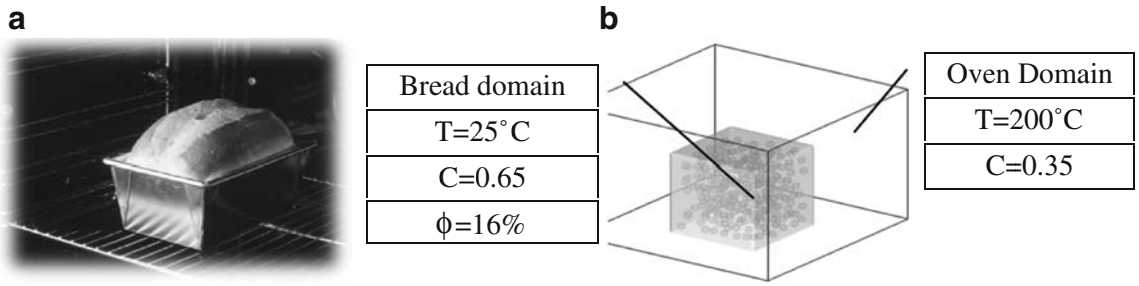

Fig. 15 **a** The coupled SHMT problem was solved in a small baking oven with cubic bread box. **b** Definition of the numerical domains: the bread domain is a cubic bread of size 20×20×20 cm has approximately 300 bubbles inside with an average porosity of 16%. The moisture content of bread at start is 0.65, and the oven has a general moisture content of 0.35 and a preheated temperature of 200°C

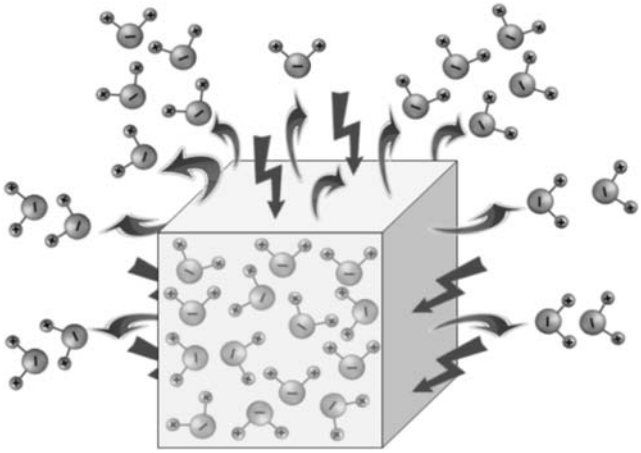

Fig. 16 As heat transfer exhibits from the hot oven surrounding to the bread, moisture diffuses out from the bread domain to the oven

From the results, it is obvious that porosity plays an important role in the heat transfer, thus, it could be surely said that, on a macroscale, the higher the porosity the higher the heat transfer.

The only weakness of this model is the involvement of the bubbles-structure volumetric expansion due to thermal expansion, in ideal gases the expansion may be assumed proportional to $1/T$. Further work should be done to include the thermal volume expansion of bubbles.

Investigation of SHMT in Dough

The coupled SHMT problem was solved in a small baking volume which has a cubic bread inside with the size of 20× 20×20 cm. The bread domain had approximately 300 bubbles inside of an average porosity of 16%. The simulation includes moisture content mass transfer and thermal diffusion between the oven internal environment and the bread. The moisture content of bread at start is 0.65, and the oven has a general moisture content of 0.35 and a preheated temperature of 200 °C.

The problem includes thermal conduction and diffusion, both convectional and radiation heat transfers are excluded in this model. The thermal interface between the bread domain and the oven is achieved by conduction. Additionally, moisture diffusion in the oven and in the bread domain is modelled as well; the transfer between the two parts is achieved by means moisture flux which has a dependency on the partial vapour pressures. The oven domain and the bread domain are seen in Figure 15a–b, the bubble distribution is seen in the figure as well.

As heat transfer exhibits from the hot oven surrounding to the bread, moisture diffuses out from the bread domain to the oven, as explained in Figure 16. The overall moisture flux proceeds until an overall equilibrium between moisture in oven volume and in bread volume, since the moisture flux functions in the moisture difference by means of vapour pressure. Another consequence of the moisture transfer between the coupled domains is the heat conduction in presence of water (moisture). As discussed earlier, water conducts heat much better than air, thus the providences of steam in the interface acts as an efficient coupling agent. The weaker thermal diffusivity of water in the dough structure presents the bread, as well, with more time to cook and coagulation of the gluten matrix.

With an un-detailed look, man can say bread baking is a daily job since ancient the time of the Egyptians, but considering all the thermo-physics persisting that reveal a highly sophisticated problem which was only achieved in the past by experience, trial and error.

The average water content time response in the bread domain is monitored; a steady linear decline with an average slope of 0.0146[min^{-1}] and the moisture flux equilibrium with the oven domain is reached at 19 min. In comparison,

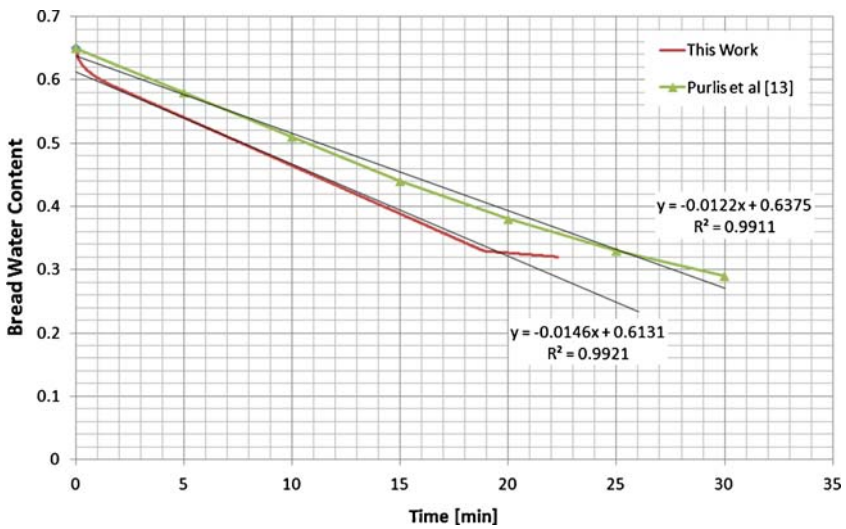

Fig. 17 Bread dehydration profile: The average water content time response in the bread domain is monitored, a steady linear decline is spotted and the moisture flux equilibrium with the oven domain is reached at 19 min. In comparison, the published experimental work of Purlis et al.[13] show the estimated equilibrium time to be between 25–30 min

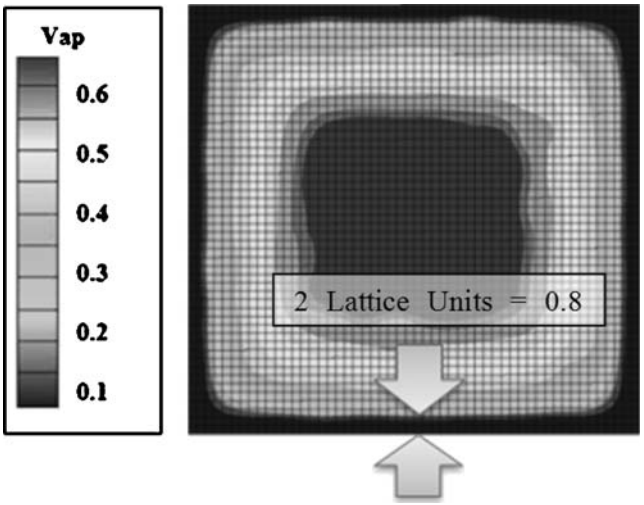

Fig. 18 The crust thickness can be numerically predicted by locating the region in the bread in vicinity of the interface which is almost depleted from moisture content, i.e. $C \approx 0.1$

the published experimental work of Purlis et al. shows as well a linear decrease in moisture content but with an average slope of 0.0122[min^{-1}] and the estimated equilibrium time to be between 25–30 min (Figure 17).

The deviations could be due to the smaller-sized oven used in the model which subjects the sample to a higher heat flux, thus heating it more and hydrating it more. Also, the fact that the results lack the modelling of evaporation–condensation, the outcome of this will reflect on the temperature and the moisture phase changes since heat is lost by evaporation. Also, the deficiency of not having a thermal expansion may have resulted into a higher heat flux in this work, since the flux will decrease slightly as the volume increases as they are inversely proportional. Nevertheless, the model has achieved to produce a similar trend for the SHMT of the bread problem. Additionally, investigation of crust thickness supports this idea as mentioned below.

Bread crust is the interfacial area between the bread and the oven, a lot of thermo-physics occur in it, such as: the conduction of the heat; the transport of the moisture flux to the oven; the strong tensional forces due to overpressure from the internal expansion of the gas cavities; the inability of the contained gases in the crust to expand due to the hardness of the crust from the continuous dehydration of the region; the caramelization of the un-fermented sugars. The crust thickness can be numerically predicted by locating the region in the bread in vicinity of the interface which is almost depleted from moisture content, i.e. $C \approx 0.1$.

The simulated crust development has shown a crust thickness of 0.8 cm (Figure 18), which is a bit higher than similar experimental results in Purlis,[12, 13] (see Table 5); both of which reported a dehydrated thickness of 0.5–0.6 cm. The crust over-estimation in this work fits to the overheating occurring in the model as mentioned earlier.

Conclusion

Bread baking is a very difficult problem to model; with an un-detailed look, man can say that bread baking is a daily job since ancient Egyptians, but considering all the thermo-physics persisting revealing a highly sophisticated problem which was only achieved in the past by experience, trial and errors.

This work represents an innovation in the modelling of SHMT problems within complex mediums such as dough, where the microscale dynamics was introduced by means of Boltzmann methods.

Several thermo-physical properties of dough were discussed based upon literature and modifications introduced by the authors of this work for the crumb–crust–bubble systems, such as: hygroscopic, porosity, constrictivity and tortuosity, diffusivity both thermal and molecular and flux transport.

As shown in this work and in literature, the moisture content difference between the oven internal environment and the moisture in the bread is the moisture flux driving force. This can be tuned by changing the oven humidity by steam spraying. Apparently, humidity tuning resembles better thermal conductivity and softer, cooked end product.

Stability analysis for the SHMT problem in absence of the viscous terms, which is an acceptable assumption in non-convective heating chambers, and for computational convenience, the SRT model which produces independent Eigen value for each equation on its own without any energy unbalances was adopted. The solver was benchmarked as well reporting an average error of 1.78 E-09, which is four to five orders of magnitude more accurate than similar solvers published.

From the results, it is obvious that two important mechanisms occur: heat transfer exhibits from the hot oven surrounding to the bread; and moisture diffuses out from the bread domain to the oven. The overall moisture flux proceeds until an overall equilibrium between moisture in oven volume and in bread volume, since the moisture flux is function in the moisture difference by means of vapour pressure. Another consequence of the moisture transfer

Table 5 The simulated crust development has shown a crust thickness of 0.8 cm, which is a bit higher than similar experimental results (Purlis et al., Salvadori et al.), both of which reported a dehydrated thickness of 0.5–0.6 cm

	Achieved dehydrated thickness
Crust thickness (Purlis)[12, 13]	0.5–0.6 cm
Crust thickness (this work)	0.8 cm

between the coupled domains is the heat conduction in presence of water (moisture). As shown earlier, water conducts heat much better than air, thus the providences of steam in the interface acts as an efficient coupling agent. The weaker thermal diffusivity of water in the dough structure presents the bread with more time to cook and coagulation of the gluten matrix as well.

This resembles quicker or slower heat spreading depending whether more or less air bubbles exist, respectively, next to the hot boundaries. On the other hand, water has very good heat-conductive properties but weak heat spreading properties, which makes it more complicated to understand the overall heat transfer process. Revealing the possibilities of reducing energy consumed by increasing the porosity—this is expected to be greatly limited due to water content reduction which will act as a limitation to this optimization—further work has to be done in this aspect.

Further work should be done to reduce the discrepancies seen for the dehydration profile of bread with experimentation, which could be due to the smaller-sized oven used in the model which subjects the sample to a higher heat flux, thus heating it more and hydrating it more. Also, the fact that the results lack the modelling of evaporation–condensation, the outcome of this will reflect on the temperature and the moisture phase change since heat is lost by evaporation. Also, the deficiency of not having a thermal expansion may have resulted into a higher heat flux in this work, since the flux will decrease slightly as the volume increases as they are inversely proportional. Nevertheless, the model has achieved the production of a similar trend for the SHMT of the bread problem. Additionally, investigation of crust thickness supports the results.

Finally, the dough heat and mass transfer have been addressed in this work with a lot of restrictions due to the complexity of the medium and the limited literature addressing the dough medium from the microscale thermo-physical point of view. The authors believe that, although the bread baking is considered by the public as a trouble-free process, nevertheless, its complexity is doubtless, and careful investigation on the process might save the world community valuable resources.

References

1. P. Sluimer, C.E. Krist-Spit, in *Heat transport in dough during the baking of bread*, ed. by I.D. Morton (Cereals in a European Context, New York, VCH, 1987), p. 355–363.
2. U. De Vries, P. Sluimer, A.H. Bloksma, A quantitative model for heat transport in dough and crumb during baking, Asp, N. G. Cereal science and Technology in Sweden. Proceedings of an International Symposium 13–16 June, Ystad, Sweden pp 174–188 (1989).
3. K. Thorvaldsson, H. Janestad, A model for simultaneous heat, water and vapour diffusion. J Food Eng **40**, 167–172 (1999)
4. M. Lostie, R. Peczalski, J. Andrieu, M. Laurent, Study of sponge cake batter baking process. II. Modeling and parameter estimation. J Food Eng **55**, 349–357 (2002)
5. F.J. Higuera, J. Jiménez, Boltzmann approach to lattice gas simulations. Europhys Lett **9**, 663–668 (1989)
6. J.M.V.A. Koelman, A simple lattice Boltzmann scheme for Navier–Stokes fluid flow. Europhys Lett **15**, 603–607 (1991)
7. M.A. Hussein, G. Baumann, A. O. Sherif, S. Esterl, T. Becker, On the Validation of a 2-D Laminar Flow Solver Using Lattice Boltzmann Method, Procee. Of The 8th Int. Cong. on Fluid Dynamics and Propulsion, ASME, Sharm el Sheikh,(2006) ICFDP8-EG 200
8. M.A. Hussein, S. Esterl, R. Poertner, K. Wiegandt, T. Becker, Impulse and mass transport in a cartilage bioreactor using the Lattice Boltzmann method. Int. J. comput fluid dyn **22**(5), 341–350 (2008)
9. M.A. Hussein, S. Esterl, R. Poertner, K. Wiegandt, T. Becker, On the Lattice Boltzmann method simulation of a two phase flow bioreactor for artificially grown cartilage cells. J Biomech **41**(16), 3455–3461 (2008)
10. I. Lind, C. Rask, Sorption isotherms of mixed minced meat, dough, and bread crust. J Food Eng **14**, 303–315 (1991)
11. J. Zhang, A.K. Datta, Mathematical modeling of bread baking process. J Food Eng **75**, 78–89 (2006)
12. E. Purlis, V.O. Salvadori, Bread baking as a moving boundary problem. Part 2: Mathematical modelling. J Food Eng **91**, 428–433 (2009)
13. E. Purlis, V.O. Salvadori, Bread baking as a moving boundary problem. Part 2: model validation and numerical simulation. J Food Eng **91**, 434–442 (2009)
14. B. Zanoni, S. Pierucci, C. Peri, Study of the bread baking process. II: mathematical modeling. J Food Eng **23**, 321–336 (1994)
15. V. Jury, J.Y. Monteau, J. Comiti, A. Le-Bail, Determination and prediction of thermal conductivity of frozen part baked bread during thawing and baking. Food Res Int **40**, 874–882 (2007)
16. C. Rask, Thermal properties of dough and bakery products: a review of published data. J Food Eng **9**, 167–193 (1989)
17. A.V. Luikov, Systems of differential equations of heat and mass transfer in capillary-porous bodies (review). Int J Heat Mass Transfer **18**, 1–14 (1975)
18. G. Mcnamara, G. Zanetti, Use of the Boltzmann equation to simulate Lattice-gas automata. Phys Rev Lett **61**, 2332–2335 (1988)
19. D. Wolf-Gladrow, Lattice–gas cellular automata and Lattice Boltzmann Models, Springer-Verlag Telos, 2000.
20. B.J. Noye, H.H. Tan, Finite difference methods for solving the two dimensional advection-diffusion equation. Int J Num Methods Fluids **26**, 1615–1629 (1988)
21. C. Kalita Jiten, D.C. Dalal, K. Dass Anoop, A class of higher order compact schemes for the unsteady two-dimensional convection-diffusion equation with variable convection coefficients. Int J Numer Methods Fluids **38**(12), 1111–1131 (2002)
22. K. Samir, J. Zhang, High order ADI method for solving unsteady convection-diffusion problems. J Comput Phys **198**(1), 1–9 (2004)

4. Conclusion & Outlook

This thesis has addressed two biotechnological applications.

1. *Modelling of biological, chemical and dynamic activity of cells*
2. *Micro-Macro Modelling of Heat and moisture transfer in food foams: Dough*

Both problems were investigated in a detailed fashion, with a trial to tackle all the necessary sophistications mentioned in chapter-1,2 and 3. The problems show a similar environment of porous medium under different physical effects. The challenges met are of scientific importance in both applications and achievements were only made possible using a multidisciplinary investigation which addressed every detailed complexity by the integration of different scientific approaches, from biology, chemistry, engineering to medical. The development of a validated three dimensional Lattice Boltzmann model which tackled those phenomena in the micro and macro scale made these investigations possible. The model used provided an accurate efficient tool, enabling the possibility of studying different cases, revealing more understanding and experience of the addressed problems.

4.1 Modelling of biological, chemical and dynamic activity of Cells

It is quite complicated to understand and predict the dynamics of living science, it's complexity has always hindered researchers and blocked their way to understand, evaluate and optimize such processes. The complexity arises from the non-homogeneity, chaotic order and non-linearity in behaviour. Several obvious examples prevail to show this, such as: The kinetics of active cells such as Osteoblast-cells is usually assumed to follow similar trends to the Michaels –Menten kinetics, which usually is not the case if exists any spatial or nutritional constrictions to the cells. Since scientist tends to inadequately assume linearity in systems, they are never able to see such complicated systems as ordered. As well the order of such processes depends greatly upon whether the correct spatial scale is used to monitor the process or not. Such as modelling microscale phenomenon using macroscale tools, for example modelling the eddies in a stirrer reactor of 20 cm diameter, using a coarse grid of minimal size of 5 cm, or modelling a reaction which occurs in the days-scale using a micro scale. In this work investigations were made in contrary to such ideas, where a higher Spatio-temporal resolution monitoring of such biological activities is held. Combination of different effects on the process achieved a more general prediction rather than the traditional approaches with heaps of simplifications and assumptions.

Two types of cells were considered: Cartilage cells and bone cells (Osteoblasts). The work focused mainly on the cell substrate consumption rates under limiting conditions and the estimation of stress levels subjected to the cells with the consequential effect.

In this part two basic problems were addressed

- *What is the limiting factor in substrate transport, is it diffusion or advection?*

Since it is common that some bred cells in bioreactors die due to malnutrition or waste contamination, it is always necessary in every bioreactor to investigate the transport mechanism around such cell in the micro-scale dynamics as the process prevails in such scale. The transport process is be divided in to two parts advective transport and diffusive transport. The transport efficiency and diffusion efficiency, namely external and internal efficiency, are used to determine the dominance of each part in limiting the whole transport with respect to different Reynolds number and inlet concentrations.

The transport performance was estimated by calculating the transfer from the fluid to the active layer through the interface surface. This is achieved by calculating the integral of the kinetics term on the interface area using the concentration values on the surface, then once more with the inlet concentration value and then dividing them together which provides a solid measure for the transport limitation of the bioreactor. To evaluate the performance of the diffusion in the active layer alone without external effects, the area integral of the kinetic term is evaluated inside the active layer, using the concentration values in the active layer and then dividing it by the same term but using the values on the surface of the active layer revealing the evaluating the diffusion limitations inside the active layer. Both calculations allow the complete evaluation of a bioreactor performance due to geometry and dynamic effects. In order to get a feeling whether the diffusion or the transport is acting as a limitation to the substrate both efficiencies are subtracted such that:

$$\eta_{Difference} = \eta_{External} - \eta_{Internal},$$
$$\eta_{Difference} \begin{cases} > 0 & Diffusion\,Limited \\ = 0 & Equilibrum \\ < 0 & Transport\,Limited \end{cases} \qquad (4.1)$$

Thus if $\eta_{Difference}$ is greater than zero then the internal efficiency is less, which means it is more limiting the process and vice versa. Figure 4.2 shows a plot of $\eta_{Difference}$ versus Reynolds number for all cases of inlet concentration.

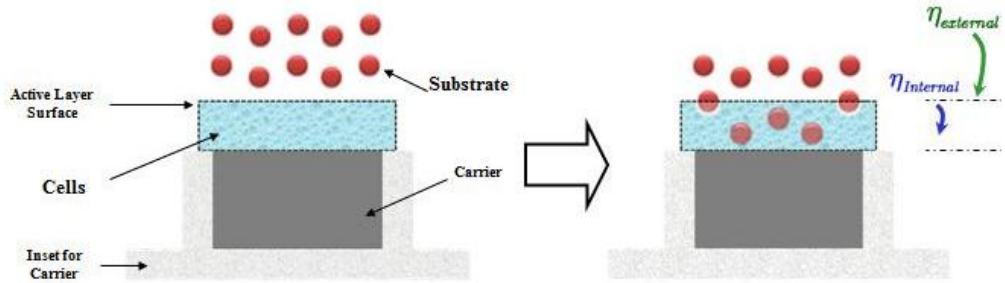

Figure 4.1: The substrate motion is divided into two parts : transport and diffusion namely external and internal motion, the efficiency of both kinds determine whether the process is transport limited or diffusion limited.

This investigation produces *'bioreactor performance map'* for a specific bioreactor which relates the different substrate concentration to the dynamics of the reactor and differentiating between each design conditions falling whether into a diffusion limited or advective limited zone.

All the data points above the equilibrium line are diffusion limited; obviously most of the points are transport limited except for some few points. It could be said that the lower the Reynolds number the more the process becomes diffusion limited. Furthermore, the higher the inlet concentration the more equilibrium the process is.

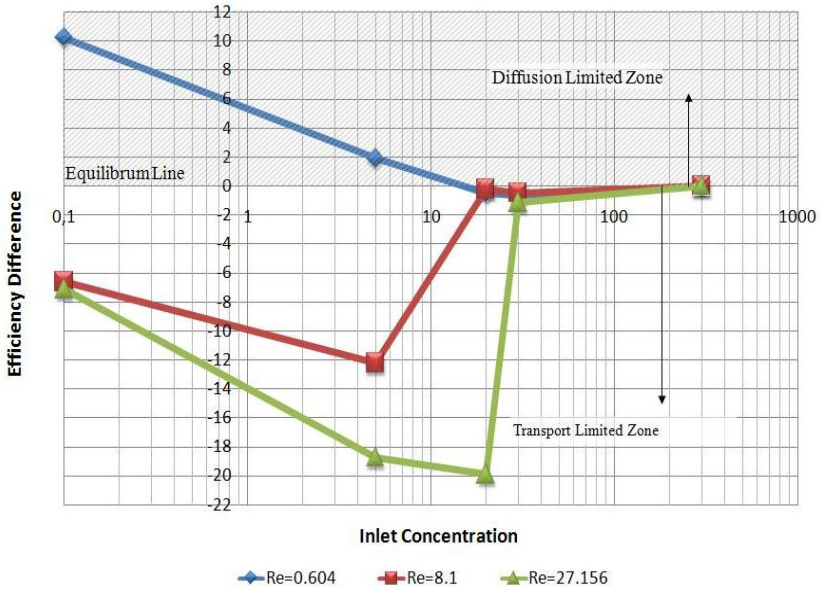

Figure 4.2: The plot of $\eta_{Difference}$ versus Reynolds number for all cases of inlet concentration. All the data points above the equilibrium line are diffusion limited; obviously most of the points are transport limited except for some few points.

The methodology can be applied in any bioreactor system, revealing a bioreactor (transport) performance chart such that from the tissue engineering point of view it would be of great help to understand much more the dynamic transport of their bioreactor at design and off-design conditions. Special attention was made on the providences of the correct nutrition in such transport reactors, both experimental and numerical work were carried for approving such levels. The activity of biological cells towards oxygen as these cells perform respiration was modelled. The oxygen transport inside the active layer was modelled by adding a sink term using the Michaels –Menten kinetics.

- *In the tissue matrix, there is no advective term, how is the substrate transported?*

Although that diffusion was always thought as the only mechanism with which the transport of molecules and ions is achieved across the endothelial layer of bone capillaries, diffusive mechanisms may not be sufficient to guarantee sufficient transport to and from osteocytes that are not in close neighbourhood of Haversian canals [58]. Theoretical investigations of

bone tissue diffusion coefficients shows values of order *O(10 μm/h)*, revealing great discrepancies in transport times towards individual osteocytes depending on their proximity towards Haversian capillary [59]. As well, the transport of large molecules through the tissue is highly dependent on tissue permeability, membranes and obstacles. Proving that the concept of free diffusion: as the major mechanism of nutrition exchange between the blood vessels and the bone tissue, is surely doubtful.

A rightful answer of the capable transport mechanism, which is able to cross all mentioned constrains, is the cyclic pressure gradient developed by physiological activity. Mechanical loading of bone tissue during physiological activity results in a tissue stress state comprising cyclic dilatational and deviatoric components. The effect of dilatation or pressure imposed by cyclically loading of bone tissue is the motor for fluid movement within tissue [58]. As well the oscillating high shear flow induced by the oscillating pumping mechanism provides the bone tissue with a stiffness education schedule, with which the bone tissue achieve its stiff-solid features. This reveals the necessity to enhance the diffusion coefficient by the inclusion of cyclic pressure driven diffusion coefficient. This may be updated as seen in figure 4.4.

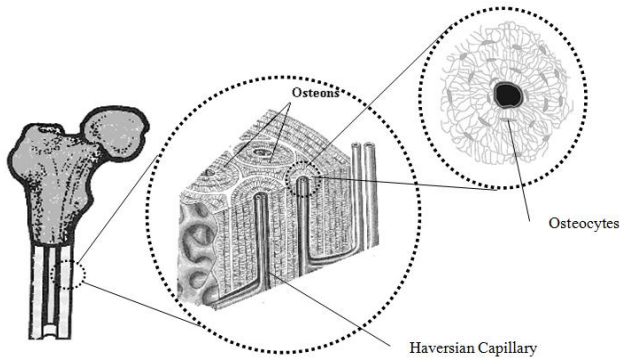

Figure 4.3: Dissection of a Femur bone, showing the Haversian channels containing the blood vessels and nerves.

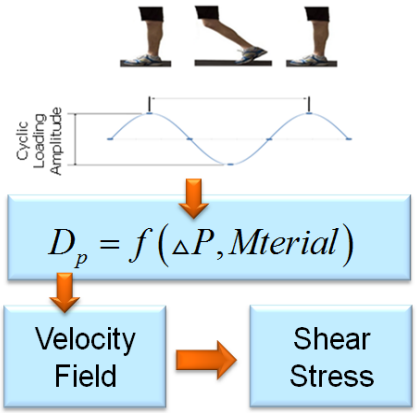

Figure 4.4: The proposed algorithm for the update of the diffusion coefficient D_p which is pressure dependent. The pressure variation could be obtained from the physiological activity of the human movement

- *Inadequacy in the cell uptake of substrate*

In this thesis monod-Michaelis-Menten kinetic model is used for simplifications and can be assumed in cases of simple kinetics, as it lacks substrate inhibition or limitations, product

inhibition or growth model. In the current status of literature [54-61], mostly a fixed value for the maximum substrate uptake is commonly used for modelling cell reaction kinetics. Although it has been often observed and described that it is not constant due to cell growth considerations. If the cell growth or the cell concentration is plotted with the cultivation time it is believed to follow a trend as in Figure 4.5 [57, 60-61]

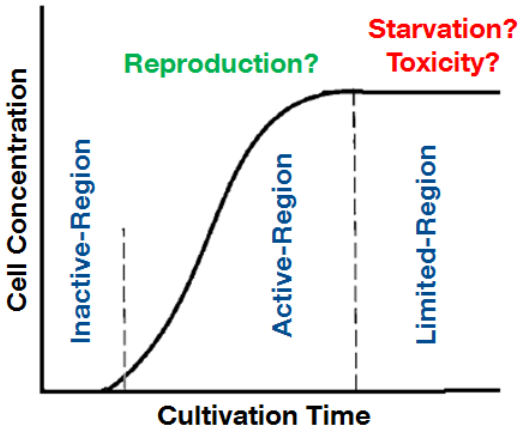

Figure 4.5: In the beginning the cells are majorly passing the inactive region. Later on when the cells have grown to a limit where the permeability, is very low limiting the substrate transport leading to starvation or toxicity due to reduced waste removal rate.

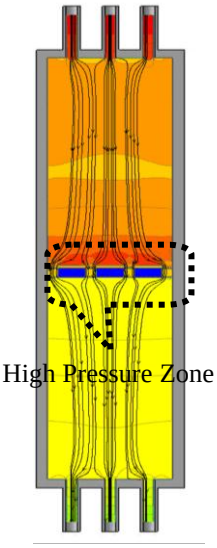

Figure 4.6: A reactor having a higher pressure field in vicinity of the cells, may have diffusion limitations especially on the reaction waste removal.

In the beginning the cells are majorly passing the inactive region. Later on when the cells have grown to a limit where the permeability, is very low limiting the substrate transport leading to starvation or toxicity due to reduced waste removal rate. Such considerations should be included in the reaction model for a better chemical and perfusion model.

Further work should be also directed in the inclusion of a more realistic reaction equations for example inclusion of the kinetics of cell waste release. This can be achieved by assuming that on the cell surface a chemical reaction occurs, where oxygen is up taken and carbon dioxide is released, concluding to the addition of a source term to the balance equation for the contribution of the carbon dioxide release.

Furthermore, a possibility to model such chemical reaction is proposed, the model is adapted from an existing model of [30]. The model initially is built for the case of a simple reaction where two reactants *(A,B)* react to form two products *(C,D)*, the reaction rate is chosen to follow an Arrhenius function such as:

$$K(T) = Ae^{\frac{-Ea}{RT}} \tag{4.1}$$

The Arrhenius equation gives the dependence of the chemical reaction rate *K* on the temperature *T*, activation energy *Ea* and reaction constant *A*. Rewriting the reaction rate for the reaction equation gives:

$$\begin{aligned} &nA + mB \xrightarrow{K} C + D \\ &reaction\,rate = AC_A^n C_B^m e^{\frac{-Ea}{RT}} \end{aligned} \tag{4.2}$$

Using the developed lattice Boltzmann equation, as in chapter 2 for both temperature distribution and reactant species distribution gives:

$$f_i^S(t+1, r+1) = f_i^S(t, r) + Q_i^S \tag{4.3}$$

Where S denotes either temperature or species distribution and the collision operator can be divided into two components such as:

$$Q_i^k = \left|Q_i^k\right|_1 + \left|Q_i^k\right|_2 \tag{4.4}$$

The first component denotes the change in distributions due to collision energy, already defined in chapter 2, whereas the second part contributes to the change in collision distributions due to reaction energy, species loss and birth and is defined as:

$$\left|Q_i^S\right|_1 = -\frac{1}{\tau_k}(f_i^S - f_i^{S(equ)}) \tag{4.5}$$

$$\begin{aligned} &\left|Q_i^S\right|_2 = -w_i^S A \cdot R^S e^{\frac{-Ea}{RT}} \\ &R^S = \rho_A{}^n \rho_B{}^m = \left[\sum_i^{S=A} f_i^S\right]^n \left[\sum_i^{S=B} f_i^S\right]^m \end{aligned} \tag{4.6}$$

Where wi are the lattice weights, R is the reactant concentrations to the stochiometric power. It's possible to neglect the second collision term in adiabatic reactions. Further work has to be done to validate this model and to implement in the life science applications.

Such an investigation is necessary due to the fact that cells get toxicity in the presence of excess waste. Such a case may occur due to reactor mal-geometry or dynamics, which might cause the toxins to accumulate on the cell surface and not get transported to the reactor exits. This is typical in reactors having a higher pressure field in vicinity of the cells, as in Figure 4.6, what makes it even more complicated: the necessity of providing such load bearing cells with high pressure.

- *Investigation on the analogy between the Realistic loads inside human bone-cartilage cells and the provided loads upon cells bred inside bioreactors.*

The loading conditions on average in a healthy femur is transported directly to the bone tissue which will experience nearly stresses ranging from *(0.1-0.7 MPa)* for *~1* second walking cycle and those stresses are the appropriate mechanical environment for a sustained growth of such load carrying cells [62, 63].

The cyclic pressure gradient developed by physiological activity is the main transport pump.Mechanical loading of bone tissue during physiological activity results in a tissue stress state, providing cyclic dilatational and deviatory components. The effect of dilatation or pressure Imposed by cyclically loading of bone tissue is the motor for fluid movement within tissue. As well the oscillating high shear flow induced by the oscillating pumping mechanism provides the bone tissue with a stiffness education schedule [52, 58].

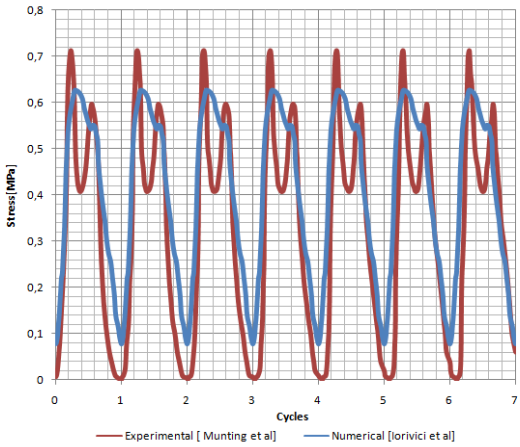

Figure 4.7: The Cross sectional load and stress inside a 70Kg femur bone showing a cyclic load on the femur while in a 7 normal walking cycle of 0.9-1 sec each [62, 63].

Specific focus was directed in applying such understandings to the bioreactor design considerations for stimulating and growing stem cells for both bone and cartilage cells. Extensive work in the literature has been made to match such loading conditions [59-61]. Three different bioreactor designs were investigated for the provision of appropriate normal and shear stress on the bred cells inside. Several modifications were made on the bioreactors in order to reach higher stresses that are more realistic. Geometrical and dynamical modifications were made in trials to improve the internal stresses in the bioreactor. The study provides a trend starting from conventional reactors of to the use of micro-scaffolds and suggestions were made for the usage of more intelligent micromechanical systems.The different designs have enhanced the shear stress 8 orders of magnitude from the initial design, but still the values are lower with 2-3 orders of magnitude in comparison to experimental values.

Table 4.1: Enhancement of Shear stress for different bioreactors, the shear stress was enlarged 8 orders of magnitude from the initial design, but still the values are lower with 2-3 orders of magnitude in comparison to experimental values [66].

Method	~Shear [MPa]
Measured (D'Lima) Walking [67]	$0.94\times10^{-1}\rightarrow 0.1$
Measured (D'Lima) Jogging [67]	$0.28\rightarrow0.7$
Modelled (Hussein-1)	$\sim1\times10^{-12}$
Modelled (Hussein-2)	0.48×10^{-11}
Modelled (A.A Moaty) [66]	1.09×10^{-6}
Modeled (Hussein-3)	5.30473×10^{-4}

Special considerations were made in order to provide the cultivated cells with symmetrical loadings. The importance of such an aspect arises from the fact that such load bearing cells are quite sensitive to loading which totally affects their growth rates. Therefore, for a symmetric bioreactor design, all cell growing pits should be surrounded by equal loadings. Figure 4.8, shows an example of a bioreactor sharing un-symmetric loading conditions on the different cell pits, it is expected that the cells which grow in the left and right pit to be totally different then the cells growing on the middle pit. As well a further look into such uneven loading case will lead into uneven substrate transport, such conditions are quite critical in bioreactor design considerations. On the other hand in Figure 4.9 showing another bioreactor sharing almost symmetric loading conditions on the cells, it is expected that cells grown in such a reactor has better possibilities to be identical then these cells which grow in the reactor of Figure 4.8.

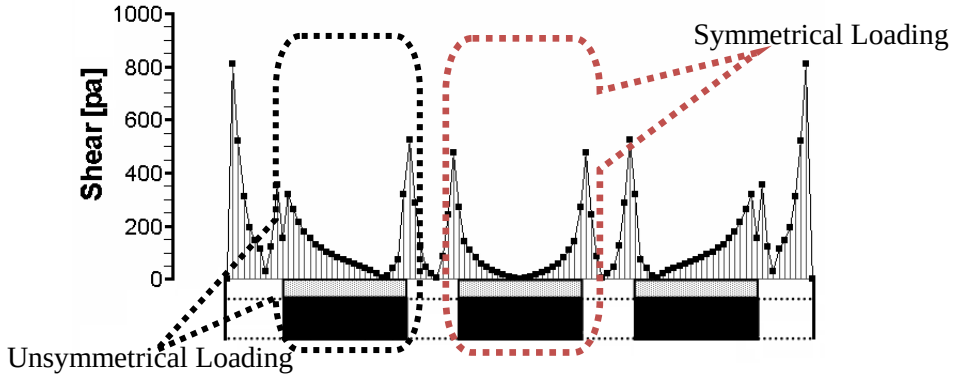

Figure 4.8: Enhancement an example of a bioreactor sharing different loading conditions on the different cell pits, it is expected that the cells which grow in the left and right pit to be totally different then the cells growing on the middle pit.

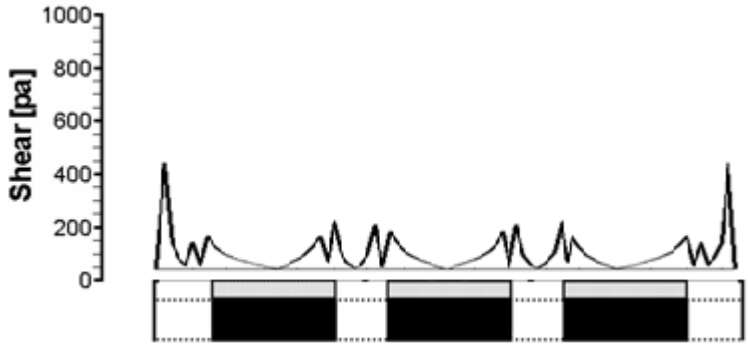

Figure 4.9: another example of a bioreactor sharing almost symmetric loading conditions on the cells, it is expected that cells grown in such a reactor has better possibilities then those which grow in Figure 4.8.

Although symmetrical loading is preferred, nevertheless, tissues in a stress state involving cyclic dilatational and deviatory components provides a more realistic diffusion coefficient and acts as the motor for fluid movement within tissue [58]. Summarizing, a symmetrical cyclic loading on the cells would be a good compromise between symmetry and cyclic loading.

Further work should be done to realize higher shear loads: thoughts of pulsating pressure fields, by means of low frequency piezo elements embedded in the bioreactor could be a promising modification. On the other hand the usage of a pulsating micro-pump by means of MEMS (Micro Electro Mechanical Systems) technology in the neighbourhood of the cells might be an alternative for the piezo elements, special considerations of the design should be made for calculations and modelling of the resultant cyclic loads reached in the bioreactor could be a promising modification.

Figure 4.10 shows a preliminary idea of the possibility of implementing an array of piezo-elements in contact with the cells; the piezo elements would provide a cyclic loading environment to the cells. Special consideration should be made for the tuning of the vibration amplitude to provide the tissues with convenient conditions.

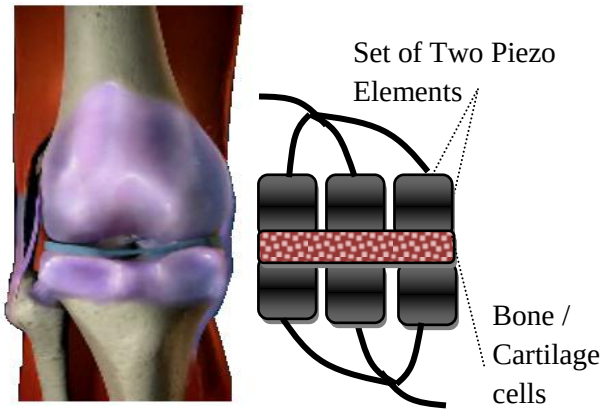

Figure 4.10: A preliminary idea of the possibility of implementing an array of piezo-elements in contact with the cells, the piezo elements would provide a cyclic loading environment to the cells. Special care should be focused on the enabling of mass transfer to the cells providing it with nutrition and a waste removal by means of porous elements.

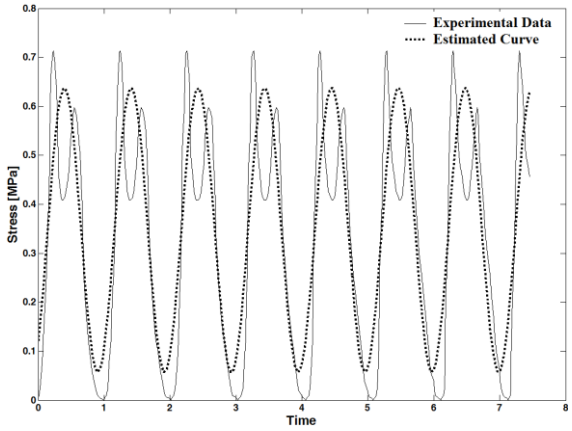

Figure 4.11: With a sinusoidal curve fitting, it could be possible to estimate the necessary sinusoidal excitation to imitate the real load on the cells, for further actuator design considerations.

Referring to figure 4.7 one can estimate the sinusoidal fitting function to the load distribution upon skeletal or cartilage cells, as in figure 4.11. This estimation could be useful for the design of the micro-actuator to imitate the real loading conditions. The fitted function takes the form:

$$load = a\sin(bt + \phi) + c$$

$$load = 0.2903\sin(6.1999t + 5.3888) + 0.3475 \tag{4.7}$$

$$Frequency = \frac{6.1999}{2\pi} = 0.987\,Hz \tag{4.8}$$

Additionally, special care should be focused on the enabling of mass transfer to the cells providing it with nutrition and a waste removal in a similar porous fashion to the proposed design in figure 4.10.

4.2 Micro-Macro Modelling of Heat and moisture transfer in Porous Dough

The second direction investigated in this thesis relates to the micro and macro scale mass and heat transfer in dough porous structures while baking. This is a crucial problem in the everyday meal member, since a substantial fraction of the energy consumed in the bread process is utilized for baking. The importance of the problem comes from the economical and political aspect of bread, further understanding of the bread process may enable the possibilities to further reduce the costs and enhance the quality.

Bread baking is a very difficult problem to model with an un-detailed look man can say bread baking is a daily job since ancient Egyptians, but considering all the thermo-physics persisting reveals a highly sophisticated problem which was only achieved in the past by experience, trial and errors.

So far, some efforts have been made to understand, predict and control the bread baking process, including both experimental and theoretical approaches. Nevertheless, most efforts previously made have avoided modelling the phenomena occurring in the microscale [36-39], although the mechanism occurs initially in the microscale. From a transport phenomena point of view, bread baking has been considered as a simultaneous heat and mass transfer (SHMT) problem in a porous medium.

In this work heat and moisture transfer models were developed to accomplish the mechanisms included, both in the microscale and the macroscale, to predict moisture transfer, heat transfer, measurement of effective moisture diffusivity, thermal conductivity and diffusivity.

Difficulties arise in such systems due to the presence of two coupled phenomena: Heat and moisture transfer. Both phenomena occur simultaneously and each contributes to the other, which boost the difficulties of understanding such a complicated system.

The work in this thesis presents an innovation in the modelling of SHMT problems, where the microscale dynamics was introduced by means of Lattice Boltzmann Methods. Further enhancement made on the methodology of LBM to include such complex phenomenon of life sciences was achieved.

Two aspects were investigated in this work:

- *Micro-scale modelling of Porous DoughStructures*

The micro porous structure of dough has an important effect on transport mechanism of moisture and heat. Ignorance to such properties may prevail into an inconsistent inaccurate modelling. In this part special consideration was made to investigate and enhance the dough micro-properties in dependency on the microstructure and on the temperature, taking into considerations that the temperature and microstructure are as well strictly dependent. Diffusion is the mechanism by which mass is transported from one part to another derived by a concentration gradient and defined usually for a substrate-solvent system together. In micro-porous systems the diffusion coefficient is corrected by the constrictivity *(δ)*, tortuosity *(τ)* and porosisty *(Φ)* such that:

$$D_{eff} = \frac{D\Phi\delta}{\tau} \tag{4.9}$$

Constrictivity is viewed to depend on the ratio of the diameter of the diffusing particle to the pore diameter. The value of constrictivity is always less than 1. The constrictivity is defined not for a single pore, but as the parameter of the entire pore space considered. The simplest mathematic method to estimate tortuosity is arc-chord ratio: ratio of the length of the curve (ξ) to the distance between the ends of it (ζ):

While crust is formed Porosity, Constrictivity and Tortuosity are changed, the microstructure of the crust pores tend to be smaller than in the crumb region as shown in Figure 2, resulting in a dense porous matrix and thus increasing the resistance to mass transport due to increasing constrictivity. The main difficulty in heating hygroscopic material is that usually shrinkage occurs with dehydration which may alter the mechanism by which moisture or vapour migrates through the material. Reversely in dough as the water moisture migrates to the outer environment heating of the crumb develops slowly inwards and the temperature of the dough will rise quickly from 25 to 50° C, during this period the fermenting agents will degrade sugar into CO_2 very rapidly and will increase the bread volume. As the temperature rises further the CO_2 bubbles thermally expand thus enhancing the development of the bread and thus allowing the formation of cavities inside, which eventually changed the porosity, constrictivity and tortuosity. Nevertheless, dough can be assumed of isotropic properties, and that the major expansion happening in the crumb is due to the higher thermal expansivity of the CO_2. Zhang [67] estimated the overall correction factor (which includes the porosity, constrictivity and tortuosity) for the diffusion coefficient in the crust to be 0.0013.

I. Mass Transfer

The modelling of the moisture transfer in the micro-channels of the dough structure was achieved for different temperature and different microstructure. The problem included

sophisticated modelling of porosity changes which was constant in the first application of the cell reactors. The diffusion coefficient is strictly temperature dependent and takes different forms in liquid phase and in solid phase. The problem arises due to the phase changing in the dough as the gluten coagulates. Therefore, subdivision into three completely different diffusion coefficients is a necessity for more consistent modelling.

$$D_{eff}\Big|_{Moisture} = \begin{cases} 5e^{-10}T - 1e^{-8} & ,in\,Crumb \\ 0.0013\times(5e^{-10}T - 1e^{-8}) & ,in\,Crust \\ 2e^{-7}T + 2e^{-5} & ,inAir \end{cases} \quad (4.10)$$

Firstly, a moisture diffusion coefficient through the dough crumb which is temperature dependent is considered. Secondly, for the crust region, the modelling of the mass diffusivity while crusting was achieved. Porosity, Constrictivity and Tortuosity were as well time varying, the microstructure of the crust pores tend to be smaller than in the crumb region, resulting in a dense porous matrix and thus increasing the resistance to mass transport due to increasing constrictivity.

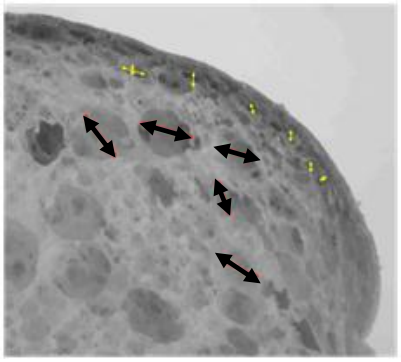

Figure 4.12: While crust is formed Porosity, Constrictivity and Tortuosity are changed, the microstructure of the crust pores tend to be smaller than in the crumb region

A diffusion coefficient including the crust correction factor is defined which corrects for the blocking of the mass transfer by the tight crusted pores. Finally, a third factor is defined for the moisture diffusion in the air region. All factors developed were strictly temperature dependent. The developed properties were validated in the macro-scale to provide a more general evaluation, since all properties in the micro-scale influence each other reaching a macroscale influence and it would be hard to isolate these phenomena.

II. Heat Transfer

In a simultaneous heat-mass transfer system two kinds of transfers occur: thermal diffusion and thermal conduction. The sophistication arises due to the varying microstructure of the dough due to the presence of the three phases together as gas, liquid and solid as mentioned in the previous section. The gas phase composes of air and carbon dioxide and as most gases diffuse heat faster. The liquid phase composes of water-flour system and

basically develops similar thermal properties as water when exists in the fluidic form, sequentially has better conductivity than gases. The solid form, the crust, exhibits gases inside and crusted dough at which the conductivity deteriorates greatly due to the dehydration effect. In the work a temperature and phase dependent model was developed which is able to differentiate between gas, liquid and solid dough phases.

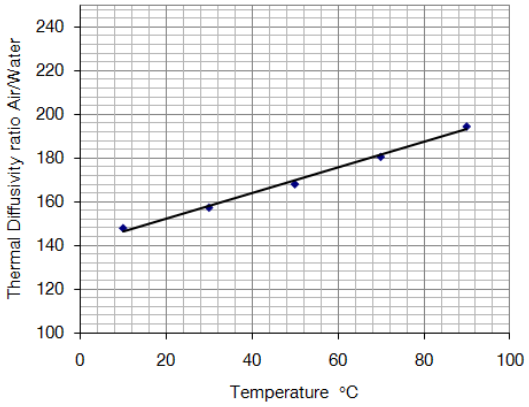

Figure 4.13: Water and air have diverse thermal diffusion coefficients which vary with temperature. Air diffuses two orders of magnitude higher than water. Meaning, air is a better diffusion medium (100 times better)

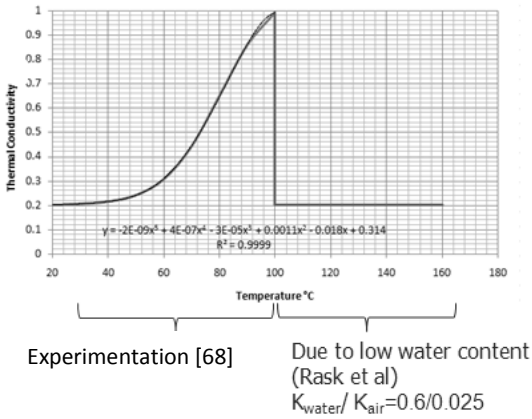

Figure 4.14: The first part of the thermal conductivity curve is obtained from experimentation made by Jury [68] and shows an increase in conductivity with temperature. The second part of the curve represent the conductivity in the crust, this drop is due to the fall of the water content in the crust which resembles a dive in the conductivity. The conductivity falls to 0.2 [W/m2°K] which was predicted in literature Rask [69].

The question comes to which phase resembles quicker or slower heat spreading. Noting that water has very good heat conductive properties, but weak heat spreading properties and Air has a better thermal diffusivity than water; air spreads heat around two orders of magnitude quicker than water, which makes it more complicated to understand the overall heat transfer, see figure 4.13 and 4.14.

Figure 4.15 provides a detailed example of the combined phenomenon occurring: Arrows (①②③) correspond to the thermal heat transfer when an air bubble is touching the hot surface; whereas arrows (⓪④) correspond to the transfer when water is the conducting medium; arrows (⑤) correspond to the heat diffusion inside the air bubbles; arrows (⑥⑦) correspond t o the diffusion inside water. Meaning that if water is the surface conducting material a higher temperature profile occurs on the boundary unlike the air and once an air bubble is crossed it transfers the heat quicker. In conclusion water is a better conductor (5 times better) and air is a better diffusion medium (100 times better), see figure 4.13 and 4.14.

From the results it's obvious that porosity play an important role in the heat transfer, thus, it could be surely said on a macroscale, that the higher the porosity the higher the heat transfer, but then the baking time has to be tuned in order to give the dough enough time to cook and still stay soft and fresh, otherwise it dries out and develops a much bigger crust.

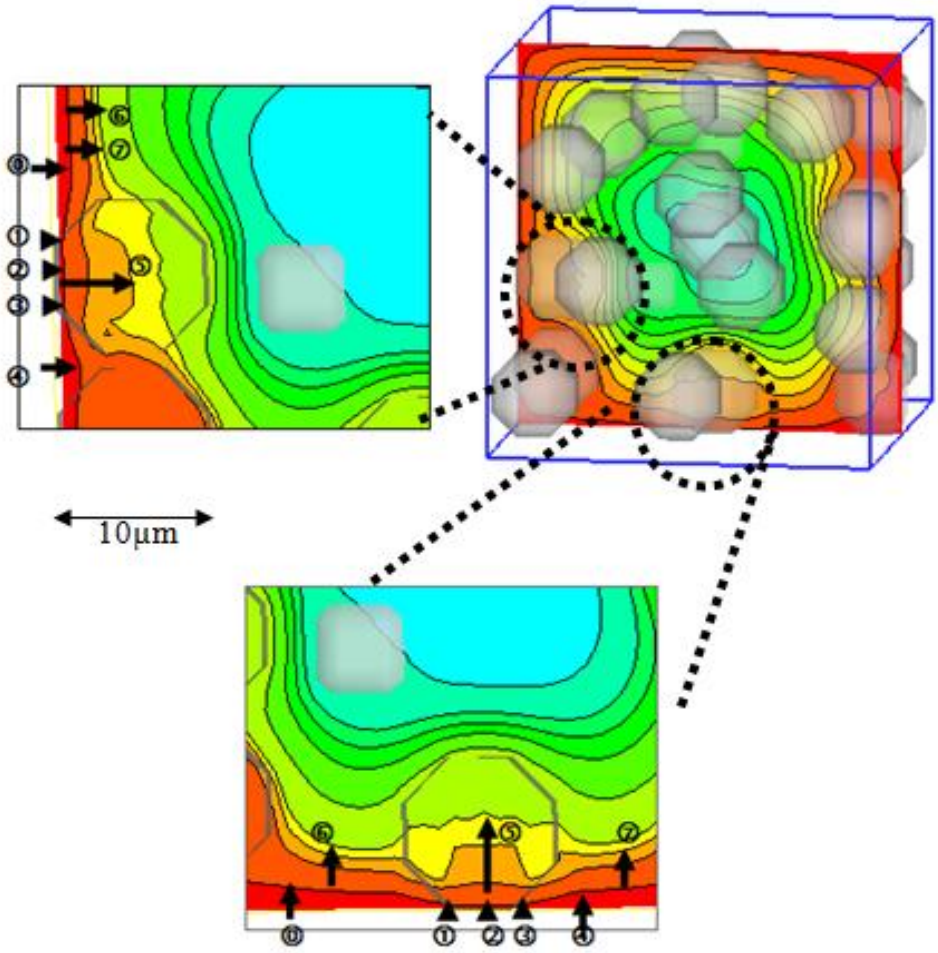

Figure 4.15: Arrows (①②③) correspond to the thermal heat transfer when an air bubble is touching the hot surface; whereas arrows (⓪④) correspond to the transfer when water is the conducting medium; arrows (⑤) correspond to the heat diffusion inside the air bubbles; arrows (⑥⑦) correspond t o the diffusion inside water.

An investigation was made to follow up this conclusion different porosity was investigated thermally; In general these testing shows on the macroscale that the higher porosity needs lower baking time, which explains why the flat bread needs only two minutes baking in comparison to the normal rolls.

Table 4.2: Different porosity was investigated for different baking time.

Porosity%	Time [minutes]
11	25
13	21.57
14	19.52
16	17.5

- *Macroscale Modelling of Dough Baking*

The thermo-physics involved in dough baking is quite complicated, in this process two phenomena work simultaneously:

- Heat transfer
- Moisture transfer

Difficulties arise in Simultaneous Heat & Mass Transfer systems due to the presence of the two coupled phenomena. In addition to occurring simultaneously each part contributes to the other, which boosts the difficulties of understanding such a complicated system.

Modelling techniques have proven of great help in combined engineering problems, due to its cheap price in comparison to experimentation. As well as it enables the isolation of each phenomena independently for intensive investigations. On the other hand it is sometimes quite complicated to propose a mathematical model for certain physics occurring.

Several previous works has addressed the same problem with trials of modelling different aspects of bread baking process but often proceeded with the assumptions that the thermo-physics occur in the macro-scale, which is in fact not true. A step to descriptive analysis and investigation of micro-macro dough baking is presented in this part using the lattice Boltzmann methods.

The coupled transport of moisture and heat transfer persistently occurs in the microscale, the micro-channelling developing while baking greatly dominates both phenomenon and reversely the channels are structured by both phenomena. The heat transfer is biased by the moisture transfer as thermal conduction and thermal diffusion vary accordingly, whether in a gas bubble or dough material. As well the heat transfer greatly depends upon the presence of moisture which greatly conducts the heat in comparison to dehydrated material. Water conducts heat much better than air, thus the providences of steam in the interface acts as an efficient coupling agent. As well, the weaker thermal diffusivity of water in the dough structure presents the bread with more time to cook and coagulation of the gluten matrix.

$$Moisture\,Flux = Moisture_{Dough} - Moisture_{Oven} \tag{4.11}$$

Dough in general is considered hygroscopic; the trend at which the moisture content inside dough dries out is commonly dependent upon the partial pressure as a function of temperature. The overall moisture flux proceeds until an overall equilibrium between moisture in oven volume and in bread volume, see equation (4.8), since the moisture flux is function in the moisture difference by means of vapour pressure. Another consequence of the moisture transfer between the coupled domains is the heat conduction in presence of water (moisture). Further understanding of the physics occurring revealed that two important

mechanisms occur: Heat transfer exhibits from the hot oven surrounding to the bread; Moisture diffuses out from the bread domain to the oven, as seen on figure 4.16.

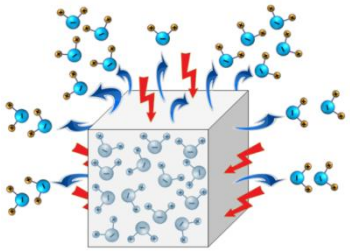

Figure 4.16: As heat transfer exhibits from the hot oven surrounding to the bread, moisture diffuses out from the bread domain to the oven.

As earlier stated the heat transfer greatly depends upon the presence of moisture which greatly conducts the heat in comparison to dehydrated material. Thus, both effects limit each other further investigations of these limitations accompanied with experimental validation would greatly tune the baking process. Overall, both aspects affect the macro properties of the baked goods, its baking time and its end quality from colour to sensory.

The average water content time response in the bread was as well reported in comparison to the published experimental work of Purlis [38-39]

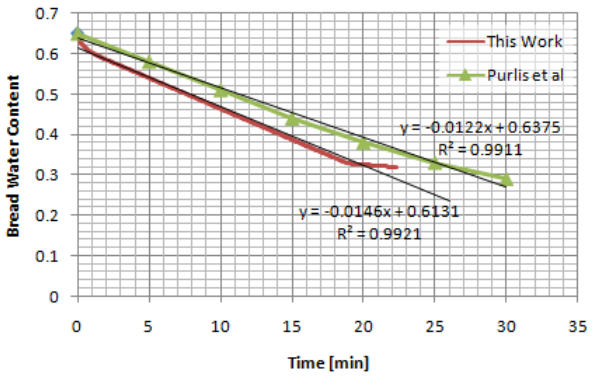

Figure 4.17: Bread Dehydration profile: The average water content time response in the bread domain is monitored, a steady linear decline is spotted and the moisture flux equilibrium with the oven domain is reached at 19 min. In comparison, the published experimental work of Purlis [43-44] show the estimated equilibrium time to be between 25-30 min.

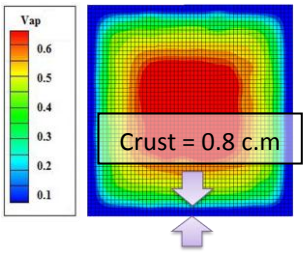

Figure 4.18: The crust thickness can be numerically predicted by locating the region in the bread in vicinity of the interface which is almost depleted from moisture content.

The deviations could be due to the smaller sized oven used in the model which subjects the sample to a higher Heat flux, thus heating it more and hydrating it more.

Bread crust is the interfacial area between the bread and the oven, a lot of thermo-physics occur in it, such as: The conduction of the heat; the transport of the moisture flux to the oven; the strong tensional forces due to overpressure from the internal expansion of the gas cavities; the inability of the contained gases in the crust to expand due to the hardness of

the crust from the continuous dehydration of the region; the caramelization of the un-fermented sugars. The crust thickness can be numerically predicted by locating the region in the bread in vicinity of the interface which is almost depleted from moisture content.

Table 4.3: The simulated crust development has shown a crust thickness of 0.8 c.m., Which is a bit higher than similar experimental results [43,44], both had which reported a dehydrated thickness of 0.5-0.6 c.m,

	Achieved Thickness	Dehydrated
Crust Thickness Purlis [12-13]	0.5-0.6 cm	
Crust Thickness (This work)	0.8 cm	

The simulated crust development has shown a crust thickness of 0.8 c.m., Figure 4.18. Which is a bit higher than similar experimental results Purlis [43-44], see table 4, both had which reported a dehydrated thickness of 0.5-0.6 c.m. The crust over-estimation in this work fits to the overheating occurring in the model as mentioned earlier.

This part lacks the modelling of evaporation-condensation, the outcome of this will reflect on the temperature and the moisture phase change. Since heat is gained and lost by condensation and evaporation, respectively. In order to increase the accuracy of the model further work should be done to incorporate this mechanism.

Also, the deficiency of not having a thermal expansion may have a powerful part in the high heat flux reported in this work, since the flux will decrease slightly as the volume increases as they are inversely proportional. Extensive work can be made as well to make sure that the bubbles will expand following the trend of ideal gas i.e. $\propto 1/\mathrm{T}$ (T is temperature), this can be achieved by obtaining the gas bubble structure with time while baking by taking out different samples at different timings and evaluating them in a Computer Tomography machine where x-rays are made for different sections providing a full 3-d file for the bubble distribution. Analysing the bubble distribution with time reveals a gas expansion response for dough with time. Additionaly such data can be used to properly estimate the Porosity, Constrictivity and Tortuosity for the crumb and crust, as too less work have been made in this direction in the literature.

As well for generalizing the profit of these model further considerations of convection and radiation heat transfer should be established. The radiation heat transfer rate can be easily included in the boundary condition acting upon the bread boundary.

$$\dot{q} = \varepsilon\sigma\left(T_s^4 - T_o^4\right) \tag{4.12}$$

Where ε is the emissivity coefficient of the oven walls; σ : is the Stefan Boltzmann constant; T_s is the heating surface temperature and T_o is the heated object temperature. This will provide the model with a more general applicability, although extensive work should then be made for stability considerations as the Eigen values reported in Appendix A, will be coupled.

Extensive validation and calibration should be achieved for the model by means of experimental work; this can be achieved easily by implementing an array of multi-sensing point thermocouple in the dough which is already in progress. As well moisture transfer validation should be carried out although the difficulties of measuring moisture content inside the bread while baking. Additionally, extensive validation and enhancement is necessary for the dough micro-properties developed such as: effective moisture diffusivity, thermal conductivity and diffusivity. Nevertheless, the model has achieved to produce a similar trend for the SHMT of the bread problem.

In conclusion this work has addressed the possibilities of modelling complex geometries and dynamics both in the micro-scale and macro-scale. The study shows the possibility to model the transport phenomena, using LBM, inside the micro-network of scaffolds. Several transport mechanisms were established such as momentum conservation, cell kinetics, moisture transfer, thermal diffusion and conduction. All outcomes prove the close trends to expected results further validating the model, whilst reducing computational effort in the memory and in the processing time, in comparison to conventional methods. Proving the lattice Boltzmann methodologies as a valid tool for modelling in biotechnological applications, were sophistication is the major trend due to the dealing with living material unlike other engineering applications were properties and kinetics are adjusted to fixed values and rates. Since the trend to model simultaneous systems, it's necessary from an energy conservation point of view to use the Boltzmann model at different time-scales, thus a further look should to the non-equilibrium distributions and the combined stability of different time scales is necessary. Further code parallelization are suggested since the processing times for the SHMT problem started to be a limitation (48hrs processing time).Which is an already existing instinct in the LBM, due to the independent propagation of particles which are not in close vicinity. On the whole much more work still persists in the field of biotechnological modelling, which are of great challenge to modellers due to the dealing with living science, which adds a magical non-equilibium touch to the equation dynamics and the unsteady boundary conditions. At the end of the day contributions in such aspects would be either a life saving or an immense economic jump for the daily life science.

5.References

References

1. Casselmann, B.: Yale Babylonian Collection (YBC 7289), Available from: www.math.ubc.ca/~cass/Euclid/ybc/ybc.html.
2. Tijskens, L.; Hertog, M.; Nicolai, B. M.: Food process modelling. Woodhead Food Series 59 (2001), ISBN: 1855735652.
3. Van der Vorst, J. G. A. J.; Tromp, S. O.; van der Zee, D. J.: Simulation modelling for food supply chain redesign; integrated decision making on product quality, sustainability and logistics. International Journal of Production Research 47 (23) (2009), 6611-6631.
4. Pharma searches for the cure through computer modelling, IBM, (2009).
5. Davis, C.: Algorithms for airlines: new math model saves money, improves service. University of Florida News (2002), Available from: http://news.ufl.edu/2002/03/04/air-schedule/.
6. Berg, J. M.; Tymoczko, J. L.; Stryer, L.: Biochemistry (Fifth Edition: International Version), W.H. Freeman (2002), ISBN: 0716746840.
7. Hussein, M. A.; Becker, T.: Numerical Modelling of Shear and Normal Stress of Micro-Porous Ceramics for Stimulated in-vitro Cultivation of Bone Cells. Microfluidics and Nanofluidics 8 (2009), 665-675.
8. MediLexicon International Ltd. (2009) Available from: www.medicalnewstoday.com.
9. McNamara, G.; Zanetti, G.: Use of the Boltzmann Equation to Simulate Lattice-Gas Automata. Phys. Rev. Lett. 61 (1988), 2332 – 2335.
10. Higuera, F. J.; Jimenez, J.: Boltzmann approach to lattice gas simulation. Europhys. Lett. 9 (1989), 663 –668.
11. Prasianakis, N. I.; Karlin, I. V.; Mantzaras, J.; Boulouchos, K. B.: Lattice Boltzmann method with restored Galilean invariance. Physical Review E 79 (6) (2009).
12. Huang, K.: Statistical Mechanics. Wiley (1987), ISBN-10: 0471815187.
13. Shan, X.W.; Chen, H.D.: Lattice Boltzmann model for simulating flows with multiple phases and components. Physical Review E 47 (3) (1993), 1815–1819.
14. Swift, M.R.; Osborn, W.R.; Yeomans, J.M.: Lattice Boltzmann simulation of non ideal fluids. Physical Review Letters 75 (5) (1995), 830.
15. Inamuro, T.; Ogata, T.; Tajima, S.; Konishi, N.: A lattice Boltzmann method for incompressible two-phase flows with large density differences. Journal of Computational Physics 198 (2) (2004), 628–644.
16. Frisch, U.; Hasslacher, B.; Pomeau, Y.: Lattice-Gas Automata for the Navier-Stokes Equation. Phys. Rev. Lett. 56 (1986), 1505.
17. Hardy, J.; Pomeau, Y.; de Pazzis, O.: Time Evolution of a Two-Dimensional Classical Lattice System. J. Math. Phys. 14 (1973), 1746.
18. Wolf-Gladrow, D. A.: Lattice-Gas Cellular Automata and Lattice Boltzmann Models. Springer (2000), ISBN 3-540-66973-6.
19. Succi, S.: The Lattice Boltzmann Equation for Fluid Dynamics and Beyond (Series Numerical Mathematics and Scientific Computation), Oxford University Press (2001), ISBN-10: 0198503989.
20. D'Humières, D.; Lallemand, P.; Frisch, U.: Lattice gas models for 3D-hydrodynamics. Europhys. Lett. 2 (4) (1986), 291–297.

21. Georgia State University, Department of Physics and Astronomy. Available from: http://hyperphysics.phy-astr.gsu.edu/hphys.html.
22. Bernsdorf, J.; Schäfer, M.: Comparison of cellular automata and finite volume techniques for simulation of incompressible flow in porous media. ERCOFTAC Bulletin 28 (1996), 24-27.
23. Koelman, J. M. V. A.: A simple lattice Boltzmann scheme for Navier–Stokes fluid flow. Europhys. Lett. 15 (1991), 603–607.
24. Skordos, P.: Initial and boundary conditions for the lattice Boltzmann method. Physical Review E 48 (1993), 4823–4841
25. Zhou, J.G.: Lattice Boltzmann methods for shallow water flows. Springer (2004), ISBN-10: 3540407464.
26. Gunstensen, A.K.; Rothman, D.H.: Lattice Boltzmann model of immiscible fluids. Physics Review A 43 (8) (1991), 4320–4327.
27. Chopard, B.; Droz, M.: Cellular automata model for diffusion processes. J. Stat. Phys.; 64 (1991), 859-892.
28. Chopard, B.; Luthi, P.O.; Masselot, A.; Dupuis, A.: Cellular automata and lattice Boltzmann techniques: An approach to model and simulate complex systems. Advances in Complex Systems, 5 (2) (2002), Available from: http://cui.unige.ch/ chopard/FTP/CA/advp.ps.gz.
29. van der Sman, R. G. M.; Ernst, M. H.: Convection diffusion lattice Boltzmann scheme for irregular lattices. J. Comp. Phys 160 (2) (2000), 766-782.
30. He, X.; Li, N.; Goldstein, B.: Lattice Boltzmann Simulation of Diffusion-Convection Systems with Surface Chemical Reaction. Molecular Simulation 25 (3 & 4) (2000), 145 – 156.
31. Agarwal, S.; Verma, N.; Mewes, D.: A lattice Boltzmann model for adsorption breakthrough. Heat and Mass Transfer 41 (9) (2005), 843-854.
32. Anwar, S.; Cortis, A.; Sukop, M. C.: Lattice Boltzmann simulation of solute transport in heterogeneous porous media with conduits to estimate macroscopic continuous time random walk model parameters. Progress in Computational Fluid Dynamics 8 (1/2/3/4) (2008), 213 – 221.
33. Hussein, M.A.; Esterl, S.; Pörtner, R.; Wiegandt, K.; Becker, T.: Impulse and Mass Transport in a Cartilage Bioreactor using the Lattice Boltzmann Method. International Journal of computational fluid dynamics 22 (5) (2008), 341-350.
34. Petrovic, B. M.: The Diffusion Hypothesis. The annual meeting of the International Studies Association, Hilton Hawaiian Village, Honolulu, Hawaii (2005).
35. Pel, L.: Moisture transport in porous building materials, Eindhoven University of Technology, Netherland. Ph. D. Thesis, (1995).
36. Thorvaldsson, K.; Janestad, H.: A model for simultaneous heat, water and vapour diffusion. J Food Eng 40 (1999), 167–172.
37. Srikiatden, J.; Roberts, J. S.: Moisture transfer in solid food materials: A review of mechanism. International Journal of Food Properties 10 (4) (2007), 739 – 777.
38. Purlis, E.; Salvadori, V. O.: Bread baking as a moving boundary problem. Part 1: Mathematical Modelling. Journal of Food Engineering 91 (2009), 428-433.
39. Purlis, E.; Salvadori, V. O.: Bread baking as a moving boundary problem. Part 2: Model validation and numerical simulation. Journal of Food Engineering 91 (2009), 434-442.

40. Samir, K.; Zhang, J.: High order ADI method for solving unsteady convection-diffusion problems. Journal of computational physics 198 (1) (2004), 1-9.
41. Leu, F.J.; Dane, J.H.: Analytical solutions of the one-dimensional advection equation and two-or three-dimensional dispersion equation. Water Resources Research (1990).
42. Sluimer, P.; Krist-Spit, C. E.: Heat transport in dough during the baking of bread, Morton, I. D. Cereals in a European Context, New York, VCH (1987), 355-363.
43. Chen, S.; Martinez, D.; Mei, R.: On boundary conditions in lattice Boltzmann method. Phys Fluids 8 (1996), 2527–2536.
44. Kuoa, L.; Chen, P.: Numerical implementation of thermal boundary conditions in the lattice Boltzmann method. International Journal of Heat and Mass Transfer 52 (1-2) (2009), 529-532.
45. Pavlidis,T.; Liow, Y.: Integrating Region Growing and Edge Detection. IEEE Transactions on Pattern Analysis and Machine Intelligence. 12 (3) (1990), 225 – 233.
46. Gonzales, R. C.; Woods, R. E.: Digital image processing. Prentice-Hall, New Jersey (2002), ISBN: 0201180758.
47. Robertson, G.R.; Aburdene, M.F.; Kozick, R. J.: Differential block coding of bilevel images. IEE Transactions on Image Processing 5 (9) (1996), 1368 - 1370.
48. Bawa, S: Edge Based Region Growing. Deemed University, India. Master of Engineering in Electronics and Communication Engineering (2006), Roll No-8044123.
49. Mei, R.W.; Yu, D.Z.; Shyy, W.; Luo, L.S.: Force evaluation in the lattice Boltzmann method involving curved geometry. Physical Review E 65 (041203) (2002),
50. Tang, G.H.; Tao, W.Q.; He, Y.L.: Simulation of fluid flow and heat transfer in a plane channel using the lattice Boltzmann method. Int. J. Mod. Phys. B 17 (2003), 183–187.
51. Kao, P.H.; Ren, T.F.; Yang, R.J.: An investigation into fixed-bed micro-reactors using lattice Boltzmann method simulations. Int. J. Heat Mass Transfer 50 (2007), 4243–4255.
52. Hussein, M. A.; Becker, T.: Numerical Modelling of Shear and Normal Stress of Micro-Porous Ceramics for Stimulated in-vitro Cultivation of Bone Cells. Microfluidics and Nanofluidics 8 (2009), 665-675.
53. Hussein, M.A.; Esterl, S.; Poertner, R.; Wiegandt, K.; Becker, T.: On the Lattice Boltzmann method simulation of a two phase flow bioreactor for artificially grown cartilage cells. J Biomech 41 (16) (2008), 3455–3461.
54. Wood, J. H.; Thakker, K. M.: Michaelis-Menten Absorption Kinetics in Drugs: Examples and Implications. European Journal of Clinical Pharmacology 23 (1982), 183-188.
55. Esterl, S.; Özmutlu, Z.; Hartmann, C.; Delgado, A.: Three-Dimensional Numerical Approach to Investigate the Substrate Transport and Conversion in an Immobilized Enzyme Reactor. Biotechnology and Bioengineering 83 (2003), 780-789.
56. Schroeter, J. D.; Kimbell, J. S.; Bonner, A. M.; Roberts, K. C.; Andersen, M. E.; Dorman, DC.: Incorporation of tissue reaction kinetics in a computational fluid dynamics model for nasal extraction of inhaled hydrogen sulfide in rats. Toxicological Sciences 90 (2006), 198–207.
57. Ataíde, F.; Hitzmann, B.: When is optimal experimental design advantageous for the analysis of Michaelis–Menten kinetics? Chemometrics and Intelligent Laboratory Systems Volume 99 (1) (2009), 9-18.
58. Cowin, S.S.: Handbook of Bone Mechanics. CRC Press (2001), ISBN-10: 0849391172.

59. Gatzka, C.; Knothe, U.; Niederer, P.; Schneider, E.; Knothe Tate, M.L.: A novel ex vivo model for investigation of fluid displacements in bone after endoprosthesis implantation. J. Mater Sci. Mater Med. 10 (1999), 801–806.
60. Drews, A.; Kraume, M.: On maintenance models in severely and long-term limited membrane bioreactor cultivations. Biotech. Bioeng. 96 (2007), 892-903.
61. Ataide, F.: Experimental design methodologies for the identification of Michaelis-Menten type kinetics. Universidade Nova De Lisboa, Faculdade de Ciências e Tecnologia. Master Thesis in Chemistry and Biochemistry (2007).
62. Munting, E.; Verhelpen, M.: Mechanical Simulator for the upper femur. Acta Orthropedicae Belgica 59 (2) (1993), 123-129.
63. Iarovici, A.; Capitanu, L.: The total hip arthroplasty effects on the mechanical behaviour of the femur. Annual Symposium of Solid Mechanics (2004).
64. Arrhenius activation energy - IUPAC Goldbook definition. Available from: http://goldbook.iupac.org/A00102.html.
65. D'Lima D. D.; Patil, S.: Tibial forces measured in vivo after total knee arthroplasty. Journal of Arthroplasty 21 (2) (2006), 255-262.
66. Moaty, A. A.; Hussein, M.A.; Becker, T.: An innovative Lattice Boltzmann model for simulating Michaelis Menten based diffusion-advection-kinetics and its application within a cartilage cell bioreactor. J. Biomech. Model Mechanobiol. 9 (2) (2010), 141-51.
67. Zhang, J.; Datta, A.K.: Mathematical modeling of bread baking process. Journal of Food Engineering 75 (2006), 78–89.
68. Jury, V.; Monteau, J. Y.; Comiti, J.; Le-Bail, A.: Determination and prediction of thermal conductivity of frozen part baked bread during thawing and baking, Food Research International 40 (2007), 874–882.
69. Rask, C.: Thermal properties of dough and bakery products: a review of published data. Journal of Food Engineering 9 (1989), 167–193.
70. Benzi, R.; Succi, S.; Vergassola, M.: The lattice Boltzmann equation: Theory and applications. Phys. Rep. 222 (3) (1992), 145-197.
71. Sterling, J. D.; Chen, S.: Stability analysis of lattice Boltzmann methods. Journal of Computational Physics 123 (1) (1996), 196-206.

Appendix-A

A-1. Weight Factors Derivation

The D2Q9 model includes three different speeds (compare Table A 1.1). The W_i for directions with identical speeds are equal for reason of symmetry.

Table A 1.1 Lattice speeds, cells an W_i of the D2Q9 lattice

c_i^2	cells	number of cells	W_i
0	0	1	W_0
1	1,2,3,4	4	W_1
2	5,6,7,8	4	W_2

The non- vanishing elements of the even moments up to the fourth order read:

- 0. Moment:

$$\sum_i W_i = W_o + 4W_1 + 4W_2 = \rho_0 \qquad \text{A-1.1}$$

Remark: The Only equation which includes W_0. It will be used to calculate W_0.

- 2. Moment:

$$\sum_i c_{i1}^2 W_i = 2c^2 W_1 + 4c^2 W_2 = \rho_0 \frac{k_B T}{m} \qquad \text{A-1.2}$$

Remark: $(k_B T)/m$ will be calculated from equations (A-1.2) and (A-1.3)

$$\sum_i c_{i2}^2 W_i = 2c^2 W_1 + 4c^2 W_2 = \rho_0 \frac{k_B T}{m} \qquad \text{A-1.3}$$

Remark: This constraint is identical with (A-1.1).

- 4. Moment:

$$\sum_i c_{i1}^4 W_i = 2c^4 W_1 + 4c^4 W_2 = 3\rho \left(\frac{k_B T}{m} \right)^2 \qquad \text{A-1.3}$$

Remark: W_1 will be calculated from Eq. (A-1.3).

$$\sum_i c_{i2}^4 W_i = 2c^4 W_1 + 4c^4 W_2 = 3\rho_0 \left(\frac{k_B T}{m} \right)^2 \qquad \text{A-1.3}$$

Remark: This constraint is identical with (A 1.3).

$$\sum_i c_{i1}^2 c_{i2}^2 W_i = 4c^4 W_2 = \rho_0 \left(\frac{k_B T}{m} \right)^2 \qquad \text{A-1.4}$$

Remark: W_2 will be calculated from Eq. (A 1.4).

The solution reads:

$$W_0/\rho_0 = \frac{4}{9} \qquad W_1/\rho_0 = \frac{1}{9}$$
$$W_2/\rho_0 = \frac{1}{36} \qquad \frac{k_B T}{m} = \frac{c^2}{3} \qquad \text{A-1.5}$$

One readily confirms that the first and third moments of the lattice velocities over W_i vanish.

For hydrodynamic simulation d'Humières et al. (1986) proposed a multi- speed lattice- gas cellular automata over a cubic lattice with 19 velocities (compare Section 3.3). This cubic lattice D3Q19 is defined by the following velocities

$$\begin{aligned} c_0 &= (0,0) \\ c_{1,2}, c_{3,4}, c_{5,6} &= (\pm 1,0,0),(0,\pm 1,0),(0,0,\pm 1) \\ c_{7,\ldots,10}, c_{11,\ldots 14}, c_{15,\ldots 18} &= (\pm 1,\pm 1,0),(\pm 1,0,\pm 1),(0,\pm 1,\pm 1). \end{aligned} \qquad \text{A-1.6}$$

The calculation of the W_i for the 3D model proceeds in close analogy with the 2D case. There are three different speeds: 1 time speed 0 (rest particle), 6 times speed 1 (1- particles) and 12 times speed √2 (√2- particles). The even moments yield four independent equations for the calculation of W_0, W_1, W_2 and k_BT/m:

- 0. Moment:

$$\sum_i W_i = W_0 + 6W_1 + 12W_2 = \rho_0 \qquad \text{A-1.7}$$

- 2. Moment:

$$\sum_i c_{\alpha x}^2 W_i = 2W_1 + 8W_2 = \rho_0 \frac{kT}{m} \qquad \text{A-1.8}$$

- 4. Moment:

$$\begin{aligned} \sum_i c_{\alpha x}^4 W_i &= 2W_1 + 8W_2 = 3\rho_0 \left(\frac{kT}{m}\right)^2 \\ \sum_i c_{\alpha x}^2 c_{\alpha y}^2 W_i &= 4W_2 = \rho_0 \left(\frac{kT}{m}\right)^2 \end{aligned} \qquad \text{A-1.9}$$

The solution reads

$$\begin{aligned} W_0 &= \frac{\rho_0}{3} \\ W_1 &= \frac{\rho_0}{2}\left(\frac{kT}{m}\right)^2 = \frac{\rho_0}{18} \\ W_2 &= \frac{\rho_0}{4}\left(\frac{kT}{m}\right)^2 = \frac{\rho_0}{36} \\ \frac{kT}{m} &= \frac{1}{3} \end{aligned} \qquad \text{A-1.10}$$

A-2. Lattice Boltzmann Model for the Incompressible Navier-Stokes Equation

The evolution equation of Lattice Boltzmann Method (LBM) is

$$f_\alpha(x + e_\alpha\delta_t, t + \delta_t) - f_\alpha(x,t) = -\frac{f_\alpha(x,t) - f_\alpha^{eq}(x,t)}{\tau} \quad \text{A-2.1}$$

Where:

$$f_\alpha^{eq} = \omega_\alpha\rho\left[1 + \frac{e_\alpha u}{c_s^2} + \frac{uu.(e_\alpha e_\alpha - c_s^2 I)}{2c_s^2}\right] \quad \text{A-2.2}$$

Where ω_α is the weight, and c_s is the speed of sound

And for D2Q9 model (9 bit model)

$$e_\alpha = \begin{cases} 0;\ \alpha = 0 \\ (cos\theta_\alpha, sin\theta_\alpha)c; \theta_\alpha = \dfrac{(\alpha-1)\pi}{2}, \alpha = 1{:}4 \\ \sqrt{2}(cos\theta_\alpha, sin\theta_\alpha)c; \theta_\alpha = \dfrac{(\alpha-5)\frac{\pi}{2} + \frac{\pi}{4}}{2}, \alpha = 5{:}8 \end{cases} \quad \text{A-2.3}$$

Where c is the speed and equals $\frac{\delta x}{\delta t}$, with δx is the lattice spacing and δt is the time increment.

$$\omega_\alpha = \begin{cases} \frac{4}{9};\ \alpha = 0 \\ \frac{1}{9};\ \alpha = 1{:}4 \\ \frac{1}{36};\ \alpha = 5{:}8 \end{cases} \quad \text{A-2.4}$$

Therefore;

$$c_s^2 I = \sum_\alpha \omega_\alpha e_\alpha e_\alpha = \frac{c^2}{3} \quad \text{A-2.5}$$

$$f_\alpha^{eq} = \omega_\alpha\rho\left[1 + 3\frac{e_\alpha u}{c^2} + \frac{9}{2}\frac{(e_\alpha u)^2}{c^4} - \frac{3}{2}\frac{u^2}{c^2}\right] \quad \text{A-2.6}$$

$$\rho = \sum_\alpha f_\alpha = \sum_\alpha f_\alpha^{eq} \quad \text{A-2.7}$$

$$\rho u = \sum_\alpha e_\alpha f_\alpha = \sum_\alpha e_\alpha f_\alpha^{eq} \quad \text{A-2.8}$$

For incompressible fluid:

$$\rho = \rho_0$$
$$M \to 0$$
$$\delta\rho = o(M^2)$$

Substitute $\rho = \rho_0 + \delta\rho$ in equation (6), and neglect terms higher than $o(M^2)$

$$f_\alpha^{eq} = \omega_\alpha\{\rho_0 + \delta\rho\}\left[1 + 3\frac{e_\alpha u}{c^2} + \frac{9}{2}\frac{(e_\alpha u)^2}{c^4} - \frac{3}{2}\frac{u^2}{c^2}\right]$$

$$= \omega_\alpha \left[(\rho_0 + \delta\rho) + 3\rho_0 \frac{e_\alpha u}{c^2} + \frac{9}{2}\rho_0 \frac{(e_\alpha u)^2}{c^4} - \frac{3}{2}\rho_0 \frac{u^2}{c^2} + 3\delta\rho \frac{e_\alpha u}{c^2} + \frac{9}{2}\delta\rho \frac{(e_\alpha u)^2}{c^4} - \frac{3}{2}\delta\rho \frac{u^2}{c^2} \right]$$

$$\therefore f_\alpha^{eq}(x,t) = \omega_\alpha \left[\rho + \rho_0 \left(3\frac{e_\alpha u}{c^2} + \frac{9}{2}\frac{(e_\alpha u)^2}{c^4} - \frac{3}{2}\frac{u^2}{c^2} \right) \right] \quad \text{A-2.9}$$

Which is the equilibrium distribution function for the LBM., and Mach Nr. $\left[M = \frac{|u|}{c} \right]$

Define the local pressure distribution function:

$$p_\alpha = c_s^2 f_\alpha \quad \text{A-2.10}$$

From (10) in (1)

$$p_\alpha(x + e_\alpha \delta_t, t + \delta_t) - p_\alpha(x,t) = -\frac{p_\alpha(x,t) - p_\alpha^{eq}(x,t)}{\tau} \quad \text{A-2.11}$$

From (10) in (9)

$$p_\alpha^{eq}(x,t) = \omega_\alpha \left[p + p_0 \left(3\frac{e_\alpha u}{c^2} + \frac{9}{2}\frac{(e_\alpha u)^2}{c^4} - \frac{3}{2}\frac{u^2}{c^2} \right) \right] \quad \text{A-2.12}$$

Where $p = \sum_\alpha p_\alpha = c_s^2 \sum_\alpha f_\alpha = c_s^2 \rho$

Equations (11) and (12) are the LBM for incompressible flow, and to develop the Navier-Stokes form, the Chapman-Enskog algorithm will be followed as shown below

Expand with Taylor series:

$$f_\alpha(x + e_\alpha \delta_t, t + \delta_t) = \sum_{n=0}^{\infty} \frac{\varepsilon^n}{n!} D_t^n f_\alpha(x,t) \quad \text{A-2.13}$$

$$f_\alpha = \sum_{n=0}^{\infty} \varepsilon^n f_\alpha^{(n)} \quad \text{A-2.14}$$

$$\partial_t = \sum_{n=1}^{\infty} \varepsilon^n \partial_{t_{(n)}} \quad \text{A-2.15}$$

Where

$$\varepsilon = \delta_t \quad \text{A-2.16}$$

is the Knudsen Nr., and

$$D_t{}^{(n)} = \partial_{t_{(n)}} + e_\alpha . \nabla \quad \text{A-2.17}$$

For incompressible flow, M is in $o(\varepsilon)$ and $\delta\rho$ is in (ε^2) , therefore the maximum important power of ε is the 2nd degree.

Eqn (13) becomes:

$$f_\alpha(x + e_\alpha \delta_t, t + \delta_t) = \varepsilon^0 D_t^{(0)} f_\alpha(x,t) + \varepsilon^1 D_t^{(1)} f_\alpha(x,t) + \frac{\varepsilon^2}{2} D_t^{(2)} f_\alpha(x,t) \quad \text{A-2.18}$$

Eqn (14) becomes:

$$f_\alpha = \varepsilon^0 f_\alpha^{(0)} + \varepsilon^1 f_\alpha^{(1)} + \varepsilon^2 f_\alpha^{(2)} \quad \text{A-2.19}$$

Eqn (15) becomes:

$$\partial_t = \varepsilon^1 \partial_{t_{(1)}} + \varepsilon^2 \partial_{t_{(2)}} \quad \text{A-2.20}$$

Substituting (17), (18), (19), and (20) in (1)

$$\varepsilon^0 D_t^{(0)} f_\alpha + \varepsilon^1 D_t^{(1)} f_\alpha + \frac{\varepsilon^2}{2} D_t^{(2)} f_\alpha - f_\alpha = -\frac{f_\alpha - f_\alpha^{eq}}{\tau}$$

$$\begin{aligned}
\therefore \varepsilon^0 D_t^{(0)} \left\{\varepsilon^0 f_\alpha^{(0)} + \varepsilon^1 f_\alpha^{(1)} + \varepsilon^2 f_\alpha^{(2)}\right\} + \varepsilon^1 \left\{\left(\varepsilon^1 \partial_{t_{(1)}}\right) + e_\alpha . \nabla\right\} \left\{\varepsilon^0 f_\alpha^{(0)} + \varepsilon^1 f_\alpha^{(1)} + \varepsilon^2 f_\alpha^{(2)}\right\} \\
+ \frac{\varepsilon^2}{2} \left\{\left(\varepsilon^1 \partial_{t_{(1)}} + \varepsilon^2 \partial_{t_{(2)}}\right) + e_\alpha . \nabla\right\} \left\{\varepsilon^0 f_\alpha^{(0)}\right\} - \left\{\varepsilon^0 f_\alpha^{(0)} + \varepsilon^1 f_\alpha^{(1)} + \varepsilon^2 f_\alpha^{(2)}\right\} \\
= -\frac{\left\{\varepsilon^0 f_\alpha^{(0)} + \varepsilon^1 f_\alpha^{(1)} + \varepsilon^2 f_\alpha^{(2)}\right\} - f_\alpha^{eq}}{\tau}
\end{aligned}$$

$$\begin{aligned}
\therefore \varepsilon^1 \left\{\left(\varepsilon^1 \partial_{t_{(1)}}\right) + e_\alpha . \nabla\right\} \left\{\varepsilon^0 f_\alpha^{(0)} + \varepsilon^1 f_\alpha^{(1)} + \varepsilon^2 f_\alpha^{(2)}\right\} \\
+ \frac{\varepsilon^2}{2} \left\{\left(\varepsilon^1 \partial_{t_{(1)}} + \varepsilon^2 \partial_{t_{(2)}}\right) + e_\alpha . \nabla\right\} \left\{\varepsilon^0 f_\alpha^{(0)}\right\} \\
= -\frac{\left\{\varepsilon^0 f_\alpha^{(0)} + \varepsilon^1 f_\alpha^{(1)} + \varepsilon^2 f_\alpha^{(2)}\right\} - f_\alpha^{eq}}{\tau}
\end{aligned} \quad \text{A-2.21}$$

The coefficient of ε^0 in both sides of eqn (21) brings:

$$0 = -\frac{\left\{f_\alpha^{(0)}\right\} - f_\alpha^{eq}}{\tau}$$

$$\therefore f_\alpha^{(0)} = f_\alpha^{eq} \quad \text{A-2.22}$$

The coefficient of ε^1 in both sides of eqn (21) brings:

$$e_\alpha . \nabla f_\alpha^{(0)} = -\frac{f_\alpha^{(1)}}{\tau}$$

$$\therefore \left(\partial_{t_{(0)}} + e_\alpha . \nabla\right) f_\alpha^{(0)} = -\frac{f_\alpha^{(1)}}{\tau}$$

$$\therefore D_t^{(0)} f_\alpha^{(0)} = -\frac{f_\alpha^{(1)}}{\tau} \quad \text{A-2.23}$$

The coefficient of ε^2 in both sides of eqn (21) brings:

$$\therefore \partial_{t_{(1)}} f_\alpha^{(0)} + e_\alpha . \nabla f_\alpha^{(1)} + \frac{e_\alpha . \nabla f_\alpha^{(0)}}{2} = -\frac{f_\alpha^{(2)}}{\tau}$$

$$\therefore \partial_{t_{(1)}} f_\alpha^{(0)} + D_t^{(0)} f_\alpha^{(1)} + \frac{D_t^{(0)} f_\alpha^{(0)}}{2} = -\frac{f_\alpha^{(2)}}{\tau}$$

With the information of eqn (23)

$$\therefore \partial_{t_{(1)}} f_\alpha^{(0)} + D_t^{(0)} f_\alpha^{(1)} - \frac{f_\alpha^{(1)}}{2\tau} = -\frac{f_\alpha^{(2)}}{\tau}$$

$$\therefore \partial_{t_{(1)}} f_\alpha^{(0)} + \left(\frac{2\tau - 1}{2\tau}\right) D_t^{(0)} f_\alpha^{(1)} = -\frac{f_\alpha^{(2)}}{\tau} \quad \text{A-2.24}$$

From eqn (7) and (8)

$$\sum_\alpha f_\alpha^{(eq)} \begin{bmatrix} 1 \\ e_\alpha \end{bmatrix} = \sum_\alpha f_\alpha^{(0)} \begin{bmatrix} 1 \\ e_\alpha \end{bmatrix} = \begin{bmatrix} \rho \\ \rho_0 u \end{bmatrix} \quad \text{A-2.25}$$

And because it is incompressible fluid

$$\sum_\alpha f_\alpha^{(n)} \begin{bmatrix} 1 \\ e_\alpha \end{bmatrix} = \begin{bmatrix} 0 \\ 0 \end{bmatrix} \quad \text{A-2.26}$$

f_α is also called Chapman-Enskog ansatz (i.e., the time dependent of f_α is through the hydrodynamic variables ρ, u, and temperature if applied $\left[\partial_t f_\alpha = \frac{\partial f_\alpha}{\partial \rho} \partial_t \rho + \frac{\partial f_\alpha}{\partial u} \partial_t u\right]$

Tensor notation for 9 bit model:

$$e_{\alpha i} = e_{\alpha j} \delta_{ij}$$

Where δ_{ij} is the kronecker of a tensor

With the aid of eqn(3)

$$\sum_{\alpha=1}^{4} e_{\alpha_i} e_{\alpha_j} = \delta_{ij} \sum_{\alpha=1}^{4} e_{\alpha_i} e_{\alpha_i} = \delta_{ij}(c.c + 0 + (-c)(-c) + 0) = 2c^2 \delta_{ij}$$

and

$$\sum_{\alpha=5}^{8} e_{\alpha_i} e_{\alpha_j} = \delta_{ij}(c.c + (-c)(-c) + (-c)(-c) + c.c) = 4c^2 \delta_{ij}$$

And the tensor form for this 9 bit model is

$$E^{(n)} = \sum_{\alpha \neq 0} \omega_\alpha e_{\alpha_1} e_{\alpha_2} \dots . e_{\alpha_n}$$

And therefore

$$E^{(2)} = \sum_{\alpha \neq 0} \omega_\alpha e_{\alpha_i} e_{\alpha_j} = \sum_{\alpha=1}^{4} \omega_\alpha e_{\alpha_i} e_{\alpha_j} + \sum_{\alpha=5}^{8} \omega_\alpha e_{\alpha_i} e_{\alpha_j} = \frac{2}{9} c^2 \delta_{ij} + \frac{4}{36} c^2 \delta_{ij} = \frac{1}{3} c^2 \delta_{ij} \quad \text{A-2.27}$$

And in the same way

$$E^{(4)} = \sum_{\alpha \neq 0} \omega_\alpha e_{\alpha_i} e_{\alpha_j} e_{\alpha_k} e_{\alpha_l} == \frac{1}{9} c^4 \delta_{ij} \quad \text{A-2.28}$$

Note that *n* should be even, because if we choose a direction, we have to take the perpendicular to it as well.

Therefore

$$\sum_{\alpha} e_{\alpha i} e_{\alpha j} f_{\alpha}^{(0)} = \frac{1}{3} c^2 \rho \delta_{ij} + \rho_0 u_i u_j \qquad \text{A-2.29}$$

And

$$\sum_{\alpha} e_{\alpha i} e_{\alpha j} e_{\alpha k} f_{\alpha}^{(0)} = \frac{1}{3} c^2 \rho_0 \left(\delta_{ij} u_k + \delta_{ki} u_j + \delta_{jk} u_i\right) \qquad \text{A-2.30}$$

From eqns (23), (24), (25), and (26)

$$\sum_{\alpha} D_t^{(0)} f_{\alpha}^{(0)} = -\frac{1}{\tau} \sum_{\alpha} f_{\alpha}^{(1)}$$

$$\sum_{\alpha} \left(\partial_{t_{(0)}} + e_{\alpha}.\nabla\right) f_{\alpha}^{(0)} = 0$$

$$\partial_{t_{(0)}} \sum_{\alpha} f_{\alpha}^{(0)} + \nabla \sum_{\alpha} e_{\alpha} f_{\alpha}^{(0)} = 0 \qquad \text{A-2.31}$$

$$\partial_{t_{(0)}} \rho + \nabla(\rho_0 u) = 0 \qquad \text{A-2.32}$$

The momentum of eqn (*31*)

$$\partial_{t_{(0)}} \sum_{\alpha} e_{\alpha} f_{\alpha}^{(0)} + \nabla \sum_{\alpha} e_{\alpha} e_{\alpha} f_{\alpha}^{(0)} = 0$$

$$\partial_{t_{(0)}} (\rho_0 u) + \nabla \pi^{(0)} = 0 \qquad \text{A-2.33}$$

Where $\pi^{(0)}$ is the zero order momentum flux tensor, and can be calculated from eqn(29)

$$\partial_{t_{(0)}} (\rho_0 u) + \nabla \left(\frac{1}{3} c^2 \rho \delta_{ij} + \rho_0 u_i u_j\right) = 0 \qquad \text{A-2.34}$$

Defining the normalized pressure to be

$$P = \frac{c_s^2 \rho}{\rho_0} \qquad \text{A-2.35}$$

Eqn (35) in equation (32)

$$\partial_{t_{(0)}} \frac{P \rho_0}{c_s^2} + \nabla(\rho_0 u) = 0$$

$$\frac{\rho_0}{c_s^2} \partial_{t_{(0)}} P + \rho_0 \nabla(u) = 0$$

$$\frac{1}{c_s^2} \partial_{t_{(0)}} P + \nabla(u) = 0 \qquad \text{A-2.36}$$

Eqn (35) in equation (34)

$$\rho_0 \partial_{t_{(0)}} u + \nabla\left({c_s}^2 \rho \delta_{ij} + \rho_0 u_i u_j\right) = 0$$

$$\rho_0 \partial_{t_{(0)}} u + \nabla\left(P\rho_0\delta_{ij} + \rho_0 u_i u_j\right) = 0$$

$$\partial_{t_{(0)}} u + u.\nabla u = -\nabla P - u\nabla.\,\mathrm{u} \qquad \text{A-2.37}$$

The same will be done with eqn(24) with a substitution of eqn (25) and (26)

$$\sum_\alpha \partial_{t_{(1)}} f_\alpha^{(0)} + \left(\frac{2\tau-1}{2\tau}\right)\sum_\alpha D_t^{(0)} f_\alpha^{(1)} = -\frac{1}{\tau}\sum_\alpha f_\alpha^{(2)} \qquad \text{A-2.38}$$

$$\partial_{t_{(1)}}\rho + \left(\frac{2\tau-1}{2\tau}\right)(0) = -\frac{1}{\tau}\ (0)$$

$$\partial_{t_{(1)}}\rho = 0 \qquad \text{A-2.39}$$

The momentum of eqn(38)

$$\sum_\alpha \partial_{t_{(1)}} e_\alpha f_\alpha^{(0)} + \left(\frac{2\tau-1}{2\tau}\right)\sum_\alpha D_t^{(0)} e_\alpha f_\alpha^{(1)} = -\frac{1}{\tau}\sum_\alpha e_\alpha f_\alpha^{(2)}$$

$$\partial_{t_{(1)}}(\rho_0 u) + \left(\frac{2\tau-1}{2\tau}\right)\nabla\sum_\alpha e_\alpha e_\alpha f_\alpha^{(1)} = -\frac{1}{\tau}\ (0)$$

$$\partial_{t_{(1)}}(\rho_0 u) + \left(\frac{2\tau-1}{2\tau}\right)\nabla\pi^{(1)} = 0 \qquad \text{A-2.40}$$

Where $\pi^{(1)}$ is the first order momentum flux tensor and can be obtained as follows by the aid of eqns (23), and (30)

$$\pi_{ij}^{(1)} = \sum_\alpha e_{\alpha_i} e_{\alpha_j} f_\alpha^{(1)} = -\tau\sum_\alpha e_{\alpha_i} e_{\alpha_j} D_t^{(0)} f_\alpha^{(0)} - \tau\sum_\alpha e_{\alpha_i} e_{\alpha_j}\left(\partial_{t_{(0)}} + e_\alpha.\nabla\right) f_\alpha^{(0)}$$

$$= -\tau\left[\partial_{t_{(0)}}\pi_{ij}^{(0)} + \frac{1}{3}c^2\rho_0\left(\delta_{ij}\nabla u + \delta_{ki}\nabla u_j + \delta_{jk}\nabla u_i\right)\right]$$

$$= -\tau\left[\rho_0\partial_{t_{(0)}}\left(u_i u_j\right) + {c_s}^2\rho_0\left(\nabla_i u_j + \nabla_j u_i\right)\right]$$

$$\pi_{ij}^{(1)} = -\tau\big[{c_s}^2\left(u_i\rho + u_j\nabla_i\rho\right) + \rho_0\left(u_i(u.\nabla)u_j + u_j(u.\nabla)u_i\right) + {c_s}^2\rho_0\left(\nabla_i u_j + \nabla_j u_i\right)\big] \qquad \text{A-2.41}$$

And neglect all the higher orders (i.e., $o(M^3)$)from eqn(41) which are terms contain $u^3, u_i\nabla_j\rho, \nabla_j\nabla_i u, \ldots$

$$\therefore \pi_{ij}^{(1)} = -\tau{c_s}^2\rho_0\left(\nabla_i u_j + \nabla_j u_i\right) + o(M^3) \qquad \text{A-2.42}$$

From eqn(42) into eqn(40)

$$\partial_{t_{(1)}}(\rho_0 u) + \left(\frac{2\tau-1}{2\tau}\right)\nabla_j\pi_{ij}^{(1)} = 0$$

$$\partial_{t_{(1)}}(\rho_0 u) + \left(\frac{2\tau-1}{2\tau}\right)\left[-\tau{c_s}^2\nabla_j\rho_0\left(\nabla_i u_j + \nabla_j u_i\right)\right] + o(M^3) = 0$$

$$\partial_{t_{(1)}}(\rho_0 u) - \left(\frac{2\tau-1}{2}\right)\left[{c_s}^2\rho_0\left(\nabla_j\nabla_i u_j + \nabla^2 u_i\right)\right] + o(M^3) = 0$$

$$\partial_{t_{(1)}}(\rho_0 u) - \left(\frac{2\tau-1}{2}\right)\left[{c_s}^2\rho_0\left(o(M^3) + \nabla^2 u_i\right)\right] + o(M^3) = 0$$

$$\partial_{t_{(1)}}(\rho_0 u) - \left(\frac{2\tau-1}{2}\right)[{c_s}^2 \rho_0 \nabla^2 u_i\,] = 0$$

$$\therefore\ \partial_{t_{(1)}} u - \left(\frac{2\tau-1}{2}\right){c_s}^2 \nabla^2 u_i = 0 \qquad \text{A-2.43}$$

Now we will add eqn(36) to eqn(39)

$$\frac{1}{c_s^2}\partial_{t_{(0)}} P + \nabla(u) + \partial_{t_{(1)}}\rho = 0$$

$$o(M^2) + \nabla.u + o(M^2) = 0$$

$$\therefore\ \nabla.u = 0 \qquad \text{A-2.44}$$

Which is the continuity equation of the Navier-Stokes eqns, with $o(M^2)$

Now we will add eqn(37) to eqn(43)

$$\partial_{t_{(0)}} u + u.\nabla u + \partial_{t_{(1)}} u - \left(\frac{2\tau-1}{2}\right){c_s}^2 \nabla^2 u_i = -\nabla P - u\nabla.\,\mathrm{u}$$

$$\partial_{t_{(0)}} u + u.\nabla u + \partial_{t_{(1)}} u - \left(\frac{2\tau-1}{2}\right){c_s}^2 \nabla^2 u = -\nabla P + o(M^3)$$

$$\left(\partial_{t_{(0)}} + \partial_{t_{(1)}}\right) u + u.\nabla u = -\nabla P + \left(\frac{2\tau-1}{2}\right){c_s}^2 \nabla^2 u$$

Since $\partial_t = \partial_{t_{(0)}} + \varepsilon\partial_{t_{(1)}}$ and taking $\varepsilon = 1$

$$\partial_t u + u.\nabla u = -\nabla P + \left(\frac{2\tau-1}{6}\right)c^2 \nabla^2 u \qquad \text{A-2.45}$$

Which is the momentum equation of the Navier-Stokes eqns, with $o(M^3)$. And the viscosity term is

$$\frac{\nu}{\delta_t} = \frac{2\tau-1}{6}c^2$$

$$\therefore\ \nu = \frac{2\tau-1}{6}\left(\frac{\delta_x}{\delta_t}\right)^2 \delta_t = \left(\frac{2\tau-1}{6}\right)\frac{{\delta_x}^2}{\delta_t} \qquad \text{A-2.46}$$

A-3. Linear and non-Linear Stability of the Lattice Boltzmann Method

The time evolution of BGK lattice Boltzmann models is described by the kinetic equation

$$F_m\left(x+c_m,t+1\right)=F_m\left(x,t\right)-\omega\left[F_m\left(x,t\right)-F_m^{(0)}\left(x,t\right)\right] \qquad \text{A-3.1}$$

Inspection of Eq. (A 3.1) shows that an initially uniform flow, in the sense

$$F_m\left(x,t_0\right)=F_m\left(t_0\right) \qquad \text{A-3.2}$$

Will remain uniform at all later times and thus

$$F_m\left(t+1\right)=F_m\left(t\right)-\omega\left[F_m\left(t\right)-F_m^{(0)}\left(t\right)\right]. \qquad \text{A-3.3}$$

Furthermore, mass and momentum density are conserved and retain their initial value

$$\rho\left(x,t\right)=\rho\left(t_0\right)=\rho_0,\quad j\left(x,t\right)=j\left(t_0\right)=j_0 \qquad \text{A-3.4}$$

$$F_m\left(t+1\right)=F_m-\omega\left[F_m\left(t\right)-F_m^{(0)}\left(\rho_0,j_0\right)\right]. \qquad \text{A-3.5}$$

Subtracting $F_m^{(0)}\left(\rho_0,j_0\right)$ on both sides leads to

$$\tilde{F}_m\left(t+1\right)=\left(1-\omega\right)\tilde{F}_m\left(t\right) \qquad \text{A-3.6}$$

With $\tilde{F}_m\left(t\right)=F_m\left(t\right)-F_m^{(0)}\left(\rho_0,j_0\right)$. The evolution is stable in the sense that the magnitude of $\tilde{F}_m$ does not increase with time $\left(\left|\tilde{F}_m\left(t+1\right)\right|\le\left|\tilde{F}_m\left(t\right)\right|\right)$ if $\left|1-\omega\right|\langle 1 \;\rightarrow\; 0\langle\omega\langle 2$ or $\frac{1}{\omega}=\tau\rangle\frac{1}{2}$

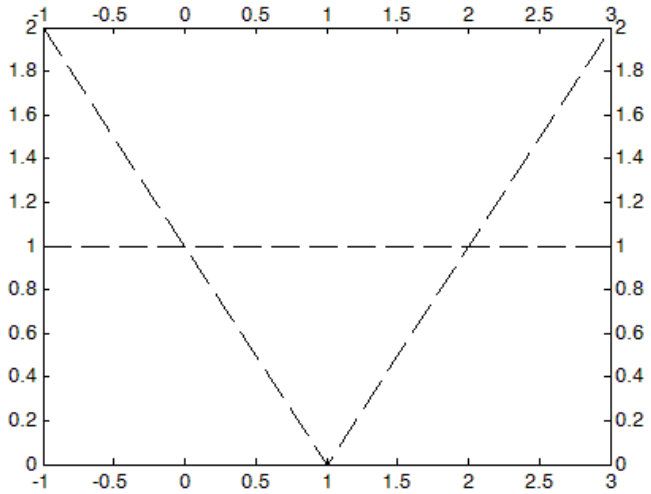

Figure A-3.1 Stability range of BGK models.

Non-Linear Stability of the Lattice Boltzmann Method

The stability of numerical schemes is a study how the error propagates with time. A scheme is stable if the errors made at one time step of the calculation do not cause the errors to

increase (remain bounded) as the computations are continued. The stability of numerical schemes can be investigated by performing von Neumann stability analysis. For time-dependent problems, stability guarantees that the numerical method produces a bounded solution whenever the solution of the exact differential equation is bounded. Stability, in general, can be difficult to investigate, especially when equations under consideration are nonlinear.

The lattice Boltzmann equation is an explicit non-linear scheme due to the presence of the quadratic equilibrium distribution function in the collision term. In a preliminary stability assessment 'Benzi et al [70], performed the LBE stability analysis while neglecting nonlinear terms. In contrast, the work of Sterling et al [71] considered a linearized stability analysis of the LB scheme.

In this work the same approach was followed in treatment of nonlinear terms, where all non linear terms were linearized about global values (denoted by an over bar) were the energy is conserved. Furthermore, the methodology was developed to include single phenomenon systems and as well multi-systems.

Expanding f_i as:

$$f_i(x,t) = \overline{f_i^{(0)}} + f_i'(x,t) \qquad \text{A-3.7}$$

The global equilibrium distributions $\overline{f_1^{(0)}}$ are constants that do not vary with space and time and depend only on the mean density and velocity. The fluctuating distributions f_i' represent the density and velocity deviation from the mean values of local equilibrium. Those local disturbances are more convenient for energy conserving methods.

The update operator g_i (f_j) of the particle distribution is defined as:

$$g_i\left(f_j\right) = f_i(x,t) - \frac{1}{\tau}\left(f_i(x,t) - f_i^{(0)}(x,t)\right) \qquad \text{A-3.8}$$

All the j distributions at a site enter through the equilibrium distribution function on the right side of the equation.

Expanding $g(\overline{f_1^{(0)}})$ using Taylor series:

$$\overline{f_i^{(0)}} + f_i'(x + e_i\Delta t, t + \Delta t) = g_i\left(\overline{f_j^{(0)}}\right) + \frac{\partial g_i\left(\overline{f_j^{(0)}}\right)}{\partial f_j} f_j'(x,t) + O\left(f_i'(x,t)^2\right) \qquad \text{A-3.9}$$

Since $\overline{f_i^{(0)}} = g_i\left(\overline{f_j^{(0)}}\right)$ It can be easily reached that:

$$f_i'(x + e_i\Delta t, t + \Delta t) = G_{ij} f_j'(x,t) \qquad \text{A-3.10}$$

Where Gij is the Jacobian matrix corresponding to the coefficient of the linearized system; e is the dimensionless discrete velocity; the matrix Mij is the Maxwellian equilibrium distribution of the mean flow particles.

$$G_{ij} = \left(1 - \frac{1}{\tau}\right)\delta_{ij} + \frac{1}{\tau} M_{ij}$$

$$M_{ij} = w_i \left[1 + 3\left(e_i . e_j\right) - \frac{3}{2}\left(2(e_j . u_0') - u_0'^2\right) + \frac{9}{2}\left(2(e_i . u_0')\left(e_i . e_j\right) - (e_j . u_0')^2\right)\right] \quad \text{A-3.11}$$

Applying the Fourier transform to the previous equation we retrieve:

$$F_i(k, t + \Delta t) = \Gamma_{ij} F_j(k, t) \quad \text{A-3.12}$$

Where

$$\Gamma_{ij} = \exp\left[-ik . e_i \Delta t\right] G_{ij} \quad \text{A-3.13}$$

The $F_{j(k,t)}$ is the Fourier transform of $f_i(x, t)$, k is the wave number in units of $1/\delta x$, u_0' is the non-dimensional uniform velocity. The eigenvalues of Γij determine the numerical stability of the linearized LBE.

The eigenvalues of the matrix Mij are $\{1,0\}$ independently of u_0'. As well the eigenvalue of the matrix Gij is $\{1 - 1/\tau\}$. It is clear that the equation will be asymptotically stable if and only if $|1 - 1/\tau| < 1$ i.e. $\tau \geq 0.5$.

A-4. Derivation of Surface Tension Interface Separation Parameter

In order to derive a theoretical expression for the value of the surface tension coefficient, recall the mechanical definition of surface tension

$$\sigma = \int_{-\infty}^{\infty} \left(P_N - P_T\right) dz \qquad \text{A-4.1}$$

Where: P_N and P_T are normal and tangential components of the pressure tensor and z is the direction perpendicular to the interface (Rowlinson and Windom, 1982). Consider a box of fluid of dimension n_i on axis x_i with an interface in the center of box (for the three dimensional model, n_4 is the set to 1 to project the 4D FCHC lattice to three dimensions). I will also assume, without loss of generality, that f_1 is the largest component of the field so that equation (A 4.1) can be converted to an integral over the x_1 axis with suitable scaling factors.

For a lattice gas at the rest, P_N and P_T are given by

$$\begin{aligned} P_N &= \sum_{i=1}^{M_m} N_i c_{iN} c_{iN} \\ P_T &= \sum_{i=1}^{M_m} N_i c_{iT} c_{iT} \end{aligned} \qquad \text{A-4.2}$$

Where c_{iN} and c_{iT} are the components of the velocity normal and tangential to the interface (Frisch et al., 1987). If the small variations in the direction of the color gradient caused by the discrete lattice are neglected and it is assumed that $f/|f|$ is constant, then

$$\begin{aligned} c_{iN} &= \frac{\left(c_i \cdot f\right)}{\left(f \cdot f\right)^{1/2}} \\ c_{iT} &= \frac{\left(c_i \cdot f^{\perp}\right)}{\left(f^{\perp} \cdot f^{\perp}\right)^{1/2}} \end{aligned} \qquad \text{A-4.3}$$

where $f^{\perp}$ is any vector perpendicular of *f*. Conversion of the integral of equation (A 4.1) to a sum over entire lattice then gives

$$\sigma = S^{-1} \cos\Theta_1 \sum_x \sum_i \left(c_{iN}^2 - c_{iT}^2\right) N_i \qquad \text{A-4.4}$$

where S ist he cross- sectional area of the box, given by

$$S = \begin{cases} n_2 & \text{in 2D} \\ n_2 n_3 & \text{in 3D} \end{cases} \qquad \text{A-4.5}$$

and Θ_1 ist he angle between f and the x_1 axis and we are averaging the calculation over S lines along the x_1 axis. Denoting $\left(c_{iN}^2 - c_{iT}^2\right)$ as U_i and observing that $\sum_i U_i N_i^{eq} = 0$ to the first order in velocity, we find that

$$\sigma = S^{-1} \cos\Theta_1 \sum_x \sum_i U_i N_i^{neq}. \qquad \text{A-4.6}$$

Sum the Boltzmann evolution equation (2.15) with the surface- tension including perturbation (2.32) over the entire lattice to find

$$\sum_x N_i\left(x+c_i,t+1\right)=\sum_x\left(N_i\left(x,t\right)+\sum_x\Omega_{ij}N_i^{neq}\left(x,t\right)+C_i\left(x,t\right)\right) \qquad \text{A-4.7}$$

For a lattice at steady state with reasonable boundary conditions such as bounce- back conditions (Cornubert et al., 1991)

$$\sum_x N_i\left(x+c_i,t+1\right)=\sum_x N_i\left(x,t\right) \qquad \text{A-4.8}$$

$$\sum_x\left(\sum_j\Omega_{ij}N_j^{neq}\left(x\right)+C_i\left(x\right)\right)=0 \qquad \text{A-4.9}$$

Multiply both sides by U_i, which is an eigenvector of Ω with eigenvector λ , and the sum over i to obtain

$$\sum_x\sum_i\left(\lambda U_i N_i^{neq}\left(x\right)+U_i C_i\left(x\right)\right)=0 \qquad \text{A-4.10}$$

Resulting in the following expression for the surface tension σ :

$$\begin{aligned}\sigma&=-\left(\lambda S\right)^{-1}\cos\Theta_1\sum_x\sum_i U_i A\left|f\right|\left[\frac{\left(c_i\cdot f\right)^2}{f\cdot f}-\frac{1}{2}\right]\\&=-\left(\lambda S\right)^{-1}\cos\Theta_1\sum_x A\left|f\right|B\end{aligned} \qquad \text{A-4.11}$$

Where:

$$\begin{aligned}B&=\sum_i U_i\left[\frac{\left(c_i\cdot f\right)^2}{f\cdot f}-\frac{1}{2}\right]\\&=\sum_i\frac{\left(c_i\cdot f\right)^2}{f\cdot f}\left(\frac{\left(c_i\cdot f\right)^2}{f\cdot f}-\frac{\left(c_i\cdot f^{\perp}\right)^2}{f^{\perp}\cdot f^{\perp}}\right)\end{aligned} \qquad \text{A-4.12}$$

For the FHP lattice B=3 and for the FCHC lattice B=8, giving

$$\sigma = \begin{cases} -(\lambda S)^{-1} 3A\cos\Theta_1 \sum_x |f| & \text{in 2D} \\ -(\lambda S)^{-1} 8A\cos\Theta_1 \sum_x |f| & \text{in 3D} \end{cases} \qquad \text{A-4.13}$$

For a thin interface we can explicitly compute the sum of $|f|$. As we integrate along the line perpendicular to the interface there are three sites which contribute to the sum. The mixed site on the interface contributes $M_m M_t d/2\cos\Theta_1$ to the sum and the two neighboring sites each contribute a term half this size. Thus the sum is given by

$$\sum_x |f| = \frac{S}{\cos\Theta_1} M_m M_t d \qquad \text{A-4.14}$$

I thus obtain an explicit, isotropic expression for the surface tension,

$$\sigma = \begin{cases} -(\lambda S)^{-1} 3A\cos\Theta_1 \sum_x |f| & \text{in 2D} \\ -(\lambda S)^{-1} 8A\cos\Theta_1 \sum_x |f| & \text{in 3D} \end{cases} \qquad \text{A-4.15}$$